Leonardo Taynô Tosetto Soethe

Extremely low-mass white dwarfs in interacting binary systems

Porto Alegre

2021

Leonardo Taynô Tosetto Soethe

Extremely low-mass white dwarfs in interacting binary systems

Thesis proposal submitted to Programa de Pós-Graduação em Física at Universidade Federal do Rio Grande do Sul as a partial requirement for the degree of Doctor of Sciences.

Universidade Federal do Rio Grande do Sul – UFRGS

Instituto de Física

Programa de Pós-Graduação em Física

Supervisor: Prof. Dr. Kepler de Souza Oliveira Filho

Co-supervisor: Prof[a]. Dra. Alejandra Daniela Romero

Porto Alegre

2021

Soethe, Leonardo Taynô Tosetto
Extremely low-mass white dwarfs in interacting binary systems / Leonardo Taynô Tosetto Soethe. – Porto Alegre, 2021.
250p. : il. (algumas color.) ; 30 cm.

Supervisor: Prof. Dr. Kepler de Souza Oliveira Filho

Tese (Doutorado) – Universidade Federal do Rio Grande do Sul – UFRGS
Instituto de Física
Programa de Pós-Graduação em Física, 2021.

1. white dwarfs. 2. extremely low mass white dwarfs. 3. magnetic braking. 4. interacting binaries. 5. close binaries. I. Kepler, S.O. II. Título

Leonardo Taynô Tosetto Soethe

Extremely low-mass white dwarfs in interacting binary systems

Thesis proposal submitted to Programa de Pós-Graduação em Física at Universidade Federal do Rio Grande do Sul as a partial requirement for the degree of Doctor of Sciences.

Trabalho aprovado. Porto Alegre, 02 de dezembro de 2021:

Prof. Dr. Kepler de Souza Oliveira Filho
Supervisor

Prof[a]. Dra. Alejandra Daniela Romero
Co-supervisor

Prof. Dr. Marcos Perez Diaz
IAG-USP/SP

Prof[a]. Dra. Cláudia Vilega Rodrigues
INPE/SJC

Prof. Dr. Alan Alves Brito
UFRGS/RS

Prof. Dr. Charles José Bonatto
UFRGS/RS

Porto Alegre
2021

Dedico este trabalho àqueles a quem possa interessar.
Que faça bom proveito!

I dedicate this work to those to whom it may interest.
Enjoy it!

Acknowledgements

I am very grateful to my mom and dad for their inspiration, support, and encouragement.

I am grateful to Kepler de Souza Oliveira Filho and Alejandra Daniela Romero, who have been wonderful supervisors, advisors, teachers, and mentors for the past four years.

Special greetings to all the teachers I've had and friends I've made from the beginning of my education until now; passing through SL, NH (FETLSVC), Pel (UFPel), SJC (ITA/INPE), and POA (UFRGS).

To TSL, my inspiration and motivation.

I am grateful to Alina G. Istrate, who first suggested investigating the modification of magnetic braking in extremely low mass white dwarf models.

I thank Ingrid Pelisoli for sharing the updated ELM WDs table and for providing the Gaia DR2 data with reddening corrections.

I would also like to thank my colleagues in Astrophysics at UFRGS and, in particular, everyone from the White Dwarf Group. I always learned a lot from you!

Special thanks to all members of the examining board, who contributed many suggestions for improvements: Marcos Perez Diaz, Cláudia Vilega Rodrigues, Alan Alves Brito, Charles José Bonatto, and Luiz Fernando Ziebell. I also thank Sílvia Helena Paixão Alencar and Elisabete Maria de Gouveia Dal Pino for their support and for being alternates.

To all Osmarini/Tosetto and Niehues/Soethe spread around the world.

Also, my sincere thanks to:

i) the Instituto de Física (IF) and the Programa de Pós-Graduação em Física (PPGFís) of the Universidade Federal do Rio Grande do Sul (UFRGS) for providing the structure and materials necessary for the development of this work;

ii) the Conselho Nacional de Desenvolvimento Científico e Tecnológico (CNPq) and Coordenação de Aperfeiçoamento de Pessoal de Nível Superior (CAPES) for the financial support;

iii) all MESA[1] team and code developers;

iv) the SAO/NASA Astrophysics Data System (ADS)[2], a digital library portal for

[1] <https://docs.mesastar.org/>,<https://zenodo.org/communities/mesa>,<http://cococubed.asu.edu/mesa_market/>,<http://mesa.sourceforge.net/>

[2] <https://ui.adsabs.harvard.edu/>

researchers in astronomy and physics. This research has made use of NASA's Astrophysics Data System;

v) the arXiv[3], an e-print service in the fields of physics and others;

vi) all *abnTEX2*[4] developers and contributors.

[3] <https://arxiv.org/archive/astro-ph>
[4] <https://www.abntex.net.br/>

"Eternal light
These gravely digs of mine
Will surely prove a sight
Astronomy — a star"
(Astronomy — Blue Öyster Cult/Metallica)

"Um homem acredita mais facilmente no que gostaria que fosse verdade.
Assim, ele rejeita coisas difíceis pela impaciência de pesquisar;
coisas sensatas, porque diminuem a esperança;
as coisas mais profundas da natureza, por superstição;
a luz da experiência, por arrogância e orgulho;
coisas que não são comumente aceitas, por deferência à opinião do vulgo.
Em suma, inúmeras são as maneiras, e às vezes imperceptíveis, pelas quais os afetos
colorem e contaminam o entendimento."
(Francis Bacon)

Abstract

Extremely low-mass white dwarfs (ELM WDs) are understood to be the result of binary evolution in which a low-mass donor star — mass of the order of that of the Sun — is stripped by its companion, leaving behind a helium-core white dwarf with a mass below 0.2–0.3 solar masses and with surface gravity ten to a thousand times smaller than a canonical white dwarf. The overall objective of this work is to obtain ELM models compatible with the observed distribution of ELMs and pre-ELMs. Prior to the interaction (i.e., the mass transfer), the binary evolution is thought to be dominated by the magnetic braking mechanism, which is the main uncertainty in modelling such systems. In published models of the formation of the ELM WDs orbiting millisecond pulsars in very compact orbits (2–9 hours), a severe fine-tuning of the initial orbital period was necessary, suggesting that standard magnetic braking formulation needs to be revised. A modification to the traditional treatment of magnetic braking has been proposed by Van & Ivanova (2019), named Convection And Rotation Boosted (CARB). This recipe for the magnetic braking law includes two recent improvements in understanding stellar magnetic fields and magnetised winds, introducing changes in the evolution of low-mass X-ray binary (LMXB) systems due to the magnetic field strength and the rotation. Computing model sequences using the stellar evolutionary code MESA, we apply the CARB formulation to the formation of ELM WDs in LMXB systems and find that fine-tuning of the initial periods is not required. In particular, we find that for initial orbital periods in the range of 4–250 days, the final product of the evolution are ELM and low mass WDs with masses in the range 0.15–0.40 solar masses. Also, the bifurcation period — the initial orbital period that separates the systems which, at the end of evolution, will have their components close together or far apart — is shifted to longer ones (from 2.75–2.8 to 20–25 days) when the CARB magnetic braking is considered. As a result, we obtain ELM white dwarf models with masses as low as 0.26 solar mass in converging binary systems even with initial orbital periods as long as 20 days. We expand the model grid to study the effects of different initial parameters. The following scenarios were considered: increase of the donor star mass from 1.0 to 1.2 times the solar mass to decrease the main sequence lifetime; study different metallicities ($Z = 0.02$, 0.01 and 0.001) because there are progenitors from different parts of the Galaxy; study high (70%) and low (20%) efficiencies in mass transfer since this is a very uncertain parameter. We then repeat the same setups described above but considering a massive white dwarf (0.8 solar mass) accretor, compatible with cataclysmic variable (CV) systems. Our conclusion indicates that the CARB prescription is adequate to reproduce the observed LMXBs and CVs properties, even in the regime of short initial orbital periods. Comparing our models with observational data from He-WDs in binary systems with millisecond pulsars, the use of CARB magnetic braking is shown to be compatible with the formation of ELM WDs in LMXBs. In addition to the LMXB and CV systems, the

use of CARB magnetic braking makes it possible to form ultra-compact X-ray binaries (UCXB) systems and wide-orbit binary millisecond pulsars, as well as detached ELM WDs companions to neutron stars and massive white dwarfs. Nevertheless, data from ELM WDs in systems with white dwarf companions present great dispersion in mass and orbital period of the binary system, suggesting that other formation channels are also present. Note that we do not simulate Common Envelope models. In addition, we found that the observational properties such as effective temperature and surface gravity of these new models are compatible with the majority of confirmed or candidate ELM WDs. The combined result of the more than three hundred models we calculated makes it clear that the final mass of ELM WDs is a highly degenerate quantity in the studied parameter space, as there are numerous interdependencies between metallicity, hydrogen shell flash occurrence, efficiency of mass transfer, the initial mass of the stars, initial orbital period, and the reaction of the orbital separation regarding the mass transfer.

Keywords: white dwarfs. extremely low mass white dwarfs. magnetic braking. interacting binaries. close binaries.

Resumo

Anãs brancas de massa extremamente baixa (ELM WDs) são entendidas como o resultado da evolução binária na qual uma estrela doadora de baixa massa — massa da ordem da do Sol — é despida por sua companheira, deixando para trás uma anã branca com núcleo de hélio de massa de 0,2–0,3 massas solares e gravidade superficial de dez a mil vezes menor do que a de uma anã branca canônica. O objetivo geral deste trabalho é obter modelos de ELM compatíveis com a distribuição observada de ELMs e pré-ELMs. Antes da interação, (i.e., da transferência de massa), acredita-se que a evolução binária é dominada pelo mecanismo do freamento magnético, o qual é a maior fonte de incertezas na modelagem desse tipo de sistema. Nos modelos de formação de ELM WDs orbitando pulsares de milissegundos em órbitas muito compactas (2–9 horas) publicados, um severo ajuste fino no período orbital inicial foi necessário, sugerindo que a formulação do freamento magnético utilizado precisava ser revisada. Uma modificação ao tratamento do freamento magnético tradicional foi proposta por Van & Ivanova (2019), nomeada Convection And Rotation Boosted (CARB). Essa receita para a lei do freamento magnético inclui duas novas melhorias no entendimento dos campos e ventos magnéticos, introduzindo modificações na evolução de sistemas binários de raios-X de baixa massa (LMXB) devido à força do campo magnético e à rotação. Computando sequências de modelos usando o código de evolução estelar MESA, nós aplicamos a formulação CARB em modelos de formação de ELM WDs em sistemas binários compactos e encontramos que o ajuste fino severo no período orbital inicial não é mais necessário. Em particular, nós encontramos que para períodos orbitais no intervalo de 4–250 dias os produtos finais da evolução são ELMs e anãs brancas de baixa massa com massas no intervalo 0,15–0,40 massas solares. Também, o período de bifurcação — o período orbital inicial que separa os sistemas em que, ao final da evolução, terão seus componentes aproximados ou afastados — é deslocado para valores maiores (de 2,75–2,8 para 20–25 dias) quando o freamento magnético CARB é levado em conta. Como resultado, obtivemos modelos de ELM WDs com massas tão baixas quando 0,26 massas solares em sistemas convergentes mesmo com períodos orbitais iniciais tão longos quanto 20 dias. Nós expandimos a nossa grade de modelos para estudar os efeitos de diferentes parâmetros iniciais. Os seguinte cenários foram considerados: o aumento da massa da estrela doadora de 1,0 para 1,2 vezes a massa do Sol a fim de diminuir o tempo na sequência principal; diferentes metalicidades ($Z = 0.02$, 0.01 and 0.001) pois há progenitores em diferentes partes da Galáxia; e estudar alta (70%) e baixa (20%) eficiência na transferência de massa, já que é um parâmetro bastante incerto. Nós então repetimos as mesmas configurações descritas acima mas considerando como acretora uma anã branca massiva (0,8 massa solar), compatível com sistemas de variáveis cataclísmicas (CV). As nossas conclusões indicam que a prescrição CARB é adequada para reproduzir as propriedades de LMXBs e CVs observadas, mesmo no regime de períodos orbitais iniciais curtos. Comparando

nossos modelos com dados observacionais de He-WDs em sistemas binários com pulsares de milissegundos, o uso do freamento magnético CARB se mostra compatível com a formação de ELM WDs em LMXBs. Em adição aos sistemas LMXB e CV, o freamento CARB torna possível a formação de binários de raios-X ultra-compactos (UCXB) e pulsares de milissegundos de órbita ampla, bem como ELM WDs separadas em companhia de estrelas de nêutrons e de anãs brancas massivas. Todavia, dados de ELM WDs em sistemas com anãs brancas apresentam grande dispersão em massa e no período orbital do sistema binário, sugerindo que outros canais de formação também estão presentes. Nota-se que não simulamos modelos de Envelope Comum (CE). Além disso, nós encontramos que as propriedades observacionais como temperatura efetiva e gravidade superficial desses novos modelos são compatíveis com a maioria das ELM WDs confirmadas ou candidatas. Os resultados combinados dos mais de trezentos modelos que calculamos deixam claro que a massa final das ELM WDs é uma quantidade extremamente degenerada no espaço de parâmetros estudado, já que existem inúmeras interdependências entre metalicidade, ocorrência de flashes de hidrogênio, eficiência na transferência de massa, a massa inicial das estrelas, o período orbital inicial, e a reação do sistema binário quanto à transferência de massa.

Palavras-chave: anãs brancas. anãs brancas de massa extremamente baixa. freamento magnético. binárias interagentes. binárias próximas.

List of Figures

List of Tables

List of abbreviations and acronyms

AGB	Asymptotic giant branch
ELM WD	Extremely low-mass white dwarf
GW	Gravitational wave
HRD	Hertzsprung-Russell diagram
HSF	Hydrogen shell flash
KD	Kiel diagram
LM WD	Low-mass white dwarf
LMXB	Low-mass X-ray binary
MESA	Modules for Experiments in Stellar Astrophysics
MS	Main sequence
MT	Mass transfer
NS	Neutron star
RGB	Red giant branch
RLOF	Roche lobe overflow
SGB	Subgiant branch
TAMS	Terminal age main sequence
UCXB	Ultra-compact X-ray binary
WD	White dwarf
ZAMS	Zero age main sequence

List of symbols

a	Binary separation
β_{mt}	Mass accretion efficiency term
$c = 299,792,458$ m/s	Speed of light in vacuum
$G = 6.674 \times 10^{-11}$ Nm^2/kg^2	Gravitational constant
g	Surface gravity
L	Luminosity
$L_\odot = 3.8418 \times 10^{33}$ erg/s $= 3.8418 \times 10^{26}$ W	Luminosity of the Sun
M_{a}	Accretor star mass
M_{d}	Donor star mass
$M_\odot = 1.988 \times 10^{30}$ kg	Approximate mass of the Sun
$\dot{M}$ $(1 \times 10^{-10}\ M_\odot/\mathrm{yr} \simeq 6.31 \times 10^{12}$ kg/s)	Mass transfer rate
P	Orbital period
pc $= 3.086 \times 10^{16}$ m	Parsec-to-meter conversion
$R_\odot = 6.9598 \times 10^8$ m	Average radius of the Sun
R_{a}	Accretor star radius
R_{d}	Donor star radius
R_{L}	Roche lobe radius
T_{eff}	Effective temperature
$T_{\mathrm{eff},\odot} = 5777$ K	Effective temperature of the Sun
Z	Metallicity

Contents

1 Introduction

Until around the end of the XVI century, the development of science was at a very slow pace compared to today. Then there was the development of thermodynamics, chemistry, and electromagnetism, fundamental to the Industrial Revolution, and by the end of the XIX century it was said that all nature was well understood (Mason, 1962; Osada, 1972; Rocha, 2002). It was a mistake. In the last hundred years, scientific and technological advances have taken an even greater step. In particular, we can mention Astronomy (Herschel, 2009), which with the help of large telescopes, space missions and great computational power, has allowed us to understand the present Universe, and also its history, in ever greater detail, but still incomplete. Current cosmological models tell us that for hundreds of thousands of years the Universe had nothing but radiation and elementary particles. It is believed that the first generation of stars — the still hypothetical population III stars — have been formed at a redshift $z = 20$–65, which corresponds to $\sim 1\%$ of the age of the Universe today (e.g., Bromm; Larson, 2004; Naoz; Noter; Barkana, 2006; Bromm et al., 2009). Population III stars, with zero metallicity ($Z = 0$), may have been born with up to 1000 solar masses, and contaminated the Universe with metals in a few thousand of years after their formation. Then, a few hundred million years after the Big Bang, the earliest generations of galaxies formed (e.g., Bromm; Yoshida, 2011).

Atoms come together to form molecules and then larger compounds. Similarly, stars are the fundamental building blocks of the Universe: they are formed in clusters — open or globular —, which in turn form galaxies. As the best example, we can cite our home, the Milky Way, which contains at least 200 billion stars and probably 100 billion planets. Although the lifespan of stars is incomparably longer than our time hosted here on Earth, we currently know that stars are also born, evolve, and die, and are responsible for the Universe as we see it today.

Most stars are not alone, and like humans, most of them change their behaviour by their company. In this chapter we will introduce binary stars, going through some history, observations, and the basic physics involved.

1.1 A bit of history of binary systems

At first glance, all stars appear to be mere points of light projected upon the surface of the celestial sphere, not allowing us to perceive their real distances. As a result, for a long time, there was no clear differentiation between truly gravitationally bound stars — binary stars — and those that were only on the same line of sight, the so called double stars.

Although not the inventor of this tool, in 1609 Galileo Galilei (1569–1642) began his observations with the telescope and soon greatly improved its capabilities. It was quickly found that some stars that appear single to the naked eye are resolved into a pair of stars by the telescope. The first historical record is a letter by Benedetto Castelli (1578–1643) to Galileo in 1617, where he noted that Mizar (ζ Ursae Majoris, see Figure 1) was, in fact, a double star. Galileo later observed Mizar himself and determined the angular distance between the two stars as $15''$.

Figure 1 – Picture of the Mizar (ζ UMa) with its fainter companion Alcor (80 UMa) in the constellation of Ursa Major on September 26, 2006. Position (J2000): RA $13^{h}23^{m}55.6^{s}$, Dec $+54°55'31''$. Instrument: $6''$ $f/8$ Newtonian reflector telescope with 150 mm aperture and 1200 mm focal length. Eyepieces/magnification: 10 mm (120x).

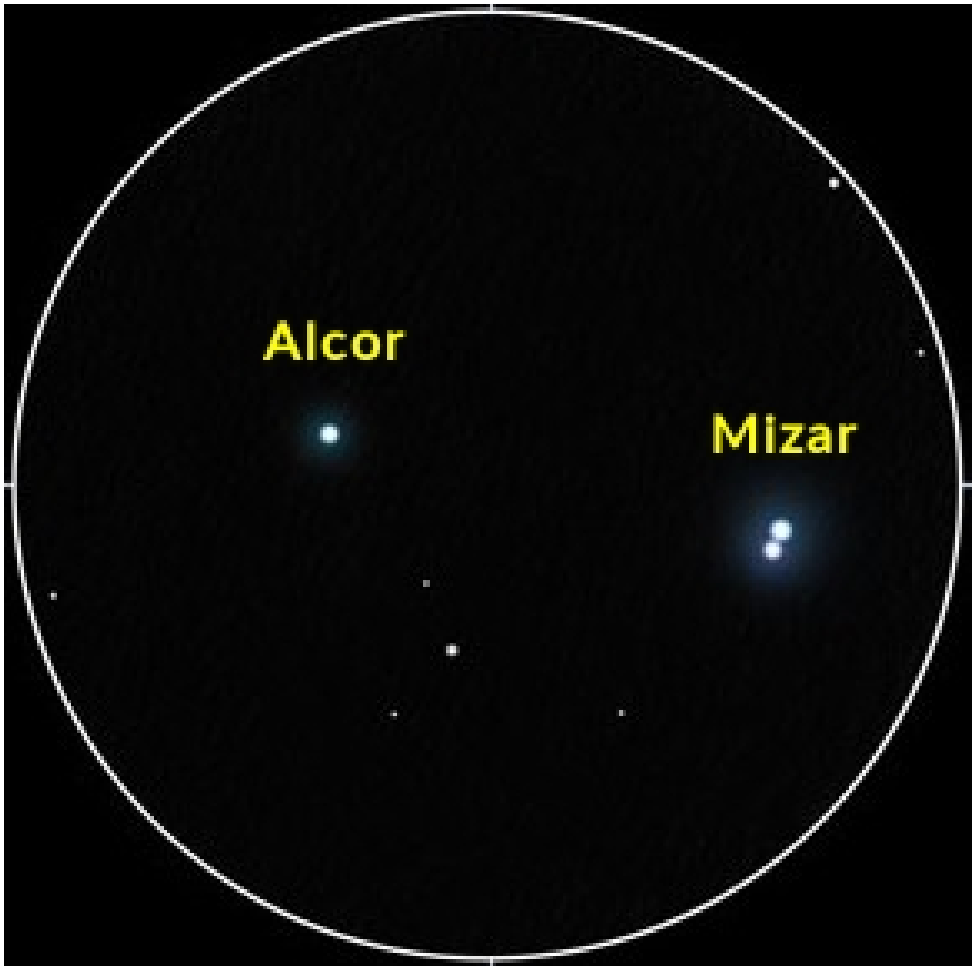

Credit: adapted from Perez (2006).

In 1750 the amateur scientist Thomas Wright (1711–1786) came up with the idea that, if the planets around the Sun form a system, the stars spread throughout space can also form a system or a series of systems. In 1755 the philosopher Immanuel Kant

(1724–1804) suggested that the nebulae seen in the sky were large sidereal systems and all the these systems could be orbiting around the same common centre. These speculations attracted the attention of the astronomer William Herschel (1738–1822) who carried out a systematic study of the motion and distribution of stars in space and recorded 269 pairs of stars, orbiting each other, which suggested that the force of gravity acted in both the solar and in the sidereal space. In fact, Herschel was the first to use the term *binary star* to designate the union of two stars that, by laws of gravitation, form together a single system (see Zinnecker, 2001). On the mathematical side, in 1767 John Michell (1724–1793) began to develop some statistics about visual binary systems that provided early indications that the closeness of the components is not due to chance, and indeed most pair are real physical pairs. In 1889 Edward Charles Pickering (1846–1919) announced the discovery of the first spectroscopic binary (β Persei, a.k.a. Algol), a class defined by the periodic shifting of spectral lines due to the variation in the radial velocity of the star(s). In fact, this story is somewhat obscure, and it is possible to find the information that actually Pickering only obtained evidence of this fact in 1981, and confirmation of the discovery of Algol radial velocity variations was given in 1989 by Hermann Carl Vogel (1841–1907, see Batten, 1989).

However, the milestone of double star astronomy can be considered the catalogue of 81 double stars by Burnham (1873). During his decades of work, Burnham contributed greatly to the astronomy of binary stars, including the discovery of several new spectroscopic binaries and the demonstration that eclipsing variable stars are binary systems.

Binary stars are generally classified according to their method of detection. In a *visual binary* system, each component star can be individually resolved through a telescope. These systems tend to be relatively close to us and are characterised by having large orbital separation, so long-term observations must be made in order to get relative positions of the members of the system.

An *eclipsing binary* is a system in which the orbital plane lies nearly edge-on — perpendicular to the plane of the sky — , so that the component stars periodically eclipse one another and variations in the flux are observed. A light curve — the graph of apparent brightness as a function of time, reveals the pattern of the eclipses and can be used to deduce the size of the stars, the distance between them and how much of one star the other covers. The shape of the light curve may also indicate the occurrence of mass transfer between the binary components and their possible tidal deformation. Only a small fraction (< 0.3 %, Guinan; Engle, 2006) of all binary stars are aligned to produce mutual eclipses of their components.

The orbital period measurement in most binary system have been determined by measuring the radial velocities variations of the components, that is, the Doppler shift effect on their spectral lines. Such systems are called *spectroscopic binaries*. Although a

very accurate method, the effect only occurs if the system's orbital plane is not face-on to us.[1] In this case, for the star moving towards us we detect blue-shifted spectral lines; while for the moving away star we see red-shifted lines.

Finally, we have the *astrometric binary* class. This method requires long-term observations and small uncertainty in position and proper motion measurement. In fact, this method consists in finding small periodic perturbations in the position of a star, evidencing that it occurs due to the gravitational influence of a companion.

Readers interested in more detail about the history of astronomy and early developments in binary systems should refer to: Aitken (1935), Kopal (1959), Mason (1962), Kopal (1978), Sahade & Wood (1978), Lipunov (1989), Sahade, McCluskey & Kondo (1993).

1.2 Basic principles of binary systems

In this section we will recall several basic facts about binary stars that will be of most importance for understanding the following sections. In particular, we will introduce the notation for the main physical quantities of the system, as the components masses, the orbital period, the orbital separation, and how some dynamical events may depend on them. Readers interested in more detailed discussions on this topic may refer to Paczyński (1971), Batten (1973), Masevich & Tutukov (1988), Hilditch (2001), Eggleton (2006), Tout (2006), Cherepashchuk (2013a), Cherepashchuk (2013b), Postnov & Yungelson (2014), de Marco & Izzard (2017), Tutukov & Cherepashchuk (2020).

1.2.1 Keplerian motion of a binary star system

The simplest way to start studying motions in binary systems is to consider the Keplerian motion. Stars in this kind of system usually have similar masses and are highly condensed objects moving with orbital velocities much smaller than the light speed. This allows us to assume that it is equivalent to two points of masses, M_1 and M_2, bound together by gravity in a Newtonian field. Far from the system — at a distance much greater than binary separation — the potential is determined by the total mass of the system

$$M_{\rm T} = M_1 + M_2 \ , \tag{1.1}$$

[1] Edge-on systems accounts for the vast majority of binary inclinations: rotation vectors are random in space, but orbital planes are biased toward large inclinations — i.e., more edge-on systems (Heintz, 1969; Malkov; Chulkov, 2017). It is generally assumed that the mean inclination angle for a random stellar sample is $i = 60°$ (e.g., Halbwachs et al., 2003; Willems; Kolb, 2004; Brown et al., 2010; Brown et al., 2011a). In fact, perfectly edge-on ($i = 90°$) or perfectly face-on ($i = 0°$) systems are rare. Most systems have an intermediate inclination.

and this problem is equivalent to that of a single mass μ in a external gravitational potential (Landau; Lifshitz, 1976), where the reduced mass is defined as

$$\mu = \frac{M_1 M_2}{M_1 + M_2} = \frac{M_1 M_2}{M_{\rm T}} \ . \tag{1.2}$$

As illustrated in Figure 2, each component M_1 and M_2 moves around the barycentre — centre of mass — with velocities $\vec{V}_1$ and $\vec{V}_2$, being the major semi-axis of each ellipse, a_1 and a_2, inversely proportional to their masses

$$\frac{a_1}{a_2} = -\frac{\|\vec{V}_1\|}{\|\vec{V}_2\|} = \frac{M_2}{M_1} \ . \tag{1.3}$$

The position vectors of each body in relation to the barycentre are $\vec{r}_1$ and $\vec{r}_2$, where

Figure 2 – Schematic geometry of a binary system with masses M_1 and M_2 governed by Newtonian gravity. The orbital separation is $a = a_1 + a_2$ (red lines). The vectors $\vec{r}_1$ and $\vec{r}_2$ (black lines) are measured from the barycentre (BC) to the binary members (black circles). The low eccentricity ($e \approx 0$) elliptical orbits are shown in blue.

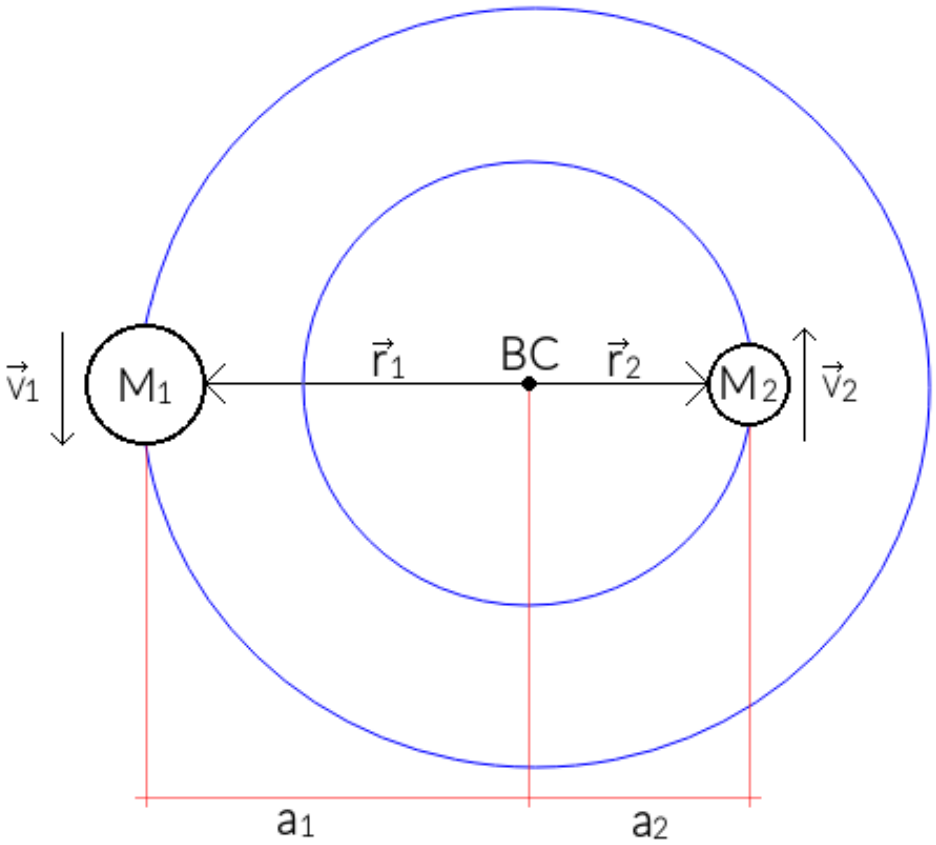

$\vec{r} = \vec{r}_1 - \vec{r}_2$ is the relative position and $\vec{V} = \vec{V}_1 - \vec{V}_2$ is the relative velocity.

Thus, if the reduced body μ moves in an elliptic orbit with eccentricity e and major semi-axis a, each individual body M_1 and M_2 moves around the barycentre, also in

elliptical orbits with eccentricity e, satisfying Kepler's third law (Kepler, 1992; Kepler, 1997)

$$\Omega^2 = \left(\frac{2\pi}{P}\right)^2 = \frac{GM_T}{a^3} \ , \tag{1.4}$$

where Ω is the orbital frequency, $P = 2\pi/\Omega$ is the orbital period, $a = a_1 + a_2$ and G is the gravitational constant. An important consequence is that we must have $M_{\rm T}P^2/a^3 = \text{cte}$. Naturally, this relation is also valid for circular orbits.

In a generic, eccentric orbit, the orbital angular momentum vector

$$\vec{J}_{\rm orb} = \mu\vec{V} \times \vec{r} \tag{1.5}$$

is perpendicular to the orbital plane. In a circular orbit ($e = 0$), the velocity is simply

$$V = \Omega a = \sqrt{\frac{GM_T}{a}} \ , \tag{1.6}$$

and the total orbital angular momentum of the system becomes

$$|\vec{J}_{\rm orb}| = J_{\rm orb} = \mu V a = \mu\Omega a^2 = M_1 M_2 \sqrt{\frac{Ga}{M_1 + M_2}} = \mu\sqrt{GM_T a} \ . \tag{1.7}$$

The total energy — kinetic plus potential — of the system is

$$E = -\frac{GM_T}{2a} \ . \tag{1.8}$$

By differentiating Equation 1.7 we obtain a general equation for the orbital evolution of a non-eccentric system

$$2\frac{\dot{J}}{J} = \frac{\dot{a}}{a} + 2\frac{\dot{M}_1}{M_1} + 2\frac{\dot{M}_2}{M_2} - \frac{\dot{M}_1 + \dot{M}_2}{M_1 + M_2} \ , \tag{1.9}$$

which can be easily resolved to express the variation of the orbital separation $\dot{a}$ or the angular momentum $\dot{J}$.

For point and sufficiently separated sources in a circular orbit, the loss of angular momentum is only due to gravitational radiation, and is given by the well-known expression (see, e.g., Peters, 1964; Landau; Lifshitz, 1975)

$$\dot{J}_{\rm gr} = -\frac{32}{5c^5}\left(\frac{2\pi G}{P}\right)^{7/3} \frac{(M_1 M_2)^2}{(M_1 + M_2)^{2/3}} \ , \tag{1.10}$$

where c is the speed of light.

1.2.2 Equipotentials and Roche lobe

A simple classification of binary systems takes into account if one star interferes in the evolution of the other. When the orbital separation is sufficiently large, i.e., significantly

larger than the radius on the asymptotic giant branch (AGB, see Appendix A), each component evolves separately, as if they were single stars, except that they are gravitationally bound. We call this case wide binaries. On the other hand, we call them close binaries if the evolutionary expansion of one or both components of the system leads to a mass exchange between the stars (Paczyński, 1967c). This is also generally understood as pairs of stars whose dimensions are not insignificant fractions of their separation (Kopal, 1956).

The Roche lobe is the geometric region around a star in a binary system, within which orbiting material is gravitationally bound to that star. If any amount of matter is inside the Roche lobe, the star's gravity guarantees that it stays there; and if it is outside, there will be overflow to the companion star or even loss from the binary system. In the case where the two stars exceed their Roche lobes, it is possible the formation of a common envelope (CE). The Roche lobe radius $R_{\rm L}$ is defined as the radius of a sphere with the same volume as the Roche lobe, i.e., $V_{\rm L} = 4\pi R_{\rm L}^3/3$. An expression for the Roche lobe radius with accuracy better than 1% in the range $0 < q < \infty$ was suggested by Eggleton (1983)

$$R_{\rm L} = \frac{0.49q^{2/3}a}{0.6q^{2/3} + \ln(1+q^{1/3})} \ , \tag{1.11}$$

where $q = M_1/M_2$ is the mass ratio.

The total potential (gravitational plus centrifugal) is approximated by the Roche potential, which takes into account the additional assumption that the components (point of masses) of the system co-rotate with the binary orbital period in a circular orbit — i.e., each stellar component has the same angular velocity as the orbit. The shape of the equipotential level surface Φ = constant determines the shape of the surface of the star. Thus, the total potential at a given point (x, y, z) in the Cartesian reference frame is

$$\begin{aligned}
\Phi &= \frac{-GM_1}{|\vec{r} - \vec{r_1}|} + \frac{-GM_2}{|\vec{r} - \vec{r_2}|} - \frac{1}{2}(\vec{\omega} \times \vec{r})^2 \\
&= \frac{-GM_1}{\sqrt{x^2+y^2+z^2}} + \frac{-GM_2}{\sqrt{(x-a)^2+y^2+z^2}} - \frac{1}{2}\Omega^2\left[(x-\mu a)^2 + y^2\right] \\
&= \frac{-GM_1}{\sqrt{x^2+y^2+z^2}} + \frac{-GM_2}{\sqrt{(x-a)^2+y^2+z^2}} - \frac{1}{2}\frac{GM_{\rm T}}{a^3}\left[\left(x - \frac{a}{1+q}\right)^2 + y^2\right] \ ,
\end{aligned} \tag{1.12}$$

whereas in the last expression the star 1 is at the origin and the star 2 at $(a, 0, 0)$. The centre of mass of the system is at the point $(\mu a, 0, 0)$. Naturally, a massive particle in an arbitrary position (x, y, z) will be under the effect of a force given by $\vec{F} = -\nabla\Phi$ if the particle velocity is zero in the rotation frame.

Figure 3 illustrates the Roche lobe potential in a binary system. For the study of the evolution of close binary systems, the most important surface is the innermost level surface that encloses the two components, defining the Roche lobe of the stellar components. Within this limit, the matter is bound to the respective star. The points

Figure 3 – Top left: shape of the Roche potential along the line connecting the two stars. The potential Φ is in units of $G(M_1 + M_2)/a$ and the horizontal scale is in units of the semi-major axis a. Right: in a detached system, both stars evolve separately. Roche lobe overflow occurs in a semi-detached system, where the donor star fills its Roche lobe and mass is transferred to the accretor star. A contact system occurs when the mass transfer rate is too fast to be accreted or even when both stars fill their Roche lobe. If the mass transfer is dynamically unstable, the accretor star is unable to accept all material, which leads to the formation of a common envelope engulfing the companion star. Bottom left: the equipotential lines in the x–y plane. The first three Lagrangian points (where $\nabla\Phi = 0$) are highlighted in red.

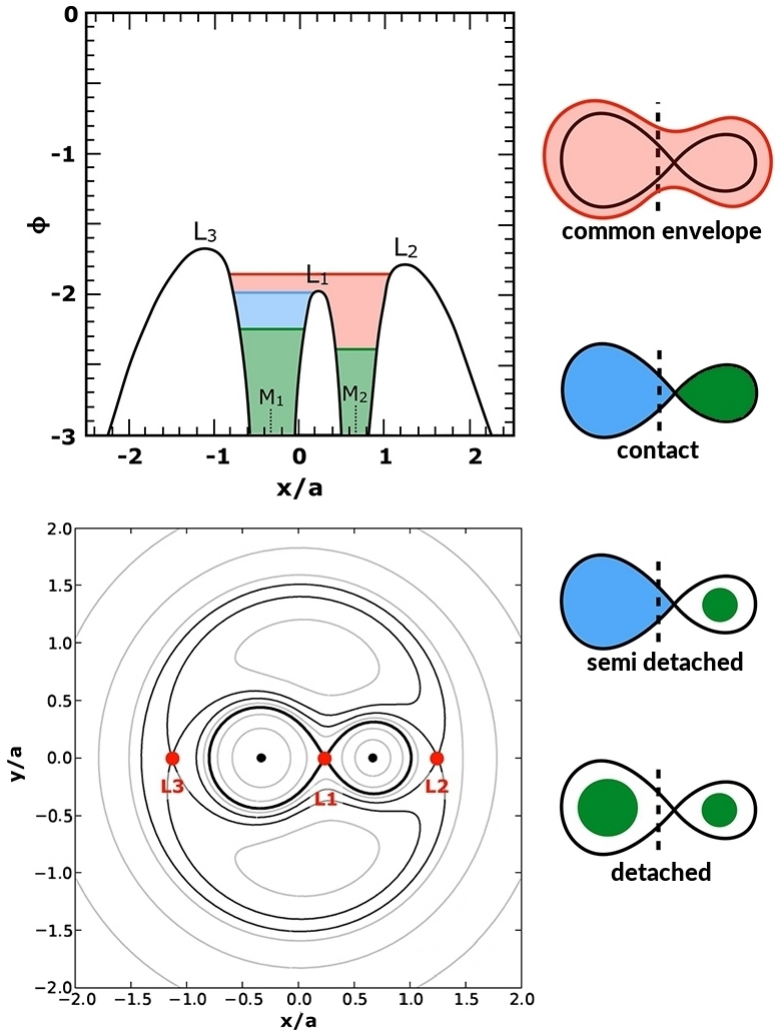

Credit: adapted from Lamers & Levesque (2017).

where a mass element in rest maintain its position relative to the large orbiting bodies are called Lagrangian points. In these points, the net force exerted onto a test particle corotating with the binary vanishes. The first three Lagrangian points, L_1, L_2 and L_3, lie on the line connecting M_1 and M_2; and the L_1 point is through which a mass flow can

occur from one star to another in the Roche-lobe overflow scenario (the wind mass loss will be discussed later in the text). In fact, if enough energy is available, mass and angular momentum can also be lost through points L_2 and L_3 (which are also unstable), but we will not consider these possibilities in this work.

The Roche-lobe overflow (RLOF) occurs when the radius of one of the stars (the donor, in our case) becomes equal to the radius of a sphere with volume equal to that of the Roche lobe. As the stellar components are considered spherical and the Roche lobe is not, we must compare them by volume and not directly by radius.

There is no absolute convention as to which star to call 1 or 2 as long as these are fixed labels. Some authors often define 1 as the initially most massive star, while others use label 1 to indicate the star that will be analysed in more detail. In most cases, 1 refers to the primary or the most massive component at a given reference time. In observational studies, one more nomenclature can be found. In a visual binary system, for example, the brighter star is usually referred to as star A, and the fainter one as star B. Other possible and valuable definitions are those of *donor* and *accretor* star, since in this way we can have an immediate outlook of the state of the system. Thus, we will refer to the radius and mass of the donor or accretor star as $R_{\rm d}$, $R_{\rm a}$, $M_{\rm d}$ and $M_{\rm a}$. This definition is especially interesting for the present work since we are studying an evolutionary phase in which mass transfer occurs only in one direction. However, these terms should be used with caution when compared to the study of other evolutionary phases, as throughout their lifetime a binary system may have the orientation of mass flow reversed several times (e.g., Postnov; Yungelson, 2014; Tutukov; Cherepashchuk, 2020).

1.2.3 Timescales

To better understand the various processes governing the evolution of a star and a binary star system, we must separate them according to their duration. Often, the timescale related to one of the stars in the system ends up governing a phenomenon related to the binary system as a whole. Therefore, we can discuss the timescales of a binary system and its components in parallel.

From equation (2) in Kraft, Mathews & Greenstein (1962), the following expression is obtained for the **merging time due to gravitational radiation**

$$\tau_{\rm gwr} = 47100 \mathcal{M}^{-5/3} P^{8/3} \text{ Myr} \ , \tag{1.13}$$

where the chirp mass ($\mathcal{M}$, see Equation B.3) and the orbital period (P) should be given in solar masses and days, respectively. This is the timescale on which coalescence can be expected to occur only due to gravitational wave radiation. The emission of gravitational radiation can decrease the separation of the double white dwarf systems, leading to a merger in less than Hubble time if the orbital period of the system is about 10 hours or

less (Shore; Livio; van den Heuvel, 1994; van den Heuvel, 1994). Therefore, we can expect this contribution to be greater at the end of evolution, when the system consists of two compact objects.

Main sequence stars with a mass within the range 0.3–1.5 $M_\odot$ have a convective envelope and a radiative core. The donor star is assumed to emit a magnetic wind, which is forced to corotate by the magnetic field to large distances. The wind thus removes spin angular momentum from the donor by exerting a torque, and assuming that there is tidally coupling and synchronous rotation with the orbit, this has the effect of removing angular momentum from the binary orbit. The characteristic **timescale of the magnetised stellar wind** is given by (e.g., Tutukov; Cherepashchuk, 2020)

$$\tau_{\rm msw} \simeq 3 \times 10^6 a^5 M_{\rm a} R_{\rm d}^{-4} M_{\rm T}^{-2} \text{ yr} , \tag{1.14}$$

where a and $R_{\rm d}$ are the orbital separation and the donor radius in units of solar radius, and $M_{\rm a}$ is the mass of the accretor (in solar mass units, as well the total mass $M_{\rm T}$). Given that we are going to deal with systems that have stellar components of very restricted masses throughout this work, the factors that will contribute most strongly to the actuation of this mechanism are the small orbital separation (i.e., short orbital period) and the radius of the donor star (which grows significantly in the red giant stage, for example).

The **mass transfer timescale** is simply defined as

$$\tau_{\rm mt} = \frac{M_{\rm d}}{\dot{M}} , \tag{1.15}$$

which can assume values over a wide range, as the mass transfer rate can vary by more than a dozen orders of magnitude. Here, $M_{\rm d}$ is the donor mass and $\dot{M}$ is the mass transfer rate (usually given in $M_\odot$/yr).

The **dynamic timescale** — also know as free-fall timescale — indicates the time taken by the star to recover its hydrostatic equilibrium state after a perturbation. It depends on the radius of the star (R) and on the average sound velocity in the stellar matter $c_{\rm s}$

$$\tau_{\rm dyn} = \frac{R}{c_{\rm s}} = \sqrt{\frac{R^3}{2GM}} \approx 0.04 \left(\frac{M_\odot}{M}\right)^{1/2} \left(\frac{R}{R_\odot}\right)^{3/2} \text{ days} , \tag{1.16}$$

where we have assumed $c_{\rm s}$ to be the escape velocity,[2] $\sqrt{2GM/R}$.

Now let us consider a single photon produced in the core of the star. Taking its motion as a random walk and considering the mean free path of the photon as ℓ, we have that the **photon diffusion timescale** is

$$\tau_\gamma \approx \frac{R^2}{\ell c} \text{ yr} . \tag{1.17}$$

[2] Because the Virial theorem implies that $c_{\rm s}^2 \sim GM/R$ (see, e.g., Lamers; Levesque, 2017).

When energy loss and energy production are no longer in balance, a star reacts on a **thermal timescale** — also known as Kelvin-Helmholtz timescale — given by

$$\tau_{\rm th} = \frac{E_{\rm th}}{L} \approx \frac{GM^2}{2LR} \approx 1.5 \times 10^7 \left(\frac{M}{M_\odot}\right)^2 \frac{R}{R_\odot}\frac{L_\odot}{L} \text{ yr} \ , \tag{1.18}$$

where $E_{\rm th}$ and L are the thermal energy and the luminosity of the star, respectively. According to the Virial theorem, the thermal energy is half the (negative) potential energy. Thermal timescale is the time during which gravitational contraction could sustain the luminosity of the star at its current value. In other words, it is the time that a star would emit its entire reservoir of thermal energy, as long as its luminosity remained constant.

Finally, the timescale in which a star uses its nuclear fuel reservoir is given by the **nuclear timescale**

$$\tau_{\rm nuc} = 0.007\frac{M_{\rm core}c^2}{L} \approx 10^{10}\frac{M}{M_\odot}\frac{L_\odot}{L} \text{ yr} \ , \tag{1.19}$$

where $M_{\rm core}$ is the mass of the stellar core and the 0.007 is the fractional mass deficit from H to He. So if we arrange our timescales considering a Sun-like star, we end up with the inequalities:

$$(\tau_{\rm nuc} \approx 10^{11}\,\text{yr}) \gg (\tau_{\rm th} \approx 10^7\,\text{yr}) \gg (\tau_\gamma \approx 10^4\,\text{yr}) \gg (\tau_{\rm dyn} \approx 19\,\text{min}) \ . \tag{1.20}$$

1.3 White dwarfs and binaries

Since the evolution of *single stars* is not the main theme of this work but it is important for the general understanding of the subject, we invite the reader to follow this topic in Appendix A before going on.

We begin this section by highlighting the importance of binary evolution in the light of some observational data and statistics. Then, we will look for evidence that differentiates the evolution of single white dwarfs from those ones from binary evolution.

Several explanations of how binary and multiple stars form have been proposed, discussed, and discarded over the years (see, e.g., Pringle, 1989; Chapman et al., 1992; Boss, 1993; Bodenheimer, 2001; White; Ghez, 2001; Clarke, 2006). In the review, Tohline (2002) remarks that the mechanisms proposed for forming binary stars can be divided into three broad categories: i) capture, ii) prompt fragmentation, and iii) delayed breakup. Recently, Tutukov & Cherepashchuk (2020) point out that two scenarios are presently suggested as the mechanisms for the formation of binary stars: the fission of rotating molecular gas clouds during the gravitational collapse, and the inelastic collisions of stars during the formation of young star clusters.

The evolution of stars in binary systems can become quite different from those that evolve as a single star. Moreover, while the evolutionary theory for single stars is already

quite well developed and the observations reproduced by simulations,[3] the evolution of multiple systems has many open questions. This is undoubtedly a great subject for research, since over 50% of field stars with one solar mass and above are in binaries (Duchêne; Kraus, 2013).[4] Out of those, 25% will interact at least once in their lifetime (Willems; Kolb, 2004). To improve our understanding of the evolution of binary systems, it is necessary to develop evolutionary theories of interacting systems, and to test them against data.

The study of low-mass stars transferring mass in binary systems has also proved useful to explain chemical anomalies among unevolved stars in globular clusters, for example. Wei et al. (2020) study the surface abundances of the accretors in low-mass binaries and found that the abundance patterns are significantly different from their initial abundances or that of normal single stars, supporting the hypothesis that mass transfer in low-mass binaries is, at least, partly responsible for the unevolved anomalous stars in globular clusters.

Also, the detection of an enhanced abundance of α-elements in the low-mass X-ray binary Cygnus X-2 was shown to be consistent with a scenario of contamination of the secondary star during the supernova event (Suárez-Andrés et al., 2015); and the study of the mass transfer in low-mass X-ray and cataclysmic variables binaries were used to make hypotheses about C/O chemical anomalies (Schenker; King, 2002).

1.3.1 White dwarfs

According to Russell (1944), the first person who reported the existence of white dwarfs was Williamina Fleming (1857–1911), publishing her discovery in 1910. A typical white dwarf is half as massive as the Sun and only slightly bigger than the Earth. This makes them part of the so called compact objects, along with neutron stars and black holes. The extremely dense and hot nature of white dwarfs (WDs) makes them excellent astrophysical laboratories, where we can test our understanding of energy transport, quantum processes, cooling processes, opacity of elements, crystallisation, equation of state, behaviour of atoms under very strong magnetic fields and more.

White dwarf stars are the most common outcome of single star evolution. Up to

[3] Some exceptions can be cited, however. For instance, it is still unclear whether the mass-radius relation anomaly in low main sequence stars seen in detached binaries is a (hidden) binarity effect or is it intrinsic to all low mass main sequence stars (Hoxie, 1970; Hoxie, 1973; Torres; Andersen; Giménez, 2010; Feiden; Chaboyer, 2012). We may also cite stellar pulsation theory (Dupret, 2019), pulsating white dwarfs (Winget; Kepler, 2008; Córsico et al., 2019), solar composition (Serenelli et al., 2009), helioseismology (Serenelli, 2016), and solar neutrinos (Orebi Gann et al., 2021). A general review of some current problems in stellar evolution — including micro- and macro-physics ingredients, convection, overshooting, semi-convection, rotation, chemical evolution, age scales, and mass loss — can be found in Weiss (2002), Buldgen (2019).

[4] The binary fraction in globular clusters is much lower ($\sim$ 2–20%) than in the field. The binary fraction strong correlates with the globular cluster mass. See, e.g., Romani & Weinberg (1991), Milone et al. (2008), Gratton, Carretta & Bragaglia (2012), Lucatello et al. (2015).

97–99% of Milky Way stars are believed to end up as WDs (Fontaine; Brassard; Bergeron, 2001; Winget; Kepler, 2008; Lauffer; Romero; Kepler, 2018). Although the main variable defining the fate of a newly formed star is its mass, several other factors can modify its end. Examples include chemical abundance, rotation, off-centre burning, and episodes of accretion or mass loss to the environment. Unfortunately, we do not have enough time to observe the complete evolution of a star, and what we know about it depends on numerical simulation models, laboratory experiments, and astronomical data. Thus, one may say that WDs are the final observable stage of stars with initial mass up to 6–11.8 $M_{\odot}$ (García-Berro; Isern; Hernanz, 1997; Poelarends et al., 2008; Siess, 2010; Langer, 2012; Doherty et al., 2014; Woosley; Heger, 2015; Lauffer; Romero; Kepler, 2018).

Studying the population of white dwarfs reveals important information about stellar formation processes and evolution (Winget et al., 1987; Tremblay et al., 2014; Campos et al., 2016). Because they are among the oldest objects in the Galaxy (e.g., García-Berro; Oswalt, 2016), they can be used to determine the age of the stellar population where they reside, e.g., set a lower limit of 9.5 Gyr on the age of the Galactic disk (Winget et al., 1987; Oswalt et al., 1996), resolving age discrepancy for individual open clusters (García-Berro et al., 2010), and calculating the age of local field (inner) halo stars to be 11.4 ± 0.7 billion years (Kalirai, 2012). Also, a pulsating white dwarf is the most stable optical clock known (Kepler et al., 2021).

White dwarfs have run out of thermonuclear fuel, and most of them have burned H and He in their interiors and are believed to have C-O cores, containing $\sim 99\%$ of the total mass, a thin He mantle ($\sim 1\%$), and a thinner but opaque H envelope ($\lesssim 0.01\%$). In the case that, for some reason, the star loses the outermost layers before the start of helium burning, it may happen that the white dwarf forms with a helium core and a hydrogen envelope. Using data from the Sloan Digital Sky Survey, spectral analysis indicates that the majority (82%) of the white dwarfs in the sample have an atmosphere dominated by hydrogen (Kepler et al., 2019; Kepler et al., 2021). As they are compact cooling bodies in hydrostatic equilibrium, they evolve at almost constant radius.

1.3.2 The lower mass limit

On the other hand, the minimum mass of a present-day white dwarf coming from single star evolution is around 0.45 $M_{\odot}$, and smaller masses can only be obtained by invoking extreme winds in high metallicity environments (Kilic; Stanek; Pinsonneault, 2007; Tremblay et al., 2016; Pelisoli; Vos, 2019). This is because a progenitor star that would become an even lower mass white dwarf has main sequence evolution time larger than the present age of the Universe.

White dwarf stars in the mass range 0.20–0.45 $M_{\odot}$ are generally referred to as low-mass white dwarfs. The discovery of white dwarfs in detached close binaries supports

the notion that evolution within a binary star is needed to obtain white dwarfs with masses below 0.45 $M_\odot$.[5] Thus, low mass WDs are most likely a product of interacting binary star evolution (Marsh; Dhillon; Duck, 1995; Marsh, 1995). Using both radial velocities and infrared photometry to study 21 WDs with $M \leqslant 0.45\ M_\odot$, Brown et al. (2011) found that the fraction of single low-mass WDs is $\leqslant 30\%$, but their sample was limited to orbital period $\leqslant 117$ h. As we will see below, although the first extremely low-mass white dwarfs were discovered in company with pulsars (i.e., neutron stars), the most recently discovered ones have another white dwarf as companions.

In parallel, white dwarfs in binary systems with masses even smaller ($M < 0.2\ M_\odot$) began to be discovered. By means of spectroscopy, van Kerkwijk, Bergeron & Kulkarni (1996) inferred the white dwarf companion of the millisecond radio-pulsar PSR J1012+5307 to have a mass of $0.16 \pm 0.02\ M_\odot$; and Liebert et al. (2004) interpreted SDSS J123410.37-022802.9 to be a very low-mass WD with a core composed of helium, with mass $\sim$ 0.18–0.19 $M_\odot$, and probably belonging to a binary system. The surface gravity of an object is given by $g = GM/R^2$. Using optical spectroscopy, Kilic et al. (2007) found the lowest gravity/mass WD until then, with $\log(g) = 5.48 \pm 0.03$ (g in cm/s^2) and an estimated mass of $M = 0.17\ M_\odot$.

This gave rise to surveys to search for the so-called extremely low-mass white dwarfs (ELM WDs),[6] such as the ELM Survey (Brown et al., 2010) containing 88 identified ELMs with surface gravity $4.71 \leqslant \log(g) \leqslant 7.76$, effective temperature $7,940 \leqslant T_{\rm eff}/{\rm K} \leqslant 34,270$, and masses $0.142 \leqslant M_1/M_\odot \leqslant 0.497$ (Brown et al., 2016). These ELMs are in systems with orbital period $0.00886 \leqslant P/{\rm d} \leqslant 2.16489$, companion masses $0.07 \leqslant M_2/M_\odot \leqslant 1.21$, and are located at distances in the range $0.104 \leqslant d/{\rm kpc} \leqslant 9.187$. The ELM Survey found that all ELM WDs in their sample belong to double WD binaries (Brown et al., 2020), considering the survey limited targeting (only North Hemisphere) and selection effects (only short $P \leqslant 36$ h orbital period systems). In a search for pulsars at the positions of eight low-mass white dwarfs that have orbital parameters suggesting that their unseen companions are either massive white dwarfs or neutron stars, Athanasiadis et al. (2021a), Athanasiadis et al. (2021b) found no significant pulsar signals and infer $\leqslant 0.10$ for the fraction of neutron stars orbiting ELM WDs, although ELM WDs are also found as companions to pulsars (see subsection 1.3.3).

In evolutionary terms, ELM WDs are connected with cataclysmic variables — CVs

[5] Actually, the exact limit is not well defined. We can cite as an example the mass loss in the asymptotic giant branch — AGB (e.g., Bloecker, 1995b; Bloecker, 1995a), which is a complex dynamic phenomenon that is still poorly understood (see Höfner; Olofsson, 2018 for a review). Mass loss can take away significant amount of matter, depending on the star's initial mass, and thus significantly modify the subsequent evolution of the star (Cummings et al., 2018).

[6] There are several definitions for the upper mass limit for the class in the literature, e.g., 0.18 $M_\odot$ (Sun; Arras, 2018), 0.20 $M_\odot$ (Kawka; Vennes, 2009; Althaus; Miller Bertolami; Córsico, 2013; Chen et al., 2017), 0.25 $M_\odot$ (Hermes et al., 2013b; Hermes et al., 2013a), 0.30 $M_\odot$ (Li et al., 2019; Pelisoli; Vos, 2019).

(e.g., Ivanova et al., 2006, Giovannelli, 2008, Knigge; Baraffe; Patterson, 2011, Knigge, 2012, Zorotovic; Schreiber, 2020, Belloni; Rivera, 2021, El-Badry et al., 2021a, El-Badry et al., 2021b), and low-mass X-ray binaries — LMXBs (e.g., Patterson, 1984, Ritter; Kolb, 2003, Liu; van Paradijs; van den Heuvel, 2007, Ivanova et al., 2008, Charles, 2011, Sazonov et al., 2020), as the former is one of the possible evolutionary continuations of the latter. The mass transfer observed in CVs and LMXBs systems occurs from the pre-ELM to a white dwarf or neutron star accretor, respectively. As such, not all CVs or LMXBs systems will host ELM WDs in the subsequent evolutionary stages.

1.3.3 Low-mass white dwarfs in binary systems with pulsars

Pulsars are high-rotating and highly magnetised neutron stars that emit beams of intense radiation at radio wavelengths. They were theoretically predicted in 1933 (Baade; Zwicky, 1934) and discovered in 1968 (Hewish et al., 1968) by observing pulses separated by 1.33 seconds that originated from the same location in the sky. Since then, the number of known pulsars in our Galaxy increased to almost 2800. The most famous application was the first indirect observational evidence for gravitational waves in the first binary pulsar discovered, the so-called Hulse–Taylor pulsar (Hulse; Taylor, 1975). The most important quantities in the study of pulsars is the spin period and its temporal derivative. The known pulsars have spin period $0.001396 \leq P_{\rm s}\ ({\rm s}) \leq 23.535378$ and $5.83 \times 10^{-22} \leq \dot{P}_{\rm s}\ ({\rm s/s}) \leq 5.49 \times 10^{-10}$, and 38 of them have $\dot{P}_{\rm s} < 0$. The fraction of pulsars that have well-determined $\dot{P}_{\rm s}$ is 82% of the known total. Different values of $P_{\rm s}$ and $\dot{P}_{\rm s}$ imply different magnetic fields strengths and ages for a pulsar. In a rough theoretical approach, we can consider the relations $B \propto \sqrt{P_{\rm s}\dot{P}_{\rm s}}$ and $\tau_{\rm PSR} = P_{\rm s}/2\dot{P}_{\rm s}$ for these quantities, where $\tau_{\rm PSR}$ is the characteristic age of the Pulsating Source of Radio (Harding, 2013; Kaspi, 2017). An important class of pulsars are the so-called millisecond pulsars (MSP) that, as the name suggests, complete a rotation within a fraction of a second (there are 465 MSPs with $P_{\rm s} < 0.01$ s in the version 1.66 of the ATNF Pulsar Catalogue, Manchester et al., 2005).

About 80% of the MSPs are in known binary systems. MSPs are thought to have originally been members of the rotation powered pulsar population (with $10^{12} \lesssim B/{\rm G} \lesssim 10^{13}$ and $10^{-1} \lesssim P_{\rm s}/{\rm s} \lesssim 10^{0}$), spun down ($10^{1} \lesssim P_{\rm s}/{\rm s} \lesssim 10^{2}$) for tens of Myr and then spun up ($10^{8} \lesssim B/{\rm G} \lesssim 10^{10}$ and $10^{-3} \lesssim P_{\rm s}/{\rm s} \lesssim 10^{1}$) by accretion from a binary companion (Backus; Taylor; Damashek, 1982; Alpar et al., 1982). A common scenario are the X-ray binary systems, where an initially low-spinning neutron star accretes matter from an early-stage donor star and, due to angular momentum gain, becomes an MSP (Bhattacharya; van den Heuvel, 1991). These pulsars are then said to be recycled (Papitto et al., 2013; Campana; Salvo, 2018; Papitto; de Martino, 2020; Patruno; Watts, 2021). In this scenario, the X-ray emission originates as a result of the conversion of the gravitational binding

energy of the accreted mater into kinetic energy. For a typical neutron star mass and radius, the energy released by the infalling matter into the deep gravitational potential well is up to $\sim 10^{20}$ erg/g. This is a tenth of the rest-mass energy, $\sim 0.1c^2$ (where c is the speed of light), making accretion an ideal source of power. Each unit of accreted mass that reaches the neutron star surface releases an amount of gravitational potential energy given by GM/R. Thus, a typical accretion rate of 10^{-9} $M_\odot$/yr generates a luminosity of $\sim 10^{37}$ erg/s. See a more complete discussion in Kylafis (1995), Wang (2016), D'Antona & Tailo (2020), Di Salvo & Sanna (2020), Bhattacharyya (2021), Dall'Osso & Stella (2021), Bhattacharyya & Roy (2021).

Figure 4 shows the distribution of masses and companion type to known pulsars as a function of the orbital period of the system. The data was taken from the ATNF (Australia Telescope National Facility) pulsar catalogue (Manchester et al., 2005). Currently, this catalogue has 2796 entries, of which 10% have identified companions. The figure shows 41 CO WD, 137 He WD, and 54 ultra-light companions (UL), in a total of 256 pulsars with identified low-mass companions. As we discussed earlier, the formation of white dwarfs with masses below 0.45 $M_\odot$ most likely depends on the mass transfer to the compact companion (a neutron star in this case). On the other hand, main sequence stars in short orbital period systems should transfer mass to the neutron star after leaving the main sequence.

Depending on the nature of the companion star, there is a possibility that recycled pulsars are formed from low-mass X-ray binaries. Low-mass X-ray binaries (LMXBs, Iben; Tutukov; Yungelson, 1995b)[7] are binary systems in which one star is a neutron star (or a black hole) and the other star is a low-mass main sequence, a white dwarf or a red giant that transfers matter onto the compact object via Roche lobe overflow (see subsection 1.2.2). Since the total number of LMXBs and their collective luminosity are directly proportional to the stellar mass of a given galaxy, they can be used as a stellar mass indicator for the host galaxy (see, e.g., Gilfanov, 2004). Despite the rarity of LMXBs, they completely dominate the X-ray emission of the old stellar population of the Milky Way (Fabbiano, 2006; Schatz; Rehm, 2006; Sazonov et al., 2020).

Figure 5 shows the possible evolutionary path of the PSR B1855+09 system, often used to compare the ages predicted by white dwarf's formation and cooling theories with the pulsar's accretion and rotation ones (Althaus; Serenelli; Benvenuto, 2001a; Althaus; Serenelli; Benvenuto, 2001b; Benvenuto; De Vito, 2005). PSR B1855+09 consists of a 0.258 $M_\odot$ white dwarf with $T_{\rm eff} = 4800 \pm 800$ K and a 1.50 $M_\odot$ MSP in a 12.3 day circular orbit (Segelstein et al., 1986; van Kerkwijk et al., 2000). In the models, at age zero, a wide orbit binary system consisting of a high mass star (15 $M_\odot$) plus a low mass star (1.6 $M_\odot$) is

[7] Their most massive equivalents are the intermediate-mass X-ray binaries (IMXB, Podsiadlowski; Rappaport; Pfahl, 2002; Pfahl; Rappaport; Podsiadlowski, 2003) and the high-mass X-ray binaries (HMXB, Iben; Tutukov; Yungelson, 1995a).

Figure 4 – Distribution of known pulsars in binary systems with CO/ONeMg WD, He WD, main sequence (MS), and ultra-light/planet (mass $< 0.08\ M_\odot$) companions in the orbital period–mass plane.

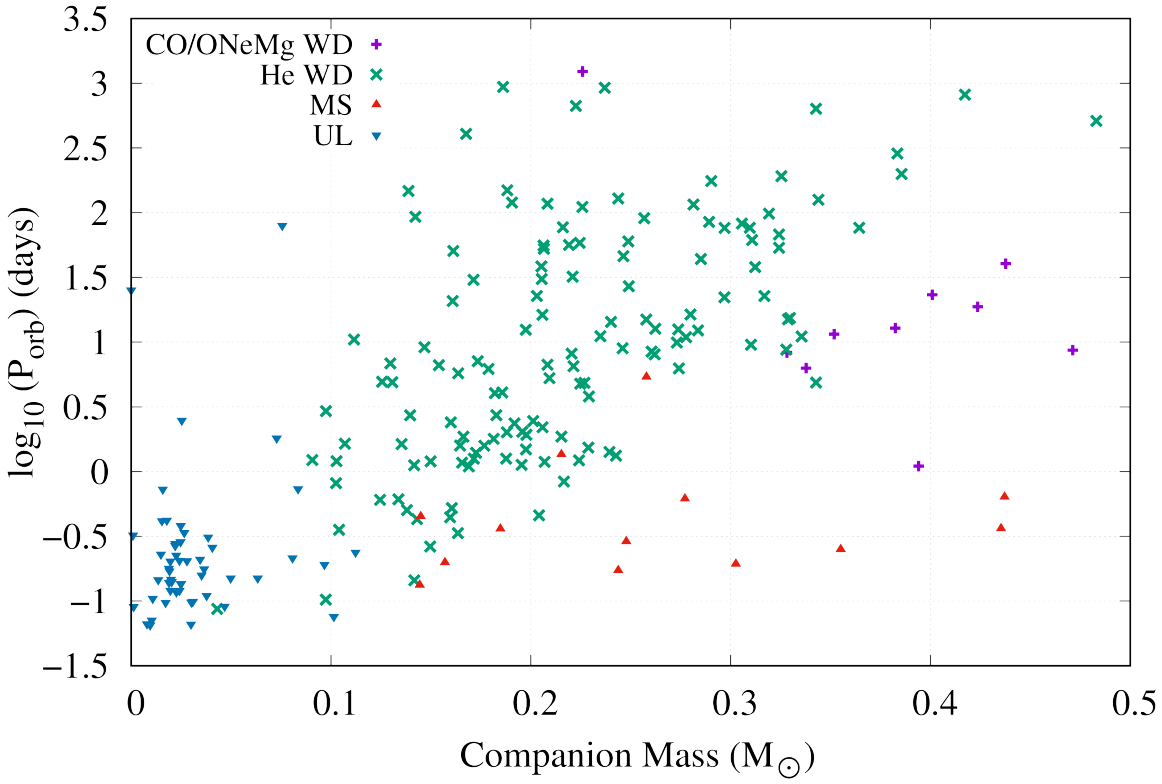

Credit: data taken from the ATNF pulsar catalogue (Manchester et al., 2005).

put together. The larger mass star evolves first, growing beyond its gravitational boundary and initiating the non-conservative mass transfer — i.e., some mass is also lost from the system — to the lowest mass star. Depending on the stability of the mass transfer, a common envelope phase may occur. A common envelope is gas that contains a binary star system. In this sense, common envelope evolution is a phase in the life of a binary star during which two stars orbit inside a single, shared envelope (Ivanova et al., 2013). After the end of the mass transfer — and the ejection of the envelope, the initially more massive star is now a naked helium star[8] (i.e., a star of spectral class O or B with strong helium lines). In the model, this star explodes in a supernova event, leaving behind a young (15 Myr) neutron star of mass 1.3 $M_\odot$. The system now has only 17% of its initial

[8] This is a typical scenario where a Be/X-ray binary with B-star mass in the range 8–20 $M_\odot$ underwent a case B or case C mass transfer (see subsection 1.4.2), giving rise to a helium star with mass of 1.5–6.7 $M_\odot$ in a binary system with a 1.4 $M_\odot$ neutron star companion (see, e.g., Dewi et al., 2002). In its turn, Be/X-ray binaries are systems where a hot star, with a B spectral type, non supergiant, whose spectrum presents hydrogen emission (Jaschek; Egret, 1982), donates mass to a compact companion, generating X-ray emission (see Reig, 2011 for a review).

mass. The next steps correspond to the evolution of the initially less massive star and last about 99% of the time of all evolution. The neutron star accretes matter from its companion that has become a giant in a low mass X-ray binary system. The final state of the system is a millisecond pulsar plus a low mass white dwarf in a 12 days orbit.

Figure 5 – An illustration showing the theoretically predicted evolutionary stages the PSR B1855+09 system has gone through, from the ZAMS stage to how we see it today. Note that the first six evolutionary stages — up to the formation of the NS — are extremely fast compared to the rest of evolution.

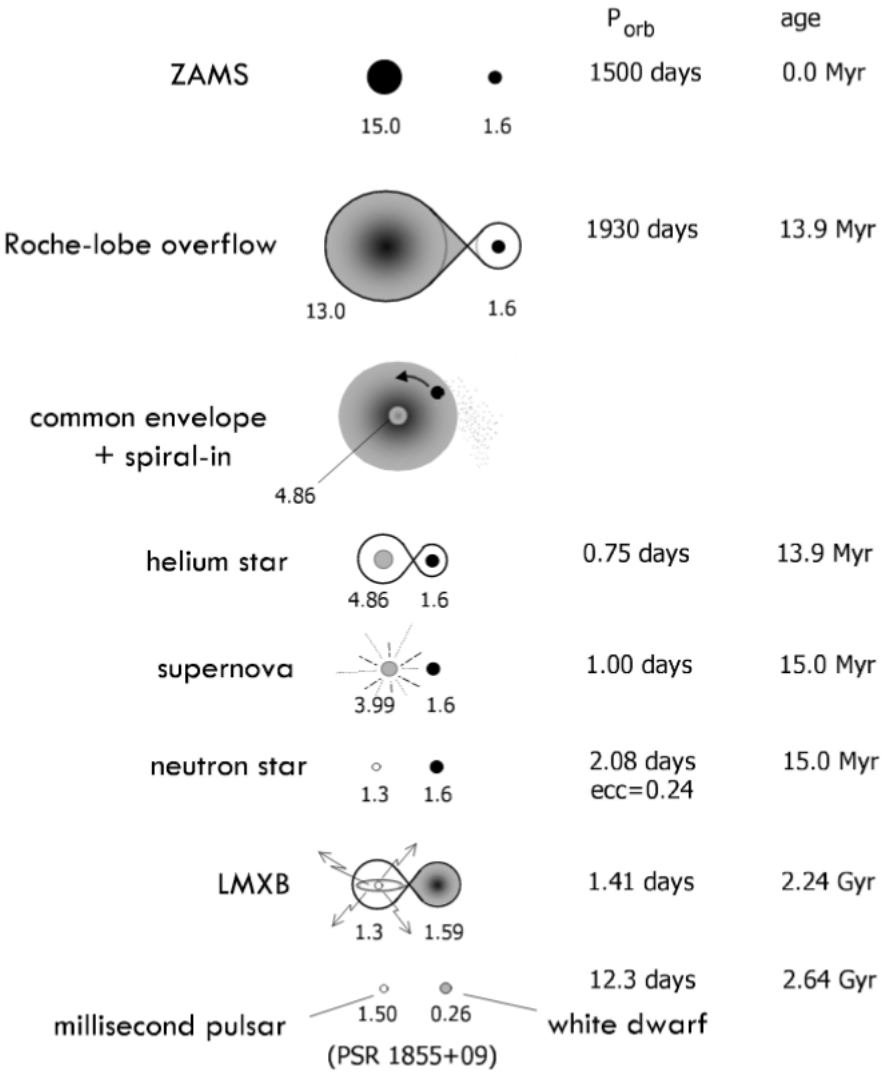

Credit: Tauris & van den Heuvel (2006).

A comprehensive review of the main evolutionary paths that a binary system can follow — from the main sequence to the formation of the compact objects — can be found in Han et al. (2020). The major problems in the theory of evolution of LMXB and LM/ELM WDs (low-mass and extremely low-mass white dwarfs, respectively) will be

discussed in section 1.5.

1.4 Mass transfer

1.4.1 Conservative mass transfer in close binaries

Once mass transfer occurs in close binary systems, the final state of a star in such a system no longer depends only on its mass at the zero-age main sequence (ZAMS). Now, the final state of the compact remnants strongly depends on parameters such as the initial orbital separation, which can easily be translated to the initial orbital period, P_i, and the mass ratio q.

We must keep in mind that this is not a specific case in close binary systems. Since the shrinking of the orbit due to angular momentum loss and the expansion of the stars due to nuclear reactions are a natural result of the evolution, the ratio R/R_L must increase with time.

From detailed calculations on a model of gas flowing through the L_1 point,[9] it is well known that there is a strong dependence of the mass transfer rate $\dot{M}$ on the radius excess of the donor, $\Delta R = R_\mathrm{d} - R_\mathrm{L}$ (e.g., Pringle; Wade, 1985), that is, the amount by which the star's radius overfills its Roche lobe. As an example, for stars with convective envelopes, i.e red giants or low-mass main-sequence stars, we have the relation

$$\dot{M} \propto \left(\frac{\Delta R}{R_\mathrm{d}}\right)^3 . \tag{1.21}$$

A more accurate equation can be found applying Bernoulli's law and assuming a polytropic star, yielding

$$\dot{M} = -A\frac{M_\mathrm{d}}{P}\left(\frac{\Delta R}{R_\mathrm{d}}\right)^3 , \tag{1.22}$$

where A is an numerical constant of order $\sim$ 10–20 that depends on the interior density distribution of the star, equation of state, and on the geometry of the mass flow (Paczyński; Sienkiewicz, 1972; Savonije, 1978; Webbink, 1985). A rough estimate using $R_\mathrm{d} = 10R_\odot$, $M_\mathrm{d} = 1M_\odot$ and $P = 5$ day with a radius excess of the donor of only 1% results in a mass transfer rate of $\dot{M} = 10^{-6}M_\odot$/day, i.e., the transfer of the entire donor mass in about a hundred thousand orbits, a thousand years. Going further, if R_d exceeds R_L by 10%, mass transfer will occur on a dynamic timescale. This alone is not a problem but rather the accretor's capability to accommodate such amount of matter. It follows that for a semi-detached system in which we observe a steady and slow mass transfer, the donor star

[9] In fact, on a more realistic model, it is as if the stream of matter were passing through a nozzle of width $\sim 0.1Pc_\mathrm{s}$, where c_s is the speed at which pressure disturbances travel through the gas (see, e.g., Frank; King; Raine, 2002).

only overfills its Roche radius by a small fraction. Thus, in this case, it is valid to a very good approximation that $R_{\rm d} = R_{\rm L}$ and $\dot{R}_{\rm d} = \dot{R}_{\rm L}$.

Although a friable phenomenological assumption, the study of conservative mass transfer helps us better understand the dynamics of this type of system. We define the conservative mass transfer as the case in which the total mass and orbital angular momentum of the binary are conserved, i.e., $\dot{M}_{\rm a} = -\dot{M}_{\rm d}$ and $\dot{J} = 0$. Therefore, Equation 1.9 becomes

$$\frac{\dot{a}}{a} = 2\frac{\dot{M}_{\rm d}}{M_{\rm d}}\left(\frac{M_{\rm d}}{M_{\rm a}} - 1\right) \ , \tag{1.23}$$

where $\dot{M}_{\rm d} < 0$ by definition. So assuming mass transfer from donor to accretor, we find that:

a) if $M_{\rm d} > M_{\rm a}$, the orbit will shrink ($\dot{a} < 0$);

b) if $M_{\rm d} < M_{\rm a}$, the orbit will expand ($\dot{a} > 0$);

c) regarding conservative mass transfer, the minimum orbital separation occurs when $M_{\rm a} = M_{\rm d}$.

A simple integration of Equation 1.23 give us

$$a(M_{\rm a}M_{\rm d})^2 = \text{constant} \ , \tag{1.24}$$

and, using Kepler's law

$$\frac{\dot{P}}{P} = 3\frac{\dot{M}_{\rm d}}{M_{\rm d}}\left(\frac{M_{\rm d}}{M_{\rm a}} - 1\right) \ . \tag{1.25}$$

This is useful because, knowing the derivative of the period and the mass of the components, we can estimate the mass transfer rate — if it is conservative — or to have some insight into non-conservative mass transfer.

1.4.2 Non-conservative mass transfer and mass transfer cases

Observationally there is evidence for both conservative and non-conservative mass transfer in evolving binaries systems. This is easy to understand since mass transfer depends on the mass ratio, the evolutionary state of each of the components, the composition of the matter in the mass current, and so on. While modelling conservative is trivial, modelling non-conservatively mass transfer is quite complicated and often depends on extra assumptions. Here we will indicate just some general aspects of this kind of evolution, and more details will be provided in subsection 2.2.2.

Let us suppose the situation in which the donor star is losing mass and only a fraction $\beta_{\rm acc}$ of the transferred mass is accreted by the companion star. We have then

$$\dot{M}_{\rm a} = -\beta_{\rm acc}\dot{M}_{\rm d} \tag{1.26}$$

and

$$\dot{M}_{\rm a} + \dot{M}_{\rm d} = (1 - \beta_{\rm acc})\dot{M}_{\rm d} \ . \tag{1.27}$$

Obviously, the lost material also takes away angular momentum. So we should take the specific angular momentum of the ejected matter to be $\gamma_{\rm eje}$ times the specific angular momentum of the binary and find

$$\frac{\dot{J}}{J} = \gamma_{\rm eje}(1 - \beta_{\rm acc})\frac{\dot{M}_{\rm d}}{M_{\rm d} + M_{\rm a}} \ , \tag{1.28}$$

and the expression for the change in the orbital separation becomes

$$\frac{\dot{a}}{a} = -2\frac{\dot{M}_{\rm d}}{M_{\rm d}}\left[1 - \beta_{\rm acc}\frac{M_{\rm d}}{M_{\rm a}} - (1 - \beta_{\rm acc})(\gamma_{\rm eje} + 1/2)\frac{M_{\rm d}}{M_{\rm a} + M_{\rm d}}\right] \ . \tag{1.29}$$

In practice, it is quite complicated to choose values for parameters $\gamma_{\rm eje}$ and $\beta_{\rm acc}$. When considering specific systems, observations may suggest some appropriate ranges for these parameters, but exact values should depend on a number of factors such as the q ratio between masses, the environment the system is in, the evolutionary stage of each star, and more.

Another common classification of the different cases of mass transfer — which is independent of mass conservation hypothesis — is due to the nuclear evolutionary state of the donor star when the RLOF starts (Kippenhahn; Kohl; Weigert, 1967; Lauterborn, 1970):

a) Case A: during core hydrogen burning (i.e., the star is still on the main sequence);

b) Case B: after hydrogen core exhaustion but before helium ignition (i.e., the star left the main sequence but has not reached the tip of the giant branch);

c) Case C: after helium core exhaustion, i.e., the star left the horizontal branch.

1.4.3 Stability of mass transfer

Once Roche-lobe overflow (RLOF) starts, the stability of the mass transfer depends on three factors. The first is the response of the donor's radius to the mass loss, which depends mainly on which evolutionary phase the star is in. The second is the orbit response to the mass transfer. As we saw in subsection 1.4.1, the increase or decrease in orbital separation depends on the mass of each star. The variation of the masses also changes the ratio q, and thus also the Roche lobe radius $R_{\rm L}$. Third and last, the stability of the mass transfer also depends on how — or if — the accretor star is capable of receiving the transferred material.

The stability of mass transfer is normally understood in terms of three derivatives of radii with respect to the mass of the donor star (e.g., Webbink, 1985; Soberman; Phinney;

van den Heuvel, 1997; Tout et al., 1997),

$$\zeta_{\rm L} = \left(\frac{\partial \ln R_{\rm L,d}}{\partial \ln M_{\rm d}} \right) \ , \tag{1.30}$$

$$\zeta_{\rm th} = \left(\frac{\partial \ln R_{\rm d}}{\partial \ln M_{\rm d}} \right)_{\rm th} \ , \tag{1.31}$$

$$\zeta_{\rm ad} = \left(\frac{\partial \ln R_{\rm d}}{\partial \ln M_{\rm d}} \right)_{\rm ad} \ , \tag{1.32}$$

where $\zeta_{\rm L}$ is the response of the Roche lobe to the mass loss, and $\zeta_{\rm th}$ and $\zeta_{\rm ad}$ are the thermal-equilibrium and the adiabatic-hydrostatic responses, respectively. Following are three possible scenarios.

a) If $\zeta_{\rm L} < \zeta_{\rm th}, \zeta_{\rm ad}$, the mass transfer is stable and occurs on the nuclear timescale of the donor or on the angular momentum loss timescale of the system, whichever is shorter.

b) If $\zeta_{\rm th} < \zeta_{\rm L} < \zeta_{\rm ad}$, the mass transfer is stable and self-regulating, i.e., driven by the thermal readjustment of the donor.

c) If $\zeta_{\rm L} > \zeta_{\rm th}, \zeta_{\rm ad}$, the star cannot maintain the hydrostatic equilibrium and mass loss proceeds unstable, on a dynamical timescale. In this case, the adiabatic response of the donor is unable to retain the star inside the Roche lobe, leading to a dramatic increase of the mass transfer and probably leading to the common-envelope case.

Since the thermal timescale is much longer than the dynamic timescale (see subsection 1.2.3), there cannot be $\zeta_{\rm th} > \zeta_{\rm ad}$.

1.5 The magnetic braking problem

In this section we will look at the main problems related to the theory of evolution of LMXB and LM/ELM WDs systems. The loss of angular momentum in the evolution of binary systems giving rise to ELM WDs can be roughly divided into three contributions. The most obvious is the loss of mass, as all matter lost by the system takes away angular momentum. The other one is gravitational waves (GW), which are disturbances in the curvature of spacetime, generated by accelerated masses, and that transport energy as gravitational radiation. This mechanism generally predominates in very compact systems, with orbital periods on the order of hours or a few days.

In addition to these two already well understood processes, there is another important physical mechanism responsible for the removal of orbital angular momentum. This is magnetic braking (MB), which is thought to be effective for main sequence and red

giant convective envelopes, i.e., G to M spectral class donor stars, approximately in the mass interval 0.3–1.2 $M_{\odot}$. The concept of magnetic braking was introduced by Verbunt & Zwaan (1981) when it became evident that momentum loss by GWs alone is unable to explain the observed mass-transfer rates in close binary systems.

The basic idea behind angular momentum loss by magnetically-coupled stellar wind is that the stellar wind is compelled by magnetic field to co-rotate with the star to rather large distances, where it carries away large specific angular momentum, making it possible to take away substantial angular momentum without evolutionary significant mass-loss by the wind. This phenomenon was theoretically anticipated by Schatzman (1962), Brandt (1966), and Weber & Davis (1967); and then inferred by Kraft (1967) and Skumanich (1972) in nearby stars.

In the original formalism, an empirically-derived formula was obtained through observations of the spin-down of rotation of single G-dwarfs in stellar clusters. The formula then expresses the phenomenological dependence of the equatorial rotational velocity on age (Skumanich, 1972). When applying this to a binary, tidal locking between the stellar axial rotation and orbital motion is assumed.

Considering that stars of different spectral types on the main sequence have different rotational speeds, Schatzman (1962) was the first to suggest that the convective envelope could be the reason for some stars to have low rotation velocities. He suggested that in convective stars the high magnetic field forces that ejected matter spinning along with the star, even at very high distances, carries a large amount of angular momentum per unit mass. The first numerical estimate came from Skumanich (1972), who showed that the equatorial rotation velocities of G-type main sequence stars decrease with time, suggesting the empirical dependence $\Omega \propto t^{-1/2}$, currently known as "Skumanich law". Here, Ω is the stellar rotational angular velocity. What followed was a wide variety of suggested parameterizations in the same form of $\Omega \propto t^{-\alpha}$, but considering stars in different evolutionary stages and different masses (e.g., see Mestel, 1968; Mestel; Spruit, 1987), giving rise to various possible relations between $\dot{J}$ and Ω.

Many computations on the formation of low-mass binaries with millisecond pulsars that took into account the magnetic braking in orbital angular momentum loss simply considered the extension of the Skumanich law to the binary system with a synchronised rotation of the primary (e.g., Muslimov; Sarna, 1993).

A more elaborate expression appeared in the seminal work of Rappaport, Verbunt & Joss (1983), where the mass, radius, and rotation of the star are time dependent quantities and the expression is parameterized by the so-called magnetic braking index $\gamma_{\rm mb}$. We will present this equation and more details of this prescription in subsection 2.2.2, along with the modifications we have implemented in our work. As we will show in the next chapters, despite being a major breakthrough, this formalism seems to be limited to reproduce the

evolution of binary systems containing ELM WDs.

Unfortunately the exact behaviour of magnetic fields and magnetic braking is considerably more complicated. It is well known that magnetic fields play an important role at all stages of stellar evolution, from star formation to the end-products. Even more, magnetic fields have been detected in most (if not all) types of stars across the Hertzsprung-Russell diagram (HRD), modifying both the stellar surface and the interior. For an overview of the subject and for a complete discussion of the results presented below, we refer the reader to Maeder et al. (2008), Donati (2010), Dudorov & Khaibrakhmanov (2015), Martin (2018). It is believed that there are two main mechanisms capable of explaining the magnetic fields in stars. They are the dynamo process and the fossil fields. Fossil fields are simply magnetic fields inherited from the earlier stages of a star's life. On the other hand, the dynamo theory describes the process through which a rotating, convecting, and electrically conducting fluid acts to maintain a magnetic field. Magnetic fields are ubiquitous to all stars with significant outer convection zone, and there is strong observational evidence that magnetic fields of cool stars are generated through dynamo processes. Differently, the fossil field hypothesis finds little support either from observations and theory since these fields should be dissipated by convection in photon diffusion timescales or even less. These results are of great importance since we are interested in main sequence donor stars of spectral types F and G.

Next, we will briefly review some models present in the literature. It is noteworthy that the aforementioned Rappaport empirical equation is, by far, the most used form for calculating the contribution of magnetic braking in the angular momentum evolution — despite variations in the $\gamma_{\rm mb}$ parameter. Occasionally, some variations based on the original equation also appear.

1.6 Review of the literature models

One of the first systematic studies on the evolution of close binaries dates back to the 1960s. Paczyński (1966) focused on the stages of mass transfer when a primary star evolves first and fills its Roche lobe during the hydrogen burning. In his models, the total mass and angular orbital momentum are conserved. Paczyński (1967a) seeks to understand the effects of considering different amounts of hydrogen in main sequence stars with masses in the range $4 \leqslant M/M_{\odot} \leqslant 16$. In Paczyński & Ziółkowski (1967) it is shown that the mass loss modifies the mass ratio of the binary system and this should affect the observed luminosity. In Paczyński (1967b) a Henyey-type code[10] was used to confirm the different evolutionary stages and their duration during the mass transfer. Several

[10] Because the structure equations of stellar evolution have to be solved simultaneously with the energy transport equations, Henyey-type codes employ an iterative implicit technique instead of a direct integration (Henyey; Forbes; Gould, 1964).

updates in the code were presented in Ziółkowski (1970a), focusing on the mass exchange. Then, Ziółkowski (1970b) focused on low and intermediate-mass stars for the first time. He found that the cases A and B of mass transfer are very similar, and the models keep almost constant position on the HRD during the mass transfer. Finally, in Paczyński & Sienkiewicz (1972) the authors studied the case when the donor star has a deep convective envelope during the mass transfer. They found that a considerable fraction of mass is transferred on a dynamical time scale.

Muslimov & Sarna (1993) studied the formation of low-mass ($< 0.3\ M_\odot$) red dwarfs with millisecond pulsars. They considered donors with initial masses of 0.5 $M_\odot$ and 1 $M_\odot$, and the beginning of the mass transfer when the orbital period of the system is 4.5 h and 9.4 h, respectively. One of the main points of the study is the consideration of the NS magnetic field and its effect on the donor's evaporation. They found that the radiation energy converted into thermal energy in the photosphere is not catastrophic but merely activates the process of mass loss.

Driebe et al. (1998) presented a grid of seven evolutionary tracks for low-mass white dwarfs with helium cores, solar composition, in the mass range from 0.179 to 0.414 $M_\odot$. They did not take into account element diffusion and did not model the binary system. Instead, they apply a large mass loss rate in 1.0 $M_\odot$ donors to emulate the RLOF. They found hydrogen shell flashes to take place only in the mass interval $0.21 < M/M_\odot < 0.3$. Assuming the same conditions, they further expanded the study to focus on thermal instabilities[11] (Driebe et al., 1999), and comparing the cooling age of WDs with the characteristic (spin-down) ages of pulsars (Schönberner; Driebe; Blöcker, 2000).

Podsiadlowski, Rappaport & Pfahl (2002) carried out a systematic study of low and intermediate-mass X-ray binaries consisting of 100 binary evolutionary sequences. They considered the accretor to be a neutron star and the donor to be a normal star with the initial mass in the range 0.6 to 7 $M_\odot$. They studied systems with initial orbital period from 4 hr to 100 d and pointed out that the evolution of this kind of system is much more complex than previously believed. In particular, they indicated discrepancies between observed and calculated luminosity, in addition to the orbital period distribution of millisecond pulsars.

Lin et al. (2011) present probably the largest grid of models of low and intermediate-mass X-ray binaries, totalizing 42,000 tracks. Despite this, they considered varying only two parameters: the initial orbital period (in the range 10–250 h) and the donor mass (in the range 1–4 $M_\odot$). They focus on explaining the then newly discovered radio pulsar PSR J1614-2230 and found that considering an initial canonical-mass neutron star (i.e., 1.4 $M_\odot$) fails to produce the observed 1.97 $M_\odot$ NS with a 0.5 $M_\odot$ WD companion in a 8.7

[11] I.e., the occurrence of hydrogen-shell flashes due to unstable hydrogen burning via CNO cycling. See also chapter 3.

day orbit.

Several theoretical models for LM and ELM WDs in binaries has been made to date. Serenelli et al. (2002) focused on low metallicity models where the low-mass He WDs were obtained by applying mass-loss rates to a 1 $M_{\odot}$ stellar model in such a way that the stellar radius remains close to the Roche lobe radius. Panei et al. (2007) obtained 11 sequences of models of white dwarfs with helium or oxygen cores. Although they used adequate physics to treat the donor star, they did not indicate how they evolved the binary system. Althaus et al. (2009) focused on high metallicity models, again without modelling the evolution of the binary system.

De Vito & Benvenuto (2010) built model sequences for low-mass WD in binary systems. For the evolution of the angular momentum of the binary system, they considered mass loss, gravitational radiation, and magnetic braking. For the donor, diffusion of elements was taken into account; and it was assumed that the accretor was able to retain 50% of the material received. They focused on studying the dependence of accretor star (NS) mass on the evolution of the system. They selected donors of mass between 0.5 and 3.5 $M_{\odot}$, and accretors between 0.8 and 1.4 $M_{\odot}$. They found that the evolution of systems heavily depends upon the mass of the neutron star, which may be the determining factor for the formation of an ultra-compact system or widely separated objects. On the other hand, they found that the final orbital period vs. white dwarf mass relation is fairly insensitive to the initial neutron star mass value. Using very similar premises, De Vito & Benvenuto (2012) expanded the study to analyse the influence of accretion efficiency on the formation of these systems. They found a weak dependence of the final donor star mass on the accretion efficiency. Likewise for the final orbital period, that exhibits moderate changes of approximately 25%, depending on the initial configuration.

Althaus, Miller Bertolami & Córsico (2013) presented models considering the evolution of the binary system, where they took into account the loss of angular momentum due to loss of mass, gravitational radiation, and magnetic braking. The accreting star was considered to be a point of mass with 1.4 $M_{\odot}$ and no magnetic field, and the donor with initial mass of 1 $M_{\odot}$. They obtained 14 He WD models of masses down to 0.155 $M_{\odot}$. Istrate et al. (2014) focused on the thermal evolution and the contraction phase towards the WD cooling track and investigated how this evolution depends on the white dwarf mass. In Istrate et al. (2016) the joint effects of diffusion and rotation in the donor star were considered for the first time. Four different metallicities were considered. Adequate treatment of the binary system was considered, as well as the interior of the donor star. They considered a donor star of mass 1.0 and 1.4 $M_{\odot}$, and the accretor as being a NS of mass in the range 1.2 and 1.4 $M_{\odot}$, producing white dwarfs with masses between 0.16–0.45 $M_{\odot}$.

Considering ELMs progenitors in the range 1–1.5 $M_{\odot}$ and accreting companions

within the range 0.4–0.9 $M_\odot$, Sun & Arras (2018) modified the Rappaport, Verbunt & Joss (1983) magnetic braking formula in order to smooth the braking when the convective zone becomes thin. Sun & Arras (2018) concluded that the formation of an ELM white dwarf with $M \lesssim 0.18$–$0.20\ M_\odot$ by unstable mass transfer or a common-envelope (CE) event is unlikely.

Also, Li et al. (2019) found that ELM WDs with $M \lesssim 0.3\ M_\odot$ in double degenerate systems may be formed either from a stable mass transfer process or common-envelope ejection, although the Roche-lobe formation channel has a greater contribution to the formation of He WD with mass $\lesssim 0.22\ M_\odot$, and the common envelope channel for higher masses.

He, Meng & Chen (2019) focused on studying accreting millisecond X-ray pulsars (AMXP), a subclass of low-mass X-ray binaries. They consider a 1.4 $M_\odot$ NS accreting mass from donors in the range 1–1.3 $M_\odot$ and found that AMXPs with main sequence donors may ultimately evolve into extremely low-mass He WD donors.

Procedures similar to those used for modelling ELM WDs are also used for modelling sdB (Wu et al., 2018) and sdA (Yu et al., 2019) stars.

In general, the models were able to reproduce with good accuracy the physical parameters observed in white dwarfs, such as rotation, chemical abundance, final mass, effective temperature, and surface gravity; and they also agree with the theory of stellar evolution regarding the occurrence of shell flashes and cooling time.

Despite these successes, there was still a big unresolved problem. A severe fine-tuning in the initial orbital period was necessary to reproduce the observed MSPs in tight binaries with He WD companions. Istrate, Tauris & Langer (2014), Istrate et al. (2016) showed that the empirical treatment of the magnetic braking by Rappaport, Verbunt & Joss (1983) leads to a fine-tuning of the order of a dozen minutes in the initial orbital period to reproduce the observed orbital periods of millisecond pulsars in compact ($2 < P/\mathrm{h} < 9$) binaries with He WD companions of mass $\lesssim 0.20\ M_\odot$. To be more precise, they found that all ELM WDs within the mass range $0.167 \leqslant M/M_\odot \leqslant 0.205$ formed in LMXB system via RLOF must have come from systems with initial orbital period within the range $3.345 \leqslant P_\mathrm{i}/\mathrm{d} \leqslant 3.42$. Fine-tuning is not prohibited — in fact, it occurs in nature. However, philosophical arguments generally agree that this phenomenon is not to be expected (e.g., Walker; Ćirković, 2006; Weinberg, 2015; Sloan et al., 2020; de Vuyst, 2020). Since the P_i–$M_\mathrm{d,f}$ relation is expected to follow a log-normal orbital period distribution (Duquennoy; Mayor, 1991; Raghavan et al., 2010; Duchêne; Kraus, 2013; Tutukov; Cherepashchuk, 2020), it was suggested that something needed to be modified or was missing in the standard input physics of LMXB modelling.

Since most angular momentum loss mechanisms are reasonably well understood

and apparently works properly, the problem seems to fall on the magnetic braking. (Li; Wickramasinghe, 1998) show, for example, that allowing an oblique inclination of the dipoles in the plane linking the two rotational axes of the binary components can have a dramatic effect on the braking rate. Also, studies considering the spinning, mass transfer, and accretions rate of specific binary systems found it difficult to construct theoretical models that reproduce the observational data when the standard magnetic braking is considered (e.g., see Xing; Li, 2019). Combining a binary population synthesis code and detailed stellar evolutionary calculations, Shao & Li (2015) confirmed the discrepancies between theoretical predictions and observations concerning mass transfer rates and orbital periods of LMXB systems, pointing out that something linked to the orbital angular momentum loss was likely missing in the modelling.

It has been shown that, for LMXBs, there is a critical initial orbital period — called the bifurcation period (Tutukov et al., 1987; Pylyser; Savonije, 1988; Pylyser; Savonije, 1989; Podsiadlowski; Rappaport; Pfahl, 2002; van der Sluys; Verbunt; Pols, 2005) — that separates the systems in converging and diverging. The converging systems are the ones that, after the RLOF, evolve with decreasing orbital period — the components approach each other — until the donor star becomes degenerate, and an ultra-compact binary is formed. The diverging systems are the ones that, after the RLOF, evolve with increasing orbital period — the components move away from each other — and a wide detached binary is formed (Pylyser; Savonije, 1988; Pylyser; Savonije, 1989). Furthermore, this important bifurcation period depends on the strength of the magnetic braking (e.g., Tauris; van den Heuvel, 2006). A systematic study made by Ma & Li (2009) comparing several formalisms of magnetic braking law and mass loss mechanisms found that the strength of the magnetic braking is the dominant factor in determining the value of bifurcation periods compared to mass loss.

In general, the different contributions to the evolution of the angular momentum of binary systems have been studied quite irregularly over the years. The most recent models take into account the loss of angular momentum by gravitational radiation, loss of mass, and magnetic braking. Despite that, there is no consensus on the ideal treatment, especially when it comes to mass loss and magnetic braking. In our models, we will combine the most recent improvements in the understanding of the magnetic braking of binary systems (see subsection 2.2.3) with one of the most robust and modern stellar evolution codes (see section 2.2).

1.7 Overview and aims

As we have already pointed out, at least half of the stars do not evolve as a single, isolated star. In fact, data from numerous surveys indicate that the properties of the binary

population (the binarity frequency, the mass distribution, the orbital period distribution, etc., and see summary in Herczeg, 1984) are a function of the spectral type of the primary star. For example, almost all stars with spectral type O, B and A are found in binary or multiple systems (e.g., Mason et al., 1998; Kobulnicky; Fryer, 2007; Kouwenhoven et al., 2007). At the other end, the estimated binary fraction among M-type stars is 30–40% (e.g., Fischer; Marcy, 1992; Leinert et al., 1997).

Furthermore, the Eggleton & Tokovinin (2008) catalogue of multiplicity among bright stellar systems identified that 40% of the 4559 targets are not single;[12] and the Raghavan et al. (2010) survey searching for multiplicity of solar-type stars found that 44% of the 454 stars in the sample are not single. Compiling all stars and brown dwarfs within 10 pc observable by *Gaia*, Reylé et al. (2021) found a multiplicity frequency of around 27%. Earlier, Abt & Levy (1976) studied 123 solar-type, bright field stars and found that 58% of those are not single stars.

Binarity gives rise to new astrophysical phenomena otherwise absent from the life of single stars. One such example of exotic objects resulting only from binary interactions are low and extremely low-mass white dwarfs (LM WDs and ELM WDs, respectively). Since the Universe is not old enough for these $M < 0.45\ M_{\odot}$ helium-core WDs to have been formed through single-star evolution, the most likely hypothesis is that ELM WDs are born in a binary system either as a result of a common-envelope phase or after a stable Roche-lobe overflow episode (e.g., Istrate et al., 2016; Li et al., 2019). The currently-observed binarity rate of known ELM WDs — close to 100% — supports these channels. Their companions include millisecond pulsars, main sequence stars, and more commonly canonical mass WDs (e.g., Tauris; Langer; Kramer, 2012; Brown; Kilic; Gianninas, 2017).

Figure 6 shows thousands of ELMs — confirmed (Brown et al., 2016) or candidate (Pelisoli; Kepler; Koester, 2018a; Pelisoli et al., 2018b; Pelisoli et al., 2018c) — in the $\log(g)$–$T_{\rm eff}$ plane (also known as Kiel Diagram, KD), along with the evolutionary track of a $1\ M_{\odot}$ star that ends as a normal $0.53\ M_{\odot}$ WD. The surface gravity is given by $g = GM/R^2$ and $\log(g)$ is around 4 for stars in the main sequence and around 8 for white dwarfs. It becomes clear that the evolution of a low-mass single star is not adequate to explain the inferred effective temperatures and surface gravities for this class of stars at all, especially if the model age is greater than 13 Gyr at 10,000 K.

At this point, an important observation should be made. Progenitors of ELM WDs are expected to have initial mass in the range 0.8–1.5 $M_{\odot}$ (e.g., Sun; Arras, 2018), most likely in the range 1.0–1.2 $M_{\odot}$ (see also chapter 3). However, the evolution of single stars of these masses does not deviate far from the $1.0\ M_{\odot}$ evolutionary track shown in Figure 6.

[12] The definition of "single stars" here should be understood as stars having no other stars as a companion. However, even if not mentioned by the studies, most of them probably have planets orbiting, due to the conservation of the angular momentum of the molecular cloud.

Figure 6 – The $\log(g)$–$T_{\rm eff}$ plane showing confirmed or candidate ELMs from different surveys (coloured signs). The evolutionary track of a 1 $M_{\odot}$ single star is also shown (solid black line) down to $L = 10^{-4}\ L_{\odot}$ (age 17.8 Gyr). Four blue large–amplitude pulsators (BLAPs) are also shown (red "△" signs).

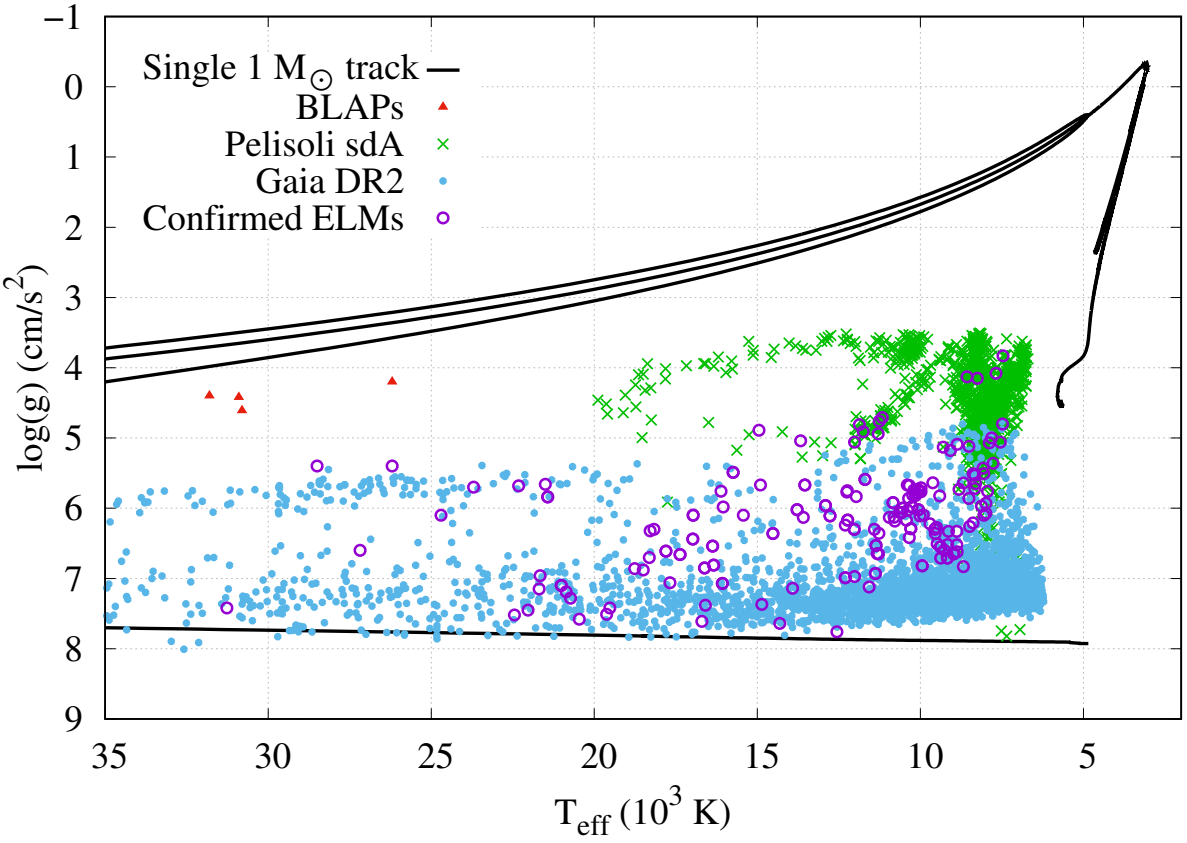

Credits for observational data: ELM WDs candidates from the sdA selection (Pelisoli; Kepler; Koester, 2018a; Pelisoli et al., 2018b; Pelisoli et al., 2018c); candidates and confirmed ELM WDs from the Gaia DR2 (Pelisoli; Vos, 2019); clean sample of the ELM Survey (Brown et al., 2020); BLAPs (Pietrukowicz et al., 2017). Gaia DR2 data were corrected by reddening following Gentile Fusillo et al. (2019).

Furthermore, lower metallicity causes the end of the main sequence to occur at slightly higher temperatures, but still far from contemplating the presented observational data. Thus, evolutionary tracks of other masses and other metallicities in the $\log(g)$–$T_{\rm eff}$ plane do not improve compatibility with the presented observational data in Figure 6.

As remnants of binary evolution, ELMs can shed light into the poorly understood yet crucial phase of common-envelope evolution (Nelemans et al., 2000) and are ideal laboratories for studying the physics of tides (Fuller; Lai, 2013).

Additionally, most known ELMs will merge in less than a Hubble time resulting in new exotic objects such as R Corona Borealis stars (e.g. Webbink, 1984; Zhang et al., 2014), under luminous supernovae (e.g. Bildsten et al., 2007; Brown et al., 2011b), and

type Ia supernovae (e.g. Iben; Tutukov, 1984). Low-mass and ELM WDs are also often related to AM CVn (e.g. Warner, 1995; Solheim, 1995; Nelemans, 2005; Solheim, 2010; Breedt et al., 2012; Piersanti; Yungelson; Tornambé, 2015; Brown et al., 2016; El-Badry et al., 2021b; Wong; Bildsten, 2021) and EL CVn (e.g. Maxted et al., 2011; Maxted et al., 2014a; Maxted et al., 2014b; Chen et al., 2017; van Roestel et al., 2018; Wang et al., 2020; Lagos et al., 2020) systems.

As strong sources of low-frequency gravitational wave radiation, WD+NS and WD+WD binary systems will have an important contribution to the signal detected by LISA (Laser Interferometer Space Antenna, see e.g., Nelemans; Yungelson; Portegies Zwart, 2001; Nelemans et al., 2001; Nelemans et al., 2001; Nissanke et al., 2012; Kupfer et al., 2018; Li et al., 2020; Korol et al., 2020), since Galactic binaries comprise primarily white dwarfs (Amaro-Seoane et al., 2017; Baker et al., 2019a). LISA will open the mHz band of gravitational waves and will represent an important step in the multi-messenger astronomy, crucial in a number of important astrophysical processes, ranging from the structure formation in the early Universe to the evolution of stellar remnant binaries in the Milky Way (Baker et al., 2019b). As an example, it is expected that accurate detection of a WD in a tight orbit with a neutron star could give accurate indications of the mass and constrains the state equation of the neutron star (Tauris, 2018).

As ultra-compact binaries, tens of millions of these systems are predicted to exist within the Galaxy, emitting gravitational waves at mHz frequencies and, combined with electromagnetic surveys (like Gaia and LSST, see e.g. Korol et al., 2017), should enable measurements of masses, radii, and orbital dynamics parameters far beyond what can be achieved by independent electromagnetic or gravitational waves studies (Shah; Nelemans; van der Sluys, 2013; Littenberg et al., 2019). In short, the era of multi-messenger Astronomy — along with computer simulations and modelling on low-mass binaries — is expected to bring advances in our understanding of various areas and topics such as common-envelope evolution, tidal interactions, mass transfer, X-ray sources, accretion physics, double degenerates and supernova survivors (e.g. Amaro-Seoane et al., 2012; Kupfer et al., 2019; Toloza et al., 2019).

There are less than 120 spectroscopically confirmed ELMs (see Pelisoli; Vos, 2019), and they were almost all discovered following-up objects from the Sloan Digital Sky Survey (SDSS, Brown et al., 2016; Pelisoli et al., 2018b; Pelisoli et al., 2018c). The ELM Survey selection criteria targeted objects hotter than 8500 K, introducing a strong bias. Only 18% of the confirmed ELMs show $T_{\rm eff} < 8500$ K, even though the evolutionary models predict much longer timescales below 8500 K. Although these objects are fainter, their longer lifetimes imply that 20–50% of the observed ELMs should be cooler than 8500 K (Pelisoli; Kepler; Koester, 2017). These observational biases prevent meaningful comparisons with the models and barred our progress in the binary evolution field.

Figure 7 shows the observational HR diagram from Gaia Data Release 2 highlighting the ELMs candidates considering predictions from theoretical models and analysing the properties of the known sample. That is a valuable asset for testing binary evolution models, since we need to further improve the agreement between observations and models. The sample in Figure 7 contains 5672 ELM candidates down to $T_{\rm eff} \approx 5000$K. They were selected according to strict criteria. The first one is that only objects with parallax over error greater than 5 were included (see colour-scale on the right). Next, proper colour cuts were done in order to exclude canonical WD (black branch in the bottom), hot subdwarfs (black branch in the top), and main sequence stars (grey area on the right side). Also excluded from the sample were all objects identified from their spectra as cataclysmic variables stars, WD + MS, quasars, or F stars. See details in Pelisoli & Vos (2019).

Figure 7 – Gaia DR2 observational HR diagram showing the selected clean sample of ELM candidates. Using predictions from theoretical models and analysing the properties of the known sample, a final sample of 5762 ELM candidates down to $T_{\rm eff} \approx 5000$K was selected.

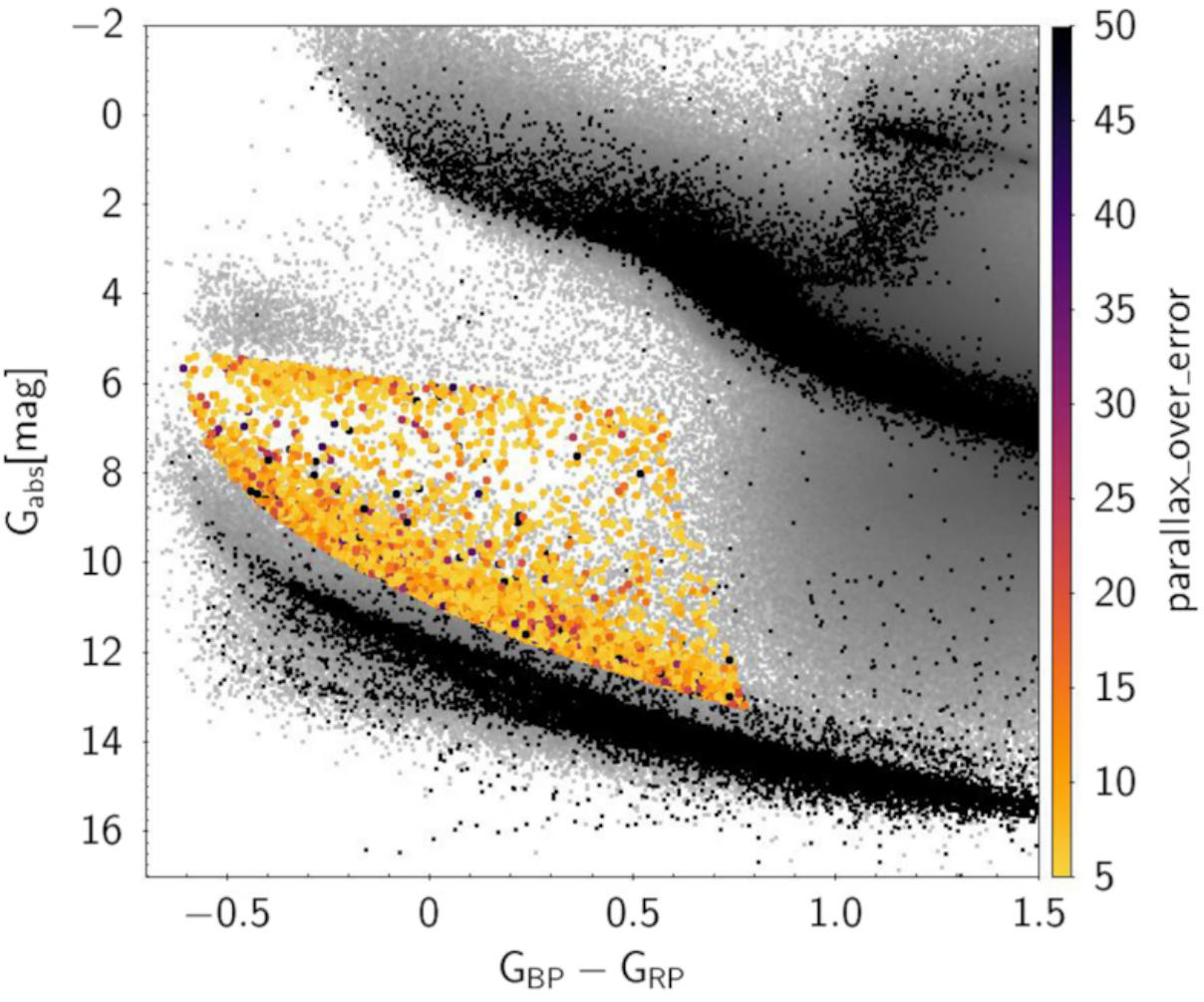

Credit: Pelisoli & Vos (2019). Data from Gaia Collaboration et al. (2018).

If on one hand the evolution of a single star depends mainly on its mass, the necessary parameters to describe the evolution of a binary system are the masses of both star components, the initial orbital separation, and the eccentricity. Going further, the way in which the system loses angular momentum ($\dot{J}$) is especially important, as this will dictate how soon the stars will approach and possibly interact. The main mechanisms by which a binary system loses angular momentum are gravitational waves, mass loss, spin-orbit coupling, and magnetic braking. Of these mechanisms, the one with the greatest uncertainty is the magnetic braking (e.g., Ivanova; Taam, 2003). Magnetic braking is thought to be the fundamental mechanism responsible for orbital angular momentum loss in a number of classes of close binaries, especially when providing a mechanism for promoting mass transfer from the low-mass donor to its more massive compact companion.

The origin of magnetic fields in white dwarfs remains a fundamental unresolved problem in stellar astrophysics (see, e.g., Ferrario; de Martino; Gänsicke, 2015, García-Berro; Kilic; Kepler, 2016, García-Berro; Kilic; Kepler, 2018, Ferrario; Wickramasinghe; Kawka, 2020). There are currently at least four scenarios that have been suggested for the origin of magnetic fields in white dwarfs. They are the fossil field scenario, the common envelope dynamo scenario, the double degenerate scenario, and the rotation- and crystallisation-driven dynamo scenario (see discussion in Bagnulo; Landstreet, 2021 and Belloni et al., 2021 and references therein).

Tout et al. (2008) hypothesised that the class of the single high-field magnetic white dwarfs, with magnetic fields within the range 10^6–10^9 G, had their high fields generated in merging binary systems while in a common envelope stage. More recently, Briggs et al. (2018) and Briggs (2019) carried out population synthesis calculations in order to study the dynamo mechanism due to differential rotation during stellar mergers and showed that the observed high fields in isolated WDs and in WDs in magnetic cataclysmic variables are consistent with stellar interaction during common envelope evolution.

Belloni & Schreiber (2020) studied the dynamo process during common envelope evolution and found that the model fails to explain the absence of young, close detached WD+M-dwarf binaries harbouring hot magnetic WDs. Also, they found that the model predicts that the overwhelming majority of WDs in close binaries should be strongly magnetic, which is in serious conflict with the observations.

Schreiber et al. (2021) presented binary star evolutionary models that include the spin evolution of accreting white dwarfs and crystallisation of their cores, as well as magnetic field interactions between the stars. The authors showed that the crystallisation- and rotation-driven dynamo model can generate strong magnetic fields in the white dwarfs in cataclysmic variables, which explains their large fraction among the observed population.

Even more, Belloni et al. (2021) found that the observed paucity of bright intermediate polars in globular clusters is a natural consequence of the newly proposed rotation-

and crystallisation-driven dynamo scenario.

Observationally, Bagnulo & Landstreet (2021) checked almost the entire population of about 152 WDs within 20 pc from the Sun for the presence of magnetic fields, and find that 33 WDs of the local 20 pc volume are magnetic. They point out that both the suggested strong increase of the dynamo efficiency, and the necessary rapid stellar rotation are still to be demonstrated. Therefore, the connection of the increased frequency with the core crystallisation must remain speculative at present. Thus, although the crystallisation dynamo may explain the general rise in the frequency of magnetic fields (i.e., the ratio between the number of magnetic WDs and the number of all WDs), this possibility needs further study before being accepted as an important mechanism. The authors conclude that the latest data suggest in fact that more than one channel for field formation in WDs exists.

Although the literature presents a significant amount of ELM WDs models, they focus on: the dependence of the final state of the ELM on its mass and on the occurrence of diffusion processes (e.g., Althaus; Serenelli; Benvenuto, 2001a; Panei et al., 2007); mass and age determinations (e.g., Althaus; Miller Bertolami; Córsico, 2013; Istrate et al., 2014); the role of rotational mixing (e.g., Istrate et al., 2016; Istrate et al., 2016); the pulsating properties of LM WDs and ELM WDs (e.g., Córsico; Althaus, 2014b; Córsico; Althaus, 2014a; Córsico; Althaus, 2016; Córsico et al., 2016; Calcaferro; Córsico; Althaus, 2017a; Calcaferro; Córsico; Althaus, 2017b; Calcaferro et al., 2018); formation channels (e.g., Sun; Arras, 2018, Li et al., 2019). To our knowledge, there are no studies focused on the evolution of the angular momentum problem in ELM binary systems (Istrate; Tauris; Langer, 2014).

Our main objective is to obtain ELM WD models compatible with the observational data, in particular in the observational HRD and in the Kiel Diagram, i.e., produce models compatible with the observational data in Figure 6. In addition, another objective is to obtain ELM WDs models that do not require severe fine-tuning in the initial orbital period to approach the lower limit of mass observed. To achieve this goal, we implement an enhanced recipe for the magnetic braking — namely, the one proposed by Van, Ivanova & Heinke (2018), Van & Ivanova (2019) — in the system's angular momentum loss to attenuate the current severe fine-tuning required to obtain ELM WDs in the low-mass binaries simulations (e.g., Istrate; Tauris; Langer, 2014; Istrate et al., 2016).

In addition, we will use the state-of-the-art equations of state, opacities, nuclear rates and reactions, chemical abundances, processes of radiation and convection, rotation, overshooting and thermohaline mixing, etc. In chapter 2 we present a brief review of the theory of stellar evolution and the code we use to run simulations and obtain our ELM WDs models. In chapter 3 we present our results and discuss them. Our main findings are summarised in chapter 4. Estimates of gravitational wave and X-ray emission are in

Appendix B, and our model grid is in Appendix C. Our main publication is presented in Appendix D, and a secondary publication is shown in Appendix E.

2 Theory and Methods

The way evolutionary codes create stellar models follows the theory of stellar evolution itself. Thus, we will first introduce the basic equations of the stellar structure, and the details will be discussed in the sections concerning the code and the simulations themselves.

2.1 Basics of stellar evolution theory

We call stellar evolution the process by which a star changes over the course of time. The lifetime of a single star — that can range from a few million years to trillions of years — and its production of chemical elements, ranging from sole hydrogen and helium to heavier elements such as iron, depend only on the star's initial mass and its initial chemical distribution — metallicity. A detailed description of nuclear astrophysics and nuclear burning stages in stars can be found in, e.g., Arnould & Takahashi (1999), Basdevant et al. (2005), Iliadis (2007), Liccardo et al. (2018). A comprehensive review of nucleosynthesis in low- and intermediate-mass stars can be found in Karakas & Lattanzio (2014). Also, we recall the seminal Burbidge et al. (1957) paper on the synthesis of the elements in stars. A great review of both theoretical and experimental nuclear physics can be found in Bethe & Bacher (1936), Bethe (1937), Livingston & Bethe (1937).

Although energy production in a star is very large, the approximation to a hydrostatic equilibrium state is valid for most of their lifetimes. The state-of-the-art of current stellar evolution theories can be found in numerous excellent books, e.g., Cox & Giuli (1968), Clayton (1983), de Loore & Doom (1992), Hansen, Kawaler & Trimble (2004), Kippenhahn, Weigert & Weiss (2012), Iben (2013a), Iben (2013b). Here we will just summarise some of the central points needed to continue our studies.

Using mass as variable, m_r is the mass contained within a radius r, and $\mathrm{d}m_r$ is the mass element in a concentric shell at radius r. So considering spherical symmetry and being the pressure P, the density ρ, the temperature T, the luminosity L_r, follow the equations for the hydrostatic equilibrium

$$\frac{\mathrm{d}P}{\mathrm{d}m_r} = -\frac{Gm_r}{4\pi r^4} \ , \tag{2.1}$$

mass continuity (or mass conservation)

$$\frac{\mathrm{d}r}{\mathrm{d}m_r} = \frac{1}{4\pi r^2 \rho} \ , \tag{2.2}$$

energy transport

$$\frac{\mathrm{d}T}{\mathrm{d}m_r} = -\frac{Gm_r T}{4\pi r^4 P}\nabla_{\mathrm{T}} \ , \tag{2.3}$$

and energy generation

$$\frac{\mathrm{d}L_r}{\mathrm{d}m_r} = \epsilon_{\mathrm{nuc}} + \epsilon_{\mathrm{grav}} - \epsilon_{\nu,\mathrm{th}} \ , \tag{2.4}$$

where ϵ_{nuc} is the total nuclear reaction specific energy generation rate minus the nuclear reaction neutrino-loss rate;[1] ϵ_{grav} is the specific rate of change of gravitational energy due to contraction or expansion; $\epsilon_{\nu,\mathrm{th}}$ is the specific thermal neutrino — and axion, if they exist — loss rate. ∇_{T} is the temperature gradient $\partial \ln T / \partial \ln P$, being that $\nabla_{\mathrm{T}} = \nabla_{\mathrm{rad}}$ if $\nabla_{\mathrm{rad}} \leq \nabla_{\mathrm{ad}}$ — corresponding to radiative transport — and $\nabla_{\mathrm{T}} = \nabla_{\mathrm{ad}}$ if $\nabla_{\mathrm{rad}} > \nabla_{\mathrm{ad}}$ — corresponding to adiabatic convection. More precisely, in the latter case, the rise of a bubble of gas is assumed to occur adiabatically. When it stops, it spreads out and mixes with the surrounding material, delivering its heat to the environment.

Here, Equation 2.1 and Equation 2.2 describe the mechanical structure of the star, while Equation 2.3 and Equation 2.4 describe the thermal and energetic structure, and that is enough to describe a star in both hydrostatic and thermal equilibrium. Even though several stages in the evolution of a star the equilibrium hypothesis is not strictly satisfied, the variations usually occur on a very long time scale, making these assumptions a reasonable approximation, but the time evolution term is added in the code for the fast evolutionary phases. These equations are coupled to each other through the fact that, for a general equation of state (EoS), P is a function of both ρ and T.

Now we shall evaluate when a given region of the star is stable against convection — i.e., all the energy is transported by radiation. Defining the gradient of mean molecular weight μ as $\nabla_\mu = \partial \ln \mu / \partial \ln P$, we have that in chemically homogeneous layers $\nabla_\mu = 0$, and the criterion for instability, i.e., for convection to occur is simply the so called Schwarzschild criterion: $\nabla_{\mathrm{rad}} > \nabla_{\mathrm{ad}}$ (Schwarzschild, 1906). On the other hand, if we also take into account a possible variation in composition we have to define the following derivatives

$$\chi_{\mathrm{T}} = \left(\frac{\mathrm{d}\ln P}{\mathrm{d}\ln T}\right)_{\rho,\mu} \ , \qquad \chi_\mu = \left(\frac{\mathrm{d}\ln P}{\mathrm{d}\ln \mu}\right)_{\rho,T} \ , \tag{2.5}$$

and the result is that at least one of the following conditions must be satisfied for convection to occur[2]

$$\Delta\mu < 0 \ , \qquad \nabla_{\mathrm{rad}} > \nabla_{\mathrm{ad}} - \frac{\chi_\mu}{\chi_{\mathrm{T}}}\nabla_\mu \equiv \nabla_{\mathrm{L}} \ , \qquad \nabla_{\mathrm{rad}} > \nabla_{\mathrm{ad}} \ , \tag{2.6}$$

where the $\Delta\mu$ is the difference in molecular weight between a given delimited region and its surroundings and ∇_{L} is the Ledoux gradient. Of course, the medium is always unstable if $\Delta\mu < 0$. Considering heavier elements are usually synthesised by nuclear reactions in the central regions of the star, $\nabla_\mu \geq 0$ in general. An exception that can be cited is the carbon burning, which begins outside the centre. The second possibility is the so-called Ledoux criterion (Ledoux, 1947). In this relation, the ratio $\chi_\mu/\chi_{\mathrm{T}}$ is positive if ∇_μ is also

[1] Assuming neutrinos are lost, not valid in the supernova phase.
[2] This is also know as Hurwitz criterion (e.g., see Kato, 1966).

positive. Thus, if the gradients satisfy the Ledoux criterion, the Schwarzschild criterion is automatically satisfied.

These combinations give rise to four possible situations, which are summarised in Figure 8. The diagram in this figure shows that the only stable region is where $\nabla_\mu \geq 0$ and $\nabla_{\rm rad} < \nabla_{\rm ad}$. If $\nabla_\mu \geq 0$ and $\nabla_{\rm ad} < \nabla_{\rm rad} < \nabla_{\rm L}$ the instability is called semiconvection; and if $\nabla_{\rm rad} - \nabla_{\rm ad} < 0$ but $\nabla_\mu < 0$ we have thermohaline mixing (also known as fingering convection, Garaud, 2018).

Figure 8 – Sketch of the ∇_μ – $(\nabla_{\rm rad} - \nabla_{\rm ad})$ stability plane with the four possible different regimes: radiative, convective, thermohaline, and semiconvective. The diagonal line dividing into half the top left and bottom right diagrams denotes $\nabla_{\rm L}$. The only stable region is the bottom left quadrant.

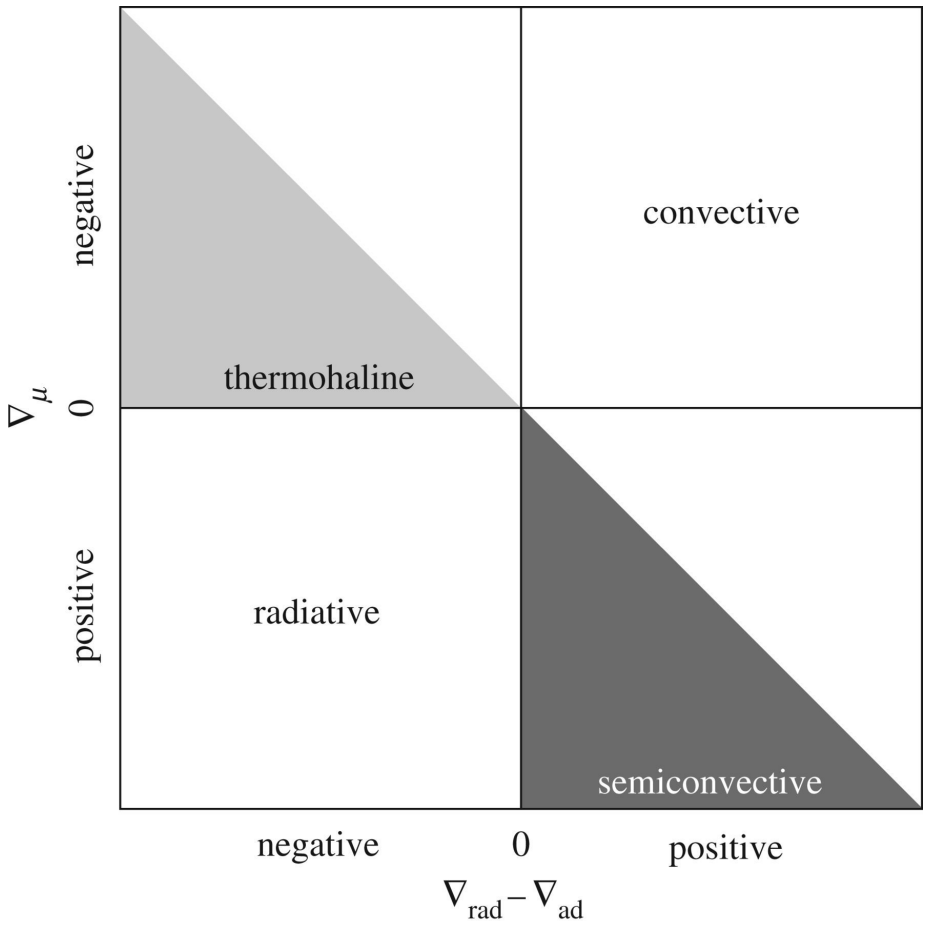

Credit: Salaris & Cassisi (2017).

2.2 The MESA code

The numerical simulations presented in this thesis were performed using the Modules for Experiments in Stellar Astrophysics (MESA) code (Paxton et al., 2011; Paxton et al.,

2013; Paxton et al., 2015; Paxton et al., 2018; Paxton et al., 2019), release version 11701 and SDK 20190503. MESA is a suite of open source, robust, efficient, thread-safe libraries written in Fortran 95 language for a wide range of applications in computational stellar astrophysics. Using a one-dimensional stellar evolution module — therefore assuming spherical symmetry, it combines many of the numerical and physics modules for simulations of a wide range of stellar evolution scenarios ranging from very low mass to massive stars, including advanced evolutionary phases. MESA solves the fully coupled structure and composition equations (2.1–2.4) simultaneously using adaptive mesh refinement and appropriate timestep controls. State-of-the-art modules provide equation of state, opacity, nuclear reaction rates, element diffusion data, and atmosphere boundary conditions. Among the main advantages of the code are the following: openness, modularity, wide applicability, modern techniques, microphysics, and performance.

The MESA evolutionary code has been extensively used to perform calculations on merging massive black holes (Marchant et al., 2016); presupernova stellar cores (Sukhbold; Woosley, 2014); core-collapse supernovae (Shiode; Quataert, 2014); supernova of electron-capture origin (Hiramatsu et al., 2021); hydrogen burning on accreting white dwarfs (Wolf et al., 2013); asteroseismology on rotating pulsating MS stars (Moravveji et al., 2015); stellar oscillations (Ball; Gizon, 2014); evolutionary sequences of massive white dwarfs (Lauffer; Romero; Kepler, 2018; Schwab, 2021a); extremely low-mass white dwarfs (Istrate et al., 2016; Sun; Arras, 2018); pulsating extremely low-mass white dwarfs (Istrate; Fontaine; Heuser, 2017); hybrid C/O/Ne white dwarfs and Type Ia SN progenitors (Jones et al., 2013; Denissenkov et al., 2013b; Chen et al., 2014; Farmer; Fields; Timmes, 2015; Brooks et al., 2017b); accreting white dwarf binaries with C/O core (Brooks et al., 2016; Wang; Podsiadlowski; Han, 2017), and O/Ne core (Schwab; Bildsten; Quataert, 2017; Brooks et al., 2017a; Lauffer; Romero; Kepler, 2018); isochrones and stellar tracks extending across all evolutionary phases for a wide range of masses and metallicities (Dotter, 2016; Choi et al., 2016; Pignatari et al., 2016; Ritter et al., 2018); dark matter (Lopes; Lopes, 2021); mass transfer in extreme mass ratio binaries (Miller et al., 2021a); accretor stars in massive binaries (Renzo; Götberg, 2021); gravitational waves from stripped binaries (Götberg et al., 2020b); cosmic reionization of hydrogen and helium (Götberg et al., 2020a); massive contact binaries (Menon et al., 2021); pulsational pair-instability supernovae (Marchant et al., 2019); fossil magnetic fields (Keszthelyi et al., 2021); irradiation-driven winds (Han; Jiang; Chen, 2021); merger remnant of C/O WDs (Schwab, 2021b); and brown dwarfs (Forbes; Loeb, 2019; Brandt et al., 2021), for example.

2.2.1 Micro and macrophysics

Figure 9 shows a schematic of how MESA calculates its cell and boundary variables to solve the structure of a given model. Depending on how these parameters vary from one

layer to its neighbour, the mesh parameter is adjusted and the next model will have more or less layers. Different routines get called at different points during MESA execution.

Figure 9 – Schematic of relevant cell and face (boundary) variables relevant for hydrodynamics in MESA. For example, for a given cell/face k in a given radial coordinate r_k we have: the luminosity (L_k), the Lagrangian mass coordinate (m_k), the pressure (P_k), the baryon mass density (ρ), the velocity (v_k), the mass associated with cell face ($\overline{dm}_k$), and so on.

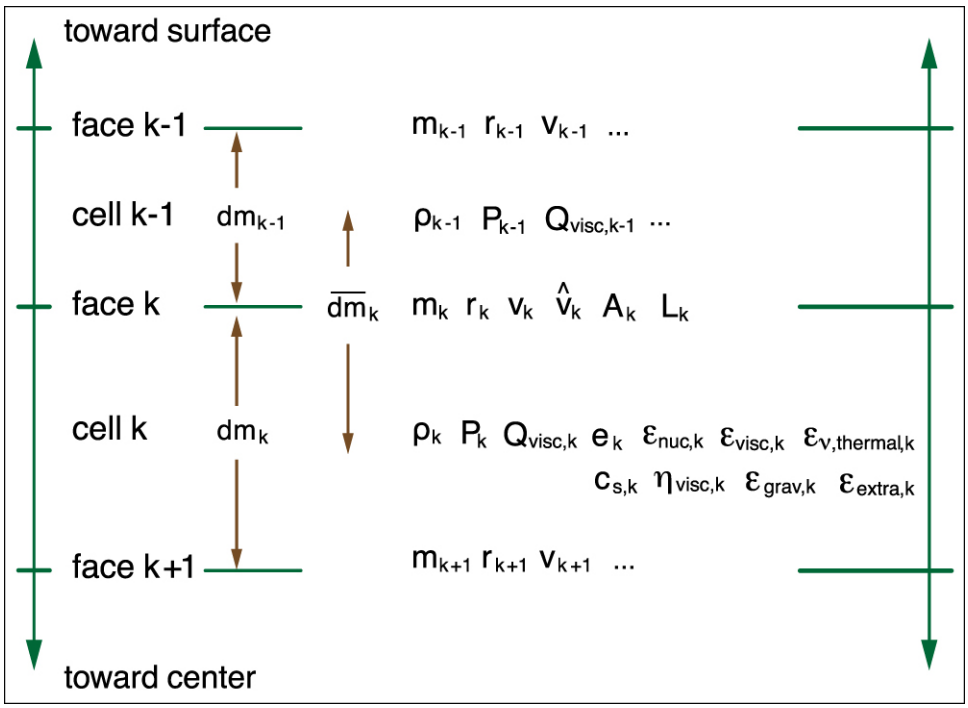

Credit: Paxton et al. (2015)

Figure 10 is a flowchart summarising this. All simulations start with the code by reading the input files written by the user. These files are called *inlists*. Inlist files have two main parts: the first is where one chooses the conditions and characteristics of the first model — such as initial mass, metallicity, rotation, net of elements, etc; and in the second one indicates which physics should be used throughout evolution - overshooting, convection, diffusion, etc. In addition, there is a specific inlist file for binary systems, which controls the evolution of the angular momentum, mass transfer, orbital synchronisation, etc. After reading the regular inlist files, the code searches for extra control files. Here is where one can add modifications not present in the original code. This can include both a different treatment of any of the items above as well as modifications to the way the code writes the output files and additional criteria for a simulation to proceed.

The MESA equation of state (EoS) is a blend of the OPAL (Rogers; Nayfonov, 2002), SCVH (Saumon; Chabrier; van Horn, 1995), PTEH (Pols et al., 1995), HELM (Timmes; Swesty, 2000), and PC (Potekhin; Chabrier, 2010) EoSs. Radiative opacities are primarily

Figure 10 – A flowchart summarising how different routines get called at different points during MESA execution. The `extra_controls` routine is particularly important: it is the place where one tells MESA exactly which subroutines it should call for all of the rest of its hooks. The core of MESA is the grey "take step" box, which contains all of the machinery by which MESA evaluates and solves the equations of stellar structure at each step.

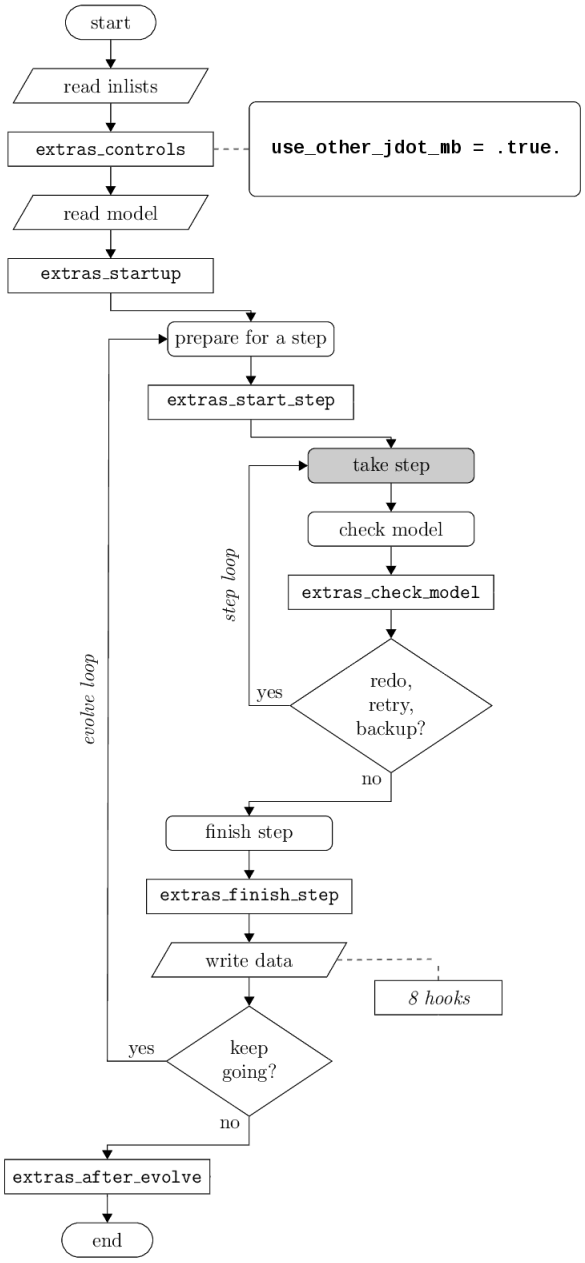

Credit: adapted from Schwab & Wong (2019).

from OPAL (Iglesias; Rogers, 1993; Iglesias; Rogers, 1996), with low-temperature data from Ferguson et al. (2005) and the high-temperature, Compton-scattering dominated regime

by Buchler & Yueh (1976). Electron conduction opacities are from Cassisi et al. (2007). Nuclear reaction rates are from JINA REACLIB (Cyburt et al., 2010) plus additional tabulated weak reaction rates (Fuller; Fowler; Newman, 1985; Oda et al., 1994; Langanke; Martínez-Pinedo, 2000). Screening is included via the prescription of Chugunov, Dewitt & Yakovlev (2007). Thermal neutrino loss rates are from Itoh et al. (1996). The p-p chain and the CNO cycle burning are guaranteed by using a network that accounts for the following 21 isotopes: ^{1}H, ^{3}He, ^{4}He, ^{12}C, ^{13}C, ^{13}N, ^{14}N, ^{15}N, ^{14}O, ^{15}O, ^{16}O, ^{17}O, ^{18}O, ^{17}F, ^{18}F, ^{19}F, ^{18}Ne, ^{19}Ne, ^{20}Ne, ^{22}Mg and ^{24}Mg. Higher reaction rates are available in the code, but require large computational facilities.

Convection is considered by using the mixing length theory (MLT, Böhm-Vitense, 1958) as presented by Henyey, Vardya & Bodenheimer (1965). This modified MLT option allows the convective efficiency to vary with the opaqueness of the convective element, an important effect for convective zones near the outer layers of stars. $\alpha_{\rm MLT} = 2$ is adopted as the mixing length parameter by us. It should be noted, however, that this is a simplification with respect to the use of theory since 3D hydrodynamic studies on the calibration of the mixing length theory for white dwarfs (see, e.g., Tremblay et al., 2013a; Tremblay et al., 2013b; Cukanovaite et al., 2019) show that this parameter is not constant along the star's structure nor throughout the evolution of the star, introducing inaccuracy in $T_{\rm eff}$ and $\log(g)$ estimates.

In order to decide whether a region is dynamically stable or not, we consider the Ledoux criterion, which takes into account the influence of composition gradients on mixing. In regions unstable to Schwarzschild but stable to Ledoux, semiconvection acts via a time-dependent diffusive process with a diffusion coefficient $D_{\rm sc}$ and efficiency parameter $\alpha_{\rm sc} = 0.001$ as shown in the equation (Langer; Fricke; Sugimoto, 1983)

$$D_{\rm sc} = \alpha_{\rm sc} \frac{1}{6} \frac{K(\nabla_T - \nabla_{\rm ad})}{\rho C_P (\nabla_{\rm L} - \nabla_T)} \ , \tag{2.7}$$

where K in the radiative conductivity and C_P is the specific heat at constant pressure.

Thermohaline mixing arises in the presence of an inversion of the mean molecular weight in regions that are stable according to the Ledoux criterion. Thermohaline mixing is treated in a diffusion approximation with coefficient (Ulrich, 1972; Kippenhahn; Ruschenplatt; Thomas, 1980)

$$D_{\rm th} = \alpha_{\rm th} \frac{3}{2} \frac{KB}{\rho C_P (\nabla_T - \nabla_{\rm ad})} \ , \tag{2.8}$$

where we use $\alpha_{\rm th} = 1$ for the efficiency parameter.

Semiconvection and overshooting have distinct implementations in MESA. Overshooting is implemented using an exponential decay of the convective diffusion coefficient

beyond the boundary of convection (Herwig, 2000)

$$D_{\rm ov} = D_0 \exp\left(-\frac{2\Delta r}{f_{\rm ov}\lambda_P}\right) , \tag{2.9}$$

where D_0 is the diffusion coefficient at the convective border, Δr is the overshooting distance, and λ_P is the local pressure scale height. The dimensionless parameter $f_{\rm ov}$ then determines the extent of the overshooting region. For the each burning/non-burning core/shell region, MESA includes an exponential overshoot below and above the interface limit by the distance of $f_{\rm ov} = 0.005$ pressure scale heights. An extra step overshooting of $f_{\rm ov} = 0.2$ above the burning H core is also included.

Particle diffusion and gravitational settling (Michaud; Alecian; Richer, 2015) are implemented by solving Burger's equations (Burgers, 1969) and using the method and diffusion coefficients of Thoul, Bahcall & Loeb (1994). The transport of material is computed using the scheme described by Iben & MacDonald (1985). While settling due to gravity and thermal effects tends to establish composition gradients, diffusion tends to smooth out such gradients (including those from nuclear reactions).

We adopt the Reimers (1975) mass loss for red giants. In this scheme, the mass loss is parametrised by simple relations of the stellar parameters luminosity L, radius R, and mass M,

$$\dot{M}_{\rm RGB} = 4 \times 10^{-13} \eta_{\rm RGB} \frac{LR}{M} \ [M_\odot/{\rm yr}] \ . \tag{2.10}$$

Following Van & Ivanova (2019), we adopt $\eta_{\rm RGB} = 1$ for the scaling factor, despite some studies often suggest lower values (e.g., McDonald; Zijlstra, 2015). This factor is constant throughout evolution. Furthermore, it is expected that RGB mass loss should correlate with metallicity (Tailo et al., 2021), and a more realistic $\eta_{\rm RGB}$ scaling factor must increase with the metallicity (Tailo et al., 2020), which we do not consider. That said, we point out that in our study the mass loss processes do not depend directly on metallicity. However, as metallicity influences radius, luminosity, photosphere conditions as mean molecular weight, density, temperature (see also subsection 2.2.2 ahead), etc., its effects are indirectly taken into account.

The effects of rotation are included by following Heger, Langer & Woosley (2000), Heger, Woosley & Spruit (2005), where we include the effects for four different rotationally induced mixing processes: Goldreich-Schubert-Fricke instability, Eddington-Sweet circulation, secular shear instability and dynamical shear instability. Since this is a very extensive topic, we referred the reader to Section 6 of Paxton et al. (2013) for details on the implementation. More details about rotation, rotational element transport mechanisms, and angular momentum transport in stellar interiors can be found in the reviews of Salaris & Cassisi (2017) and Aerts, Mathis & Rogers (2019).

The Spruit-Tayler dynamo transports angular momentum and chemicals by magnetic fields. Here we must set two efficiency factors to calibrate the diffusion coefficients:

the contribution of the rotationally induced instabilities to the diffusion coefficient is reduced by the factor $f_c = 1/30$, and the sensitivity of the rotationally induced mixing is $f_\mu = 0.05$. These values follow Istrate et al. (2016). See Heger, Langer & Woosley (2000) for a discussion of these calibration parameters.

For the atmosphere boundary conditions we consider the simple photosphere option (do not integrate, just estimate $T_{\rm eff}$ for optical depth $\tau = 2/3$) for the pre-WD phase and the hydrogen atmosphere tables for cool white dwarfs from Rohrmann; Althaus; Kepler (2011) for $T_{\rm eff} < 10$ kK and $\log_{10}(L/L_\odot) < -2$.

Even with all the advances in the stellar modelling area, we must emphasise that there are still numerous uncertainties and inaccuracies. Most uncertainties are related to the initial parameters, and most inaccuracies occur when we treat parameters that are variable throughout evolution as constants. For example, see Bahcall, Serenelli & Basu (2006), Weiss et al. (2007), Weiss & Schlattl (2008), Mowlavi et al. (2012), Serenelli (2016), Serenelli et al. (2021), Christensen-Dalsgaard (2021). Furthermore, different stellar evolution codes show somehow different results from each other,[3] even when considering the same input physics and initial parameters (Martins; Palacios, 2013; Stancliffe et al., 2016; Weiss; Aguirre; Christensen-Dalsgaard, 2018). Not to mention, of course, that the vast majority of stellar evolution studies are carried out using codes that consider only one-dimensional treatment.

2.2.2 Binaries

In addition to the initial masses (accretor and donor), the initial orbital period ($P_{\rm i}$) is another of the initial parameters of each simulation. The orbital separation (a) is automatically adjusted via Kepler's third law (see Equation 1.4). Before evolution begins, a relaxation routine causes the angular frequency of the donor to equal the orbital angular frequency, forcing synchronicity on a viscous dissipation time scale. Tidal interaction is modelled by adjusting the model of Hut (1981) to include the case of differentially rotating stars. The time evolution of the angular frequency for each component is

$$\frac{{\rm d}\Omega_{i,j}}{{\rm d}t} = \frac{\Omega_{\rm orb} - \Omega_{i,j}}{\tau_{{\rm sync},j}} \ , \tag{2.11}$$

with

$$\frac{1}{\tau_{{\rm sync},j}} = \frac{3}{(q_j r_{g,j})^2} \left(\frac{k}{T}\right)_{c,j} \left(\frac{R_j}{a}\right)^6 \ , \tag{2.12}$$

where $j = 1, 2$ is the index of each star; $\Omega_{i,j}$ is the angular frequency at the face of cell i toward the surface; $r_{g,j}^2 = I_j/(M_j R_j^2)$ is the radius of gyration (with I_j being the moment of inertia of each star); and $(k/T)_{c,j}$ is the ratio of the apsidal motion constant to the

[3] We are referring to quantitative differences, such as evolution time and chemical abundances, for example. Qualitative differences in results occur only in very specific cases.

viscous dissipation timescale for convective envelopes, computed as in Hurley, Tout & Pols (2002). The synchronisation mode is uniform, such that each layer is synced independently given the synchronisation timescale $\tau_{\rm sync}$. Thus, tides act mostly on the outer layers, and whether the core synchronises or not depends on the coupling between the core and the envelope.

Roche lobe radii in binary systems are computed using the fit of Eggleton (1983), cf. Equation 1.11. Mass transfer rates in Roche lobe overflowing binary systems are determined following the "Kolb scheme" prescription of Ritter (1988), Kolb & Ritter (1990).[4] In this formalism the mass transfer rate via RLOF, $\dot{M}_{\rm RLOF}$, is an exponential function of $\Delta R = R_{\rm d} - R_{\rm L,d}$, so that there may be mass flow via L_1 even if $R_{\rm d} \leqslant R_{\rm L,d}$. In this case, the expression reads

$$\dot{M}_{\rm RLOF} = -\dot{M}_0 \exp\left(\frac{\Delta R}{H_P/\gamma}\right) \ , \tag{2.13}$$

where γ is a fitting function that depends on the mass ratio, H_P is the pressure scale height at the photosphere of the donor, and $\dot{M}_0$ is a smooth function of the donor structure

$$\dot{M}_0 = \frac{2\pi}{\sqrt{\rm e}} F \frac{R_{\rm L,d}^3}{GM_{\rm d}} \left(\frac{k_{\rm B}T_{\rm eff}}{m_{\rm p}\mu_{\rm ph}}\right)^{3/2} \rho_{\rm ph} \ , \tag{2.14}$$

where $k_{\rm B}$ is the Boltzmann constant, $m_{\rm p}$ is the proton mass, and $\mu_{\rm ph}$ and $\rho_{\rm ph}$ are the mean molecular weight and density at the photosphere of the donor.

In turn, if $R_{\rm d} > R_{\rm L,d}$,

$$\begin{aligned} \dot{M}_{\rm RLOF} &= -(\dot{M}_0 + f_{\rm RLOF}) \\ &= -\dot{M}_0 - 2\pi F \frac{R_{\rm L,d}^3}{GM_{\rm d}} \int_{P_{\rm ph}}^{P_{\rm L}} \Gamma_1^{1/2} \left(\frac{2}{\Gamma_1+1}\right)^{(\Gamma_1+1)/(2\Gamma_1-2)} \left(\frac{k_{\rm B}T}{m_{\rm p}\mu}\right)^{1/2} d{\rm P} \ , \end{aligned} \tag{2.15}$$

where $f_{\rm RLOF}$ is a function that, similarly, depends on the donor radius and its Roche lobe radius; the pressure scale height at the inner Lagrange point (L1, that is linked to the pressure scale height at the star surface); the donor star mass; the pressure at L1 ($P_{\rm L}$) and at the stellar photosphere ($P_{\rm ph}$); a fitting function (F) that depends on the mass ratio (i.e., the Roche geometry); the first adiabatic exponent (Γ_1); and the mean molecular weight, the density and temperature of the donor between the photosphere and the Roche lobe.

The fitting functions are

$$\gamma = \begin{cases} 0.954 + 0.025\log(q) - 0.038\left[\log(q)\right]^2 & \text{if } 0.04 \lesssim q \leqslant 1 \ , \\ 0.954 + 0.039\log(q) + 0.114\left[\log(q)\right]^2 & \text{if } 1 \leqslant q \lesssim 20 \ , \end{cases} \tag{2.16}$$

[4] A discussion of the impact of the chosen mass transfer schemes on the mass–orbital period relation can be found in Zhang et al. (2021).

and

$$F = 1.23 + 0.5\log(q), \quad 0.5 \lesssim q \lesssim 10 \ . \tag{2.17}$$

Outside the ranges of validity, these functions are evaluated using the value of q at the edge of their respective ranges. Note that both γ and F have an order of magnitude ~ 1.

The evolution of the orbital angular momentum of the system is considered by computing the rate of change of orbital angular momentum considering the contributions of gravitational waves radiation, mass loss, magnetic braking and spin–orbit (LS) coupling

$$\dot{J}_{\rm orb} = \dot{J}_{\rm gr} + \dot{J}_{\rm ml} + \dot{J}_{\rm mb} + \dot{J}_{\rm ls} \ . \tag{2.18}$$

The expression for $\dot{J}_{\rm gr}$ is simply Equation 1.10. The spin-orbit coupling term, that describes the exchange of angular momentum between the orbit and the donor star due to its expansion or contraction, is given by

$$\dot{J}_{\rm ls} = \frac{-1}{\delta t}\left(\delta S_1 - S_{1,\rm lost}\frac{\dot{M}_{1,\rm w}}{\dot{M}_1} + \delta S_2 - S_{2,\rm lost}\right) \ . \tag{2.19}$$

where δS_1 and δS_2 are the changes in spin angular momenta of each binary component, and $S_{1,\rm lost}$ and $S_{2,\rm lost}$ are the amounts of spin angular momentum removed in a step (with timestep δt) from each star due to mass loss (including RLOF and winds). In the absence of RLOF only the wind term contributes, and then $\dot{M}_{1,\rm w}/\dot{M}_1 = 1$. Equation 2.19 should be seen simply as a statement about the conservation of angular momentum, since it does not depend on how tides and angular momentum work. In this sense, we have that tidal interaction and mass transfer modify the spin angular momentum of the stars in a binary system, acting as both sources and sinks for orbital angular momentum. Tauris & van den Heuvel (2006) points out that this effect is most efficient for binaries with $2 < P/\rm d < 5$. The spin-orbit coupling has a major effect in systems of uneven masses, i.e., $q \ll 1$. Since we are dealing with systems with initial mass ratios $q \sim 1$, its effect is minimal. Therefore, we refer the reader to Paxton et al. (2015) for more details.

Now we must consider a more realistic situation for mass transfer and mass loss. Considering that both stars can gain/lose mass either by the RLOF as by winds, we have the following new expressions for $\dot{M}$

$$\dot{M}_{\rm d} = \dot{M}_{\rm d,w} + \dot{M}_{\rm RLOF} \tag{2.20}$$

and

$$\dot{M}_{\rm a} = \dot{M}_{\rm a,w} - f_{\rm mt}\dot{M}_{\rm RLOF} \ , \tag{2.21}$$

where the stellar wind mass loss rates are $\dot{M}_{\rm a,w}$ and $\dot{M}_{\rm d,w}$, and $\dot{M}_{\rm RLOF}$ is the mass transfer rate from RLOF. The factor $f_{\rm mt}$ represents the efficiency of mass transfer in absence of winds and is given by

$$f_{\rm mt} = (1 - \alpha_{\rm mt} - \beta_{\rm mt} - \delta_{\rm mt}) \ , \tag{2.22}$$

where $\alpha_{\rm mt}$, $\beta_{\rm mt}$ and $\delta_{\rm mt}$ are the fractions of mass transferred that is lost from the vicinity of the donor, accretor and circumbinary toroid, respectively. In MESA the outer Lagrange point (L2) can be modelled as a circumbinary toroid with radius $R_{\rm toroid} = \gamma_{\rm mt}^2 a$ following Pennington (1985), but we are not taking this into account. Thus, the case of an escaping gas with energy beyond the gravitational potential of the accretor should be included within the $\beta_{\rm mt}$ term.

Finally, the angular momentum change due to the mass loss is computed using

$$\begin{aligned}\dot{J}_{\rm ml} = &\left[(\dot{M}_{\rm d,w} + \alpha_{\rm mt}\dot{M}_{\rm RLOF})M_{\rm d}^2 + (\dot{M}_{\rm a,w} + \beta_{\rm mt}\dot{M}_{\rm RLOF})M_{\rm a}^2\right]\frac{a^2}{(M_{\rm d}+M_{\rm a})^2}\frac{2\pi}{P} \\ &+ \gamma_{\rm mt}\delta_{\rm mt}\dot{M}_{\rm RLOF}\sqrt{G(M_{\rm d}+M_{\rm a})a}\ ,\end{aligned} \tag{2.23}$$

where $\gamma_{\rm mt}^2 a$ is the radius of the toroid. In MESA, constants $\alpha_{\rm mt}$, $\beta_{\rm mt}$, $\delta_{\rm mt}$, and $\gamma_{\rm mt}$ are fixed throughout evolution. Since we are dealing with low-mass stars in the subgiant or in the giant phase in binary system with $q \sim 1$, is quite reasonable to assume that there is no mass lost from the donor as fast winds, so we adopt $\alpha_{\rm mt} = 0$. Therefore, we do not consider possible irradiation induced winds effects in our simulations. Still, a simple study on the effects of donor irradiation is presented in section 3.8.

As we are not going to consider the mass loss through the Lagrangian point L2, we also have that $\delta_{\rm mt} = 0$ and $\gamma_{\rm mt} = 0$. For the fraction of mass lost from the vicinity of the accretor as fast wind, we adopt $\beta_{\rm mt} = 0.3$ and 0.8. The reason for these values will be presented in due course, but we advance that this choice makes little difference in the overall result.

We are going to ignore the magnetic field of the accretor (either a neutron star or a massive white dwarf) throughout this thesis. Mass loss due to surface flashes, nova explosions, jets, discs, hot spots, etc., are also not considered since we are treating the accretor as a point of mass. Obviously, these events could contribute to mass and angular momentum losses, since they change the dynamics of the system. For example, if a certain fraction of matter is accreted by the accretor and this leads to a nova explosion to occur, some of that matter is actually lost rather than absorbed. Although this can bring small changes in the results of a given binary system, it does not affect the general results that we will present in this work. More discussions on this topic will be presented in subsection 3.5.4, where we will evaluate the extreme cases of accretion efficiency — maximum ($\beta_{\rm mt} = 0$), and null ($\beta_{\rm mt} = 1$).

When accretion is limited by the Eddington limit, $\dot{M}_{\rm Edd}$, the efficiency of accretion is given by

$$f_{\rm mt} = \min(1 - \alpha_{\rm mt} - \beta_{\rm mt} - \delta_{\rm mt}, |\dot{M}_{\rm Edd}/\dot{M}_{\rm RLOF}|)\ , \tag{2.24}$$

where the Eddington limit is the maximum luminosity a star can achieve when there is

balance between the radiation and gravitational forces. The Eddington limit is given by

$$\dot{M}_{\rm Edd} = \frac{4\pi c R_{\rm a}}{\kappa_e} \approx \frac{3.4}{1+X} 10^{-8}\ M_\odot/{\rm yr}\ , \tag{2.25}$$

where κ_e is the Thomson electron scattering opacity, $\kappa_e = 0.19(X+1)$ cm^2/g, and X is the hydrogen mass fraction in the material transferred from the donor. The estimate in Equation 2.25 takes into account the radius of a neutron star of 11.5 km. This is, therefore, a much smaller threshold than for white dwarfs, which are much larger.

The default and most commonly magnetic braking recipe used in binary systems modelling is (Skumanich, 1972; Rappaport; Verbunt; Joss, 1983)

$$\dot{J}_{\rm mb} = -6.82 \times 10^{34} \left(\frac{M_{\rm d}}{M_\odot}\right) \left(\frac{R_{\rm d}}{R_\odot}\right)^{\gamma_{\rm mb}} \left(\frac{1\ {\rm d}}{P}\right)^3\ . \tag{2.26}$$

This is also the default option in the MESA code. Although this expression represents an advance in the modelling of binary systems since it lets the stellar quantities vary in time, it is nothing but an empirical fit that takes into account the star's radius, mass, and rotational angular frequency. In order to reproduce the results of Istrate et al. (2016) and validate our approach, our initial calculations used this prescription. Following this work, we chose the magnetic braking index to be $\gamma_{\rm mb} = 4$.

2.2.3 Implementation of a different magnetic braking

Considering the discussion presented in the section 1.5, in subsequent models (chapter 3) we adopted the recent CARB (Convection And Rotation Boosted)[5] prescription of Van, Ivanova & Heinke (2018) and Van & Ivanova (2019), that combines the recent improvements in understanding stellar magnetic fields and magnetised winds. Motivated by the discrepancies between the observed mass transfer rates and the theoretical models of LMXBs, the authors showed that the default form of the braking law (i.e., Equation 2.26) is not suitable to explain most of the observed persistent LMXBs. On the other hand, they found that considering the dependence of the Alfvén radius on the donor's rotation rate, and the dependence of the magnetic field strength on the outer convective zone, does a better job reproducing transient and persistent LMXBs. We also derived the equations obtained by the authors,[6] but now we will show only the main steps.

The Alfvén surface is the surface where the ram pressure[7] is equal to the magnetic pressure (Mestel; Spruit, 1987). This is the maximum distance at which the stellar wind is

[5] <https://doi.org/10.5281/zenodo.3647683>

[6] In fact, there are two typos in the published work. The first is that, in equation (5) of Van & Ivanova (2019), the exponential argument of $\dot{M}$ should read $-1/3$ instead of $1/3$. The second is in the code available online (<https://zenodo.org/record/3543922/files/reville_mb.f?download=1>), where the argument 2/3 of the exponential in line 320 should be 1/3 in order to make it correctly fit in the corresponding equations in the paper. This typo was confirmed by the author.

[7] Ram pressure is a pressure exerted on a body moving through a fluid medium, caused by relative bulk motion of the fluid. It causes a drag force to be exerted on the body (Clarke; Carswell, 2007).

still in corotation with the star; at larger distances, the mass is assumed to be lost from the star. Spherical symmetry is assumed, which results in the angular momentum lost by magnetic breaking through an Alfvén surface to be (Weber; Davis, 1967; Mestel, 1968)

$$\dot{J}_{\rm mb} = -\frac{2}{3}\Omega \dot{M}_{\rm W} R_{\rm A}^2 \ , \tag{2.27}$$

where Ω is the rotation rate, $\dot{M}_W$ is the wind mass-loss rate, and R_A is the Alfvén radius. The assumed isotropic wind mass-loss rate can be described using the following equation

$$\dot{M}_{\rm W} = 4\pi R_{\rm A}^2 \rho_{\rm A} v_{\rm A} \ , \tag{2.28}$$

where $\rho_{\rm A}$ and $v_{\rm A}$ are the density and the velocity of the mass flux through the Alfvén surface. The Alfvén radius is the distance where the magnetic energy density is equal to the kinetic energy density (Belenkaya; Khodachenko; Alexeev, 2015). When including the effects of rotation, the expression for the Alfvén radius reads (Matt et al., 2012; Réville et al., 2015)

$$R_{\rm A} = R\left[\frac{B_{\rm s}^4 R^4}{\dot{M}_{\rm W}^2}\left(v_{\rm esc}^2 + \frac{2\Omega R^2}{K_2^2}\right)^{-1}\right]^{1/3} \ , \tag{2.29}$$

where $v_{\rm esc} = \sqrt{2GM/R}$ is the escape velocity and $K_2 = 0.07$ is a constant obtained via simulations (Réville et al., 2015). $B_{\rm s}$ is the surface magnetic field, assumed as (Ivanova, 2006; Van; Ivanova; Heinke, 2018)

$$\begin{aligned} B_{\rm s} &= \tau_{\rm conv}\Omega \\ &= \frac{\tau_{\rm conv}}{P} \ , \end{aligned} \tag{2.30}$$

where

$$\tau_{\rm conv} = \int_{R_{\rm bot}}^{R_{\rm top}} \frac{{\rm d}r}{v_{\rm conv}} \tag{2.31}$$

is the turnover time of convective eddies. $v_{\rm conv}$ is the local convective velocity and the integration limits, $R_{\rm bot}$ and $R_{\rm top}$, are the bottom and the top of the outer convective zone, respectively. Thus, this description assumes the total magnetic field is generated by the convection eddies, i.e., no fossil fields.

Substituting Equation 2.30 into Equation 2.29 and then Equation 2.29 into Equation 2.27 one obtains the CARB modified magnetic braking prescription

$$\dot{J}_{\rm mb,CARB} = -\frac{2}{3}\Omega \dot{M}_{\rm W}^{-1/3} R^{14/3}\left(v_{\rm esc}^2 + \frac{2\Omega R^2}{K_2^2}\right)^{-2/3} \Omega_\odot B_\odot^{8/3}\left(\frac{\Omega}{\Omega_\odot}\right)^{11/3}\left(\frac{\tau_{\rm conv}}{\tau_{\odot,\rm conv}}\right)^{8/3} \ . \tag{2.32}$$

Finally, the last terms of the Equation 2.32 is normalised according to solar calibration, resulting in $\Omega_\odot \approx 3 \times 10^{-6}$ s^{-1} and $\tau_{\odot,\rm conv} = 2.8 \times 10^6$ s (Van; Ivanova, 2019). Here we again emphasise that the prescriptions of Rappaport and Van differ essentially by the fact that the former is an empirical fit, and the latter is obtained through a self-consistent

deduction considering wind mass lost, rotation, and that the magnetic field is generated due to motion in the convective zone.

We again draw attention to the fact that the CARB model is still considerably simplified — only radial magnetic fields are considered and the dipole approximation is used, the Alfvenic surface estimated does not depend on the polar angle, and the wind is considered isotropic (i.e., the rotation axis is assumed aligned to the magnetic field axis).

An example of our inlist files is shown in Appendix F. Comparisons between other, less-used recipes for the magnetic braking in different types of stars and systems can be found in, e.g., Knigge, Baraffe & Patterson (2011), Deng et al. (2021), Gossage et al. (2021).

3 Results and discussions

The main publication related to the work of this thesis is presented in Appendix D. A secondary publication by the author is shown in Appendix E.

The results presented in this chapter were obtained using the `star` and `binary` MESA modules. Moreover, in order to describe the results, we shall use new indices to refer to the initial and final states of the system. For example, the initial orbital period of the system is $P_{\rm i}$; the final donor star mass is $M_{\rm d,f}$, etc.

3.1 Rappaport vs CARB magnetic braking in the formation of ELM WDs

With the exception of the modification of magnetic braking — and hence also the evolution of orbital angular momentum —, our models are very similar to those defined as "basic" in Istrate et al. (2016). Istrate's basic models consider, for Z=0.02, the initial binary configuration with a 1.4 $M_{\odot}$ donor star and a 1.2 $M_{\odot}$ neutron star accretor. For Z=0.01, the models were calculated with a 1.0 $M_{\odot}$ donor star and a 1.4 $M_{\odot}$ neutron star. The neutron star was treated as a point mass with no magnetic field. The models followed the detailed binary evolution of the donor star from the zero-age main sequence (ZAMS) until it reached the model age of 14 Gyr.[1] The nuclear network used takes into account the p-p and CNO burning with 21 isotopes, from H to Mg. Proper treatment of radiative and conductive opacities are considered. Convective regions are treated using the mixing-length theory. The rate of change of orbital angular momentum accounts for contributions from gravitational wave radiation, mass loss, and magnetic braking. It is assumed that 30% of the transferred mass is ejected ($\beta_{\rm mt} = 0.3$) from the neutron star as a fast wind carrying its specific orbital angular momentum. We previously reproduced the models presented by Istrate to validate our approach and the results obtained in the present work. We will not discuss these models in detail here, but the main results will be presented in several figures in the next sections for comparison purposes.

Taking the Istrate models with the standard Rappaport magnetic braking as a starting point, we build up models considering the CARB magnetic braking of Van & Ivanova (2019). The main differences are that we allow rotation and mass loss by winds to take place in the donor star, which are mandatory features of the CARB prescription.

[1] Two important remarks: i) the elapsed time of a massive progenitor star ($\sim$ 8–25 $M_{\odot}$) to become a neutron star (NS) is very short (few Myr, see, e.g., de Loore; Doom, 1992; Fortin et al., 2016) compared to the evolution time of the progenitor of the ELM WD; ii) the evolution of this massive star until the formation of the NS is supposed not to influence the less massive companion prior to its ZAMS.

Following Van & Ivanova (2019), we adopt the Reimers (1975) wind mass loss scheme in the red giant branch. We first consider the initial donor/accretor star masses to be $M_{\rm d,i} = 1.2\ M_\odot$ and $M_{\rm a,i} = 1.4\ M_\odot$, respectively. This is justified because for initial stellar mass below 0.8 $M_\odot$ the main sequence life time for solar metallicity is longer than 15 Gyr and therefore the WD cannot reach the WD cooling phase within a Hubble time (e.g., Sun; Arras, 2018). That is, a low-mass He WD with solar metallicity in the cooling track cannot have being formed from a progenitor with a mass less than 0.8 $M_\odot$ if single evolution is assumed. It should be noted, however, that for a 0.85 $M_\odot$ model with $Z = 0.001$, the main sequence duration is 11.885 Gyr, and it reaches its maximum $T_{\rm eff}$ ∼70 kK at age 13.322 Gyr (Renedo et al., 2010; Romero; Campos; Kepler, 2015). In addition, 1.4 $M_\odot$ is the average neutron star mass (e.g., Lattimer, 2012; Özel; Freire, 2016). The internal structure of the *accretor star* has not been modelled — i.e., the neutron star is considered to be a point of mass.[2] $Z = 0.02$ initial metallicity is adopted in this chapter for all models, compatible with the fact that only 35% of the ELM WDs are in the halo (Brown et al., 2020). Computations considering a more massive donor star, a less massive accretor star, and other metallicities will be discussed from section 3.4 onwards. To better compare our results with those of Istrate et al. (2016), we first choose $\beta_{\rm mt} = 0.3$ in Equation 2.22, indicating that 30% of the total amount of mass going towards the neutron star is lost from the vicinity of the accretor as fast wind. There is however observational evidence that mass transfer during the LMXB phase is extremely inefficient (Jacoby et al., 2005), corresponding to accretion efficiencies of only ∼ 5–40 % (Antoniadis et al., 2012; Antoniadis et al., 2013; Antoniadis et al., 2016). The effects of low accreting efficiency (with $\beta_{\rm mt} = 0.8$) will be considered from section 3.4 onwards.

In the code, during the Roche-lobe overflow (RLOF), the rate of mass transfer is recomputed for each model, increasing or decreasing progressively. Its value is given in units of $\log(M_\odot/{\rm yr})$. For reference, the Sun wind mass loss is around $3 \times 10^{-14}\ M_\odot/{\rm yr}$ (Carroll; Ostlie, 2017); and beyond $10^{-4}\ M_\odot/{\rm yr}$ the mass transfer is generally assumed to be unstable and a common envelope phase will proceed (Ivanova et al., 2013). Thus, when analysing the results, it is convenient to define a threshold to indicate whether or not there is RLOF in a model. In our analysis, RLOF is considered to take place when the mass transfer rate exceeds the value of $\dot{M} = 10^{-10}\ M_\odot/{\rm yr}$. That is, we will refer to the start and end of mass transfer when this limit is crossed. We stress that this is just an arbitrary limit to flag the occurrence of mass transfer and guide our analysis, having no role in the simulations themselves.

Figure 11 shows the evolutionary tracks for two systems with $P_{\rm i} = 20$ d in the

[2] In fact, MESA is able to model both stars through the *evolve both stars* option. Obviously, this makes the simulations considerably slower. In fact, to date, it is not possible to find in the literature simulations of the formation of ELM WDs in LMXBs modelling the two stars of the binary system. We will comment a little more about this possibility at the end of this work (chapter 4).

HRD, an example of the formation of an ELM WD through the LMXB channel. The only difference between the tracks is the magnetic braking prescription used to compute $\dot{J}_{\rm mb}$. The blue dashed line considers the standard Rappaport, Verbunt & Joss (1983) recipe, i.e., Equation 2.26, and the black solid line is considering the CARB prescription of Van & Ivanova (2019) — i.e., Equation 2.32. $M_{\rm d,i} = 1.2\ M_\odot$ and $M_{\rm a,i} = 1.4\ M_\odot$ for both tracks. These two evolutionary sequences will be considered in the discussion through the end of this subsection.

Figure 11 – Hertzsprung-Russel diagram showing the formation and cooling of a 0.26 $M_\odot$ and a 0.32 $M_\odot$ helium WD, similar to those produced in LMXB systems. One of the systems is evolved considering the standard magnetic braking by Rappaport; Verbunt; Joss, 1983 (R83, blue dashed line) and does not undergo a hydrogen shell flash. The other system takes into account the CARB magnetic braking (black solid line) produced in the rotating convection zone prescription by Van & Ivanova (2019) and undergoes a hydrogen shell flash. Both systems consider the initial progenitor mass $M_{\rm d,i} = 1.2\ M_\odot$, the neutron star mass $M_{\rm a,i} = 1.4\ M_\odot$, and the initial orbital period $P_{\rm i} = 20$ d. Start and end of mass transfer phases are indicated with green triangle and purple squares, respectively. Key points are indicated with red dots and are discussed in the text. See Table 1 for ages and masses at each stage of the CARB system.

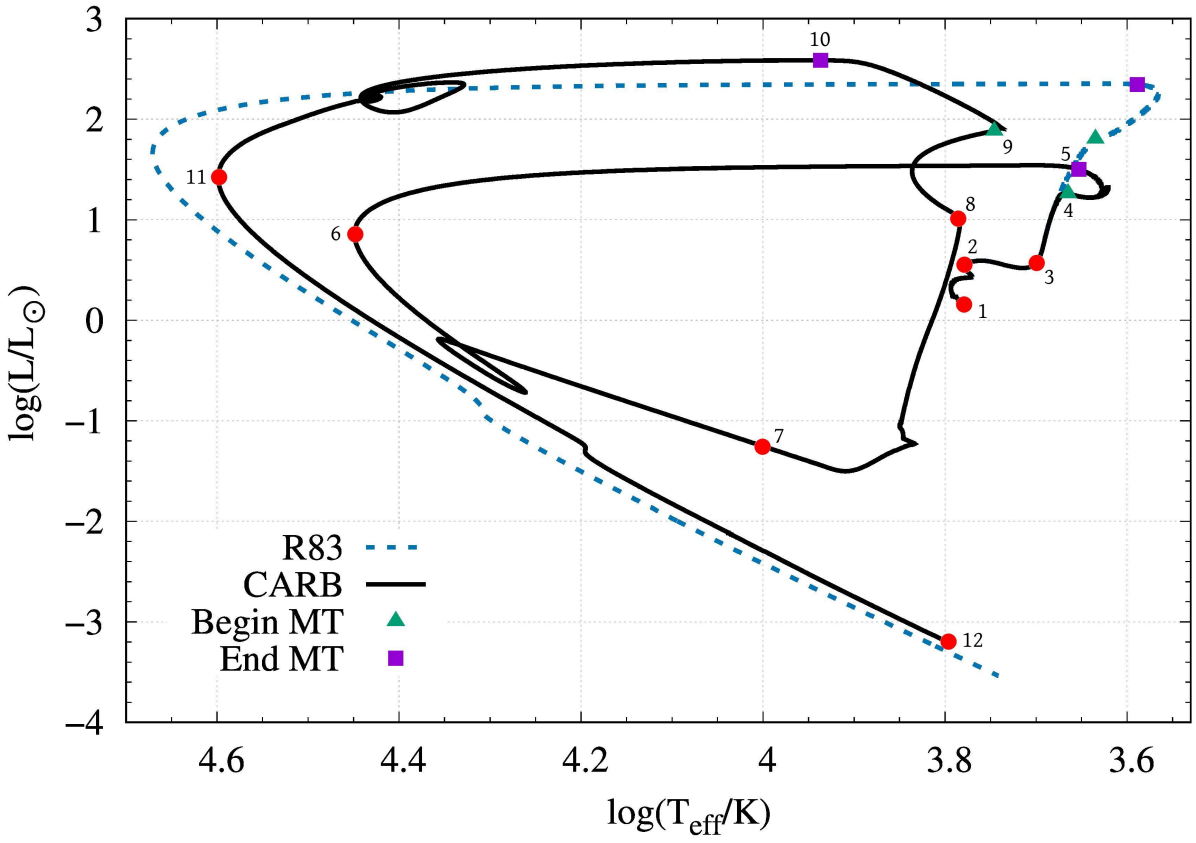

Evolutionary sequences are computed from the ZAMS (point 1) until the donor

star reaches the maximum model age of 14 Gyr (point 12 in the black solid track). For points from 1 to 4 the evolutionary path in the HRD is the same for both models. This occurs because, from ZAMS up to this point, the NS does not interfere in the evolution of the companion because of our no magnetic field point mass assumption. For each track, the green triangles and the purple squares indicate the beginning and end of the mass transfer (MT), respectively.

Two major differences can be noted by analysing Figure 11. First: after leaving the main sequence, mass transfer (MT) episodes occur with different luminosity and effective temperature. This was expected because the change in the treatment of angular momentum evolution alters the evolutionary stage the star is in when it begins to lose mass. Since in the HRD the stellar radius grows towards the upper right, the radius of each model at the beginning of the MT is also quite different. RLOF begins at the moment when $R_{\rm d} \approx 14.3\ R_{\odot}$ for the Rappaport magnetic braking and $R_{\rm d} \approx 6.7\ R_{\odot}$ for the CARB magnetic braking. Second: after MT, the model with Rappaport magnetic breaking (blue dashed line model) immediately raises its temperature by ∼43 kK at constant luminosity and then enters the cooling track as a WD. On the other hand, for the model with CARB magnetic breaking (black solid line), a hydrogen shell flash occur after the MT — the counterclockwise loop in the plot — before cooling to temperature and brightness similar to the previous model. The physical reason for the flash or its absence is related to the size of the envelope and the amount of hydrogen burning in the shell. Less massive hydrogen envelopes prevent hydrogen burning from being a major source of energy.[3] In fact, at maximum $T_{\rm eff}$ just after the RLOF, the envelope mass and the hydrogen total mass are 1.8 and 1.9 times greater in the CARB (black solid line) model than in the blue dashed line model, respectively.

Now we shall analyse the model that uses the boosted $\dot{J}_{\rm mb,CARB}$ in more detail (i.e., the model shown in black solid line). For each point discussed, some important quantities are shown in Table 1, which will be presented in more detail later. Between points 1 and 2 the nuclear burning in the nucleus increases, reaching about 40% (by mass) of the model. At this point, the envelope is convective only in a small fraction ($\lesssim 4\%$, by mass) near the surface. At point 3 the envelope becomes fully convective, and nuclear reactions occur only in a thin shell around the nucleus. Just before RLOF begins (point 4), the envelope mass is 0.98 $M_{\odot}$ and the total masses of ^{1}H and ^{4}He are 0.66 $M_{\odot}$ and 0.50 $M_{\odot}$, respectively. The RLOF reduces the envelope mass to just 0.016 $M_{\odot}$, and the donor now has only $M_{\rm d} = 0.269\ M_{\odot}$. Therefore, most of the mass is lost in this relatively short phase (see also Table 1). Precisely, this is the stage at which the system can be

[3] Historically, Kippenhahn, Thomas & Weigert (1968) were the first to find a hydrogen shell flash in a low-mass star model. Several nomenclatures are used equivalently in the literature: thermal pulses, thermal flashes, CNO flashes, hydrogen shell flashes. See Gautschy (2013) for a recent discussion of the topic.

observed as a low-mass X-ray binary (LMXB, see, e.g., Truemper; Lewin; Brinkmann, 1986; van den Heuvel; Rappaport, 1992; Giovannelli; Sabau Graziati, 1993; Lewin; van der Klis, 2006; Bhattacharyya, 2009; Charles, 2011; Sazonov et al., 2020). After the first RLOF (point 5), the pre-WD goes through a phase of contraction at almost constant luminosity but increasing effective temperature (to point 6). At this point the total mass of ^{4}He is 0.26 $M_\odot$, and the surface is composed (by mass) of about 68% ^{1}H and 30% ^{4}He. From that point on, the temperature in the burning shell is too low to sustain CNO burning, and at point 7 the intermediate layer between the surface and the nucleus has already burned much of its H into He. In the loop between points 6 and 7 is when the burning of hydrogen in the shell abruptly intensifies. The density–temperature profile inside the model is no longer approximately a straight line (in log) and now has a large peak in temperature at the base of the envelope. At point 7 we can easily distinguish three zones inside the model: the helium core; the mixed shell around the core, where nuclear reactions are at maximum energy production; and the envelope, mostly composed of hydrogen. In the low luminosity part after point 7, the convective zone is fully developed, and the hydrogen shell flash is about to begin. Around point 8 few convective regions remain, but thermohaline mixing acts efficiently. On the way to a significant increase in radius, at point 9, the Roche lobe is now filled again and a new episode of RLOF occurs between points 9 and 10. This second mass transfer episode reduces the total mass by 0.001 $M_\odot$, and the hydrogen shell flash makes helium now more abundant than hydrogen in every part of the model. Point 11 indicates the highest effective temperature reached during all evolution of the model with the CARB magnetic braking, $\log(T_{\rm eff}/K) \approx 4.59$ at age 6.34 Gyr. At this point the ELM WD is completely formed and will then enter its cooling track. At point 12 the model reaches 14 Gyr years, and we stop our simulation. An 0.263 $M_\odot$ ELM WD with $T_{\rm eff} \approx 6,400$ K and $\log(L/L_\odot) \approx -3.2$ is formed as the end-product of this evolution.

Table 1 shows the time interval for each of the above described phases. The envelope mass, the total mass, and the total mass of ^{1}H and ^{4}He are also shown. Point 1 sets the zero age main sequence (ZAMS). Point 2 marks the end of the main sequence (MS), when hydrogen runs out in the nucleus. The interval between points 2 and 3 is called the subgiant branch (SGB). From point 3 on, the model ascends the red-giant branch. The mass transfer — via Roche lobe overflow (RLOF) — takes place between points 4 and 5. After mass transfer and before entering the cooling track, the donor star is called pre-ELM WD (i.e., between points 5 and 11). At point 6 the model starts to cool down, but in the loop between points 6 and 7 the energy production via the CNO cycle is intensified in the shell around the core. Near point 7 the energy production at the base of the envelope reaches its maximum. The location of point 8 strongly depends on metallicity: for smaller metallicities, the abrupt increase in luminosity occurs at higher temperatures. Between points 9 and 10, the donor star has its radius increased to such a point that it ends up filling its Roche lobe again, losing a small fraction of its mass again. Point 11 marks

entry into the cooling track. Point 12 indicates the end of the evolution of the sequence of models.

Table 1 – Evolution as a function of time for a starting model of $M_{\rm d,i} = 1.2\ M_\odot$ and $M_{\rm a,i} = 1.4\ M_\odot$ in a $P_{\rm i} = 20$ d orbit binary. The CARB magnetic braking is considered. The ZAMS is at point 1, and the terminal age (14 Gyr) is at point 12. In MESA the envelope mass is considered to be the total mass minus the He-core mass.

point	**age (Gyr)**	**donor mass ($M_\odot$)**	**envelope mass ($M_\odot$)**	**total ^{1}H mass ($M_\odot$)**	**total ^{4}He mass ($M_\odot$)**
1	0	1.200	1.200	0.838	0.337
2	4.97	1.195	1.120	0.722	0.448
3	5.80	1.193	1.043	0.689	0.479
4	6.17	1.189	0.976	0.659	0.505
5	6.28	0.269	0.016	0.010	0.253
6	6.30	0.264	0.003	0.002	0.257
7	6.34	0.264	0.003	0.002	0.257
8	6.34	0.264	0.003	0.002	0.257
9	6.34	0.264	0.003	0.002	0.257
10	6.34	0.263	0.002	0.001	0.257
11	6.34	0.263	0.002	9×10^{-4}	0.257
12	14.00	0.263	0.002	4×10^{-4}	0.257

It is worth noting that, between points 6 and 7 (Figure 11), the models have an effective temperature and luminosity very similar to that of the final cooling track (between points 11 and 12). In fact, the time spent between points 6 and 7 is much longer than between points 7 and 8. So we might wonder if we are not seeing some fraction of ELM WDs in the hydrogen shell flash phase. And the answer is yes. As such, the use of the term "(pre-)ELM WDs" helps to expose our ignorance of this fact. However, as we will see later, other parameters can be used to try to solve this plurivocity.

Regarding the dynamics of the binary systems for each magnetic braking prescription,[4] we found that they begin the mass transfer episodes for different reasons. When the Rappaport magnetic braking is used, the binary separation and the Roche lobe radius of the donor star remain constant from the ZAMS until the beginning of the RLOF. In other words, the donor star starts overflowing only because its radius increases as a result of nuclear evolution. On the other hand, when the CARB magnetic braking acts, the decrease in orbital separation, and consequently the Roche lobe, due to loss of angular momentum is the main reason for the start of the RLOF. As we already saw, another reason that leads to different end products is that the modification of the magnetic braking alters the way the orbital separation of the system reacts to mass loss, leading to a greater amount of mass transferred to the accretor or lost from the system, depending on the efficiency factor.

[4] Important to note, we do not turn the magnetic braking on and off depending on the evolutionary phase, as is often found in the literature. Magnetic braking is always on in our models, although it can assume virtually null values depending on the evolutionary phase.

Figure 12 – Comparison between the empirical fit of Rappaport; Verbunt; Joss, 1983 (R83, upper panel) and the Convection And Rotation Boosted (CARB, Van; Ivanova, 2019, lower panel) magnetic braking prescriptions. The CARB prescription takes into account the dependence of the Alfvén radius on the donor's rotation rate, and the dependence of the magnetic field strength on the outer convective zone. The size of the donor radius (purple solid line), donor Roche lobe radius (red dashed line), the binary separation (green solid line), and the mass transfer rate (black dashed line) as a function of age at the time of the RLOFs are shown. Characteristic sizes correspond to the left y-axis. Mass transfer rate correspond to the right y-axis, in log scale. The initial configuration is $M_{\rm d,i} = 1.2\ M_\odot$, $M_{\rm a,i} = 1.4\ M_\odot$ and $P_{\rm i} = 20$ d for both models. From the ZAMS until an age of 6 Gyr, the donor Roche lobe radius and the binary separation is almost constant for both models. The top panel shows that the mass transfer begins as a natural consequence of the donor's increase in radius due to nuclear evolution. On the other hand, the bottom panel shows that the main reason for the RLOF to begin is the proximity of the accreting star.

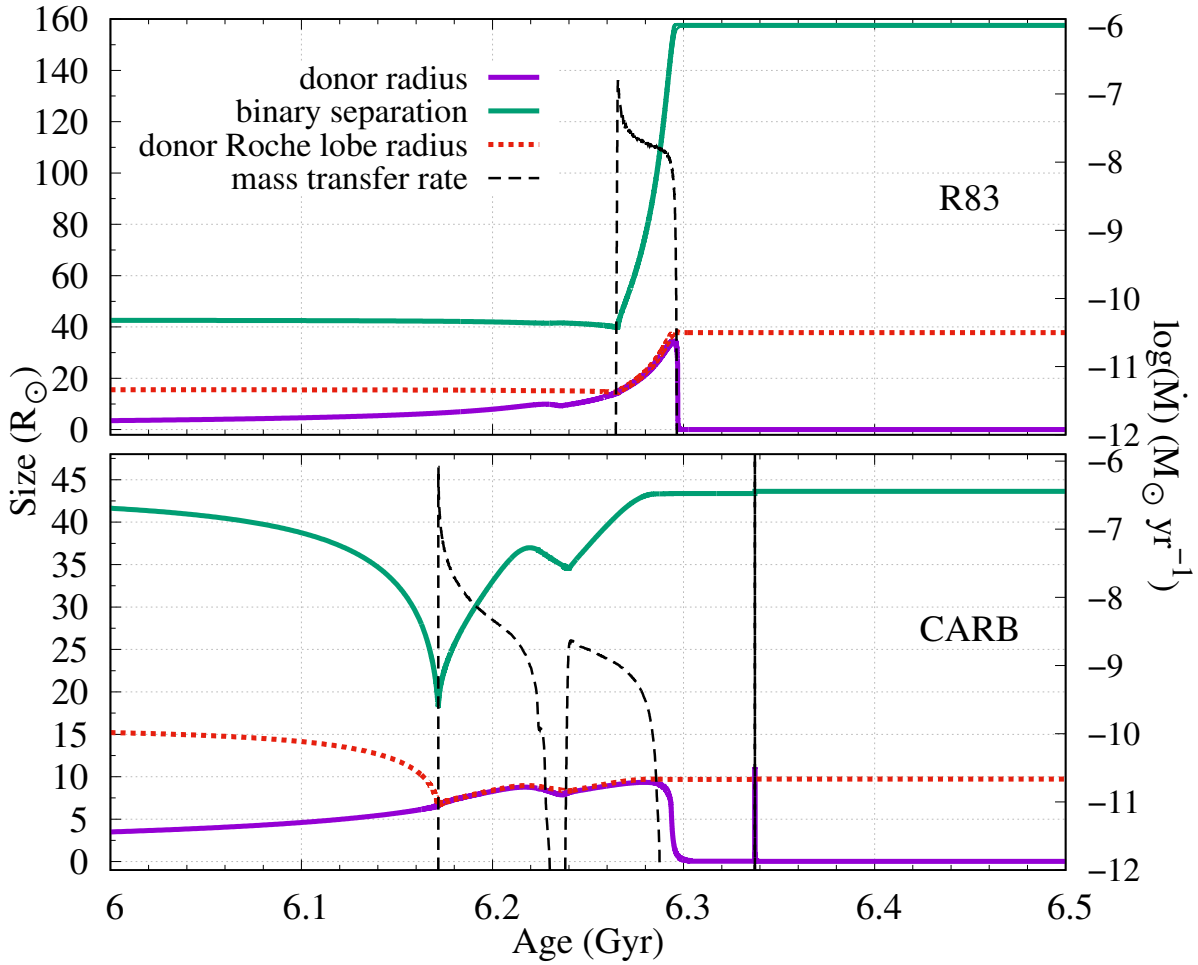

Figure 12 shows the behaviour of the radii of the star and the Roche lobe when orbital separation decreases due to angular momentum losses, leading to mass transfer episodes. The two configurations compared here are the same as those presented in Figure 11. Before an age of 6 Gyr, all quantities vary insignificantly. When the standard Rappaport magnetic braking is used (upper panel in Figure 12), the binary separation and the donor Roche lobe radius remain unchanged until the beginning of the RLOF. In this case, the donor star starts to lose mass because its radius reaches the Roche lobe. During the RLOF the donor star radius keeps increasing, and the orbital separation increases drastically. The RLOF ends when the donor star contracts because it no longer has a convective envelope. When the outer part of a convective envelope is lost, the star tends to increase in radius, maintaining the mass loss. On the other hand, if a radiative envelope loses mass, the star tends to maintain its radius and the mass loss stops. The orbital period becomes constant from this point on.

When the CARB magnetic braking is used (lower panel in Figure 12), the donor radius increases smoothly and the orbital separation decreases from $a \approx 42\ R_\odot$ to $a \approx 20\ R_\odot$ before the RLOF begins. This is because of the larger angular momentum loss. This leads to a decrease in the Roche's lobe, getting closer and closer to the donor's radius. Around age 6.1 Gyr the orbital angular momentum loss is such that the binary separation decreases by $\approx 20\ R_\odot$ in just 0.2 Gyr. This causes the $R_{\rm L,d}$ also to decrease (see Equation 1.11) until it becomes equal to $R_{\rm d}$. As long as $R_{\rm L,d}$ is equal to $R_{\rm d}$, RLOF is occurring. The first RLOF is the longest, and it removes the envelope, preventing the donor from increasing in radius. In this case, the RLOF remains with $R_{\rm d}$ almost constant, and it lasts longer than when the standard magnetic braking is used. At age 6.29 Gyr, the donor contracts, ceasing the RLOF. From that point on, $R_{\rm L,d}$ and a will remain practically constant. The last RLOF episode can be noticed during the very short phase of hydrogen shell flash, when the donor expand its radius again during 123 yr and loses about 0.001 $M_\odot$. This causes a slight increase in orbital separation, equivalent to $\sim$5 h increase in the orbital period.

3.2 Different braking scenarios

We now vary the initial orbital period, searching for representative cases of different evolutionary scenarios.

Figure 13 shows the orbital period evolution as a function of the donor mass for three systems, with $M_{\rm d,i} = 1.2\ M_\odot$ and $M_{\rm a,i} = 1.4\ M_\odot$, and for three different initial orbital periods, $P_{\rm i} = 3$ (green), 20 (red), and 100 (blue) days. Each configuration is shown for both Rappaport; Verbunt; Joss, 1983 (dashed lines) and CARB (Van; Ivanova, 2019, solid lines) magnetic braking, totalizing six evolutionary sequences. The evolution of the

main physical quantities that govern magnetic braking are shown in Figure 14 for the cases of $P_{\rm i} = 3$ and 100 days. All other parameters are identical for all sequences. All sequences produce detached He-core ELM white dwarf + neutron star binaries as output.

Figure 13 – The evolution of orbital period as a function of decreasing donor mass. Two prescriptions for magnetic braking are compared: Rappaport; Verbunt; Joss, 1983 (dashed lines) and the CARB prescription of Van; Ivanova, 2019 (solid lines). For each prescription, three initial orbital periods are analysed: 3 (green), 20 (red), and 100 (blue) days. Initial masses are $M_{\rm d,i} = 1.2\ M_\odot$ and $M_{\rm a,i} = 1.4\ M_\odot$ for all sequences.

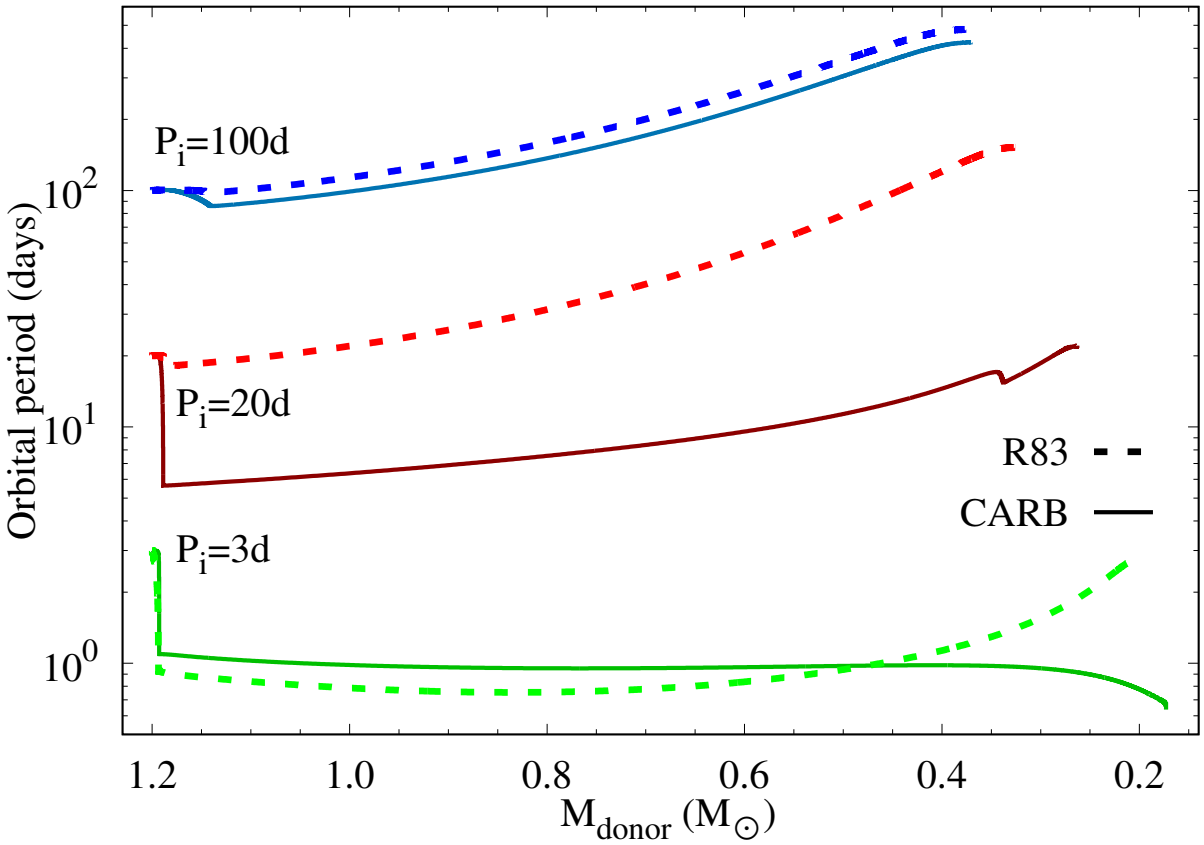

From short to long initial orbital periods, the final masses for CARB (Rappaport) sequences are 0.173 (0.205), 0.263 (0.325), and 0.371 (0.377) solar masses, respectively. The respectively final orbital periods are 0.64 (2.55), 22 (152), and 424 (481) days.

Figure 13 shows the existence of two different evolutionary scenarios when we compare the prescriptions of Rappaport and CARB for magnetic braking. The first scenario corresponds to intermediate and long initial orbital periods (∼20–100 days), where the evolution of the donor mass star has similar shapes for the two prescriptions of magnetic braking. The orbital period increases as the donor star loses mass, regardless of the adopted magnetic braking. The second scenario corresponds to the case of short initial orbital periods (∼3 days), and is characterised by a decrease in the orbital period at the end of the evolution of the sequences that consider the CARB prescription.

Figure 14 – The evolution of key parameters during the mass transfer epoch. Two prescriptions for magnetic braking are compared: Rappaport; Verbunt; Joss, 1983 (dashed lines) and Van; Ivanova, 2019 (solid lines). For each prescription, two initial orbital periods are analysed: 3 (green) and 100 (blue) days. Initial masses are $M_{\rm d,i} = 1.2\ M_\odot$ and $M_{\rm a,i} = 1.4\ M_\odot$ for all sequences. Magnetic braking (first panel); mass transfer rate (second panel); surface rotational velocity at the equator (third panel); wind mass loss (fourth panel); and radius of the donor star (fifth panel) are shown.

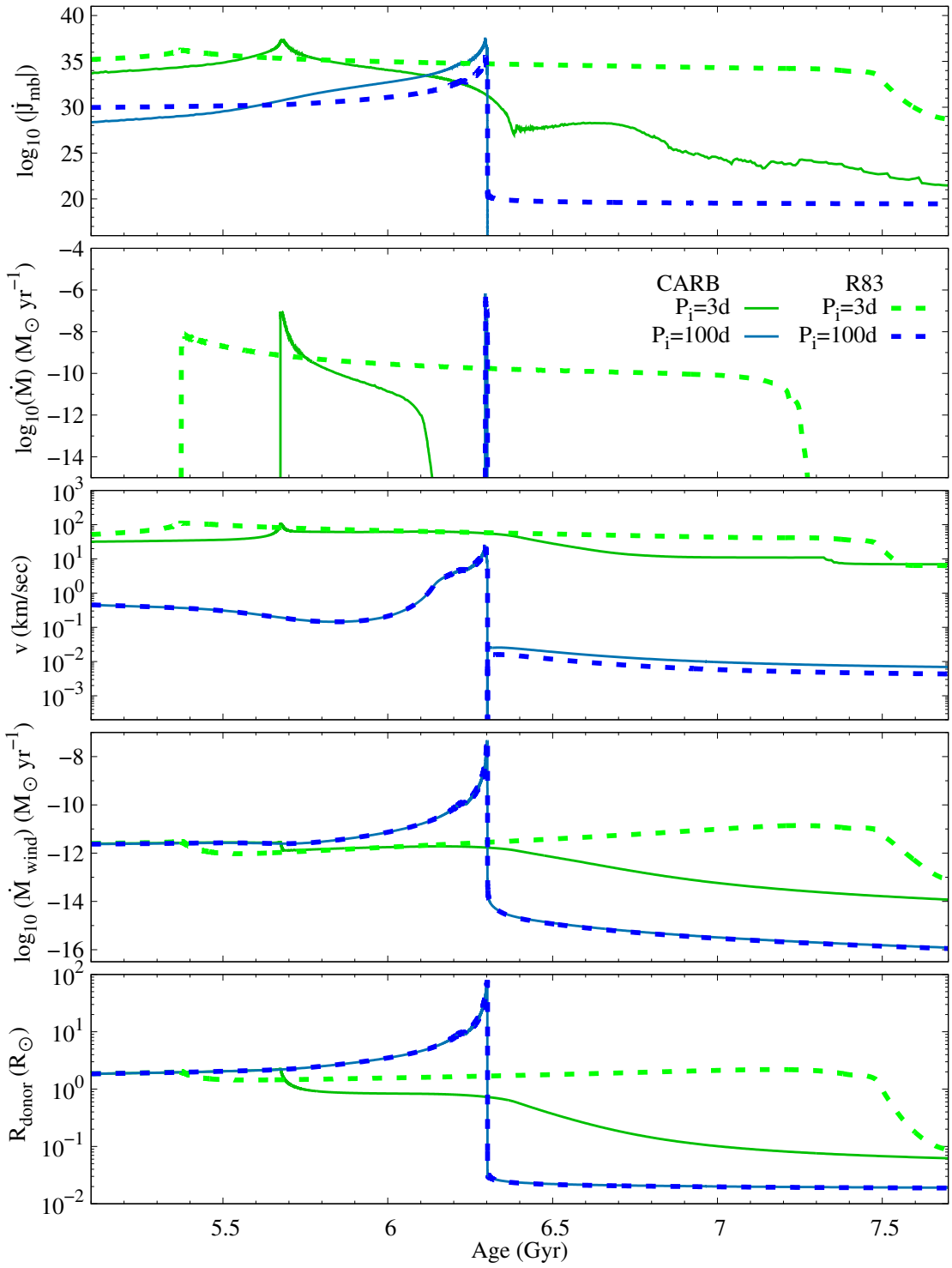

Also, for intermediate and long initial orbital periods, the binary components do not come closer before RLOF begins if the Rappaport magnetic braking is considered. When the CARB magnetic braking is considered, the components get closer before the beginning of the RLOF, and the difference in relation to the prescription of R83 is as large as the shorter the $P_{\rm i}$. Finally, in the case of short initial orbital periods, both prescriptions for magnetic braking (Rappaport and CARB) considerably decrease the separation of the binary components before the RLOF begins. In summary, the effect of magnetic braking increases with the decreasing of orbital periods for both prescriptions, but it alters differently along initial orbital periods for each prescription.

For $P_{\rm i} = 100$ d, both Rappaport and CARB prescriptions results in diverging systems; and for $P_{\rm i} = 3$ d, they both converge. The relation between the initial and final orbital periods for each magnetic braking prescription is, however, completely different. Looking for the limit that separates the converging from the diverging systems (i.e, $P_{\rm i} = P_{\rm f}$), we find ~ 3 d for the Rappaport magnetic braking but 20 d if the CARB prescription is used. With the only exception of the $P_{\rm i} = 100$ d models, in all other cases the use of the CARB prescription causes the mass transfer to start earlier when compared to the Rappaport prescription (second panel in Figure 14). Also, the duration of the mass transfer is longer for shorter $P_{\rm i}$. In fact, for $P_{\rm i} = 100$ d the mass transfer phase is so fast that we can barely distinguish it in the figure.

We now examine how the variables that determine the intensity of magnetic braking evolve. During most of the evolution, the Rappaport prescription results in stronger magnetic braking than the CARB prescription (first panel in Figure 14). The exception occurs during mass transfer, where the CARB braking prescription becomes more intense. This inversion can occur up to about 500 Myr before the mass transfer begins. Although these two prescriptions for magnetic braking differ for systems of any initial orbital period, their effects are much more intense in systems of short and intermediate orbital periods ($P_{\rm i} \sim 3$–50 d) than in long orbital periods ($P_{\rm i} \sim 100$ d). Note that the CARB prescription compensates exactly when braking is most intense, and the scale is logarithmic. Therefore, the net value of CARB braking over the course of evolution may be greater and the exact value must be studied on a case-by-case basis.

The $P_{\rm i} = 100$ d sequences show minimal differences in the evolution of the orbital period and donor mass (Figure 13). This occurs because the rotation rate, the radius of the donor, and the donor mass evolve in a very similar way in both prescriptions, for this initial orbital period (third and fifth panels in Figure 14). The small difference in the orbital period behaviour during the evolution of these sequences is due to the role of the size of the convective zone in the CARB prescription, which, in turn, affects the magnetic braking (first panel in Figure 14). For the $P_{\rm i} = 100$ d sequence with the CARB formula, the convective zone at the beginning of the RLOF accounts for $\sim 0.82\ M_{\odot}$ of the model.

Finally, the angular momentum loss from magnetic braking has a very limited impact on the evolution of binaries with long orbital periods. During the pre-RLOF evolution of the $P_{\rm i} = 100$ d systems, magnetic braking has an almost null contribution in both prescriptions. On the other hand, for $P_{\rm i} = 3$ d, magnetic braking is the dominant mechanism in the Rappaport prescription; and has an increasing contribution in the CARB prescription, dominating from 2 Gyr before RLOF onwards.

In the second scenario, $P_{\rm i} = 3$ d, the mass transfer begins when the donor star has just left the main sequence and the convective zone is not extended enough ($\sim 0.25\ M_\odot$ in the CARB sequence) to contribute significantly with magnetic braking. Thus, the consideration of the size of the convective zone foreseen by the CARB prescription has little effect. Until the beginning of the RLOF, the wind mass loss and the radius of the donor star behave similarly in both prescriptions, assuming values of $10^{-11.5}\ M_\odot\,{\rm yr}^{-1}$ and $2\ R_\odot$ immediately before the beginning of the mass transfer, respectively (fourth and fifth panels in Figure 14). On the other hand, the rotation rate in the CARB (Rappaport) prescription is 32 km/s (59 km/s) at age 5.2 Gyr (third panel in Figure 14). Since the donor mass and the donor radius behave similarly in this case, contributions are limited to the rotation rate, the wind mass loss, and the convection turnover time in this case. These are the contributions that make the mass transfer start when the system has an orbital period of 1.1 days (CARB) and 0.9 days (Rappaport). When the Rappaport prescription is used in the $P_{\rm i} = 3$ d system, the rotation rate, the radius of the donor star, and the donor mass react smoothly to the mass loss (third and fifth panels in Figure 14). Thus, the magnetic braking in this case also remains approximately constant $\log_{10}(|\dot{J}_{\rm mb,Rapp}|) = 35$ during a few Gyr after the mass transfer (first panel in Figure 14). On the other hand, when the CARB prescription is considered, the donor star contracts, and the wind mass loss decays after the end of the RLOF, causing the magnetic braking to be reduced to $\log_{10}(|\dot{J}_{\rm mb,CARB}|) = 28$. In the case where $P_{\rm i} = 3$ d, although the Rappaport prescription results in a considerably longer RLOF, the CARB prescription reaches $\dot{M}_{\rm CARB} = 10^{-7}\ M_\odot\ {\rm yr}^{-1}$, while Rappaport's only $\dot{M}_{\rm Rapp} = 10^{-8.2}\ M_\odot\ {\rm yr}^{-1}$. In addition, the moment the mass transfer ends, the system using the Rappaport prescription has an increasing orbital period, while the CARB prescription has a decreasing orbital period. At this point, the contributions of magnetic braking and mass loss to the total angular momentum loss are around 88 (98) and 12 (2) per cent for Rappaport (CARB), respectively. Gravitational radiation will dominate the angular momentum loss only about 2 Gyr after the RLOF terminates. Furthermore, at this point, the donor star has a radius about 2.3 times larger for Rappaport than for CARB. In both cases the donor radius remains close to the Roche lobe after the end of the mass transfer, but for Rappaport these two quantities are increasing, and for CARB they are decreasing. The analysis of these factors makes it clear that the evolution of the donor star and the binary system combine differently for each prescription of magnetic braking, which will be presented in more detail in the next section.

Although the $P_{\rm i} = 20$ d sequences behave similarly to the $P_{\rm i} = 100$ d sequences, they differ in the evolution of the orbital period before the RLOF. For $P_{\rm i} = 20$ d, the RLOF starts when $P = 18$ d in the case of Rappaport magnetic braking and when $P = 5.7$ d in the case of the CARB prescription (see Figure 13). This means that the entire mass transfer takes place with the stars much closer together when CARB magnetic braking is considered. This reinforces the fact that each magnetic braking prescription leads to a different shrinkage of the orbit, and therefore to a different evolutionary stage of the donor and orbital separation at the onset of the mass transfer. Both the radius of the donor star and the loss of mass by winds reach higher values (around 60 $R_\odot$ and 10^{-8} $M_\odot\,{\rm yr}^{-1}$, respectively) during mass transfer when Rappaport braking is considered. On the other hand, when CARB braking is considered, the radius of the donor star remains stable around 9 $R_\odot$ during mass transfer. In addition, the loss of mass by winds intensifies in this case and remains around $10^{-9.5}$ $M_\odot\,{\rm yr}^{-1}$ for about 1.5 Gyr. For both braking prescriptions, these two variables drop dramatically as soon as the RLOF ends. The consequence is that the mass transfer lasts about three times longer when the CARB prescription is considered.

For any $P_{\rm i}$, the CARB magnetic braking is more intense than the Rappaport prescription at a time when the mass transfer rate is maximum (first panel in Figure 14). In addition, for any initial orbital period, the CARB magnetic braking is less intense than the Rappaport prescription braking after mass transfer.

Here is an important caveat. The field configuration is at the heart of the most sensitive variable in the problem — the braking torque. There is one underlying assumption regarding the magnetic field: Equation 2.29 includes an undisturbed magnetic dipole scaling from the surface field to the Alfvén radius. The bipolar geometry for the magnetic field stimulates torque as it allows coupling over longer distances. In fact, there are several examples where the field geometry is far from a dipole field (the field in the solar corona for instance). And it is even more structured in less massive main sequence stars than it is in the Sun. Therefore, the CARB prescription represents a maximum efficiency scenario for braking when compared to more complex field geometries. As we will show throughout this work, the CARB prescription seems more realistic than the Skumanich and Rappaport, Verbunt & Joss (1983). However, precautions on the exact predicted quantities are advisable given that they are highly sensitive to the braking prescription. In this sense, a study on what happens with the expected field dwarf rotation period distribution if we compare Skumanich and Rappaport, Verbunt & Joss (1983) against CARB taking into account different field configurations seems necessary, which we will not evaluate in this work.

3.3 Orbital period evolution and period bifurcation

From this subsection onwards, we will study only sequences of models that consider the CARB magnetic braking. In this section, we expand our model grid using the CARB prescription of the magnetic braking into the initial orbital period parameter space.

Figure 15 – The evolution of the orbital period as a function of age for selected models between $2.7 \leqslant P_{\rm i}/{\rm d} \leqslant 300$. Initial orbital periods, from top to bottom: 300, 200, 150, 100, 70, 50, 40, 30, 25, 20, 15, 10, 9, 8, 7, 6, 5, 4, 3.5, 3.25, 3.2, 3 and 2.7 days. The bifurcation period occurs between 20 and 25 d. The extra-thick line marks the first convergent system. Above it, all systems are divergent. The beginning and end of the mass transfer are indicated by green triangles and pink squares, respectively. The colour of each line indicates the mass of the donor at the end of the mass transfer. The sequence shown in grey never becomes detached. The initial configuration is $M_{\rm d,i} = 1.0\ M_\odot$ and $M_{\rm a,i} = 1.4\ M_\odot$ for all sequences. The CARB magnetic braking is considered. Convergent binaries will continue to contract their orbits, forming a cataclysmic variable or an ultra-compact X-ray binary system. Divergent binaries will become relatively wide systems containing a recycled NS and a He or CO WD.

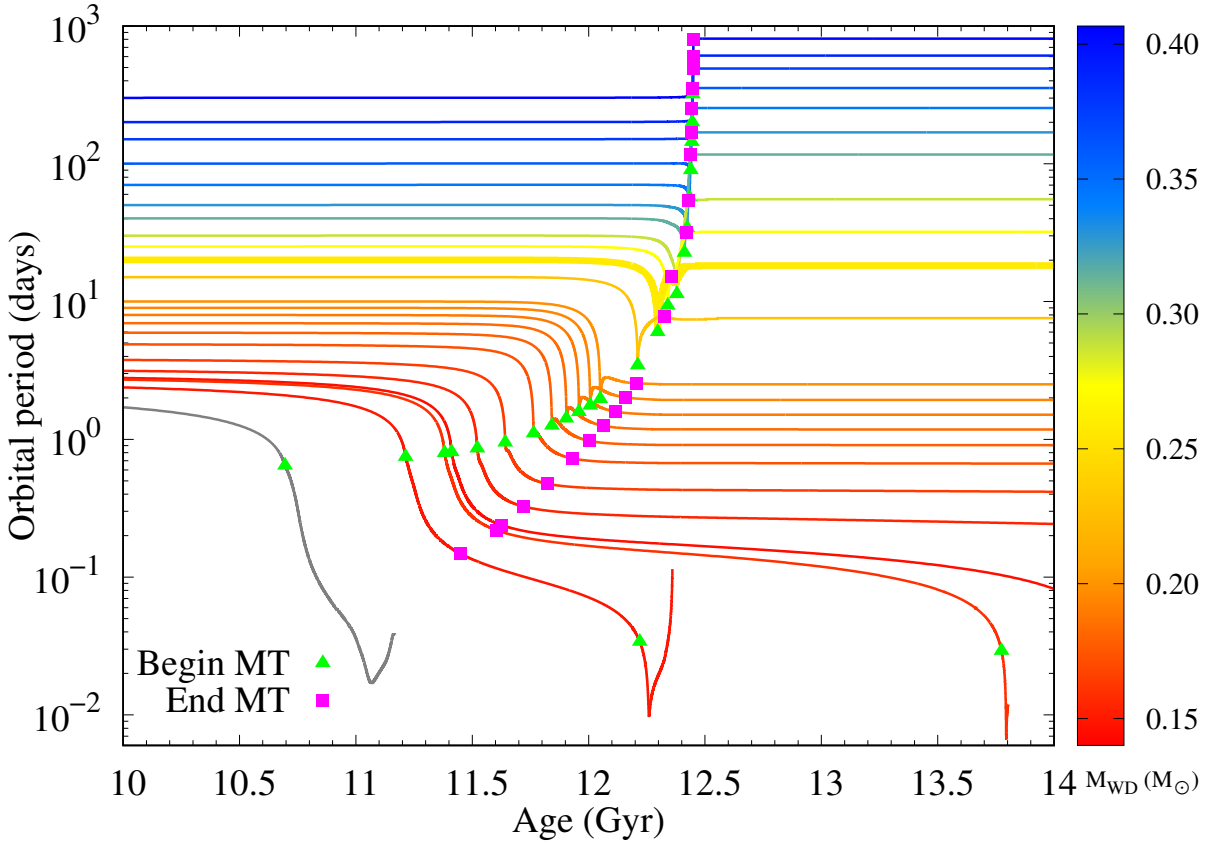

Figure 15 shows the evolution of the orbital period as a function of age for the CARB prescription, for initial masses $M_{\rm d,i} = 1.0\ M_\odot$ and $M_{\rm a,i} = 1.4\ M_\odot$. As the donor is now initially less massive (in the previous section we considered 1.2 $M_\odot$), its time in the main sequence is ~ 5.5 Gyr shorter, as well as the mass transfer occurring earlier. The

initial orbital periods range from 2.7 to 300 days. No model shows a significant orbital period change before a model age of 10 Gyr. The shorter the $P_{\rm i}$, the sooner the systems starts mass transfer. Up to this point, we are only discussing models without element diffusion. However, we draw attention to the fact that this does not affect the main results discussed so far, as diffusion has a small effect on the quantities studied.

Using the Rappaport magnetic braking, Istrate et al. (2016) found that the bifurcation period that separates the converging systems from the diverging ones occurs between 2.75 and 2.8 days if $M_{\rm d,i} = 1.0\ M_\odot$ and $M_{\rm a,i} = 1.4\ M_\odot$. Considering the CARB magnetic braking prescription of Van & Ivanova (2019), a $P_{\rm i} = 20$ d system with the same initial masses is still a convergent system. This corresponds to a 0.255 $M_\odot$ ELM white dwarf — the thickest line in Figure 15. Green triangles and pink squares mark the beginning and the end of mass transfer, respectively. We note that, for diverging systems, these points are so close to each other that we can barely distinguish between them.

We should emphasise that we define the lower limit to the initial orbital period of our model grid in such a way that our models are completely detached at a model age of 14 Gyr. That is, simulations considering even shorter initial orbital periods still have a small rate of mass transfer ($\dot{M} < 10^{-10}\ M_\odot\ {\rm yr}^{-1}$) at the final computed age, and therefore are not part of our model grid. In such cases, the donor star is expected to be completely consumed, i.e., transfer all its mass to the neutron star within a few billion years — or they may merge due to emission of gravitational radiation, similar to the known ultra-compact binaries (bottom three sequences in Figure 15).

The bifurcation period is shifted to longer ones (from 2.75–2.8 to 20–25 days) when the CARB magnetic braking is considered. Therefore the CARB magnetic braking allows us to get ELM WDs models with masses as low as 0.26 $M_\odot$ in converging binary systems even with initial orbital periods as long as 20 days, which is not possible with the magnetic braking of Rappaport. This is important because it shows that the entire extension of low-mass and ELM WDs in systems with pulsars can be obtained via RLOF evolution from a more uniform distribution of initial orbital periods (on a logarithmic scale), without favouring only the most massive He-WDs.

Although not the focus of this work, the upper and lower sequences in Figure 15 show that the use of CARB magnetic braking makes it possible to form ultra-compact X-ray binaries (UCXB) systems and wide-orbit binary millisecond pulsars, which is not possible with the Van, Ivanova & Heinke (2018) prescription,[5] as was shown by Chen et al. (2021).

At this point, we should consider whether there are new problems appearing with the use of CARB, since even the binaries with $P_{\rm i} = 20$ d can produce ELM WDs

[5] Do not confuse Van, Ivanova & Heinke (2018) with Van & Ivanova (2019). The first is a less elaborate version of the second (CARB), and has 3 free parameters. Still, much of the formalism is the same.

in millisecond pulsar systems. In fact, the analysis of Istrate, Tauris & Langer (2014) indicates with a high level of confidence that the distribution of orbital periods of observed recycled pulsars with He WD companions in the Galactic field is not compatible with the simulations that use the Rappaport prescription. They pointed out that the range of initial orbital periods that lead to the formation of this type of system must be expanded. In addition, the $P_{\rm i}$–$M_{\rm d,f}$ relation we found (see also section 3.4) is much closer to the expected log-normal orbital period distribution (Raghavan et al., 2010; Duchêne; Kraus, 2013; Tutukov; Cherepashchuk, 2020) than when using the Rappaport prescription. Thus, the results we found using the CARB prescription are encouraging, and a study comparing these results with simulations of binary population synthesis looks promising.

3.4 ELM WD companions to neutron stars

In this section, we expand our study of systems with point mass accretors of 1.4 $M_{\odot}$. All results presented in this section refer to sequences of models that take into account rotation and diffusion. The main properties of these models are presented in Appendix C: Table 5, Table 6, and Table 7 for $M_{\rm d,i} = 1.0\ M_{\odot}$; and Table 8, Table 9, and Table 10 for $M_{\rm d,i} = 1.2\ M_{\odot}$. We emphasise that in our models the accretor mass never exceeds the limit of the most massive neutron stars observed (e.g., Antoniadis et al., 2013; Cromartie et al., 2020; Fonseca et al., 2021).

3.4.1 Initial orbital period and final mass

In this subsection we show how the relation between the initial orbital period and the final white dwarf mass ($P_{\rm i}$–$M_{\rm d,f}$) is modified when we change the initial mass of the donor star and the metallicity. Considering that LMXBs are also found in relatively low metallicity environments (e.g., Cadelano et al., 2015; Rivera-Sandoval et al., 2015; Cromartie et al., 2020), we compute models with three different metallicities: $Z = 0.02$, 0.01, and 0.001.

In Figure 16 we depict the relation between the initial orbital period (y-axis) and the low-mass/ELM WD final mass (x-axis). Green squares, red triangles, and blue circles correspond to metallicities of $Z = 0.02$, 0.01, and 0.001, respectively. Dark colours represent 1.0 $M_{\odot}$ donors, and light colours are for 1.2 $M_{\odot}$ donors. For comparison, Istrate et al. (2016) LMXB models using the Rappaport, Verbunt & Joss (1983) magnetic braking prescription are shown in black "$\times$" signs. Our models also considering the Rappaport magnetic braking (see section 3.1) are shown in "+" black signs.

As we already mentioned in section 1.6, the empirical treatment of the magnetic braking by Rappaport, Verbunt & Joss (1983) leads to a fine-tuning of the order of a dozen minutes in the initial orbital period to reproduce the observed orbital periods of

Figure 16 – The relation between the initial orbital period and the ELM WD mass at the end of 14 Gyr evolution for different setups. Istrate et al. (2016) LMXB models using the Rappaport, Verbunt & Joss (1983) magnetic braking prescription are shown in black "×" signs. Our models also considering the Rappaport magnetic braking (see section 3.1) are shown in "+" black signs. Green squares, red triangles, and blue circles correspond to metallicities of $Z = 0.02$, 0.01, and 0.001, respectively. Dark colours represent 1.0 $M_\odot$ donors, and light colours are for 1.2 $M_\odot$ donors. All configurations take into account both rotation and diffusion and have $M_{\rm a,i} = 1.4$ $M_\odot$ and $\beta_{\rm mt} = 0.8$.

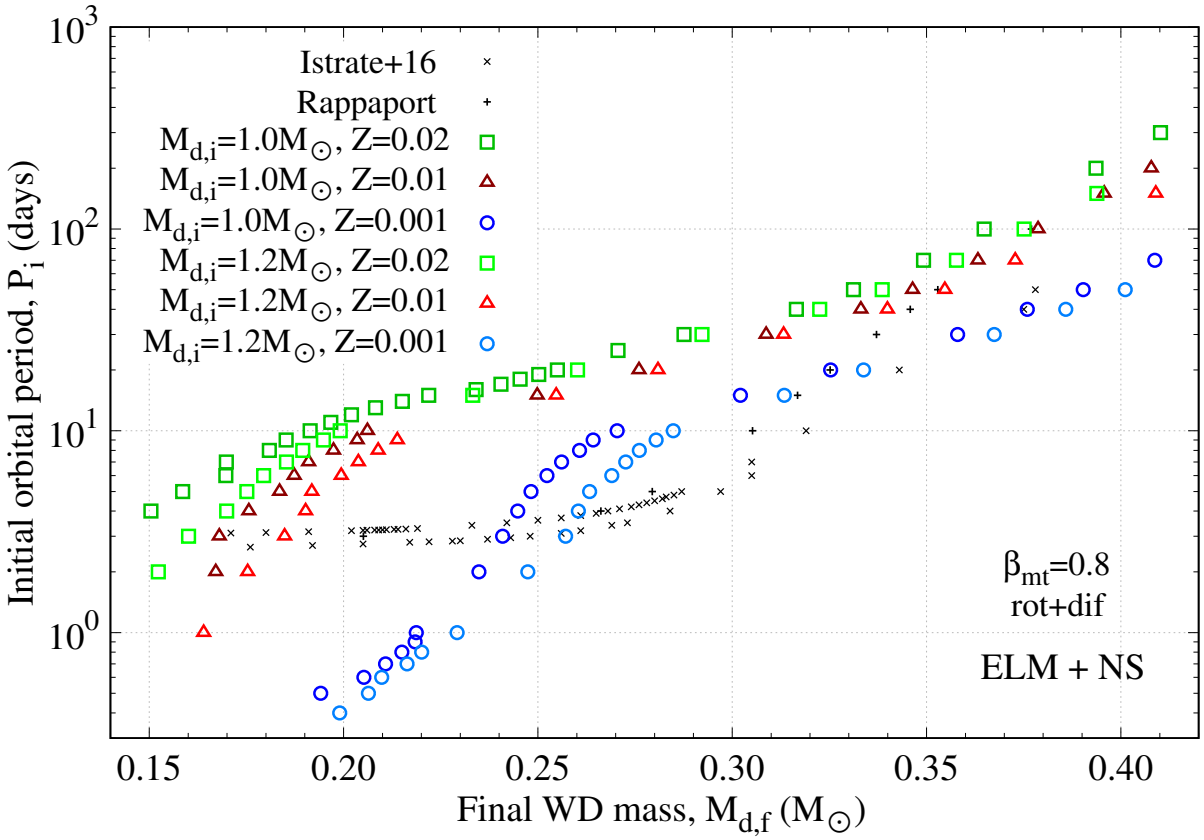

millisecond pulsars in compact ($2 < P/\mathrm{h} < 9$) binaries with He WD companions of mass $\lesssim 0.20$ $M_\odot$ (Istrate; Tauris; Langer, 2014).

Also importantly, Istrate, Tauris & Langer (2014) studied systems with donors initially as massive as 1.6 $M_\odot$ and found that the problem of fine-tuning persists, although it somewhat alters the occurrence of hydrogen shell flashes (Istrate et al., 2014).

It is notable that each prescription for magnetic braking has a completely different pattern in the $P_{\rm i}$–$M_{\rm d,f}$ plane. For final donor masses between 0.17 and 0.25 $M_\odot$, we can see in Figure 16 that the range of corresponding initial orbital periods is extremely narrow (between 2 and 4 days) for the prescription of Rappaport. On the other hand, when the CARB formulation is considered, the same range of final masses is obtained for initial orbital periods between 2 and 20 days. Thus, the use of the CARB prescription does not

require a fine-tuning of initial periods for the formation of ELM white dwarfs. Using initial masses $M_{\rm d,i} = 1.0\ M_\odot$ and $M_{\rm a,i} = 1.4\ M_\odot$, we were able to produce detached white dwarf systems within the range $4 \leqslant P_{\rm i}/{\rm d} \leqslant 300$, which corresponds to ELM and low-mass WDs with masses in the range $0.1504 \leqslant M_{\rm d,f}/M_\odot \leqslant 0.4102$.

Now we compare the case of high metallicity ($Z = 0.02$), where $M_{\rm d,i} = 1.0\ M_\odot$ against an initially more massive donor, with $1.2\ M_\odot$ (dark and light green squares in Figure 16, respectively). There is a systematic shift of the final mass towards larger masses, for the same initial period $P_{\rm i}$, in comparison to the case when the donor mass is $M_{\rm d,i} = 1.0\ M_\odot$. The difference in final masses increases for shorter initial orbital periods. For example, for $P_{\rm i} = 5$ d, we find the final donor mass to be $0.1751\ M_\odot$ if $M_{\rm d,i} = 1.2\ M_\odot$, but $0.1586\ M_\odot$ if $M_{\rm d,i} = 1.0\ M_\odot$. For $Z = 0.02$, all sequences undergoes hydrogen shell flashes, regardless of the initial mass of the donor.

Using a $M_{\rm d,i} = 1.2\ M_\odot$ donor instead of $1.0\ M_\odot$ does not significantly affect the binary evolution. The difference in the ELMs final mass is due to the more massive model being able to burn more H into He before mass transfer begins. For example, for the $P_{\rm i} = 20$ d case with $Z = 0.02$, this is reflected in the He core to be $0.0052\ M_\odot$ more massive for the initially more massive donor. This difference increases to $0.015\ M_\odot$ for $P_{\rm i} = 300$ d. Note that for this metallicity ($Z = 0.02$) and $M_{\rm d,i} = 1.0\ M_\odot$, because of the long main sequence lifetime (Renedo et al., 2010; Romero; Campos; Kepler, 2015), it is difficult to produce (pre-)ELMs in less than 10–11 Gyr. Thus, younger (pre-)ELMs require either lower metallicity or initially more massive donors.

Looking at other metallicities, the configurations with $M_{\rm d,i} = 1.2\ M_\odot$ always need a shorter initial orbital period in order to obtain an ELM WD with a given final mass. Similarly, for a given initial orbital period and donor mass, higher metallicities always lead to less massive ELM WDs. This difference is noticed at the end of the mass transfer epoch. That is, at the end of the mass transfer, donors with lower metallicity always have a mass a little larger than higher metallicity donors, given an initial donor mass and initial orbital period. This can be understood since the mass transfer rate depends on several factors related to the structure of the donor star, such as the pressure at the photosphere and at the inner Lagrange point, the radius, the Roche lobe radius, the mean molecular weight, the density in the donor's photosphere, and the effective temperature (see Equation 2.13 and Equation 2.15). These quantities, in turn, change with metallicity.

Finally, we note that the minimum mass obtained for the ELM WDs are different for each metallicity: around $M_{\rm d,f} = 0.151\ M_\odot$ for $Z = 0.02$, $M_{\rm d,f} = 0.165\ M_\odot$ for $Z = 0.01$, and $M_{\rm d,f} = 0.196\ M_\odot$ for $Z = 0.001$. Each of these cases represents the sequence with the shorter initial orbital period, for a given initial configuration. Sequences with a shorter initial orbital period will not detach. That is, for a even shorter initial orbital period, the mass transfer is maintained and the accretor star tends to consume all the mass of the

donor star before the model age of 14 Gyr. For $Z = 0.001$ and $M_{\rm d,i} = 1.2\ M_\odot$, however, the sequence with $P_{\rm i} = 0.3$ d cannot be started as there is RLOF already in the ZAMS (i.e., in the first model), and this would require adaptations in the mass transfer parameters.

3.4.2 Initial and final orbital period

Figure 17 – The relation between the final ($P_{\rm f}$) and the initial orbital period ($P_{\rm i}$). Green squares, red triangles, and blue circles correspond to metallicities of $Z = 0.02$, 0.01, and 0.001, respectively. Dark colours represent 1.0 $M_\odot$ donors, and light colours are for 1.2 $M_\odot$ donors. All configurations take into account both rotation and diffusion and have $M_{\rm a,i} = 1.4\ M_\odot$ and $\beta_{\rm mt} = 0.8$. The purple dot-dashed line serves as an indicator to distinguish between convergent and divergent systems (i.e., $P_{\rm f} = P_{\rm i}$). For comparison, Istrate et al. (2016) LMXB models using the Rappaport, Verbunt & Joss (1983) magnetic braking prescription are shown in black "×" signs. Our models also considering the Rappaport magnetic braking (see section 3.1) are shown in "+" black signs.

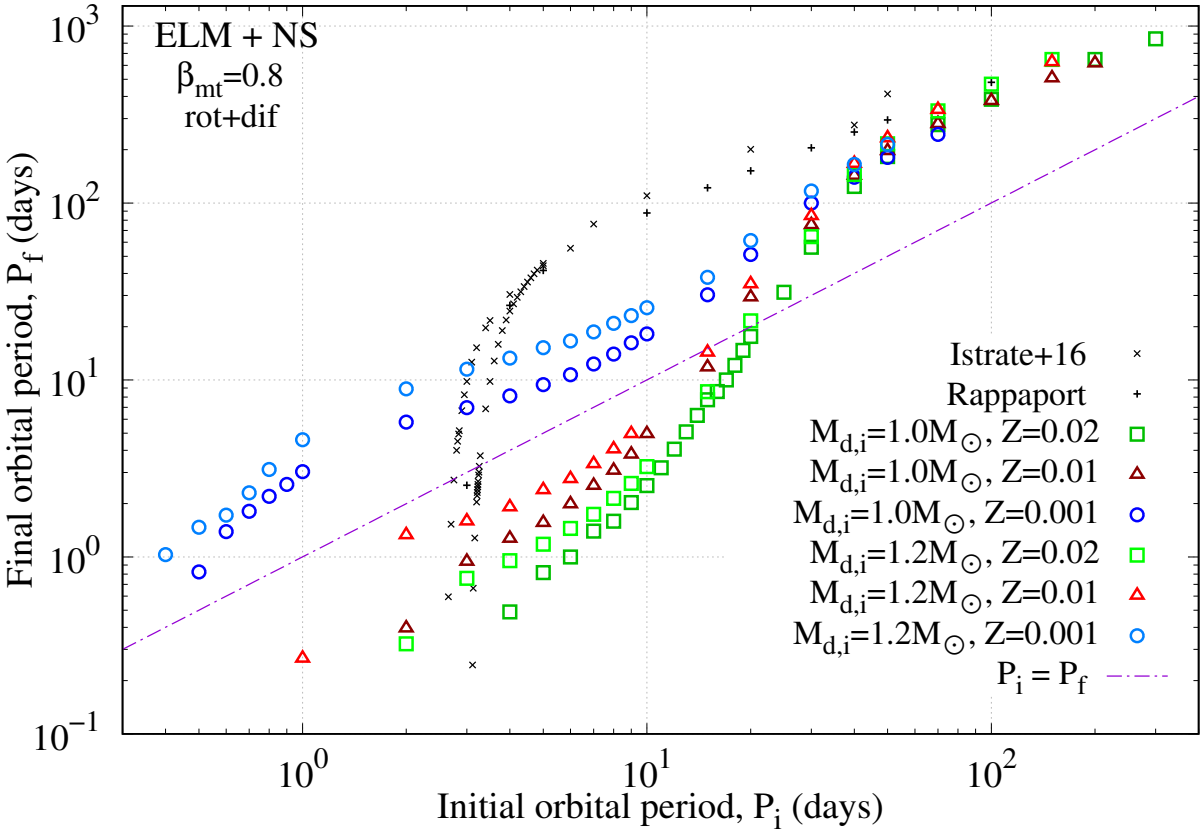

In Figure 17 we show the final orbital period (y-axis) as a function of the initial orbital period (x-axis), with all models taking into account rotation and diffusion. We set $\beta_{\rm mt} = 0.8$ and $M_{\rm a,i} = 1.4\ M_\odot$ in all models. We compare systems with different metallicities and accretor mass. Green squares, red triangles, and blue circles correspond to metallicities of $Z = 0.02$, 0.01, and 0.001, respectively. Dark colours represent 1.0 $M_\odot$ donors, and

light colours are for 1.2 $M_\odot$ donors. The purple dot-dashed line serves as an indicator to distinguish between convergent and divergent systems, i.e., $P_\mathrm{i} = P_\mathrm{f}$.

The division between convergent and divergent systems is around $P_\mathrm{i} \approx 20$ d for $Z = 0.02$, and $P_\mathrm{i} \approx 16$ d for $Z = 0.01$. For $Z = 0.001$, however, no system converges. All systems with $P_\mathrm{i} \gtrsim 30$ d will diverge, regardless of the initial metallicity and donor mass.

Figure 17 also shows that different metallicities and initial donor masses affects the P_i–P_f relation mainly in the short orbital period region, and above $P_\mathrm{i} = 30$ d all setups shown are practically indistinguishable. Furthermore, for a given initial orbital period and metallicity, a $M_\mathrm{d,i} = 1.0\ M_\odot$ donor always leads to a more compact system than the $M_\mathrm{d,i} = 1.2\ M_\odot$ donor case. This behaviour can be understood by analysing the intensity of magnetic braking and the evolution of the binary system in the pre-RLOF period. For example, for $P_\mathrm{i} = 5$ d, in the sequence with a less massive donor, the orbital period is about 0.5 days shorter by 0.1 Gyr before RLOF than in the case where the donor is more massive.

Finally, it is evident from Figure 17 that the P_i–P_f relation is also strongly affected when considering the CARB magnetic braking instead of the Rappaport one. The results from CARB and Rappaport agree only for systems with $P_\mathrm{f} \geqslant 500$ d, where magnetic braking has reduced impact (see section 3.2). For models that use Rappaport braking, convergent systems are obtained only for $P_\mathrm{i} \lesssim 3$ d. Furthermore, CARB braking predicts the existence of systems originated with $P_\mathrm{i} \leqslant 1$ d for low ($Z = 0.001$) and intermediate ($Z = 0.01$) metallicities, which does not occur in the case where Rappaport braking is considered.

3.4.3 Final mass and orbital period

The determination of relations between the orbital period and the mass of low-mass and ELM WDs in systems with neutron stars is of great interest because this relation can be used to examine the evolutionary channel for such a binary. These relations allow the estimation of the masses of ELM WDs from the orbital period of the binary system, which is, in general, easier to measure and independent of the T_eff and $\log(g)$ determinations.

The cores masses and radii of low-mass stars in the red giant branch follow a tight, well-known relation (Refsdal; Weigert, 1971; Webbink; Rappaport; Savonije, 1983; Joss; Rappaport; Lewis, 1987). For a red giant donor in a binary system, its radius is approximately equal to its Roche lobe radius during the mass transfer phase. The latter, in turn, depends on the binary separation and on the mass ratio. At the end of the mass transfer phase, the H-rich envelope is almost completely removed, and the final mass of the donor star is approximately the mass of its He core. Therefore, the final mass of a degenerate-core donor and the orbital period are correlated quantities.

Figure 18 – The relation between the final orbital period ($P_{\rm f}$) and the final donor mass ($M_{\rm d,f}$). Green squares, red triangles, and blue circles correspond to metallicities of $Z = 0.02$, 0.01, and 0.001, respectively. Dark colours represent 1.0 $M_{\odot}$ donors, and light colours are for 1.2 $M_{\odot}$ donors. All configurations take into account both rotation and diffusion and have $M_{\rm a,i} = 1.4\ M_{\odot}$ and $\beta_{\rm mt} = 0.8$.

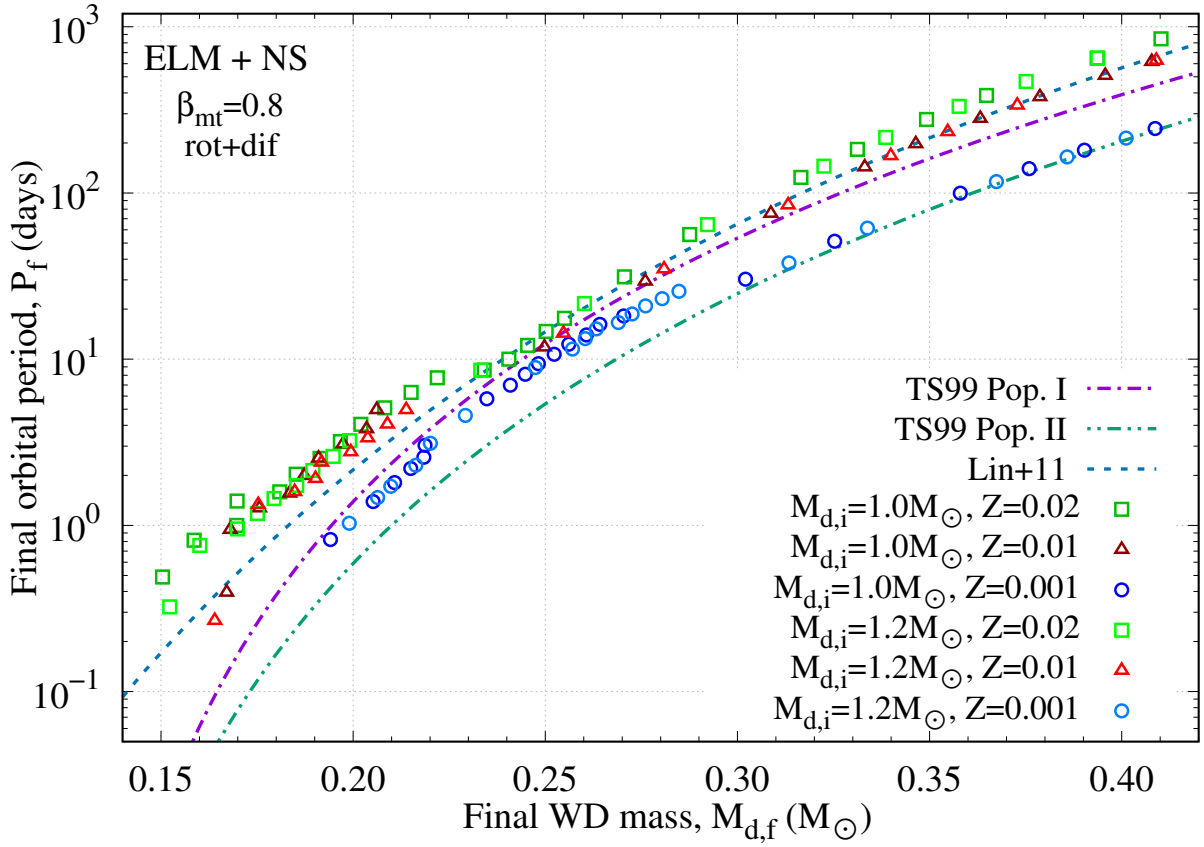

Figure 18 shows the final mass of donor vs. final orbital period ($M_{\rm d,f} - P_{\rm f}$) relation for all computed model sequences that takes into account rotation and diffusion and that have a 1.4 $M_{\odot}$ accretor. Although the CARB prescription for the magnetic braking completely changes the relation between $P_{\rm i}$ and $M_{\rm d,f}$, the relation between the final orbital period ($P_{\rm f}$) and final donor mass ($M_{\rm d,f}$) is much less affected when compared to the models calculated with the Rappaport magnetic braking formalism.

The use of the CARB prescription produces models that maintain agreement with other theoretical adjustments and also with observational data. Our results for high ($Z = 0.02$) and intermediate ($Z = 0.01$) metallicity are in good agreement with the Lin et al. (2011) theoretical fit, which is based on low and intermediate-mass X-ray binaries models computed with gravitational radiation, mass loss, and the Rappaport magnetic braking contributions to the angular momentum loss. For low metallicity ($Z = 0.001$), our results for $M_{\rm d,f} \gtrsim 0.30\ M_{\odot}$ are in excellent agreement with the fit from Tauris & Savonije (1999) for Population II stars (TS99 Pop. II in Figure 18). For $M_{\rm d,f} \lesssim 0.23\ M_{\odot}$, we found

orbital periods slightly longer than Lin et al. (2011), for a given mass. We note that this is probably due to the effects of diffusion, since our models without diffusion of elements (not shown in the figure) are much closer to the fit of Lin. The diffusion effects are less significant in the $M_{\rm d,f} - P_{\rm f}$ relation for $M_{\rm d,f} \gtrsim 0.24$. Between $M_{\rm d,f} = 0.23$ and 0.29 $M_{\odot}$, our models are in good agreement with both Lin et al. (2011) fit and Tauris & Savonije (1999) fit for Population I stars. It is important to note that these fits were made based on a broader initial donor masses distribution than we are considering here.

In Appendix D we present the same $M_{\rm d,f} - P_{\rm f}$ relation, but comparing the results of our theoretical models against observational data of pulsar + He WD systems.

3.5 ELM WD companions to massive white dwarfs

Although most of the first ELMs discovered had neutron stars as companions (van Kerkwijk; Bergeron; Kulkarni, 1996; van Kerkwijk et al., 2005), none of the ELMs in the clean sample of the ELM Survey was proven to have an neutron star as a companion (Brown et al., 2020; Athanasiadis et al., 2021a; Athanasiadis et al., 2021b). Motivated by this result, we next consider the accreting star as having $M_{\rm a,i} = 0.8\ M_{\odot}$, equivalent to a massive WD.

When modeling binary systems with accreting WDs, besides the change made in the accretor mass, several differences regarding the NS case are worth attention. With much shallower potential well, they differ when not considered as point sources. Possibly the most relevant difference for these models are nova explosions, whose frequency depends on $\dot{M}$ and the white dwarf mass itself. The accretor mass may even decrease with time due to nova shell ejections. Nova shells not only affect $\beta_{\rm mt}$, making its value highly uncertain and variable with time, but also carry and remove orbital angular momentum by dynamical friction.

The accretion efficiency on the surface of WDs is uncertain and depends heavily on chemical composition, surface temperature and accretion rate. For a massive WD, the simulations that best fit the observations suggest small ($\lesssim 50\%$) values for this parameter (Wu et al., 2017; Liu; Li, 2016; Piersanti; Tornambé; Yungelson, 2014; Piersanti; Yungelson; Tornambé, 2015; Wijnen; Zorotovic; Schreiber, 2015; Starrfield, 2014; Meng; Chen; Han, 2009). We chose here to keep $\beta_{\rm mt} = 0.8$ (i.e., accretion efficiency of 20%) to facilitate the comparison with the results from the previous section.

Taking all of the above caveats into account, in this section we will again consider the accretor as a point of mass, neglecting all effects of its non-zero size, nova explosions, time-varying accretion efficiency, chemical abundance in the atmosphere, etc.

The main properties of these models are presented in Appendix C: Table 11,

Table 12, and Table 13. We emphasise that in our models the accretor mass never exceeds the limit of the most massive white dwarfs observed (e.g., Cummings et al., 2016; Hollands et al., 2020; Pshirkov et al., 2020; Caiazzo et al., 2021; Kilic et al., 2021a; Miller et al., 2021b; Fleury; Caiazzo; Heyl, 2021).

3.5.1 Initial orbital period and final mass

In this subsection, we show how the relation between the initial orbital period and the final white dwarf mass ($P_{\rm i} - M_{\rm d,f}$) is modified when we change the initial mass of the accretor star to $M_{\rm a,i} = 0.8\ M_\odot$, consistent with a massive white dwarf.

In Figure 19 we depict the relation between the initial orbital period (y-axis) and the low-mass/ELM WD final mass (x-axis). Green squares, red triangles, and blue circles correspond to metallicities of $Z = 0.02$, 0.01, and 0.001, respectively. All configurations take into account both rotation and diffusion, and have $M_{\rm a,i} = 0.8\ M_\odot$ and $\beta_{\rm mt} = 0.8$. For comparison, corresponding models for NS accretors are also show in tiny symbols.

In this case, we find that there is a systematic shift towards final lower masses, given a $P_{\rm i}$, when compared to that the NS accretor case. The difference in mass is 0.0052 $M_\odot$ for $P_{\rm i} = 5$ d and reaches 0.0243 $M_\odot$ for $P_{\rm i} = 40$ d. This result can be easily understood, since the evolution of the orbital separation depends on the mass ratio (see subsection 1.4.1 and Equation 1.23). When the donor star has a more massive companion, a NS, the orbital separation between them tends to increase when the mass transfer begins. When the companion is less massive, a WD, the stars tend to get closer. As a consequence, the mass transfer episodes last longer with the WD accretor, which causes the donor star to end up with a smaller mass, given an initial orbital period. In addition, our results show that the maximum value of the mass transfer rate is higher in cases where the accreting star is less massive. The mass loss increases from $10^{-6.5}\ M_\odot\ {\rm yr}^{-1}$ to $10^{-4}\ M_\odot\ {\rm yr}^{-1}$ in some cases. Combined, these two facts explain the difference in the final mass of the donor stars when the mass of the accreting star changes.

Leaving aside the shift to low masses described in the previous paragraph, it is noteworthy that the way the points are distributed in the $P_{\rm i}$–$M_{\rm d,f}$ plane shown in Figure 19 is very similar between NS and WD accretors, for a given metallicity. That is, it still holds that higher metallicities lead to less massive ELM WDs, given an initial setup. This occurs because the duration of the RLOF is shorter for smaller metallicities. Furthermore, for $Z = 0.02$, the lowest ELM mass obtained is approximately the same, regardless of the accretor; but for $Z = 0.01$ we obtained $M_{\rm d,f} = 0.1560\ M_\odot$, considerably less than in the case of an NS accretor ($M_{\rm d,f} = 0.1671\ M_\odot$).

Moreover, in the low metallicity case, even for $P_{\rm i} = 1$ d we find it difficult to obtain ELMs with masses below 0.21 $M_\odot$. This is because the metallicity primarily affects nuclear

Figure 19 – The relation between the initial orbital period and the ELM WD mass at the end of 14 Gyr evolution for systems with massive white dwarf accretors. Green squares, red triangles, and blue circles correspond to metallicities of $Z = 0.02$, 0.01, and 0.001, respectively. Donors have 1.0 $M_\odot$ in all cases. All configurations take into account both rotation and diffusion, and have $M_{\rm a,i} = 0.8$ $M_\odot$ and $\beta_{\rm mt} = 0.8$. For comparison, corresponding models for NS accretors are also show in tiny symbols.

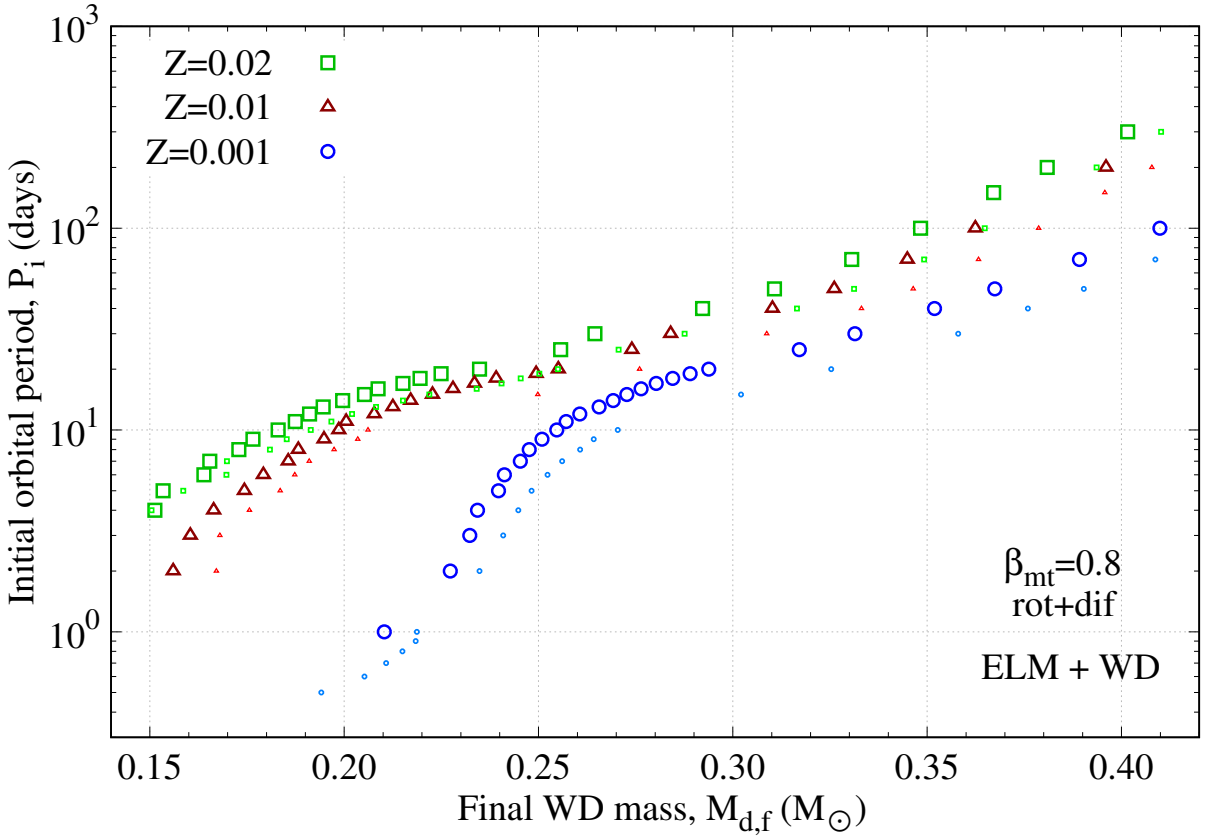

burning in the pre-RLOF evolution, but it also affects the occurrence of hydrogen shell flashes after the mass transfer since it changes the amount of hydrogen burning in the shell at the base of the envelope. For example, if $P_{\rm i} = 6$ d, we find two, three, or four hydrogen shell flashes, depending on metallicity. Although it is difficult to qualify all the effects of the change in metallicity in a single form, it is possible to conclude that it strongly affects the evolution of ELM WDs.

3.5.2 Initial and final orbital period

In Figure 20 we show the final orbital period (y-axis) as a function of the initial orbital period (x-axis) for binary systems containing ELM WDs and massive white dwarf accretors. All models take rotation and diffusion into account. We set $\beta_{\rm mt} = 0.8$ and $M_{\rm d,i} = 1.0$ $M_\odot$ to better compare the effects of changing other parameters. The purple dot-dashed line serves as an indicator to distinguish between convergent and divergent

systems. For comparison, corresponding models for NS accretors are also show in tiny symbols.

Figure 20 – The relation between the final ($P_{\rm f}$) and the initial orbital period ($P_{\rm i}$) for binary systems containing ELM WDs and massive white dwarf accretors. Green squares, red triangles, and blue circles correspond to metallicities of $Z = 0.02$, 0.01, and 0.001, respectively. All configurations take into account both rotation and diffusion and have $M_{\rm a,i} = 0.8\ M_{\odot}$ and $\beta_{\rm mt} = 0.8$. The purple dot-dashed line serves as an indicator to distinguish between convergent and divergent systems. For comparison, corresponding models for NS accretors are also show in tiny symbols.

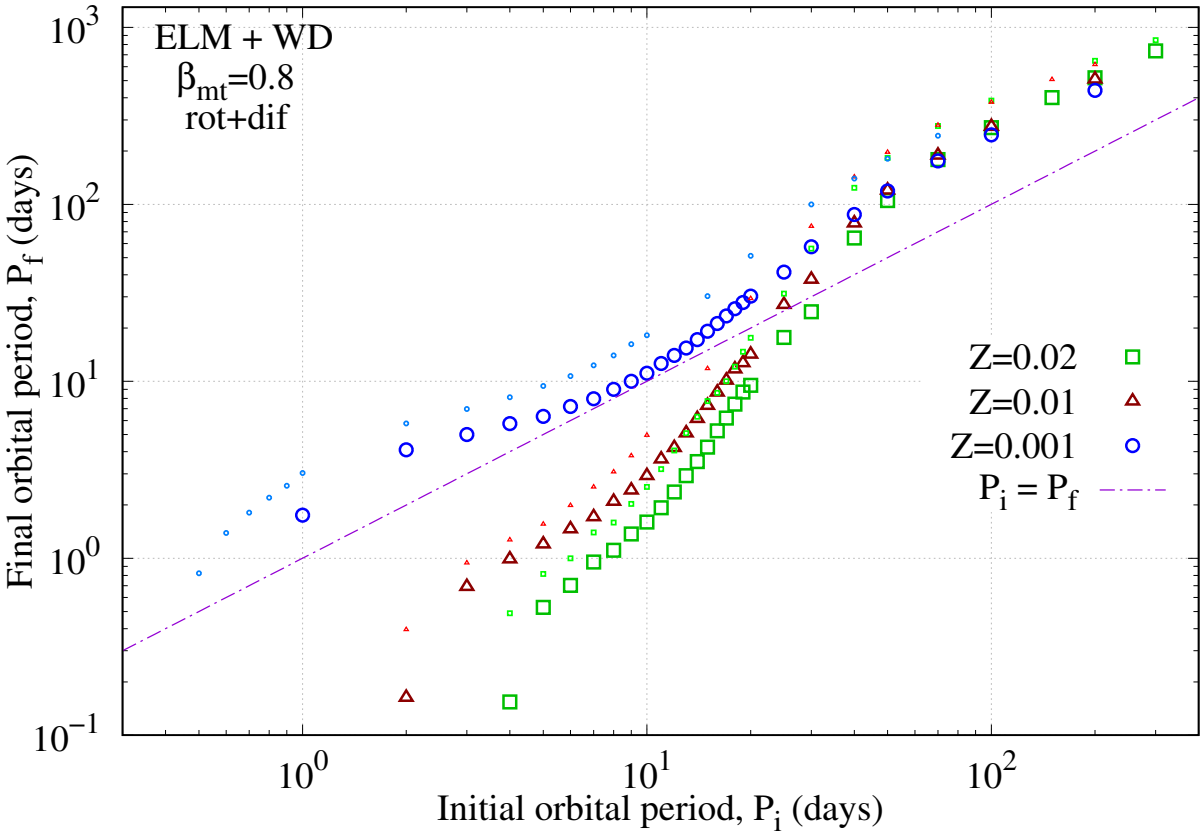

Again, in the case of massive WD accretors, the general behaviour is quite similar to that of NS accretors. The biggest difference is that, for a given initial orbital period and metallicity, systems with WD accretors have a shorter final orbital period. Once again, this is because the mass transfer phase is longer in these cases, and the loss of mass for a less massive star tends to decrease orbital separation.

In general, the division between convergent and divergent systems is around $P_{\rm i}$ = 20-30 d, i. e., all systems with $P_{\rm i} \gtrsim 35$ d will diverge, regardless of the initial configuration. The case of low metallicity ($Z = 0.001$, blue circles) is peculiar due to the fact that these systems will never be convergent. Still, we find that $P_{\rm f} \approx P_{\rm i}$ if $P_{\rm i} \approx 10$ d, which does not happen in the case where the accretor is an NS.

Note that almost all objects in the ELM Survey (Brown et al., 2020) — mainly by selection effects — have $P < 1$ d; probably have another WD as a companion; and are located in the Galactic disk, indicating high metallicity progenitors. Even more, such close systems are strong candidates to be observed in both gravitational waves and electromagnetic radiation (Li et al., 2020). Simple estimates of the amplitude, the characteristic strain, and the frequency of the gravitational waves emitted by our models at final age are described in Appendix B and presented in Appendix C.

We also found a clear relation between the final orbital period and the rotation rate of the white dwarf. Systems with a short initial orbital period present greater synchronisation with the orbit, at the end of the evolution. For example, for metallicities of $Z = 0.02$ and $Z = 0.01$, the lower-mass ELM WDs models present almost perfect synchronisation between the rotation of the star and the orbital period of the binary system. More generally, the ratio between the rotation rate of the ELM WD and the orbital period of the system assumes values between 1 and 0.1 for almost all short orbital period ($P_{\rm f} \lesssim 10$ d) systems. On the other hand, this ratio in $P_{\rm f} \gtrsim 50$ d systems is $P_{\rm rot}/P_{\rm f} \simeq 0.1$–$10^{-3}$, indicating white dwarfs rotating more slowly than the orbital period. For systems between these two period intervals, the exact behaviour depends on masses and metallicity. Looking at the $P_{\rm i} - P_{\rm f}$ diagram in Figure 20, we notice that this value of the initial orbital period (20–30 d) coincides with the bifurcation period. Thus, convergent systems are more likely to have synchronisation between the rotation of the white dwarf and the orbit. This occurrence might be a tool to observationally estimate the convergence period. Even for systems with a shorter initial orbital period, we find that from ∼1 Gyr after the end of RLOF onwards, the time needed for synchronisation exceeds the age of the Universe. This means that we should not expect tidal forces to change the rotation of the newly formed low-mass/ELM WDs. Important to note, this analysis holds for both WD and NS accretors.

3.5.3 Final mass and orbital period

Figure 21 shows the final mass of donor vs. final orbital period ($M_{\rm d,f} - P_{\rm f}$) relation for all computed model sequences that takes into account rotation and diffusion and that have a 0.8 $M_\odot$ accretor. Green squares, red triangles, and blue circles correspond to metallicities of $Z = 0.02$, 0.01, and 0.001, respectively. All configurations take into account both rotation and diffusion and have initially 1.0 $M_\odot$ donors and 0.8 $M_\odot$ accretors.

An important result is that the relation between the orbital period and the mass of ELM WDs is not significantly affected when we consider a massive-WD accretor instead of an NS (i.e., comparing Figure 21 with Figure 18). This is in line with the results found by De Vito & Benvenuto (2010), De Vito & Benvenuto (2012). It still holds that for low metallicities ($Z = 0.001$) always lead to closer systems, for a given mass; and intermediate

Figure 21 – The relation between the final orbital period ($P_{\rm f}$) and the final donor mass ($M_{\rm d,f}$). Green squares, red triangles, and blue circles correspond to metallicities of $Z = 0.02$, 0.01, and 0.001, respectively. All configurations take into account both rotation and diffusion and have $M_{\rm d,i} = 1.0\ M_{\odot}$, $M_{\rm a,i} = 0.8\ M_{\odot}$, and $\beta_{\rm mt} = 0.8$. Observational data: ELM WDs from the ELM Survey (Brown et al., 2020) are shown in black asterisks, and the confirmed ELMs compiled by Pelisoli & Vos (2019) are shown in black dotted-circles.

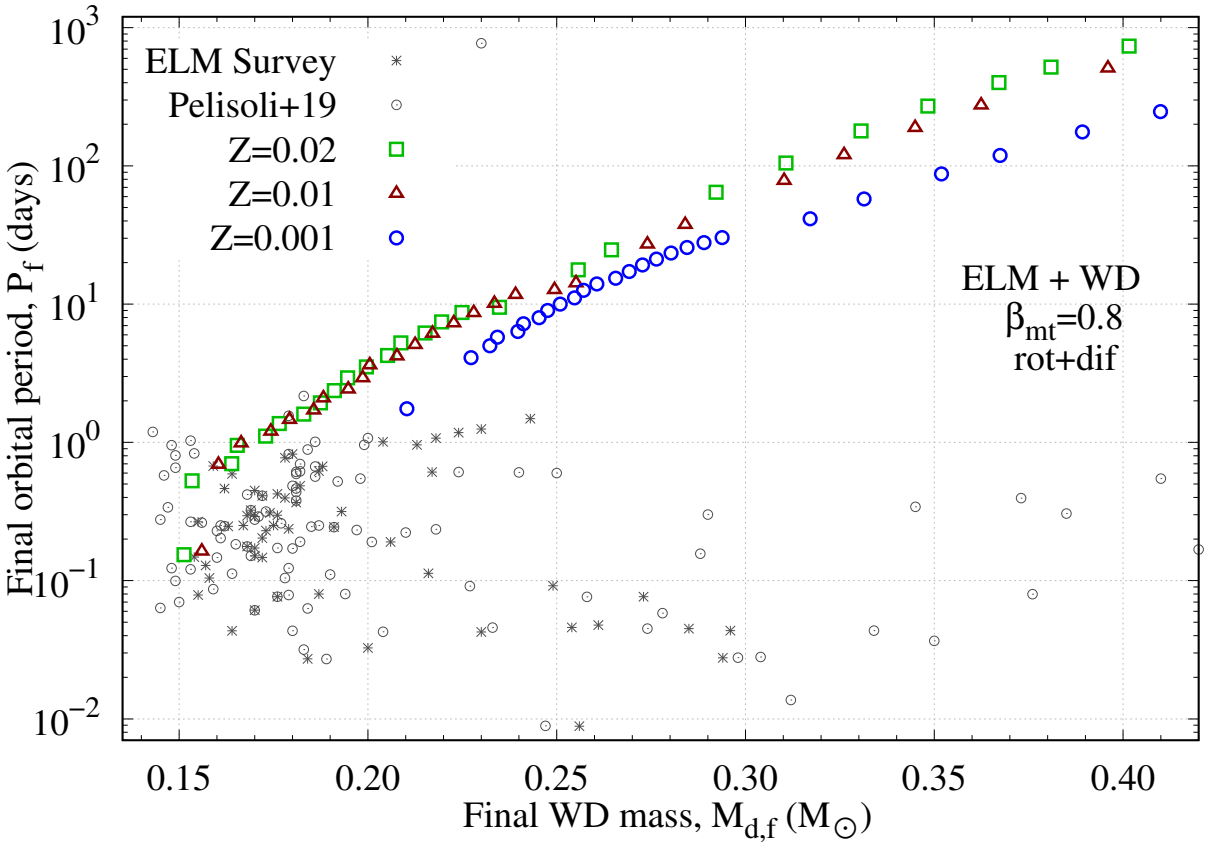

($Z = 0.01$) and high metallicities ($Z = 0.02$) present very similar results. In addition, it is known that different initial donor masses also modifies this relation (Istrate; Tauris; Langer, 2014), which can also be noticed by analysing the Figure 18. However, it should be noted that even considering all these variations (initial donor mass and metallicity), the theoretical models occupy only a small part of the parameter space shown in Figure 21.

Considering this, we also show in Figure 21 observational data, which include the ELM WDs from the ELM Survey (black asterisks, Brown et al., 2020), and the list of confirmed ELMs compiled by Pelisoli; Vos, 2019 (black dotted-circles). It is clear that the observational data is widely dispersed, moving away from the theoretical RLOF models for both sides of the diagram. This seems to indicate that objects that are not in the region of the quoted theoretical models should have been formed via evolutionary channels other than stable mass transfer, such as common envelope, mergers, triple systems, etc.

Of course, the model also has its limitations and may not be a perfect representation of the physical mechanism considered. However, we emphasise that, in the $M_{\rm d,f} - P_{\rm f}$ plane, the results obtained for the Rappaport and for the CARB prescriptions are very similar. Furthermore, different metallicities, initial masses, and accretion efficiencies only slightly affect the results, supporting the idea that the distribution of results in the $M_{\rm d,f} - P_{\rm f}$ plane does not have a strong dependence on the prescription for the magnetic braking used. In summary, we do not see evidence that adjustments in the initial parameters would be able to explain the ELM WDs of mass $M_{\rm d,f} \gtrsim 0.25\ M_\odot$ formed via RLOF in binary systems with orbital periods $P_{\rm f} \lesssim 1$ d.

On the other hand, the fact that the different theoretical models present small dispersion can be used to indicate the stable mass transfer as the formation channel of the systems that fit well to the curve, as well as a reliable estimate of the mass of ELM WDs from the orbital period measurements. More generally, this reinforces the idea that the formation of WD in binary interacting systems is an extremely degenerate phenomenon, with no univocality between the currently observed systems and their respective progenitor systems.

3.5.4 Effects of different accretion efficiencies

When we modify the efficiency in the accretion of matter on the surface of the white dwarf, the results are different for different initial orbital periods, although the overall results are that the ELM WD final mass hardly changes. For $P_{\rm i} \geqslant 50$ d, low efficiency in accretion (20% instead of 70%) results in ELMs with only a slightly higher final mass ($\sim$ 0.0015–0.0045 $M_\odot$), for a given $P_{\rm i}$. However, the effect is reversed for the interval $10 \leqslant P_{\rm i}/{\rm d} \leqslant 30$. This can be understood by the fact that the peak in the mass transfer rate and the duration of the mass transfer behave differently in this case. For all $P_{\rm i}$ we found that the peak in the mass transfer rate is higher if the mass accretion efficiency in the WD is lower. On the other hand, the duration of the mass transfer depends on the $P_{\rm i}$: for short $P_{\rm i}$, it lasts longer when $\beta_{\rm mt}$ is smaller; but it lasts less time in the case of large $P_{\rm i}$ and same $\beta_{\rm mt}$. Combined, these two facts explain the difference in the final mass of the donor stars when we modify the mass transfer efficiency to the accreting star.

In a more extreme case, we make a comparison between $\beta_{\rm mt} = 0$ and $\beta_{\rm mt} = 1$. If $P_{\rm i} = 5$ d, we find that the final mass is equal (0.1518 $M_\odot$) in both cases, as a different number of hydrogen shell flashes occurs in each sequence of models. On the other hand, the final orbital period is $P_{\rm f} = 0.612$ d if $\beta_{\rm mt} = 0$ and $P_{\rm f} = 0.520$ d if $\beta_{\rm mt} = 1$.

Moreover, for $P_{\rm i} = 50$ d, we find $P_{\rm f} = 96.2$ d and $M_{\rm d,f} = 0.3075\ M_\odot$ if $\beta_{\rm mt} = 0$; and $P_{\rm f} = 105.8$ d and $M_{\rm d,f} = 0.3108\ M_\odot$ if $\beta_{\rm mt} = 1$.

Therefore, we conclude that different accretion efficiencies have only a very small

effect on the final orbital period (<5–8%) and final mass of the ELM WDs (<0.003 $M_{\odot}$) in our models. However, this parameter is the main one to regulate the final mass of the accretor.

3.6 Chemical profiles

Figure 22 shows the chemical profiles in terms of the outer mass fraction at the terminal age for different initial configurations. Hydrogen (dashed lines) and helium (solid lines) mass fractions (y-axis) are normalised to one. The outer mass fractions (x-axis) are in log-scale, with the zero in the scale representing the centre of the model. All models have $M_{\rm d,i} = 1.0\ M_{\odot}$ and take into account rotation and diffusion of elements.

The top and the middle panels compare models with the same metallicity (Z=0.02), but that have evolved in companion to different accretors, a NS (top panel) or a massive WD (middle panel). Note that for each of the lines in the plot, the initial mass of the accreting star is the only modified parameter. Also note that, in the top and middle panels, although the initial orbital periods are the same, the final masses are not. This indicates that changes in the dynamics of mass transfer can strongly modify the final chemical profile. Obviously, this occurs indirectly, as the intermediate steps are the different masses of the donors after the mass transfer phase and also the number of hydrogen shell flashes. At the limit of the lowest initial orbital period, and therefore less massive ELM WDs, we find that considering the accreting star as a massive WD decreases the number of hydrogen shell flashes during the evolution of the ELM WD. This, in turn, modifies the chemical profile, since in addition to going through a phase of intense burning of H into He at the base of the envelope, the donor loses part of its outer layers again in another episode of RLOF.

Taking into account the caveats described above, if we compare two models that have suffered the same number of hydrogen shell flashes, the chemical profiles are similar. More interestingly, in the case of a lower initial orbital period of the middle panel ($P_{\rm i} = 4$ d, black line), no hydrogen shell flash occurs. This leads to a very different chemical profile than when one or more hydrogen shell flashes occur. In this case, hydrogen and helium are already well mixed in the outer four per cent in mass of the star. When hydrogen shell flashes occur, they are only mixed in the outer 0.01 per cent.

The non-flashing model is the only one with a large hydrogen envelope, reaching up to 3% of the total mass of the model. The envelopes of the flashing models, on the other hand, hardly sums 0.1%. Another striking fact of systems that do not suffer from hydrogen shell flashes is that the surface of the models can have a considerable amount of helium, about 10 per cent.

Finally, in the lower panel we see that for low metallicity ($Z = 0.001$), the occurrence

Figure 22 – Chemical profiles in terms of the outer mass fraction at terminal age (14 Gyr) on the cooling sequence for different initial configuration. The top and middle panels show models with initial metallicity $Z = 0.02$, and the bottom panel considers $Z = 0.001$. The top panel considers a neutron star as an accretor, and the middle and bottom panels a massive white dwarf. In each panel, we chose some key initial orbital periods (P_i) to show. The number of hydrogen shell flashes (#HSF) suffered during the whole evolution is also indicated. Rotation and diffusion of elements are considered in all models.

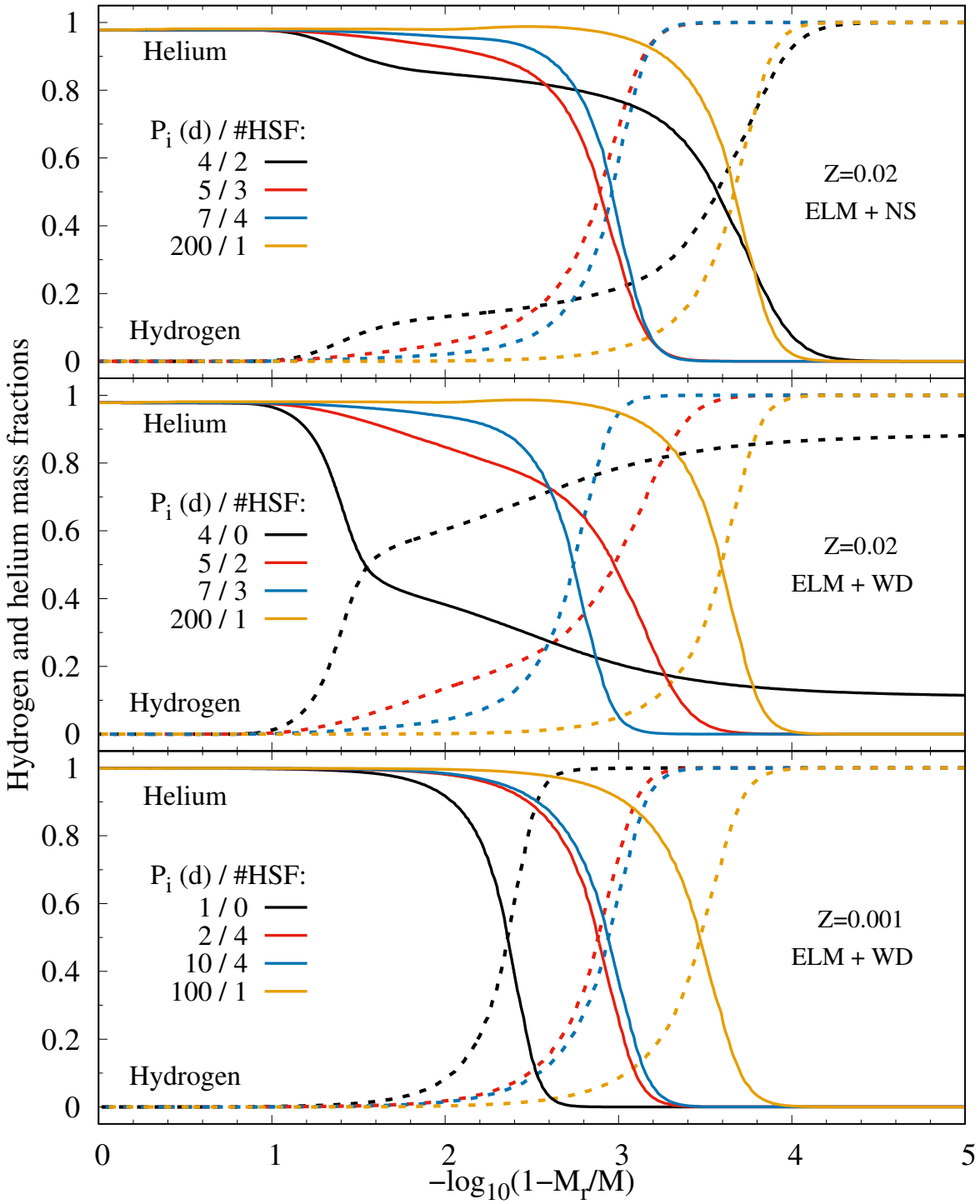

(or not) of hydrogen shell flashes has less influence on the chemical profile. As a general rule, less massive ELM WDs have a greater amount of hydrogen on the surface. The transition between the hydrogen- and the helium-dominated regions occurs around $M_r/M = 0.996019$ for the less massive model ($M_{\rm d,f} \approx 0.21\ M_\odot$) and around $M_r/M = 0.999684$ for the more massive one ($M_{\rm d,f} \approx 0.40\ M_\odot$).

At this point, we might be wondering how close the low metallicity, $P_{\rm i} = 1$ d model (bottom panel of Figure 22, black line) is to undergo a hydrogen shell flash. In fact, the answer is not simple and must be analysed on a case-by-case basis. This is because there are two conditions for a flash to occur: i) the shell must be thin enough to ensure that the pressure reaction during expansion remains sufficiently weak so that the temperature in the shell continues to grow, ii) but it must be not too thin in order for the heat perturbation to remain contained in the shell (see discussion in Gautschy, 2013). Let us use two cases from the bottom panel (Figure 22) as an example. If we compare the models of $P_{\rm i} = 1$ d and $P_{\rm i} = 2$ d at the maximum effective temperature right after the RLOF, we will find that, in fact, the hydrogen envelope of the $P_{\rm i} = 1$ d model is more massive (0.011 against 0.009 $M_\odot$). This is because the $P_{\rm i} = 2$ d model had more time to burn H into He before the mass loss begin. Thus, great caution is needed when comparing the initial orbital period with the envelope mass and the number of hydrogen shell flashes.

3.7 Kiel diagram and comparison with observational data

3.7.1 General remarks on different metallicities and accretor masses

Figure 23 shows the Kiel diagram, i.e., the $T_{\rm eff} - \log(g)$ plane, featuring selected evolutionary tracks and observational data of confirmed or candidate ELM WDs from different surveys. Evolutionary tracks are for $P_{\rm i} = 5$ d (black dotted lines), 15 d (orange solid lines) and 100 d (red dashed lines). Each panel compares a different initial configuration regarding the nature of the accreting star and the metallicity. The top and middle panels show models with initial metallicity Z=0.02, and the bottom panel considers Z=0.001. The top panel considers a neutron star as an accretor, and the middle and bottom panels a massive white dwarf. $M_{\rm d,i} = 1.0\ M_\odot$ in all cases. Observational data: ELM WDs candidates from the sdA selection (green multiplication signs, Pelisoli; Kepler; Koester, 2018a; Pelisoli et al., 2018b; Pelisoli et al., 2018c); ELM WDs candidates from the Gaia DR2 (blue dots, Pelisoli; Vos, 2019); clean sample of the ELM Survey plus other confirmed ELM WDs (purple plus signs, Brown et al., 2020, Pelisoli; Vos, 2019); BLAPs (dark blue triangles, Pietrukowicz et al., 2017). Gaia DR2 data were corrected by reddening following Gentile Fusillo et al. (2019). We draw attention to the fact that these data have great uncertainty, especially in the log (g) determination of the sdA stars. For example, Pelisoli et al. (2018b) points out an uncertainty of 5% for $T_{\rm eff}$ and 0.5 dex for log (g).

Figure 23 – Kiel diagram featuring selected evolutionary tracks and observational data. Different metallicities and initial accretor mass are compared in each panel, which one has three evolutionary tracks. See text for a complete description.

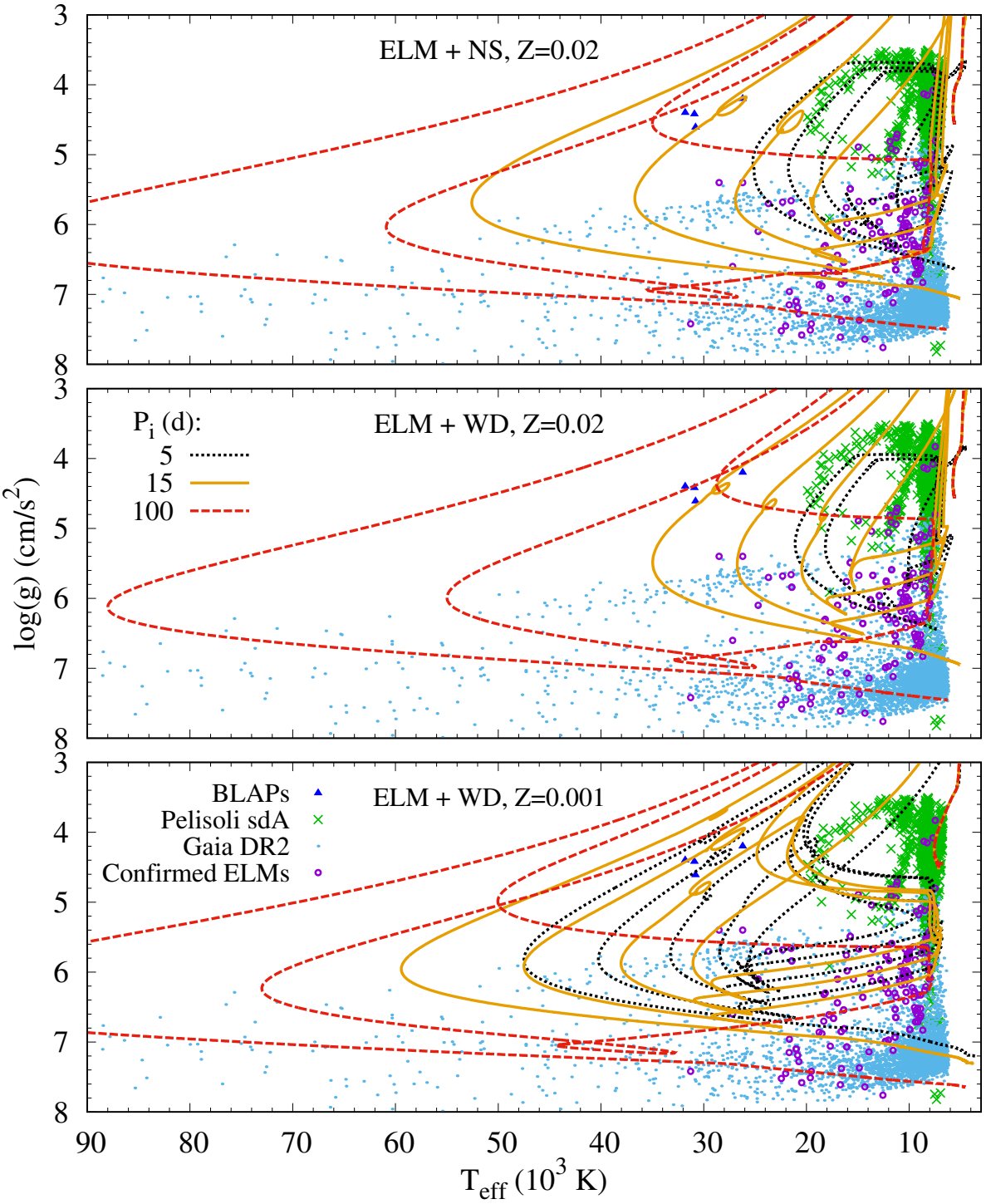

In a Kiel diagram (KD), the ZAMS is in the upper-right corner of the plot, i.e., in the region of low effective temperature and low surface gravity. From the ZAMS until the start of the RLOF, all models move towards even lower surface gravities and effective temperatures in the KD. During mass transfer, donors get hotter and also with higher

surface gravities. Counterclockwise loops indicate hydrogen shell flashes. At the end of the cooling track, models are typically around $\log(g) \sim 7$ and $T_{\rm eff} \sim 10$ kK. All models shown take into account rotation and diffusion of elements. We find that when elements diffusion is taken into account, hydrogen shell flashes take place in almost all pre-ELM WDs, regardless of specific mass ranges. The only exceptions are some models of the lowest mass for each initial setup.

Both the top and the middle panels show models with $Z = 0.02$, but they differ regarding the nature of the accretor: NS and massive WD, respectively. For $P_{\rm i} = 5$ d, despite both configurations ending up as ELM WDs of very similar masses ($M_{\rm d,f} \approx 0.15\ M_{\odot}$), the evolutionary tracks are slightly different. In the case where the companion is a NS, the pre-ELM reaches lower $\log(g)$ during hydrogen shell flashes. In addition, the number of hydrogen shell flashes is different in each case: three if the companion is a NS and two if it is a massive WD. In this case we also find that the effective temperature at the end of the evolution is about 1800 K cooler when the accretor is a NS. This is because the extra hydrogen shell flash decreases the amount of hydrogen in the envelope, accelerating cooling. In the case where $P_{\rm i} = 15$ d, the difference in the final masses increases: $M_{\rm d,f} = 0.221\ M_{\odot}$ if the accretor is a NS and $M_{\rm d,f} = 0.205\ M_{\odot}$ if it is a massive WD. On the other hand, the number of hydrogen shell flashes is the same (four), and the final temperatures are practically identical (≈ 5040 K).

In Figure 23 we also compare the cases where the accreting star is a massive WD but the metallicity is different, $Z = 0.02$ (middle panel) and $Z = 0.001$ (bottom panel). For $Z = 0.001$, we note that the evolutionary tracks avoid the upper right region of the graph during the hydrogen shell flash inflation epoch. In fact, in many cases, RLOF does not happen during hydrogen shell flashes in the case of low metallicity. In other words, in cases of low metallicity, the increase in luminosity during hydrogen shell flashes occurs in a way that the models increase the radius less (and therefore have a higher temperature) when compared to models with higher metallicity. Also, the low metallicity case is clearly the one that the models can cool to lower temperatures in the same 14 Gyr. As we have already pointed out, this is directly linked to the fact that low metallicity stars leave the main sequence much faster. In the bottom panel, the three ELM WDs models finish the evolution with masses 0.23, 0.27 and 0.40 $M_{\odot}$, with $T_{\rm eff} = 3475$, 3703 and 4537 K, respectively.

Although only three evolutionary tracks are represented on each panel of Figure 23, note that they fit very well the ELM Survey objects (purple "+" signs), either at the final cooling epoch or before a hydrogen shell flash.

From Figure 23 we can see that these tracks pass through (when in the pre-ELM stage) the region of ELM candidates marked as "Pelisoli sdA" (green "×" signs) — subdwarf stars with spectral type A (Pelisoli; Kepler; Koester, 2018a; Pelisoli et al., 2018b; Pelisoli

et al., 2018c). This corresponds to the highly populated region around $T_{\rm eff} \approx 8,000$ K and $3.5 \lesssim \log(g) \lesssim 5$. In the cooling epoch, near the terminal age, our tracks fit well the majority of the confirmed ELM WDs (Brown et al., 2020; Pelisoli; Vos, 2019) in the range $8,800 \lesssim T_{\rm eff}/{\rm K} \lesssim 21,500$ and $5.5 \lesssim \log(g) \lesssim 7.1$.

Tracks corresponding to the most massive models, i.e., longer initial orbital period, in this figure end the cooling epoch with $\log(g) > 7$, matching the most populated area of ELM candidates from the Gaia DR2 mission (light blue "·" signs, Pelisoli; Vos, 2019). These more massive models also pass through the region of the BLAPs (dark blue "▲" signs), which are extremely rare blue pulsators characterised by light variations with periods in the range of 20–40 min and amplitudes of 0.2–0.4 mag in the optical pass-bands (Pietrukowicz et al., 2017). They have $T_{\rm eff} \approx 30$ kK and their estimated masses are $M \approx 0.30$–$0.35\ M_{\odot}$ (e.g., Romero et al., 2018, Byrne; Jeffery, 2018). In our models, this mass range corresponds to $20{\rm d} \lesssim P_{\rm i} \lesssim 100{\rm d}$, depending on the metallicity.

The occurrence of hydrogen shell flashes is related to the size of the hydrogen-burning shell at the base of the envelope. When combined with temperatures of the order of 1.5×10^7 K, this leads to the CNO burning becoming dominant and a phase of unstable nuclear burning. Moreover, a large hydrogen envelope makes it difficult for the star to cool, affecting the cooling time.

Physically, hydrogen shell flashes are characterised by a period of expansion followed by a period of high $T_{\rm eff}$. These maxima in $T_{\rm eff}$ occur approximately in the range $5 \lesssim \log(g) \lesssim 6$. In the Kiel diagram (and also in the HR diagram), each hydrogen shell flash is shaped like a loop, always counterclockwise. Notably, the left side of the loop ($\log(g)$ increasing, higher $T_{\rm eff}$) occurs on much longer timescales than the right side of the loop ($\log(g)$ decreasing, lower $T_{\rm eff}$). See also Figure 24. Especially for low metallicities, unstable hydrogen burning via pp nuclear reactions can also occur, characterised by smaller loops during the main loop (see Serenelli et al., 2002 for more details).

During each flash, some models may reach 30–100 kK. This is the region of the observed sdBs and sdOs, subdwarf stars with spectral type B and O, respectively, understood as central He burning stars (Heber, 2009; Heber, 2016). But i) the observational data, using Gaia astrometry, shows the mass distribution of hot subdwarf extends down to at least 0.3 $M_{\odot}$ (Schneider et al., 2019); ii) the discovery of an ultra-compact hot subdwarf binary as part of the Zwicky Transient Facility survey (Kupfer et al., 2020); iii) the discovery of an eclipsing binary containing a cool, low mass subdwarf star ($M = 0.1501\ M_{\odot}$) with a white dwarf companion (Rebassa-Mansergas et al., 2019); and iv) the bright low-mass sdB/pre-ELM WD with unusual position in the KD ($T_{\rm eff} = 21,500$ K and $\log(g) = 5.66$, Latour et al., 2016) point to possible different evolutionary channels. That is, our (pre-)ELM WDs models have several points in compatibility with these peculiar subdwarfs; and since we cannot be sure about the core composition of the subdwarfs, we point out

that more detailed studies in this regard seem to be promising (see also Chen et al., 2013).

3.7.2 Halo objects?

We should emphasise that hydrogen shell flashes are very rapid phenomena (∼500 Myr in total, a little more than the thermal timescale) and a much longer time must be spent in the cooling track (∼1.5 Gyr if $Z = 0.02$, ∼9 Gyr if $Z = 0.001$). Still, the time spent during the flash is not negligible, affecting the estimated cooling time of the WDs (e.g., Althaus; Miller Bertolami; Córsico, 2013).

In Figure 24, we present nine evolutionary tracks in the Kiel diagram, now focusing on the low $T_{\rm eff}$ region and showing points every 30 Myr. Three key models are presented for each metallicity, where the symbols and colours are distinct for each subset: green squares ($Z = 0.02$), red triangles ($Z = 0.01$), blue circles ($Z = 0.001$). Confirmed ELM WDs from Brown et al. (2020), Pelisoli & Vos (2019) are shown in orange crosses.

In addition to the $P_{\rm i} = 100$ d models, for each metallicity we show in Figure 24 the two models with the shortest initial orbital period. Note that the shortest $P_{\rm i}$ model of each metallicity does not undergo hydrogen shell flashes. These three models reach very similar $T_{\rm eff}$ (between 8000 and 8300 K) at final age (14 Gyr), but their surface gravities at this age differ by a factor greater than twenty.

Although for each metallicity the evolutionary tracks do not cross each other in the cooling epoch, when considering different metallicities it is not possible to relate a final mass with only a single initial configuration. As a general rule, the lower the initial metallicity, the cooler the ELM WD will be at the end of the cooling track, for the same total age. In addition, except for the case of low metallicity, the vast majority of objects in the ELM Survey are not compatible with the few models that do not suffer from flashes. Thus, we point out that these objects have gone or will undergo episodes of hydrogen shell flashes.

In Figure 23 we can clearly notice the formation of two branches by the observational data. They are in the region of $10 \lesssim T_{\rm eff}/{\rm kK} \lesssim 20$ and $3.5 \lesssim \log(g) \lesssim 5.5$. The observational data in this region is from the ELM candidates from Pelisoli; Kepler; Koester, 2018a (188 objects) and Pelisoli et al., 2018c (9 objects). We found that mainly the pre-ELM WDs with low metallicity ($Z = 0.001$) and that undergo hydrogen shell flashes spend significant time in this region. We then search for the tangential and radial velocities for these 197 objects in the Gaia DR2 and SDSS DR16, respectively. Selecting only objects with `parallax_over_error` > 3, we find that 19/35 (∼ 54 per cent) of these objects have a total velocity greater than 200 km/s, indicating that they are most probably halo objects and therefore should have low metallicity. In this way, we have shown that approximately half of the (pre-)ELM WDs candidate objects that are in the KD branches are compatible

Figure 24 – Isochronous Kiel diagram of theoretical models with different metallicities along with observational data. In the theoretical tracks, the coloured symbols are spaced in 30 Myr intervals. In total, nine models are presented, three for each metallicity: $Z = 0.02$ (green squares, $P_{\rm i} = 4$, 5 and 100 d); $Z = 0.01$ (blue circles, $P_{\rm i} = 2$, 3 and 100 d); and $Z = 0.001$ (red triangles, $P_{\rm i} = 1$, 2 and 100 d). Here, the least massive models for each metallicity do not undergo hydrogen shell flashes. Confirmed ELM WDs from Brown et al. (2020), Pelisoli & Vos (2019) are shown in orange crosses.

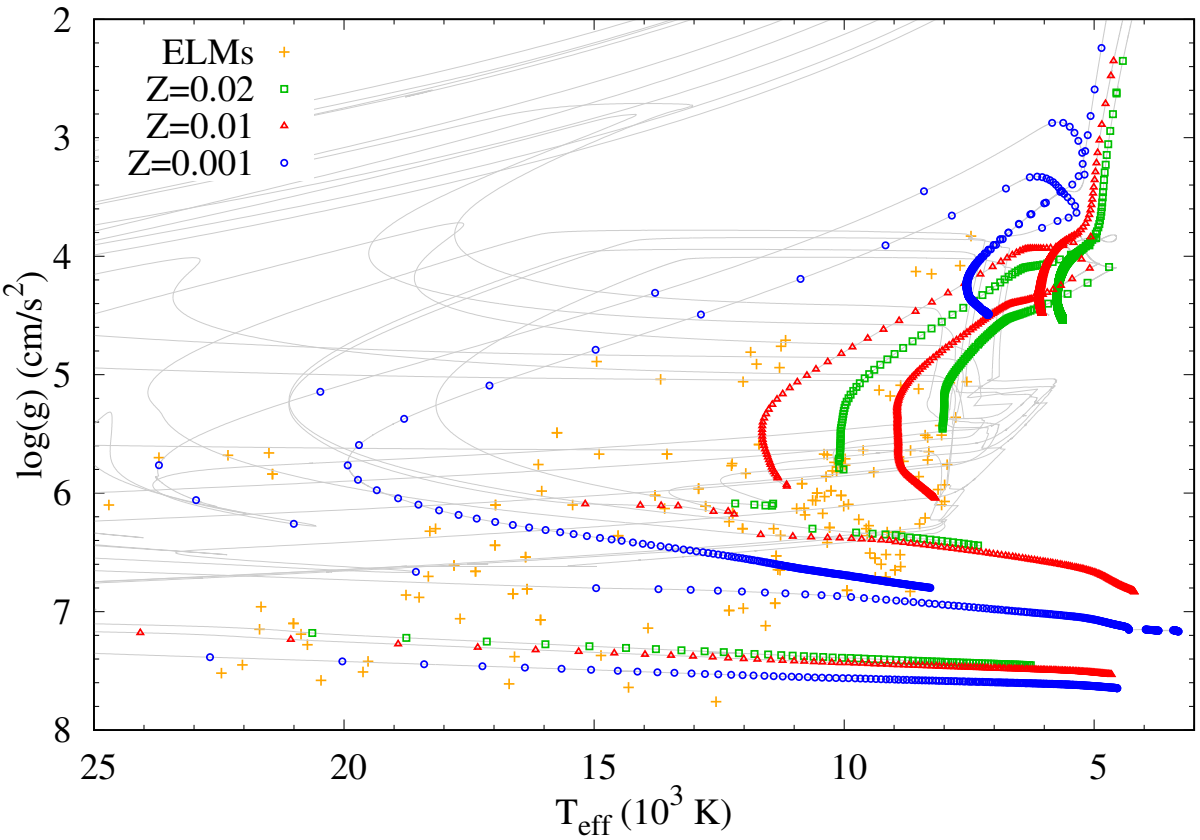

with low-metallicity pre-ELM WDs models.

Finally and equally importantly, we found that the use of the CARB prescription for magnetic braking instead of the Rappaport, Verbunt & Joss (1983) prescription does not affect the behaviour of (pre-) ELM in the $\log(g) - T_{\rm eff}$ plane. That is, our models have both $\log(g)$ and $T_{\rm eff}$ fully compatible with observational data. This was expected and required. It was expected because magnetic braking only affects the dynamics of the binary system, altering the loss of angular momentum, but the impact on the stellar components occurs indirectly, via RLOF, etc. Lastly, as highlighted in the introduction, it is one of the required objectives of this work.

3.8 Donor irradiation by accretion of matter in the neutron star

Whether the radiation emitted by the accretion of matter in a NS can influence the properties (temperature, radius, luminosity, mass, etc.) of the donor star and, consequently, the evolution of the binary system, has been studied for a long time (Ruderman et al., 1989; Podsiadlowski, 1991; Hameury et al., 1993; Harpaz; Rappaport, 1994; Hameury; Ritter, 1997; Ritter; Zhang; Kolb, 2000; Ritter, 2008).

We then choose a representative evolutionary sequence to test the aforementioned effects, namely: $M_{\rm d,i} = 1.0\ M_\odot$, $M_{\rm a,i} = 1.4\ M_\odot$, $P_{\rm i} = 5$ d, $\beta_{\rm mt} = 0.3$, and $Z = 0.02$. We follow the simple approach of Quintin (2013), Goodwin & Woods (2020). For steady spherical accretion onto a neutron star, neglecting the magnetic field, one has the X-ray luminosity

$$L_{\rm X} = \frac{G M_{\rm NS} \dot{M}_{\rm acc}}{R_{\rm NS}} \eta_{\rm X} \ , \tag{3.1}$$

where $M_{\rm NS}$ is the neutron star mass, $\dot{M}_{\rm acc}$ is the accretion rate — that is, the total mass transfer rate times the accretion efficiency $\beta_{\rm mt}$—, $R_{\rm NS}$ is the (assumed constant) radius of the neutron star, set to 13 km following the recent result of Adhikari et al., 2021, Reed et al., 2021, and $\eta_{\rm X}$ is the X-ray efficiency term.

Assuming that the X-rays are emitted isotropically, the irradiating flux at the surface of the donor star can be written as

$$F_{\rm irr} = \frac{L_{\rm X}}{4\pi a^2} \varepsilon_{\rm irr} \ , \tag{3.2}$$

where a is the binary separation (as in subsection 1.2.1), $L_{\rm X}$ is given by Equation 3.1, and $\varepsilon_{\rm irr}$ is the irradiation efficiency term.

Energy from irradiation will be deposited in the outer $4\pi R_{\rm d}^2 C_{\rm depth}$ grams of the donor star. $C_{\rm depth}$ is a free parameter representing the column depth, given in units of g/cm^2. However, we do not consider any change in the boundary conditions of the atmosphere or in the opacities treatment due to irradiation. That is, it is treated in the same way as described in chapter 2.

Following the studies mentioned above, we set $C_{\rm depth} = 0.1$, 1, 10, and 100 g/cm^2. We chose $\eta_{\rm X} = 1$ and $\varepsilon_{\rm irr} = 1$, not limiting the X-ray and irradiation efficiency terms. Instead, we limit $F_{\rm irr}$ to $F_{\rm irr,max} = 1 \times 10^9$, 5×10^9, and 1×10^{10} erg/(cm^2 s).

We look for significant differences in the quantities of temperature, radius, mass transfer rate, orbital period, and donor mass, especially during the mass transfer and its states at the end of the evolution. We do not find any significant change in these quantities during the evolution or at the end of the simulations.

Our conclusion is that, up to the maximum limit of $F_{\rm irr,max} = 1 \times 10^{10}$ erg/(cm^2 s), there is no significant change in the evolution of an ELM WD in a $P_{\rm i} = 5$ d binary system

with an NS accretor. For systems with a longer initial orbital period, the orbital separation a increases, so the effects of irradiation decrease.

However, we draw attention to the fact that the studies cited above indicate much lower values for the efficiency terms, namely, $\eta_{\rm X} \approx 0.2$, and $\varepsilon_{\rm irr} \approx 0.01$ (for instance, these are the same values that we chose to estimate X-ray luminosities in Appendix B). We note that even considering these lower efficiency values, $F_{\rm irr}$ in Equation 3.2 may reach values as high as 2.5×10^{11} erg/(cm^2 s) during the peak of the mass transfer rate. We also note that Goodwin & Woods (2020) set $F_{\rm irr,max} = 3 \times 10^9$ erg/(cm^2 s) in their simulations, therefore a stricter limit compared to what we use in our work. Thus, we point that a more detailed investigations in this regard should be considered in modelling the irradiation due to accretion in the formation of ELM WDs in companion to neutron stars.

In MESA version release r11701, these results can be achieved using the following commands, for example:

`accretion_powered_irradiation = .true.`

`max_F_irr = 1d10` [erg/(cm^2 s)]

`accreteor_radius_for_irrad = 1.3d6` [cm]

`col_depth_for_eps_extra = 1` [g/cm^2]

3.9 Effects of different microphysics

To test the effects of how elements are grouped together in diffusion calculations, we created some models lumping elements into 10 element classes, as in Istrate et al. (2016). We found that the difference is minimal. When compared to the case where the full net is used, the final ELM mass changes by $\leq 0.001\ M_\odot$, the final orbital period by $\lesssim 0.8$ per cent, and the number of hydrogen shell flashes remains the same. Moreover, we did not find significant difference in computing time. Therefore, we encourage the use of the full net for such calculations.

We also compare the results in the case where the diffusion coefficients of Paquette et al. (1986) or Stanton & Murillo (2016) are considered. Again, the effects on the orbital period and final mass are not significant. Nevertheless, when the initial metallicity is low, we find that differences in the mass of the envelope and in the total mass of ^{1}H can appear. For example, for the case of $Z = 0.001$, a model of 0.25 $M_\odot$ has an envelope of mass 3.30×10^{-3} when considering the Iben & MacDonald (1985) coefficients, and this value changes to 4.51×10^{-3} and 2.12×10^{-3} when the Paquette et al. (1986) and Stanton & Murillo (2016) coefficients are used, respectively. Also, the total ^{1}H mass is 4.69×10^{-4} when we consider the Iben coefficients, being ~ 25 per cent higher for the Paquette et al. (1986) coefficients and ~ 66 percent lower for Stanton & Murillo (2016).

We also explore the effects of considering more intense overshooting mixing. We doubled the values of the overshooting coefficients, as mentioned in subsection 2.2.1, and found that the effects on the final ELM WDs are insignificant. This is not surprising since overshooting is expected to be more decisive in forming the core of intermediate and high mass stars, leading to big differences in behaviour on the subgiant and giant phases.

Unlike Althaus et al. (2009), Althaus, Miller Bertolami & Córsico (2013), Istrate et al. (2016), we found that, except for a few models with a mass of $\approx 0.15\ M_{\odot}$, all models undergo at least one hydrogen shell flash during evolution when considering the rotation and diffusion of the entire network of elements. In addition, the maximum number of hydrogen shell flashes of our models is four, regardless of metallicity or mass; while Althaus, Miller Bertolami & Córsico (2013) and Istrate et al. (2016) points out that up to ten and twenty flashes can occur in some configurations, respectively. However, we found no evidence that this could be related to the chosen magnetic braking recipe. It is more likely to have to do with the details of the chosen microphysics, or the numerical treatment of diffusion in each code/version. In any case, our results agree with the well-known fact that hydrogen shell flashes strongly depends on how diffusion is considered, in addition to altering the structure of the models and directly influencing their cooling. Our models also confirm that it is possible to obtain ELM WDs as cold as $T_{\rm eff} = 5000$ K within Hubble time, and even cooler for low metallicity.

We do confirm that the time spent at the bottom of the hydrogen shell flash loops (see Figure 24) is not negligible (e.g., Althaus et al., 2009); and that the shell flashes are less intense (see Figure 23) as the metal content is decreased (e.g., Serenelli et al., 2002). As was shown by previous works (e.g., Althaus; Miller Bertolami; Córsico, 2013), there is a degeneracy in the $\log(g) - T_{\rm eff}$ plane in the sense that, given a $\log(g)$ and $T_{\rm eff}$, there are multiple solutions for the stellar mass. That is, since the evolutionary tracks cross each other in this region of the Kiel diagram, knowing the $\log(g)$ and the $T_{\rm eff}$ of a star is not enough to guarantee a unique solution in terms of mass and age. Even more, this degeneracy of solutions increases with metallicity, since tracks of different metallicities also overlap. On the other hand, our models indicate that there are several quantities that are affected by hydrogen shell flashes, such as the amounts of ^{1}H and ^{4}He in the surface, the chemical profile, the rotation velocity, and also its synchronisation with the orbital period. In this way, the degeneracy problem could be alleviated if sufficient accurate measurements could provide us such information. On the other hand, we find that there is a region in the low-$T_{\rm eff}$ and high-$\log(g)$ corner of the Kiel diagram Figure 23 which is sufficiently far from the loops region and can allow, in principle, a more precise determination of the parameters mentioned above, as long as the metallicity is known. This region is widely populated by the ELM candidates from the Pelisoli & Vos (2019) selection.

4 Conclusions

Below we list the main conclusions of this work.

- The CARB (Convection And Rotation Boosted) magnetic braking prescription was obtained by Van & Ivanova (2019) through a self-consistent deduction considering wind mass loss, rotation, and the magnetic field is generated due to motions in the convective zone. Although the CARB model is still considerably simplified — only radial magnetic fields are considered and the dipole approximation is used, the Alfvenic surface estimated does not depend on the polar angle, and the wind is considered isotropic (i.e., the rotation axis is assumed aligned to the magnetic field axis) — it has a consistent physical deduction (see subsection 2.2.3) and we find that it presents more plausible results (the distribution in the initial orbital period–final mass plane, for example) compared to the Rappaport, Verbunt & Joss (1983) magnetic braking when modelling ELM WDs in binary systems.

- The use of the CARB magnetic braking prescription strongly modifies the loss of the total angular momentum of the binary systems and, as a natural consequence, also the relation between $P_{\rm i}$ and $M_{\rm WD}$ becomes completely different. In particular, fine-tuning the initial orbital period is not required to produce ELM WDs. A large range of final masses for the ELM WDs (0.15–0.25 $M_{\odot}$) can be obtained from a wide range of initial orbital periods (1–25 d). See section 3.1 and section 3.2.

- Furthermore, using the CARB braking we obtained low-mass WDs of 0.40 $M_{\odot}$ from systems with an initial orbital period of about 300 days. In the relation between the initial orbital period of the system and the final mass of the low-mass WDs, the 0.40 $M_{\odot}$ region is the only one that has some similarity between the results of Rappaport, Verbunt & Joss (1983) and CARB (Van; Ivanova, 2019). See section 3.1 and section 3.2.

- The bifurcation period is shifted to longer ones (from 2.75–2.8 to 20–25 days) when the CARB magnetic braking is considered. That is, the CARB magnetic braking allows us to get ELM WDs models with masses as low as 0.26 $M_{\odot}$ in converging binary systems even with initial orbital periods as long as 20 days, which is not possible with the magnetic braking of Rappaport. See section 3.3.

- For a given initial orbital period and donor mass, higher metallicities always lead to less massive ELM WDs. This is valid for both neutron stars and massive white dwarf accretors. See subsection 3.4.1 and subsection 3.5.1.

- The effects of element diffusion on the final mass of the ELM WDs are especially important for short initial orbital periods, which produce less massive ELM WDs. Also, calculating the diffusion considering all elements independently rather than lumping them into classes does not significantly increase processing time, so we encourage its use.

- When taking into account rotation and diffusion, virtually all model sequences go through at least one hydrogen shell flash. The number of hydrogen shell flashes is greater in the $M_{\rm d,f}$ range 0.16–0.22 $M_\odot$ if $Z = 0.02$, and 0.23–0.26 $M_\odot$ if $Z = 0.001$.

- The main parameters that govern the ELM WD age are the metallicity and the initial donor mass — here taken to be 1.0 or 1.2 $M_\odot$. If metallicity is known, the ELM WD mass indicates the initial orbital period of the system, and its age indicates its initial mass.

- ELM WDs in converging systems seem to have a rotation rate closer to the orbital period, while the diverging systems are not so synchronised. See subsection 3.5.2.

- The relation between the orbital period of the system and the ELM WD mass remains in line with observations of pulsars with He-WD companions when using CARB magnetic braking. See section 3.4.

- On the other hand, data from ELM WDs in systems with white dwarf companions present great dispersion in mass and orbital period of the binary system, suggesting that other formation channels are also present. See section 3.5.

- Different accretion efficiencies have a little effect on the binary evolution and in the final ELM WD mass and final orbital period. However, this parameter is the most important to regulate the final mass of the accretor star. See subsection 3.5.4.

- The use of the CARB prescription (Van; Ivanova, 2019) for magnetic braking instead of the Rappaport, Verbunt & Joss (1983) prescription does not affect the behaviour of (pre-) ELM in the $T_{\rm eff} - \log(g)$ plane. That is, our models have both $\log(g)$ and $T_{\rm eff}$ fully compatible with observational data. See subsection 3.7.1.

- Looking at the ELM WD candidates in the $T_{\rm eff} - \log(g)$ plane, we note the formation of two branches. We find that $\sim 54\%$ of these objects have a total velocity greater than 200 km/s, indicating that they are most probably halo objects and therefore should have low metallicity. We show that approximately half of the (pre-) ELM WDs candidate objects that are in the KD branches are compatible with low-metallicity pre-ELM WD models. See subsection 3.7.2.

- Up to the maximum limit of $F_{\rm irr,max} = 1 \times 10^{10}$ erg/(cm^2 s) of the donor irradiation by accretion of matter in the neutron star, there is no significant change in the

evolution of an ELM WD in a $P_{\rm i} = 5$ d binary system with an NS accretor. See section 3.8.

- Gravitational waves from the nearest ELM WDs will have a chance of being detected by ASTROD-GW since the pre-ELM phase, especially considering the extended operating time of the detector. See Appendix B.

- Systems with an even shorter initial orbital period ($\lesssim 0.4$–4 days, depending on the metallicity) give rise to UCXBs, whose X-ray emission from the second mass transfer phase is likely to be observed along with gravitational waves by LISA and TianQin detectors with high signal-to-noise. See Appendix B.

- Tables with the main properties of our model grid are presented in Appendix C.

- Papers published by the author during the course are presented in Appendix D and Appendix E.

- Input data to reproduce the results obtained in this work and the models generated as output can be obtained by asking directly from the author or will be made available online elsewhere. A preliminary version of the `inlist` and `extras` files can be found in Appendix F.

- A press release, written in Portuguese, is presented in Appendix G.

The writing and development of this work also yielded insights into possible advances and improvements. Therefore, suggestions for future work or an upcoming project include:

- To evolve both stars (i.e., also model the accretor star). An important limitation regarding the computational modelling of ELM WDs in binary systems with neutron star companions is that there is no stellar evolutionary code capable to model a binary system from the ZAMS of both stars until the cooling track of the stellar remnants. This is because the evolution of this kind of system involves at least one supernova explosion episode (see Figure 5 as an example). These are very fast and extremely energetic events, and therefore need special codes and extra computational power. Nevertheless, nothing prevents us from modelling the structure of both stars of the binary system considering some point after the occurrence of supernova explosion. The most immediate step in this direction is to create a cool WD model via a single evolution and then start the evolution of a binary system consisting of this WD as the accretor plus a ZAMS donor. The accretor star being an object with finite size (and not a point of mass) should modify the details of the mass transfer episodes. This is also a unique opportunity to study the changes in the accretor's structure after the mass transfer episodes. A rapid examination of this scenario allows us to anticipate

that we will have three limiting factors for the timestep: the evolution of the donor, the evolution of the accretor, and the evolution of the binary. Unfortunately, the evolution of the accretor during the nova flashes, for example, takes a long processing time in order to simulate only a few seconds or years of evolution (José; Hernanz, 2007; Wolf et al., 2013; Denissenkov et al., 2013a; Denissenkov et al., 2014; Wu et al., 2017; José; Shore; Casanova, 2020). Thus, some simplifications should be assumed (e.g., block the nuclear reactions on the surface of the accretor) if we are willing to evolve a star from the ZAMS until the ELM WD cooling track.

- As already mentioned, the CARB magnetic braking also has its limitations. The field configuration is at the heart of the most sensitive variable in the problem — the braking torque. There is a lot of evidence (the Sun, for example) that the magnetic field structure in low-mass stars is much more complex than the dipole approximation. One suggestion is to study how the Alfvén radius changes when we change the structure of the magnetic field. A possible way to do this would be to parameterise the magnetic field geometry and coupling on CARB prescription.

- In our models we do not consider the possible magnetic field of the accretor star. Most pulsars in binaries have magnetic fields in the range 10^7–10^{12} G (Manchester et al., 2005; Jawor; Tauris, 2021). Magnetars — a type of neutron star — are known to have magnetic fields of up to 10^{15} G (Harding, 2013; Beskin et al., 2016; Kaspi, 2017), and magnetic white dwarfs of up to 10^9 G (Kepler et al., 2013; García-Berro; Kilic; Kepler, 2016; García-Berro; Kilic; Kepler, 2018; Ferrario; Wickramasinghe; Kawka, 2020). Including torques due to these fields in the evolution of LMXBs and CVs systems is another suggestion for future work.

Bibliography

Abt, H. A.; Levy, S. G. Multiplicity among solar-type stars. *Astrophysical Journal, Suppl. Ser.*, v. 30, p. 273–306, mar. 1976. Available at: <https://doi.org/10.1086/190363>. Cited on page 53.

Adhikari, D. et al. Accurate Determination of the Neutron Skin Thickness of ^{208}Pb through Parity-Violation in Electron Scattering. *Physical Review Letters*, v. 126, n. 17, p. 172502, apr. 2021. Available at: <https://doi.org/10.1103/PhysRevLett.126.172502>. Cited 2 times on pages 113 and 178.

Aerts, C.; Mathis, S.; Rogers, T. M. Angular Momentum Transport in Stellar Interiors. *Annual Review of Astronomy and Astrophysics*, v. 57, p. 35–78, aug. 2019. Available at: <https://doi.org/10.1146/annurev-astro-091918-104359>. Cited on page 68.

Aitken, R. G. *The binary stars*. New York: Dover Publications, Inc., 1935. Cited on page 28.

Alpar, M. A. et al. A new class of radio pulsars. *Nature*, v. 300, n. 5894, p. 728–730, Dec 1982. Available at: <https://doi.org/10.1038/300728a0>. Cited on page 39.

Althaus, L. G.; Miller Bertolami, M. M.; Córsico, A. H. New evolutionary sequences for extremely low-mass white dwarfs - homogeneous mass and age determinations and asteroseismic prospects. *Astronomy & Astrophysics*, v. 557, p. A19, sep 2013. Available at: <https://doi.org/10.1051/0004-6361/201321868>. Cited 5 times on pages 38, 50, 58, 111, and 115.

Althaus, L. G. et al. Evolution and colors of helium-core white dwarf stars with high-metallicity progenitors. *Astronomy & Astrophysics*, v. 502, n. 1, p. 207–216, 2009. Available at: <https://doi.org/10.1051/0004-6361/200911640>. Cited 2 times on pages 50 and 115.

Althaus, L. G.; Serenelli, A. M.; Benvenuto, O. G. Diffusion and the occurrence of hydrogen-shell flashes in helium white dwarf stars. *Monthly Notices of the Royal Astronomical Society*, v. 323, n. 2, p. 471–483, 05 2001. ISSN 0035-8711. Available at: <https://doi.org/10.1046/j.1365-8711.2001.04227.x>. Cited 2 times on pages 40 and 58.

Althaus, L. G.; Serenelli, A. M.; Benvenuto, O. G. The impact of element diffusion on the formation and evolution of helium white dwarf stars. *Monthly Notices of the Royal Astronomical Society*, v. 324, n. 3, p. 617–622, 06 2001. ISSN 0035-8711. Available at: <https://doi.org/10.1046/j.1365-8711.2001.04324.x>. Cited on page 40.

Amaro-Seoane, P. et al. Low-frequency gravitational-wave science with eLISA/NGO. *Classical and Quantum Gravity*, IOP Publishing, v. 29, n. 12, p. 124016, jun 2012. Available at: <https://doi.org/10.1088%2F0264-9381%2F29%2F12%2F124016>. Cited on page 55.

Amaro-Seoane, P. et al. Laser Interferometer Space Antenna. *arXiv e-prints*, p. arXiv:1702.00786, Feb 2017. Cited on page 55.

Antoniadis, J. et al. A Massive Pulsar in a Compact Relativistic Binary. *Science*, American Association for the Advancement of Science, v. 340, n. 6131, 2013. ISSN 0036-8075. Available at: <https://science.sciencemag.org/content/340/6131/1233232>. Cited 2 times on pages 78 and 92.

Antoniadis, J. et al. The millisecond pulsar mass distribution: Evidence for bimodality and constraints on the maximum neutron star mass. *arXiv e-prints*, p. arXiv:1605.01665, may 2016. Available at: <https://arxiv.org/pdf/1605.01665.pdf>. Cited on page 78.

Antoniadis, J. et al. The relativistic pulsar-white dwarf binary PSR J1738+0333 - I. Mass determination and evolutionary history. *Monthly Notices of the Royal Astronomical Society*, v. 423, n. 4, p. 3316–3327, 07 2012. ISSN 0035-8711. Available at: <https://doi.org/10.1111/j.1365-2966.2012.21124.x>. Cited on page 78.

Arnould, M.; Takahashi, K. Nuclear astrophysics. *Reports on Progress in Physics*, v. 62, p. 395–464, jan. 1999. Available at: <https://doi.org/10.1088/0034-4885/62/3/003>. Cited on page 61.

Athanasiadis, T. M. et al. A search for pulsar companions around low-mass white dwarfs. *Monthly Notices of the Royal Astronomical Society*, v. 505, n. 4, p. 4981–4988, aug. 2021. Available at: <https://doi.org/10.1093/mnras/stab1580>. Cited 2 times on pages 38 and 98.

Athanasiadis, T. M. et al. No Pulsar Companion Around the Nearest Low Mass White Dwarf. *arXiv e-prints*, p. arXiv:2112.02914, dec. 2021. Cited 2 times on pages 38 and 98.

Baade, W.; Zwicky, F. Remarks on Super-Novae and Cosmic Rays. *Physical Review*, v. 46, n. 1, p. 76–77, Jul 1934. Cited on page 39.

Backus, P. R.; Taylor, J. H.; Damashek, M. Improved parameters for 67 PSR from timing observations. *Astrophysical Journal*, v. 255, p. L63–L67, apr. 1982. Available at: <https://doi.org/10.1086/183770>. Cited on page 39.

Bagnulo, S.; Landstreet, J. D. New insight into the magnetism of degenerate stars from the analysis of a volume-limited sample of white dwarfs. *Monthly Notices of the Royal Astronomical Society*, v. 507, n. 4, p. 5902–5951, nov. 2021. Available at: <https://doi.org/10.1093/mnras/stab2046>. Cited 2 times on pages 57 and 58.

Bahcall, J. N.; Serenelli, A. M.; Basu, S. 10,000 Standard Solar Models: A Monte Carlo Simulation. *Astrophysical Journal Supplement*, v. 165, n. 1, p. 400–431, jul. 2006. Available at: <https://doi.org/10.1086/504043>. Cited on page 69.

Bailes, M. et al. Gravitational-wave physics and astronomy in the 2020s and 2030s. *Nature Reviews Physics*, v. 3, n. 5, p. 344–366, apr. 2021. Available at: <https://doi.org/10.1038/s42254-021-00303-8>. Cited on page 175.

Baker, J. et al. The Laser Interferometer Space Antenna: Unveiling the Millihertz Gravitational Wave Sky. *arXiv e-prints*, p. arXiv:1907.06482, jul. 2019. Cited on page 55.

Baker, J. et al. Multimessenger science opportunities with mHz gravitational waves. *Bulletin of the American Astronomical Society*, v. 51, n. 3, p. 123, May 2019. Cited 2 times on pages 55 and 175.

Ball, W. H.; Gizon, L. A new correction of stellar oscillation frequencies for near-surface effects. *Astronomy and Astrophysics*, v. 568, p. A123, Aug 2014. Cited on page 64.

Bartos, I.; Kowalski, M. *Multimessenger Astronomy*. Bristol, UK: IOP Publishing, 2017. (2399-2891). ISBN 978-0-7503-1369-8. Available at: <http://dx.doi.org/10.1088/978-0-7503-1369-8>. Cited on page 175.

Basdevant, J. et al. *Fundamentals in Nuclear Physics: From Nuclear Structure to Cosmology*. New York: Springer, 2005. (Advanced Texts in Physics). ISBN 9780387016726. Cited on page 61.

Batten, A. H. *Binary and multiple systems of stars*. New York: Pergamon, 1973. (International Series in Natural Philosophy). ISSN 00748064. Available at: <https://doi.org/10.1016/C2013-0-02510-8>. Cited on page 28.

Batten, A. H. Two Centuries of Study of Algol Systems. *Space Science Reviews*, v. 50, n. 1-2, p. 1–8, jun. 1989. Available at: <https://doi.org/10.1007/BF00215914>. Cited on page 27.

Belenkaya, E. S.; Khodachenko, M. L.; Alexeev, I. I. Alfvén Radius: A Key Parameter for Astrophysical Magnetospheres. In: _____. *Characterizing Stellar and Exoplanetary Environments*. Cham: Springer International Publishing, 2015. p. 239–249. ISBN 978-3-319-09749-7. Available at: <https://doi.org/10.1007/978-3-319-09749-7_12>. Cited on page 74.

Belloni, D.; Rivera, L. Properties of Cataclysmic Variables in Globular Clusters. In: *The Golden Age of Cataclysmic Variables and Related Objects V*. Trieste TS, Italy: PoS-SISSA, 2021. v. 2-7, p. 13. Available at: <https://pos.sissa.it/368/013/pdf>. Cited on page 39.

Belloni, D.; Schreiber, M. R. Are white dwarf magnetic fields in close binaries generated during common-envelope evolution? *Monthly Notices of the Royal Astronomical Society*, v. 492, n. 1, p. 1523–1529, feb. 2020. Available at: <https://doi.org/10.1093/mnras/stz3601>. Cited on page 57.

Belloni, D. et al. Magnetic dynamos in white dwarfs - I. Explaining the dearth of bright intermediate polars in globular clusters. *Monthly Notices of the Royal Astronomical Society*, v. 505, n. 1, p. L74–L78, jul. 2021. Available at: <https://doi.org/10.1093/mnrasl/slab054>. Cited on page 57.

Bennett, J. O. et al. *The Cosmic Perspective*. 8th. ed. Boston: Pearson, 2017. ISBN 0134059069,9780134059068. Cited on page 171.

Benvenuto, O. G.; De Vito, M. A. The formation of helium white dwarfs in close binary systems - II. *Monthly Notices of the Royal Astronomical Society*, v. 362, n. 3, p. 891–905, 09 2005. ISSN 0035-8711. Available at: <https://doi.org/10.1111/j.1365-2966.2005.09315.x>. Cited on page 40.

Beskin, V. S. et al. *The Strongest Magnetic Fields in the Universe*. New York: Springer, 2016. v. 54. Available at: <https://doi.org/10.1007/978-1-4939-3550-5>. Cited on page 120.

Bethe, H. A. Nuclear Physics B. Nuclear Dynamics, Theoretical. *Reviews of Modern Physics*, v. 9, n. 2, p. 69–244, apr. 1937. Available at: <https://doi.org/10.1103/RevModPhys.9.69>. Cited on page 61.

Bethe, H. A.; Bacher, R. F. Nuclear Physics A. Stationary States of Nuclei. *Reviews of Modern Physics*, v. 8, n. 2, p. 82–229, apr. 1936. Available at: <https://doi.org/10.1103/RevModPhys.8.82>. Cited on page 61.

Bhattacharya, D.; van den Heuvel, E. P. J. Formation and evolution of binary and millisecond radio pulsars. *Physics Reports*, v. 203, n. 1-2, p. 1–124, jan. 1991. Available at: <https://doi.org/10.1016/0370-1573(91)90064-S>. Cited on page 39.

Bhattacharyya, B.; Roy, J. Radio Millisecond pulsars. *arXiv e-prints*, p. arXiv:2104.02294, apr. 2021. Cited on page 40.

Bhattacharyya, S. X-ray views of neutron star low-mass x-ray binaries. *Current Science*, Current Science Association, v. 97, n. 6, p. 804–820, 2009. ISSN 00113891. Available at: <http://www.jstor.org/stable/24112117>. Cited on page 81.

Bhattacharyya, S. Nuclear-powered X-ray millisecond pulsars. *arXiv e-prints*, p. arXiv:2103.11258, mar. 2021. Cited on page 40.

Bildsten, L. et al. Faint thermonuclear supernovae from AM canum venaticorum binaries. *The Astrophysical Journal Letters*, IOP Publishing, v. 662, n. 2, p. L95–L98, jun 2007. Available at: <https://doi.org/10.1086%2F519489>. Cited on page 54.

Bloecker, T. Stellar evolution of low- and intermediate-mass stars. II. Post-AGB evolution. *Astronomy and Astrophysics*, v. 299, p. 755, Jul 1995. Cited on page 38.

Bloecker, T. Stellar evolution of low and intermediate-mass stars. I. Mass loss on the AGB and its consequences for stellar evolution. *Astronomy and Astrophysics*, v. 297, p. 727, May 1995. Cited on page 38.

Bodenheimer, P. The Formation of Binary Stars. In: Podsiadlowski, P. et al. (Ed.). *Evolution of Binary and Multiple Star Systems*. University of Michigan: Astronomical Society of the Pacific, 2001. (Astronomical Society of the Pacific Conference Series, v. 229), p. 67. Cited on page 35.

Böhm-Vitense, E. Über die Wasserstoffkonvektionszone in Sternen verschiedener Effektivtemperaturen und Leuchtkräfte. Mit 5 Textabbildungen. *Zeitschrift fur Astrophysik*, v. 46, p. 108, Jan 1958. Cited on page 67.

Boss, A. P. Formation of binary stars. In: _____. *The Realm of Interacting Binary Stars*. Dordrecht: Springer Netherlands, 1993. p. 355–379. ISBN 978-94-011-2416-4. Available at: <https://doi.org/10.1007/978-94-011-2416-4_19>. Cited on page 35.

Brandt, G. M. et al. Improved Dynamical Masses for Six Brown Dwarf Companions Using Hipparcos and Gaia EDR3. *arXiv e-prints*, p. arXiv:2109.07525, sep. 2021. Available at: <https://ui.adsabs.harvard.edu/abs/2021arXiv210907525B>. Cited on page 64.

Brandt, J. C. Consequences of the Torque Exerted on the Sun by the Solar Wind. *Astrophysical Journal*, v. 144, p. 1221, jun. 1966. Available at: <https://doi.org/10.1086/148720>. Cited on page 47.

Breedt, E. et al. CSS100603:112253-111037: a helium-rich dwarf nova with a 65 min orbital period. *Monthly Notices of the Royal Astronomical Society*, v. 425, n. 4, p. 2548–2556, 10 2012. ISSN 0035-8711. Available at: <https://doi.org/10.1111/j.1365-2966.2012.21724.x>. Cited on page 55.

Briggs, G. P. *The Genesis of Magnetic Fields in White Dwarfs*. Tese (Doutorado) — Australian National University, Jul 2019. Available at: <https://openresearch-repository.anu.edu.au/bitstream/1885/148886/1/Briggs%20G%20P%20Thesis%202018.pdf>. Cited on page 57.

Briggs, G. P. et al. Origin of magnetic fields in cataclysmic variables. *Monthly Notices of the Royal Astronomical Society*, v. 481, n. 3, p. 3604–3617, 09 2018. ISSN 0035-8711. Available at: <https://doi.org/10.1093/mnras/sty2481>. Cited on page 57.

Bromm, V.; Larson, R. B. The First Stars. *Annual Review of Astronomy and Astrophysics*, v. 42, n. 1, p. 79–118, 2004. Available at: <https://doi.org/10.1146/annurev.astro.42.053102.134034>. Cited on page 25.

Bromm, V.; Yoshida, N. The First Galaxies. *Annual Review of Astronomy and Astrophysics*, v. 49, n. 1, p. 373–407, 2011. Available at: <https://doi.org/10.1146/annurev-astro-081710-102608>. Cited on page 25.

Bromm, V. et al. The formation of the first stars and galaxies. *Nature*, v. 459, n. 7243, p. 49–54, May 2009. Cited on page 25.

Brooks, J. et al. Carbon Shell or Core Ignitions in White Dwarfs Accreting from Helium Stars. *The Astrophysical Journal*, American Astronomical Society, v. 821, n. 1, p. 28, apr 2016. Available at: <https://doi.org/10.3847%2F0004-637x%2F821%2F1%2F28>. Cited on page 64.

Brooks, J. et al. Accretion-induced Collapse from Helium Star + White Dwarf Binaries. *The Astrophysical Journal*, American Astronomical Society, v. 843, n. 2, p. 151, jul 2017. Available at: <https://doi.org/10.3847%2F1538-4357%2Faa79a6>. Cited on page 64.

Brooks, J. et al. Convection Destroys the Core/Mantle Structure in Hybrid C/O/Ne White Dwarfs. *The Astrophysical Journal*, American Astronomical Society, v. 834, n. 2, p. L9, jan 2017. Available at: <https://doi.org/10.3847%2F2041-8213%2F834%2F2%2Fl9>. Cited on page 64.

Brown, J. M. et al. The Binary Fraction of Low-mass White Dwarfs. *The Astrophysical Journal*, IOP Publishing, v. 730, n. 2, p. 67, mar 2011. Available at: <https://doi.org/10.1088%2F0004-637x%2F730%2F2%2F67>. Cited on page 38.

Brown, W. R. et al. The ELM Survey. VII. Orbital Properties of Low-Mass White Dwarf Binaries. *The Astrophysical Journal*, American Astronomical Society, v. 818, n. 2, p. 155, feb 2016. Available at: <https://doi.org/10.3847%2F0004-637x%2F818%2F2%2F155>. Cited 3 times on pages 38, 53, and 55.

Brown, W. R. et al. The ELM Survey. I. A Complete Sample of Extremely Low-mass White Dwarfs. *The Astrophysical Journal*, IOP Publishing, v. 723, n. 2, p. 1072–1081, oct 2010. Available at: <https://doi.org/10.1088%2F0004-637x%2F723%2F2%2F1072>. Cited 2 times on pages 28 and 38.

Brown, W. R. et al. The ELM Survey. III. A Successful Targeted Survey for Extremely Low Mass White Dwarfs. *The Astrophysical Journal*, IOP Publishing, v. 744, n. 2, p. 142, dec 2011. Available at: <https://doi.org/10.1088%2F0004-637x%2F744%2F2%2F142>. Cited on page 28.

Brown, W. R. et al. The merger rate of extremely low mass white dwarf binaries: links to the formation of AM CVn stars and underluminous supernovae. *Monthly Notices of the Royal Astronomical Society: Letters*, v. 411, n. 1, p. L31–L35, 02 2011. ISSN 1745-3925. Available at: <https://doi.org/10.1111/j.1745-3933.2010.00986.x>. Cited 2 times on pages 54 and 175.

Brown, W. R. et al. A 1201 s Orbital Period Detached Binary: The First Double Helium Core White Dwarf LISA Verification Binary. *The Astrophysical Journal Letters*, v. 892, n. 2, p. L35, apr. 2020. Available at: <https://doi.org/10.3847/2041-8213/ab8228>. Cited on page 175.

Brown, W. R.; Kilic, M.; Gianninas, A. The physical nature of subdwarf a stars: White dwarf impostors. *The Astrophysical Journal*, American Astronomical Society, v. 839, n. 1, p. 23, apr 2017. Available at: <https://doi.org/10.3847%2F1538-4357%2Faa67e4>. Cited on page 53.

Brown, W. R. et al. Most Double Degenerate Low-mass White Dwarf Binaries Merge. *The Astrophysical Journal*, American Astronomical Society, v. 824, n. 1, p. 46, jun 2016. Available at: <https://doi.org/10.3847%2F0004-637x%2F824%2F1%2F46>. Cited on page 55.

Brown, W. R. et al. The ELM Survey. VIII. Ninety-eight Double White Dwarf Binaries. *The Astrophysical Journal*, American Astronomical Society, v. 889, n. 1, p. 49, jan 2020. Available at: <https://doi.org/10.3847%2F1538-4357%2Fab63cd>. Cited 11 times on pages 38, 54, 78, 98, 102, 103, 107, 110, 111, 112, and 177.

Buchler, J. R.; Yueh, W. R. Compton scattering opacities in a partially degenerate electron plasma at high temperatures. *Astrophysical Journal*, v. 210, p. 440–446, dec. 1976. Cited on page 67.

Buldgen, G. Current problems in stellar evolution. *arXiv e-prints*, p. arXiv:1902.10399, feb. 2019. Proceedings of the PHOST (PHysics of Oscillating STars) meeting. Cited on page 36.

Burbidge, E. M. et al. Synthesis of the Elements in Stars. *Reviews of Modern Physics*, v. 29, n. 4, p. 547–650, jan. 1957. Available at: <https://doi.org/10.1103/RevModPhys.29.547>. Cited on page 61.

Burgers, J. M. *Flow Equations for Composite Gases*. New York: Academic Press, 1969. (Applied mathematics and mechanics). Cited on page 68.

Burnham, S. W. Catalogue of eighty-one double stars observed at Chicago. *Monthly Notices of the Royal Astronomical Society*, v. 33, p. 351, Mar 1873. Cited on page 27.

Burns, E. et al. Opportunities for Multimessenger Astronomy in the 2020s. *Bulletin of the American Astronomical Society*, v. 51, n. 3, p. 250, may 2019. Cited on page 175.

Byrne, C. M.; Jeffery, C. S. Post-common envelope binary stars, radiative levitation, and blue large-amplitude pulsators. *Monthly Notices of the Royal Astronomical Society*, v. 481, n. 3, p. 3810–3820, 09 2018. ISSN 0035-8711. Available at: <https://doi.org/10.1093/mnras/sty2545>. Cited on page 110.

Cadelano, M. et al. Optical Identification of He White Dwarfs Orbiting Four Millisecond Pulsars in the Globular Cluster 47 Tucanae. *Astrophysical Journal*, v. 812, n. 1, p. 63, oct. 2015. Available at: <https://doi.org/10.1088/0004-637X/812/1/63>. Cited on page 92.

Caiazzo, I. et al. A highly magnetized and rapidly rotating white dwarf as small as the Moon. *Nature*, v. 595, n. 7865, p. 39–42, jun. 2021. Available at: <https://doi.org/10.1038/s41586-021-03615-y>. Cited on page 99.

Calcaferro, L. M.; Córsico, A. H.; Althaus, L. r. G. Pulsating low-mass white dwarfs in the frame of new evolutionary sequences. IV. The secular rate of period change. *Astronomy & Astrophysics*, v. 600, p. A73, 2017. Available at: <https://doi.org/10.1051/0004-6361/201630376>. Cited on page 58.

Calcaferro, L. M.; Córsico, A. H.; Althaus, L. r. G. Pulsating low-mass white dwarfs in the frame of new evolutionary sequences. V. Asteroseismology of ELMV white dwarf stars. *Astronomy & Astrophysics*, v. 607, p. A33, 2017. Available at: <https://doi.org/10.1051/0004-6361/201731230>. Cited on page 58.

Calcaferro, L. M. et al. Pulsating low-mass white dwarfs in the frame of new evolutionary sequences. VI. Thin H-envelope sequences and asteroseismology of ELMV stars revisited. *Astronomy & Astrophysics*, v. 620, p. A196, 2018. Available at: <https://doi.org/10.1051/0004-6361/201833781>. Cited on page 58.

Camp, J. B.; Cornish, N. J. Gravitational Wave Astronomy. *Annual Review of Nuclear and Particle Science*, v. 54, p. 525–577, dec. 2004. Available at: <https://doi.org/10.1146/annurev.nucl.54.070103.181251>. Cited on page 175.

Campana, S.; Salvo, T. D. Accreting pulsars: Mixing-up accretion phases in transitional systems. In: _____. *The Physics and Astrophysics of Neutron Stars*. Cham: Springer International Publishing, 2018. p. 149–184. ISBN 978-3-319-97616-7. Available at: <https://doi.org/10.1007/978-3-319-97616-7_4>. Cited on page 39.

Campos, F. et al. A comparative analysis of the observed white dwarf cooling sequence from globular clusters. *Monthly Notices of the Royal Astronomical Society*, v. 456, n. 4, p. 3729–3742, 01 2016. ISSN 0035-8711. Available at: <https://doi.org/10.1093/mnras/stv2911>. Cited on page 37.

Carroll, B. W.; Ostlie, D. A. *An Introduction to Modern Astrophysics*. 2. ed. Cambridge, UK: Cambridge University Press, 2017. ISBN 1108422160,9781108422161. Cited 2 times on pages 78 and 170.

Cassisi, S. et al. Updated Electron-Conduction Opacities: The Impact on Low-Mass Stellar Models. *Astrophysical Journal*, v. 661, p. 1094–1104, jun. 2007. Cited on page 67.

Chapman, S. et al. The formation of binary and multiple star systems. *Nature*, v. 359, n. 6392, p. 207–210, sep. 1992. Available at: <https://doi.org/10.1038/359207a0>. Cited on page 35.

Charles, P. LMXBs: An Overview. In: Schmidtobreick, L.; Schreiber, M. R.; Tappert, C. (Ed.). *Evolution of Compact Binaries*. California, United States: Astronomical Society of the Pacific, 2011. (Astronomical Society of the Pacific Conference Series, v. 447), p. 19. Available at: <http://aspbooks.org/custom/publications/paper/447-0019.html>. Cited 2 times on pages 39 and 81.

Chen, H.-L. et al. Formation of millisecond pulsars with helium white dwarfs, ultra-compact X-ray binaries, and gravitational wave sources. *Monthly Notices of the Royal Astronomical Society*, v. 503, n. 3, p. 3540–3551, may 2021. Available at: <https://doi.org/10.1093/mnras/stab670>. Cited on page 91.

Chen, M. C. et al. The dependence of the evolution of Type Ia SN progenitors on the C-burning rate uncertainty and parameters of convective boundary mixing. *Monthly Notices of the Royal Astronomical Society*, v. 440, n. 2, p. 1274–1280, 03 2014. ISSN 0035-8711. Available at: <https://doi.org/10.1093/mnras/stu108>. Cited on page 64.

Chen, W.-C.; Liu, D.-D.; Wang, B. Detectability of Ultra-compact X-Ray Binaries as LISA Sources. *The Astrophysical Journal Letters*, v. 900, n. 1, p. L8, sep. 2020. Available at: <https://doi.org/10.3847/2041-8213/abae66>. Cited on page 180.

Chen, X. et al. The orbital periods of subdwarf B binaries produced by the first stable Roche Lobe overflow channel. *Monthly Notices of the Royal Astronomical Society*, v. 434, n. 1, p. 186–193, sep. 2013. Available at: <https://doi.org/10.1093/mnras/stt992>. Cited on page 111.

Chen, X. et al. The Formation of EL CVn-type Binaries. *Monthly Notices of the Royal Astronomical Society*, v. 467, n. 2, p. 1874–1889, May 2017. Available at: <https://doi.org/10.1093/mnras/stx115>. Cited 2 times on pages 38 and 55.

Cherepashchuk, A. M. Tesnye Dvoinye Zvezdy (Close Binary Stars). Fizmatlit, Moscow, v. 1, 2013. Cited on page 28.

Cherepashchuk, A. M. Tesnye Dvoinye Zvezdy (Close Binary Stars). Fizmatlit, Moscow, v. 2, 2013. Cited on page 28.

Choi, J. et al. Mesa Isochrones and Stellar Tracks (MIST). I. Solar-scaled Models. *The Astrophysical Journal*, American Astronomical Society, v. 823, n. 2, p. 102, may 2016. Available at: <https://doi.org/10.3847%2F0004-637x%2F823%2F2%2F102>. Cited on page 64.

Christensen-Dalsgaard, J. Solar structure and evolution. *Living Reviews in Solar Physics*, v. 18, n. 1, p. 2, dec. 2021. Available at: <https://doi.org/10.1007/s41116-020-00028-3>. Cited on page 69.

Chugunov, A. I.; Dewitt, H. E.; Yakovlev, D. G. Coulomb tunneling for fusion reactions in dense matter: Path integral MonteCarlo versus mean field. *Physical Review D*, v. 76, n. 2, p. 025028, jul 2007. Cited on page 67.

Clarke, C.; Carswell, B. *Principles of Astrophysical Fluid Dynamics*. Cambridge University Press, 2007. ISBN 9780521853316. Available at: <https://books.google.com.br/books?id=odiiDgAAQBAJ>. Cited on page 73.

Clarke, C. J. The formation of binary stars. *Proceedings of the International Astronomical Union*, Cambridge University Press, v. 2, n. S240, p. 337–346, 2006. Available at: <https://doi.org/10.1017/S1743921307004279>. Cited on page 35.

Clayton, D. D. *Principles of Stellar Evolution and Nucleosynthesis*. Chicago: University of Chicago Press, 1983. (Astronomy/Astrophysics). ISBN 9780226109534. Cited on page 61.

Córsico, A. H.; Althaus, L. G. Pulsating low-mass white dwarfs in the frame of new evolutionary sequences. I. Adiabatic properties. *Astronomy & Astrophysics*, v. 569, p. A106, 2014. Available at: <https://doi.org/10.1051/0004-6361/201424352>. Cited on page 58.

Córsico, A. H.; Althaus, L. G. Short-period g-mode Pulsations in Low-mass White Dwarfs Triggered by H-shell Burning. *The Astrophysical Journal*, IOP Publishing, v. 793, n. 1, p. L17, sep 2014. Available at: <https://doi.org/10.1088%2F2041-8205%2F793%2F1%2Fl17>. Cited on page 58.

Córsico, A. H.; Althaus, L. G. Pulsating low-mass white dwarfs in the frame of new evolutionary sequences. II. Nonadiabatic analysis. *Astronomy & Astrophysics*, v. 585, p. A1, 2016. Available at: <https://doi.org/10.1051/0004-6361/201527162>. Cited on page 58.

Córsico, A. H. et al. Pulsating white dwarfs: new insights. *Astronomy and Astrophysics Reviews*, v. 27, n. 1, p. 7, sep. 2019. Available at: <https://doi.org/10.1007/s00159-019-0118-4>. Cited on page 36.

Córsico, A. H. et al. Pulsating low-mass white dwarfs in the frame of new evolutionary sequences. III. The pre-ELM white dwarf instability strip. *Astronomy & Astrophysics*, v. 588, p. A74, 2016. Available at: <https://doi.org/10.1051/0004-6361/201528032>. Cited on page 58.

Cox, J. P.; Giuli, R. T. *Principles of stellar structure*. New York: Gordon and Breach, 1968. Cited on page 61.

Creighton, J.; Anderson, W. *Gravitational-Wave Physics and Astronomy: An Introduction to Theory, Experiment and Data Analysis.* John Wiley & Sons, Ltd, 2011. ISBN 9783527636037. Available at: <https://doi.org/10.1002/9783527636037>. Cited on page 176.

Cromartie, H. T. et al. Relativistic Shapiro delay measurements of an extremely massive millisecond pulsar. *Nature Astronomy*, v. 4, p. 72–76, jan. 2020. Available at: <https://doi.org/10.1038/s41550-019-0880-2>. Cited on page 92.

Cukanovaite, E. et al. Calibration of the mixing length theory for structures of helium-dominated atmosphere white dwarfs. *Monthly Notices of the Royal Astronomical Society*, 09 2019. ISSN 0035-8711. Stz2656. Available at: <https://doi.org/10.1093/mnras/stz2656>. Cited on page 67.

Cummings, J. D. et al. An Ultramassive 1.28 $M_{\odot}$ White Dwarf in NGC 2099. *Astrophysical Journal Letters*, v. 820, n. 1, p. L18, mar. 2016. Available at: <https://doi.org/10.3847/2041-8205/820/1/L18>. Cited on page 99.

Cummings, J. D. et al. The White Dwarf Initial-Final Mass Relation for Progenitor Stars from 0.85 to 7.5 $M_{\odot}$. *The Astrophysical Journal*, American Astronomical Society, v. 866, n. 1, p. 21, oct 2018. Available at: <https://doi.org/10.3847%2F1538-4357%2Faadfd6>. Cited on page 38.

Cyburt, R. H. et al. The JINA REACLIB Database: Its Recent Updates and Impact on Type-I X-ray Bursts. *Astrophysical Journal, Supplement*, v. 189, p. 240–252, jul 2010. Available at: <https://doi.org/10.1088/0067-0049/189/1/240>. Cited on page 67.

Dall'Osso, S.; Stella, L. Millisecond Magnetars. *arXiv e-prints*, p. arXiv:2103.10878, mar. 2021. Cited on page 40.

D'Antona, F.; Tailo, M. Origin and binary evolution of millisecond pulsars. *arXiv e-prints*, p. arXiv:2011.11385, nov. 2020. Cited on page 40.

de Loore, C. The evolution of massive stars. *Space Science Reviews*, v. 26, n. 2, p. 113–155, jun. 1980. Available at: <https://doi.org/10.1007/BF00167369>. Cited on page 172.

de Loore, C.; Doom, C. *Structure and Evolution of Single and Binary Stars*. Dordrecht: Springer Netherlands, 1992. (Astrophysics and Space Science Library). ISBN 9780792317685. Cited 2 times on pages 61 and 77.

de Marco, O. The origin and shaping of planetary nebulae: Putting the binary hypothesis to the test. *Publications of the Astronomical Society of the Pacific*, IOP Publishing, v. 121, n. 878, p. 316–342, apr 2009. Available at: <https://doi.org/10.1086%2F597765>. Cited on page 172.

de Marco, O.; Izzard, R. G. Dawes Review 6: The Impact of Companions on Stellar Evolution. *Publications of the Astronomical Society of Australia*, Cambridge University Press, v. 34, p. e001, jan. 2017. Available at: <https://doi.org/10.1017/pasa.2016.52>. Cited on page 28.

De Vito, M. A.; Benvenuto, O. G. Evolution of low-mass close binary systems with a neutron star: its dependence with the initial neutron star mass. *Monthly Notices of the Royal Astronomical Society*, v. 401, n. 4, p. 2552–2560, feb. 2010. Available at: <https://doi.org/10.1111/j.1365-2966.2009.15830.x>. Cited 2 times on pages 50 and 102.

De Vito, M. A.; Benvenuto, O. G. The evolution of low-mass, close binary systems with a neutron star component: a detailed grid. *Monthly Notices of the Royal Astronomical Society*, v. 421, n. 3, p. 2206–2222, apr. 2012. Available at: <https://doi.org/10.1111/j.1365-2966.2012.20459.x>. Cited 2 times on pages 50 and 102.

de Vuyst, J. A Natural Introduction to Fine-Tuning. *arXiv e-prints*, p. arXiv:2012.05617, dec. 2020. Available at: <https://arxiv.org/abs/2012.05617>. Cited on page 51.

Deng, Z.-L. et al. Evolution of LMXBs under Different Magnetic Braking Prescriptions. *Astrophysical Journal*, v. 909, n. 2, p. 174, mar. 2021. Available at: <https://doi.org/10.3847/1538-4357/abe0b2>. Cited on page 75.

Denissenkov, P. A. et al. MESA Models of Classical Nova Outbursts: The Multicycle Evolution and Effects of Convective Boundary Mixing. *Astrophysical Journal*, v. 762, n. 1, p. 8, jan. 2013. Available at: <https://doi.org/10.1088/0004-637X/762/1/8>. Cited on page 120.

Denissenkov, P. A. et al. The C-flame Quenching by Convective Boundary Mixing in Super-AGB Stars and the Formation of Hybrid C/O/Ne White Dwarfs and SN Progenitors. *The Astrophysical Journal*, IOP Publishing, v. 772, n. 1, p. 37, jul 2013. Available at: <https://doi.org/10.1088%2F0004-637x%2F772%2F1%2F37>. Cited on page 64.

Denissenkov, P. A. et al. MESA and NuGrid simulations of classical novae: CO and ONe nova nucleosynthesis. *Monthly Notices of the Royal Astronomical Society*, v. 442, n. 3, p. 2058–2074, aug. 2014. Available at: <https://doi.org/10.1093/mnras/stu1000>. Cited on page 120.

Deutsch, E. W.; Margon, B.; Anderson, S. F. Ultracompact X-Ray Binaries in Globular Clusters: Variability of the Optical Counterpart of X1832-330 in NGC 6652. *Astrophysical Journal Letters*, v. 530, n. 1, p. L21–L24, feb. 2000. Available at: <https://doi.org/10.1086/312486>. Cited on page 180.

Dewi, J. D. M. et al. The evolution of naked helium stars with a neutron star companion in close binary systems. *Monthly Notices of the Royal Astronomical Society*, v. 331, n. 4, p. 1027–1040, 04 2002. ISSN 0035-8711. Available at: <https://doi.org/10.1046/j.1365-8711.2002.05257.x>. Cited on page 41.

Dexheimer, V. et al. Phase transitions in neutron stars. *International Journal of Modern Physics E*, v. 27, n. 11, p. 1830008, nov. 2018. Available at: <https://doi.org/10.1142/S0218301318300084>. Cited on page 205.

Di Salvo, T.; Sanna, A. Accretion powered X-ray millisecond pulsars. *arXiv e-prints*, p. arXiv:2010.09005, oct. 2020. Cited on page 40.

Dieball, A. et al. An Ultracompact X-Ray Binary in the Globular Cluster M15 (NGC 7078). *Astrophysical Journal Letters*, v. 634, n. 1, p. L105–L108, nov. 2005. Available at: <https://doi.org/10.1086/498712>. Cited on page 180.

Doherty, C. L. et al. Super- and massive AGB stars – IV. Final fates – initial-to-final mass relation. *Monthly Notices of the Royal Astronomical Society*, v. 446, n. 3, p. 2599–2612, 11 2014. ISSN 0035-8711. Available at: <https://doi.org/10.1093/mnras/stu2180>. Cited on page 37.

Donati, J. F. Large-scale magnetic fields of low-mass dwarfs: the many faces of dynamo. *Proceedings of the International Astronomical Union*, Cambridge University Press, v. 6, n. S271, p. 23–31, 2010. Available at: <https://doi.org/10.1017/S1743921311017431>. Cited on page 48.

Dopcke, G. et al. On the Initial Mass Function of Low-metallicity Stars: The Importance of Dust Cooling. *The Astrophysical Journal*, IOP Publishing, v. 766, n. 2, p. 103, Apr 2013. Cited on page 167.

Dotter, A. MESA Isochrones and Stellar Tracks (MIST) 0: Methods for the Construction of Stellar Isochrones. *The Astrophysical Journal Supplement Series*, American Astronomical Society, v. 222, n. 1, p. 8, jan 2016. Available at: <https://doi.org/10.3847%2F0067-0049%2F222%2F1%2F8>. Cited on page 64.

Driebe, T. et al. The evolution of helium white dwarfs. II. Thermal instabilities. *Astronomy and Astrophysics*, v. 350, p. 89–100, oct. 1999. Available at: <https://arxiv.org/abs/astro-ph/9908156>. Cited on page 49.

Driebe, T. et al. The evolution of helium white dwarfs. I. The companion of the millisecond pulsar PSR J1012+5307. *Astronomy and Astrophysics*, v. 339, p. 123–133, nov. 1998. Available at: <https://arxiv.org/abs/astro-ph/9809079>. Cited on page 49.

Duchêne, G.; Kraus, A. Stellar multiplicity. *Annual Review of Astronomy and Astrophysics*, v. 51, n. 1, p. 269–310, 2013. Available at: <https://doi.org/10.1146/annurev-astro-081710-102602>. Cited 3 times on pages 36, 51, and 92.

Dudorov, A. E.; Khaibrakhmanov, S. A. Theory of fossil magnetic field. *Advances in Space Research*, v. 55, n. 3, p. 843 – 850, 2015. ISSN 0273-1177. Cosmic Magnetic Fields. Available at: <http://www.sciencedirect.com/science/article/pii/S027311771400341X>. Cited on page 48.

Dupret, M.-A. Current problems in stellar pulsation theory. *arXiv e-prints*, p. arXiv:1901.08809, jan. 2019. Proceedings of the PHOST (PHysics of Oscillating STars) meeting. Cited on page 36.

Duquennoy, A.; Mayor, M. Multiplicity among solar-type stars in the solar neighbourhood. II - Distribution of the orbital elements in an unbiased sample. *Astronomy and Astrophysics*, v. 500, p. 337–376, aug. 1991. Available at: <https://ui.adsabs.harvard.edu/abs/1991A&A...248..485D>. Cited on page 51.

Eggleton, P. *Evolutionary Processes in Binary and Multiple Stars*. Cambridge: Cambridge University Press, 2006. (Cambridge Astrophysics). Cited on page 28.

Eggleton, P. P. Approximations to the radii of Roche lobes. *Astrophysical Journal*, v. 268, p. 368, may 1983. Cited 2 times on pages 31 and 70.

Eggleton, P. P.; Tokovinin, A. A. A catalogue of multiplicity among bright stellar systems. *Monthly Notices of the Royal Astronomical Society*, v. 389, n. 2, p. 869–879, 09 2008. ISSN 0035-8711. Available at: <https://doi.org/10.1111/j.1365-2966.2008.13596.x>. Cited on page 53.

El-Badry, K. et al. LAMOST J0140355 + 392651: an evolved cataclysmic variable donor transitioning to become an extremely low-mass white dwarf. *Monthly Notices of the Royal Astronomical Society*, v. 505, n. 2, p. 2051–2073, aug. 2021. Available at: <https://doi.org/10.1093/mnras/stab1318>. Cited on page 39.

El-Badry, K. et al. Birth of the ELMs: a ZTF survey for evolved cataclysmic variables turning into extremely low-mass white dwarfs. *Monthly Notices of the Royal Astronomical Society*, v. 508, n. 3, p. 4106–4139, dec. 2021. Available at: <https://doi.org/10.1093/mnras/stab2583>. Cited 2 times on pages 39 and 55.

Evans, C. R.; Iben, I. J.; Smarr, L. Degenerate Dwarf Binaries as Promising, Detectable Sources of Gravitational Radiation. *Astrophysical Journal*, v. 323, p. 129, dec. 1987. Available at: <https://doi.org/10.1086/165812>. Cited on page 176.

Fabbiano, G. Populations of X-Ray Sources in Galaxies. *Annual Review of Astronomy and Astrophysics*, v. 44, n. 1, p. 323–366, sep. 2006. Available at: <https://doi.org/10.1146/annurev.astro.44.051905.092519>. Cited on page 40.

Farmer, R.; Fields, C. E.; Timmes, F. X. On Carbon Burning in Super Asymptotic Giant Branch Stars. *The Astrophysical Journal*, IOP Publishing, v. 807, n. 2, p. 184, jul 2015. Available at: <https://doi.org/10.1088%2F0004-637x%2F807%2F2%2F184>. Cited on page 64.

Feiden, G. A.; Chaboyer, B. Reevaluating the Mass-Radius Relation for Low-mass, Main-sequence Stars. *Astrophysical Journal*, v. 757, n. 1, p. 42, sep. 2012. Available at: <https://doi.org/10.1088/0004-637X/757/1/42>. Cited on page 36.

Ferguson, J. W. et al. Low-Temperature Opacities. *Astrophysical Journal*, v. 623, p. 585–596, apr 2005. Cited on page 66.

Ferrario, L.; de Martino, D.; Gänsicke, B. T. Magnetic White Dwarfs. *Space Science Reviews*, v. 191, n. 1-4, p. 111–169, oct. 2015. Available at: <https://doi.org/10.1007/s11214-015-0152-0>. Cited on page 57.

Ferrario, L.; Wickramasinghe, D.; Kawka, A. Magnetic fields in isolated and interacting white dwarfs. *Advances in Space Research*, v. 66, n. 5, p. 1025–1056, sep. 2020. Available at: <https://doi.org/10.1016/j.asr.2019.11.012>. Cited 2 times on pages 57 and 120.

Fischer, D. A.; Marcy, G. W. Multiplicity among M Dwarfs. *Astrophysical Journal*, v. 396, p. 178, Sep 1992. Cited on page 53.

Fleury, L.; Caiazzo, I.; Heyl, J. The Cooling of Massive White Dwarfs from Gaia EDR3. *arXiv e-prints*, p. arXiv:2110.00598, oct. 2021. Cited on page 99.

Fonseca, E. et al. Refined Mass and Geometric Measurements of the High-mass PSR J0740+6620. *Astrophysical Journal Letters*, v. 915, n. 1, p. L12, jul. 2021. Available at: <https://doi.org/10.3847/2041-8213/ac03b8>. Cited on page 92.

Fontaine, G.; Brassard, P.; Bergeron, P. The potential of white dwarf cosmochronology. *Publications of the Astronomical Society of the Pacific*, IOP Publishing, v. 113, n. 782, p. 09–435, apr 2001. Available at: <https://doi.org/10.1086%2F319535>. Cited on page 37.

Forbes, J. C.; Loeb, A. On the Existence of Brown Dwarfs More Massive than the Hydrogen Burning Limit. *Astrophysical Journal*, v. 871, n. 2, p. 227, feb. 2019. Available at: <https://doi.org/10.3847/1538-4357/aafac8>. Cited on page 64.

Fortin, M. et al. Progenitor neutron stars of the lightest and heaviest millisecond pulsars. *Astronomy and Astrophysics*, v. 586, p. A109, feb. 2016. Available at: <https://doi.org/10.1051/0004-6361/201424911>. Cited on page 77.

Frank, J.; King, A.; Raine, D. J. *Accretion Power in Astrophysics: Third Edition*. Cambridge, UK: Cambridge University Press, 2002. ISBN 0521620538. Cited on page 43.

Fuller, G. M.; Fowler, W. A.; Newman, M. J. Stellar weak interaction rates for intermediate-mass nuclei. IV - Interpolation procedures for rapidly varying lepton capture rates using effective log (ft)-values. *Astrophysical Journal*, v. 293, p. 1–16, jun 1985. Cited on page 67.

Fuller, J.; Lai, D. Dynamical tides in compact white dwarf binaries: helium core white dwarfs, tidal heating and observational signatures. *Monthly Notices of the Royal Astronomical Society*, v. 430, n. 1, p. 274–287, 01 2013. ISSN 0035-8711. Available at: <https://doi.org/10.1093/mnras/sts606>. Cited on page 54.

Gaia Collaboration et al. Gaia data release 2 - observational hertzsprung-russell diagrams. *Astronomy & Astrophysics*, v. 616, p. A10, 2018. Available at: <https://doi.org/10.1051/0004-6361/201832843>. Cited on page 56.

Garaud, P. Double-Diffusive Convection at Low Prandtl Number. *Annual Review of Fluid Mechanics*, v. 50, n. 1, p. 275–298, jan. 2018. Available at: <https://doi.org/10.1146/annurev-fluid-122316045234>. Cited on page 63.

García-Berro, E.; Isern, J.; Hernanz, M. The cooling of oxygen—neon white dwarfs. *Monthly Notices of the Royal Astronomical Society*, v. 289, n. 4, p. 973–978, 08 1997. ISSN 0035-8711. Available at: <https://doi.org/10.1093/mnras/289.4.973>. Cited on page 37.

García-Berro, E.; Kilic, M.; Kepler, S. O. Magnetic white dwarfs: Observations, theory and future prospects. *International Journal of Modern Physics D*, v. 25, n. 1, p. 1630005, jan. 2016. Available at: <https://doi.org/10.1142/S0218271816300056>. Cited 2 times on pages 57 and 120.

García-Berro, E.; Kilic, M.; Kepler, S. O. Magnetic white dwarfs: Observations, theory and future prospects. In: Bianchi, M.; Jansen, R. T.; Ruffini, R. (Ed.). *Fourteenth Marcel Grossmann Meeting - MG14*. Singapore: World Scientific Publishing, 2018. p. 988–1005. Available at: <https://doi.org/10.1142/9789813226609_0052>. Cited 2 times on pages 57 and 120.

García-Berro, E.; Oswalt, T. D. The white dwarf luminosity function. *New Astronomy Reviews*, v. 72-74, p. 1 – 22, 2016. ISSN 1387-6473. Available at: <http://www.sciencedirect.com/science/article/pii/S138764731630046X>. Cited on page 37.

García-Berro, E. et al. A white dwarf cooling age of 8 Gyr for NGC 6791 from physical separation processes. *Nature*, v. 465, n. 7295, p. 194–196, May 2010. Available at: <https://www.nature.com/articles/nature09045>. Cited on page 37.

Gautschy, A. The Thermal Pulses of Very-Low-Mass Stars. *arXiv e-prints*, p. arXiv:1303.6652, mar. 2013. Available at: <https://arxiv.org/abs/1303.6652>. Cited 2 times on pages 80 and 107.

Gentile Fusillo, N. P. et al. A Gaia Data Release 2 catalogue of white dwarfs and a comparison with SDSS. *Monthly Notices of the Royal Astronomical Society*, v. 482, n. 4, p. 4570–4591, feb. 2019. Available at: <https://doi.org/10.1093/mnras/sty3016>. Cited 2 times on pages 54 and 107.

Gilfanov, M. Low-mass X-ray binaries as a stellar mass indicator for the host galaxy. *Monthly Notices of the Royal Astronomical Society*, v. 349, n. 1, p. 146–168, mar. 2004. Available at: <https://doi.org/10.1111/j.1365-2966.2004.07473.x>. Cited on page 40.

Giovannelli, F. Cataclysmic Variables: A Review. *Chinese Journal of Astronomy and Astrophysics Supplement*, v. 8, p. 237–258, oct. 2008. Available at: <http://articles.adsabs.harvard.edu/pdf/2008ChJAS...8..237G>. Cited on page 39.

Giovannelli, F.; Sabau Graziati, L. An overview of X-Ray and Gamma-ray sources. In: Giovannelli, F.; Mannocchi, G. (Ed.). *Frontier Objects in Astrophysics and Particle Physics*. Bologna: Società Italiana di Fisica, 1993. p. 15. Cited on page 81.

Giovannelli, F.; Sabau-Graziati, L. The Impact of Space Experiments on our Knowledge of the Physics of the Universe. *Space Science Reviews*, v. 112, n. 1, p. 1–443, may 2004. Available at: <https://doi.org/10.1023/B:SPAC.0000032807.99883.09>. Cited on page 175.

Goodwin, A. J.; Woods, T. E. The binary evolution of SAX J1808.4-3658: implications of an evolved donor star. *Monthly Notices of the Royal Astronomical Society*, v. 495, n. 1, p. 796–805, jun. 2020. Available at: <https://doi.org/10.1093/mnras/staa1234>. Cited 2 times on pages 113 and 114.

Gossage, S. et al. MESA Models with Magnetic Braking. *Astrophysical Journal*, v. 912, n. 1, p. 65, may 2021. Available at: <https://doi.org/10.3847/1538-4357/abebdf>. Cited on page 75.

Götberg, Y. et al. Contribution from stars stripped in binaries to cosmic reionization of hydrogen and helium. *Astronomy and Astrophysics*, v. 634, p. A134, feb. 2020. Available at: <https://doi.org/10.1051/0004-6361/201936669>. Cited on page 64.

Götberg, Y. et al. Stars Stripped in Binaries: The Living Gravitational-wave Sources. *Astrophysical Journal*, v. 904, n. 1, p. 56, nov. 2020. Available at: <https://doi.org/10.3847/1538-4357/abbda5>. Cited on page 64.

Gratton, R. G.; Carretta, E.; Bragaglia, A. Multiple populations in globular clusters. Lessons learned from the Milky Way globular clusters. *Astronomy and Astrophysics Reviews*, v. 20, p. 50, feb. 2012. Available at: <https://doi.org/10.1007/s00159-012-0050-3>. Cited on page 36.

Greenwood, N. N.; Earnshaw, A. *Chemistry of the Elements*. Amsterdam, Netherlands: Elsevier Science, 2012. ISBN 9780080501093. Cited on page 173.

Guinan, E. F.; Engle, S. G. The Brave New World of Binary Star Studies. *Astrophysics and Space Science*, v. 304, n. 1-4, p. 5–11, aug. 2006. Available at: <https://doi.org/10.1007/s10509-006-9069-0>. Cited on page 27.

Güver, T. et al. The Mass and Radius of the Neutron Star in 4U 1820-30. *Astrophysical Journal*, v. 719, n. 2, p. 1807–1812, aug. 2010. Available at: <https://doi.org/10.1088/0004-637X/719/2/1807>. Cited on page 180.

Halbwachs, J. L. et al. Multiplicity among solar-type stars. III. Statistical properties of the F7-K binaries with periods up to 10 years. *Astronomy and Astrophysics*, v. 397, p. 159–175, jan. 2003. Available at: <https://doi.org/10.1051/0004-6361:20021507>. Cited on page 28.

Hameury, J. M. et al. Structure and evolution of X-ray heated compact binaries. *Astronomy and Astrophysics*, v. 277, p. 81–92, sep. 1993. Available at: <https://ui.adsabs.harvard.edu/abs/1993A&A...277...81H>. Cited on page 113.

Hameury, J. M.; Ritter, H. Illumination in binaries. *Astronomy and Astrophysics Supplement Series*, v. 123, p. 273–277, jun. 1997. Available at: <https://doi.org/10.1051/aas:1997160>. Cited on page 113.

Han, X.-Q.; Jiang, L.; Chen, W.-C. Influence of Irradiation-driven Winds on the Evolution of Intermediate-mass Black Hole X-ray Binaries. *Astrophysical Journal*, v. 914, n. 2, p. 109, jun. 2021. Available at: <https://doi.org/10.3847/1538-4357/abfcc3>. Cited on page 64.

Han, Z.-W. et al. Binary Population Synthesis. *Research in Astronomy and Astrophysics*, v. 20, n. 10, p. 161, oct. 2020. Available at: <https://doi.org/10.1088/1674-4527/20/10/161>. Cited on page 42.

Hansen, C.; Kawaler, S.; Trimble, V. *Stellar Interiors: Physical Principles, Structure, and Evolution*. 2. ed. Springer-Verlag New York, 2004. (Astronomy and Astrophysics Library). ISBN 978-1-4612-6497-2,978-1-4419-9110-2. Available at: <http://gen.lib.rus.ec/book/index.php?md5=2e998a4e1aed38d32e3f3843e1d78b4e>. Cited 2 times on pages 61 and 170.

Harding, A. K. The neutron star zoo. *Frontiers of Physics*, v. 8, n. 6, p. 679–692, dec. 2013. Available at: <https://doi.org/10.1007/s11467-013-0285-0>. Cited 2 times on pages 39 and 120.

Harpaz, A.; Rappaport, S. Episodic Mass Transfer in Binaries with X-Ray Heating. *Astrophysical Journal*, v. 434, p. 283, oct. 1994. Available at: <https://doi.org/10.1086/174726>. Cited on page 113.

Harris, W. E. A Catalog of Parameters for Globular Clusters in the Milky Way. *Astronomical Journal*, v. 112, p. 1487, oct. 1996. Available at: <https://doi.org/10.1086/118116>. Cited on page 180.

Hawking, S. W.; Israel, W. *Three Hundred Years of Gravitation*. Cambridge UK: Cambridge University Press, 1989. (Philosophiae Naturalis, Principia Mathematica). ISBN 9780521379762. Cited on page 175.

He, X.; Meng, X.-C.; Chen, H.-L. Formation of accreting millisecond X-ray pulsars. *Research in Astronomy and Astrophysics*, IOP Publishing, v. 19, n. 8, p. 110, aug 2019. Available at: <https://doi.org/10.1088%2F1674-4527%2F19%2F8%2F110>. Cited on page 51.

Heber, U. Hot Subdwarf Stars. *Annual Review of Astronomy and Astrophysics*, v. 47, n. 1, p. 211–251, sep. 2009. Available at: <https://doi.org/10.1146/annurev-astro-082708-101836>. Cited on page 110.

Heber, U. Hot Subluminous Stars. *Publications of the Astronomical Society of the Pacific*, v. 128, n. 966, p. 082001, aug. 2016. Available at: <https://doi.org/10.1088/1538-3873/128/966/082001>. Cited on page 110.

Heger, A.; Langer, N.; Woosley, S. E. Presupernova Evolution of Rotating Massive Stars. I. Numerical Method and Evolution of the Internal Stellar Structure. *Astrophysical Journal*, v. 528, n. 1, p. 368–396, Jan 2000. Cited 2 times on pages 68 and 69.

Heger, A.; Woosley, S. E.; Spruit, H. C. Presupernova Evolution of Differentially Rotating Massive Stars Including Magnetic Fields. *Astrophysical Journal*, v. 626, n. 1, p. 350–363, Jun 2005. Cited on page 68.

Heinke, C. O.; Edmonds, P. D.; Grindlay, J. E. Identification of the Low-Mass X-Ray Binary and Faint X-Ray Sources in NGC 6652. *Astrophysical Journal*, v. 562, n. 1, p. 363–367, nov. 2001. Available at: <https://doi.org/10.1086/323493>. Cited on page 180.

Heintz, W. D. A Statistical Study of Binary Stars. *Journal of the Royal Astronomical Society of Canada*, v. 63, p. 275, dec. 1969. Available at: <https://ui.adsabs.harvard.edu/abs/1969JRASC..63..275H>. Cited on page 28.

Henyey, L.; Vardya, M. S.; Bodenheimer, P. Studies in Stellar Evolution. III. The Calculation of Model Envelopes. *Astrophysical Journal*, v. 142, p. 841, Oct 1965. Cited on page 67.

Henyey, L. G.; Forbes, J. E.; Gould, N. L. A New Method of Automatic Computation of Stellar Evolution. *Astrophysical Journal*, v. 139, p. 306, jan. 1964. Available at: <https://doi.org/10.1086/147754>. Cited on page 48.

Herczeg, T. Duplicity on the Main Sequence. *Astrophysics and Space Science*, v. 99, n. 80, p. 29, feb. 1984. Available at: <https://doi.org/10.1007/BF00650228>. Cited on page 53.

Hermes, J. J. et al. A new class of pulsating white dwarf of extremely low mass: the fourth and fifth members. *Monthly Notices of the Royal Astronomical Society*, v. 436, n. 4, p. 3573–3580, dec. 2013. Available at: <https://doi.org/10.1093/mnras/stt1835>. Cited on page 38.

Hermes, J. J. et al. Discovery of Pulsations, Including Possible Pressure Modes, in Two New Extremely Low Mass, He-core White Dwarfs. *Astrophysical Journal*, v. 765, n. 2, p. 102, mar. 2013. Available at: <https://doi.org/10.1088/0004-637X/765/2/102>. Cited on page 38.

Herschel, J. F. W. *A Treatise on Astronomy*. Cambridge, UK: Cambridge University Press, 2009. (Cambridge Library Collection - Astronomy). ISBN 9780511694325,9781108005548. Cited on page 25.

Herwig, F. The evolution of AGB stars with convective overshoot. *Astronomy and Astrophysics*, v. 360, p. 952–968, Aug 2000. Cited on page 68.

Hewish, A. et al. Observation of a Rapidly Pulsating Radio Source. *Nature*, v. 217, n. 5130, p. 709–713, Feb 1968. Cited on page 39.

Hilditch, R. W. *An Introduction to Close Binary Stars*. Cambridge: Cambridge University Press, 2001. (Cambridge Astrophysics). ISBN 9780521798006. Cited on page 28.

Hiramatsu, D. et al. The electron-capture origin of supernova 2018zd. *Nature Astronomy*, v. 5, p. 903–910, jun. 2021. Available at: <https://doi.org/10.1038/s41550-021-01384-2>. Cited on page 64.

Höfner, S.; Olofsson, H. Mass loss of stars on the asymptotic giant branch. Mechanisms, models and measurements. *The Astronomy and Astrophysics Review*, v. 26, n. 1, p. 1, Jan 2018. ISSN 1432-0754. Available at: <https://doi.org/10.1007/s00159-017-0106-5>. Cited on page 38.

Hollands, M. A. et al. An ultra-massive white dwarf with a mixed hydrogen-carbon atmosphere as a likely merger remnant. *Nature Astronomy*, v. 4, p. 663–669, mar. 2020. Available at: <https://doi.org/10.1038/s41550-020-1028-0>. Cited on page 99.

Homer, L. et al. Periodic UV modulation of X1850-087: a double degenerate binary in the globular cluster NGC 6712? *Monthly Notices of the Royal Astronomical Society*, v. 282, n. 3, p. L37–L46, oct. 1996. Available at: <https://doi.org/10.1093/mnras/282.3.L37>. Cited on page 180.

Hoxie, D. T. The Structure and Evolution of Stars of Very Low Mass. *Astrophysical Journal*, v. 161, p. 1083, sep. 1970. Available at: <https://doi.org/10.1086/150609>. Cited on page 36.

Hoxie, D. T. The low-mass main-sequence: the comparison between theory and observation. *Astronomy and Astrophysics*, v. 26, p. 437, aug. 1973. Cited on page 36.

Huang, S.-J. et al. Science with the TianQin Observatory: Preliminary results on Galactic double white dwarf binaries. *Physical Review D*, v. 102, n. 6, p. 063021, sep. 2020. Available at: <https://doi.org/10.1103/PhysRevD.102.063021>. Cited on page 176.

Hulse, R. A.; Taylor, J. H. Discovery of a pulsar in a binary system. *Astrophysical Journal*, v. 195, p. L51–L53, Jan 1975. Cited on page 39.

Hurley, J. R.; Pols, O. R.; Tout, C. A. Comprehensive analytic formulae for stellar evolution as a function of mass and metallicity. *Monthly Notices of the Royal Astronomical Society*, v. 315, n. 3, p. 543–569, jul. 2000. Available at: <https://doi.org/10.1046/j.1365-8711.2000.03426.x>. Cited on page 170.

Hurley, J. R.; Tout, C. A.; Pols, O. R. Evolution of binary stars and the effect of tides on binary populations. *Monthly Notices of the Royal Astronomical Society*, v. 329, n. 4, p. 897–928, Feb 2002. Cited on page 70.

Hut, P. Tidal evolution in close binary systems. *Astronomy and Astrophysics*, v. 99, p. 126–140, jun. 1981. Cited on page 69.

Iben, I.; Tutukov, A. V.; Yungelson, L. R. A Model of the Galactic X-Ray Binary Population. I. High-Mass X-Ray Binaries. *Astrophysical Journal Supplement*, v. 100, p. 217, sep. 1995. Available at: <https://doi.org/10.1086/192217>. Cited on page 40.

Iben, I.; Tutukov, A. V.; Yungelson, L. R. A Model of the Galactic X-Ray Binary Population. II. Low-Mass X-Ray Binaries in the Galactic Disk. *Astrophysical Journal Supplement*, v. 100, p. 233, sep. 1995. Available at: <https://doi.org/10.1086/192218>. Cited on page 40.

Iben, I. J. Erratum: Stellar Evolution. I. The Approach to the Main Sequence. *Astrophysical Journal*, v. 142, p. 421, jul. 1965. Cited on page 169.

Iben, I. J. Stellar Evolution. I. The Approach to the Main Sequence. *Astrophysical Journal*, v. 141, p. 993, apr. 1965. Cited on page 169.

Iben, I. J. Stellar Evolution. II. The Evolution of a 3 $M_{\odot}$ Star from the Main Sequence Through Core Helium Burning. *Astrophysical Journal*, v. 142, p. 1447, nov. 1965. Cited on page 169.

Iben, I. J. Stellar Evolution. III. The Evolution of a 5 $M_{\odot}$ Star from the Main Sequence Through Core Helium Burning. *Astrophysical Journal*, v. 143, p. 483, feb. 1966. Cited on page 169.

Iben, I. J. Stellar Evolution. IV. The Evolution of a 9 $M_{\odot}$ Star from the Main Sequence Through Core Helium Burning. *Astrophysical Journal*, v. 143, p. 505, feb. 1966. Cited on page 169.

Iben, I. J. Stellar Evolution. V. The Evolution of a 15 $M_{\odot}$ Star from the Main Sequence Through Core Helium. *Astrophysical Journal*, v. 143, p. 516, feb. 1966. Cited on page 169.

Iben, I. J. Stellar Evolution: Comparison of Theory with Observation. *Science*, v. 155, n. 3764, p. 785–796, feb. 1967. Cited on page 169.

Iben, I. J. Stellar Evolution. VI. Evolution from the Main Sequence to the Red-Giant Branch for Stars of Mass 1 $M_{\odot}$, 1.25 $M_{\odot}$, and 1.5 $M_{\odot}$. *Astrophysical Journal*, v. 147, p. 624, feb. 1967. Cited on page 169.

Iben, I. J. Stellar Evolution. VII. The Evolution of a 2.25 $M_{\odot}$ Star from the Main Sequence to the Helium-Burning Phase. *Astrophysical Journal*, v. 147, p. 650, feb. 1967. Cited on page 169.

Iben, I. J. Stellar Evolution Within and off the Main Sequence. *Annual Review of Astronomy and Astrophysics*, v. 5, p. 571, jan. 1967. Cited on page 169.

Iben, I. J. Single and Binary Star Evolution. *Astrophysical Journal Supplement*, v. 76, p. 55, may 1991. Cited on page 169.

Iben, I. J. *Stellar Evolution Physics, Volume 1: Physical Processes in Stellar Interiors*. Cambridge, UK: Cambridge University Press, 2013. ISBN 9781107602533. Cited on page 61.

Iben, I. J. *Stellar Evolution Physics, Volume 2: Advanced Evolution of Single Stars*. Cambridge, UK: Cambridge University Press, 2013. ISBN 9781107016569. Cited on page 61.

Iben, I. J.; MacDonald, J. The effects of diffusion due to gravity and due to composition gradients on the rate of hydrogen burning in a cooling degenerate dwarf. I - The case of a thick helium buffer layer. *Astrophysical Journal*, v. 296, p. 540–553, Sep 1985. Cited 2 times on pages 68 and 114.

Iben, I. J.; Tutukov, A. V. Supernovae of type I as end products of the evolution of binaries with components of moderate initial mass. *Astrophysical Journal Supplement Series*, v. 54, p. 335–372, Feb 1984. Cited on page 55.

Iglesias, C. A.; Rogers, F. J. Radiative opacities for carbon- and oxygen-rich mixtures. *Astrophysical Journal*, v. 412, p. 752–760, aug 1993. Cited on page 66.

Iglesias, C. A.; Rogers, F. J. Updated Opal Opacities. *Astrophysical Journal*, v. 464, p. 943, jun 1996. Cited on page 66.

Iliadis, C. *Nuclear Physics of Stars*. Weinheim: Wiley, 2007. Cited on page 61.

in't Zand, J. J. M.; Jonker, P. G.; Markwardt, C. B. Six new candidate ultracompact X-ray binaries. *Astronomy and Astrophysics*, v. 465, n. 3, p. 953–963, apr. 2007. Available at: <https://doi.org/10.1051/0004-6361:20066678>. Cited on page 180.

Istrate, A. G. et al. Asteroseismic test of rotational mixing in low-mass white dwarfs. *Astronomy & Astrophysics*, v. 595, p. L12, 2016. Available at: <https://doi.org/10.1051/0004-6361/201629876>. Cited on page 58.

Istrate, A. G.; Fontaine, G.; Heuser, C. A model of the pulsating extremely low-mass white dwarf precursor WASP 0247–25B. *The Astrophysical Journal*, American Astronomical Society, v. 847, n. 2, p. 130, sep 2017. Available at: <https://doi.org/10.3847%2F1538-4357%2Faa8958>. Cited on page 64.

Istrate, A. G. et al. Models of low-mass helium white dwarfs including gravitational settling, thermal and chemical diffusion, and rotational mixing. *Astronomy & Astrophysics*, v. 595, p. A35, 2016. Available at: <https://doi.org/10.1051/0004-6361/201628874>. Cited 15 times on pages 50, 51, 53, 58, 64, 69, 73, 77, 78, 91, 92, 93, 95, 114, and 115.

Istrate, A. G.; Tauris, T. M.; Langer, N. The formation of low-mass helium white dwarfs orbiting pulsars - evolution of low-mass x-ray binaries below the bifurcation period. *Astronomy & Astrophysics*, v. 571, p. A45, 2014. Available at: <https://doi.org/10.1051/0004-6361/201424680>. Cited 5 times on pages 51, 58, 92, 93, and 103.

Istrate, A. G. et al. The timescale of low-mass proto-helium white dwarf evolution. *Astronomy & Astrophysics*, v. 571, p. L3, 2014. Available at: <https://doi.org/10.1051/0004-6361/201424681>. Cited 3 times on pages 50, 58, and 93.

Itoh, N. et al. Neutrino Energy Loss in Stellar Interiors. VII. Pair, Photo-, Plasma, Bremsstrahlung, and Recombination Neutrino Processes. *Astrophysical Journal, Supplement*, v. 102, p. 411, feb 1996. Available at: <https://doi.org/10.1086/192264>. Cited on page 67.

Ivanova, N. Low-Mass X-Ray Binaries with Pre-Main-Sequence Companions. *The Astrophysical Journal*, IOP Publishing, v. 653, n. 2, p. L137–L140, dec 2006. Available at: <https://doi.org/10.1086%2F510672>. Cited on page 74.

Ivanova, N. et al. Formation and evolution of compact binaries in globular clusters - I. Binaries with white dwarfs. *Monthly Notices of the Royal Astronomical Society*, v. 372, n. 3, p. 1043–1059, nov. 2006. Available at: <https://doi.org/10.1111/j.1365-2966.2006.10876.x>. Cited on page 39.

Ivanova, N. et al. Formation and evolution of compact binaries in globular clusters - II. Binaries with neutron stars. *Monthly Notices of the Royal Astronomical Society*, v. 386, n. 1, p. 553–576, may 2008. Available at: <https://doi.org/10.1111/j.1365-2966.2008.13064.x>. Cited on page 39.

Ivanova, N. et al. Common envelope evolution: where we stand and how we can move forward. *The Astronomy and Astrophysics Review*, v. 21, p. 59, feb. 2013. Available at: <https://doi.org/10.1007/s00159-013-0059-2>. Cited 2 times on pages 41 and 78.

Ivanova, N.; Taam, R. E. Magnetic braking revisited. *The Astrophysical Journal*, IOP Publishing, v. 599, n. 1, p. 516–521, dec 2003. Available at: <https://doi.org/10.1086%2F379192>. Cited on page 57.

Jacoby, B. A. et al. The Mass of a Millisecond Pulsar. *The Astrophysical Journal*, v. 629, n. 2, p. L113–L116, aug. 2005. Available at: <https://doi.org/10.1086/449311>. Cited on page 78.

Jaschek, M.; Egret, D. Catalog of Be stars. In: Jaschek, M.; Groth, H. G. (Ed.). *Be Stars*. Dordrecht: D. Reidel Publishing, 1982. (IAU Symposium, v. 98), p. 261. Cited on page 41.

Jawor, J. A.; Tauris, T. M. Modelling spin evolution of magnetars. *arXiv e-prints*, p. arXiv:2109.07484, sep. 2021. Available at: <https://ui.adsabs.harvard.edu/abs/2021arXiv210907484J>. Cited on page 120.

Jeans, J. H. The Stability of a Spherical Nebula. *Philosophical Transactions of the Royal Society of London Series A*, v. 199, p. 1–53, Jan 1902. Cited on page 167.

Jet Propulsion Laboratory. *Stellar Evolution*. 2019. Available at: <https://www.jpl.nasa.gov/infographics/uploads/infographics/full/10737.jpg>. Accessed on: 18 sep 2019. Cited on page 168.

Johnson, J. *The Origin of the Elements in the Solar System*. 2017. The Origin of the Elements. Available at: <http://www.astronomy.ohio-state.edu/~jaj/nucleo>. Accessed on: 14 oct 2021. Cited on page 172.

Jones, S. et al. Advanced Burning Stages and Fate of 8–10 $M_{\odot}$ Stars. *The Astrophysical Journal*, IOP Publishing, v. 772, n. 2, p. 150, jul 2013. Available at: <https://doi.org/10.1088%2F0004-637x%2F772%2F2%2F150>. Cited on page 64.

José, J.; Hernanz, M. Nucleosynthesis in classical nova explosions. *Journal of Physics G Nuclear Physics*, v. 34, n. 12, p. R431–R458, dec. 2007. Available at: <https://doi.org/10.1088/0954-3899/34/12/R01>. Cited on page 120.

José, J.; Shore, S. N.; Casanova, J. 123-321 models of classical novae. *Astronomy and Astrophysics*, v. 634, p. A5, feb. 2020. Available at: <https://doi.org/10.1051/0004-6361/201936893>. Cited on page 120.

Joss, P. C.; Rappaport, S.; Lewis, W. The Core Mass–Radius Relation for Giants: A New Test of Stellar Evolution Theory. *Astrophysical Journal*, v. 319, p. 180, aug. 1987. Available at: <https://doi.org/10.1086/165443>. Cited on page 96.

Kalirai, J. S. The age of the Milky Way inner halo. *Nature*, v. 486, n. 7401, p. 90–92, Jun 2012. Cited on page 37.

Karakas, A. I.; Lattanzio, J. C. The Dawes Review 2: Nucleosynthesis and Stellar Yields of Low- and Intermediate-Mass Single Stars. *Publications of the Astronomical Society of Australia*, v. 31, p. e030, jul. 2014. Available at: <https://doi.org/10.1017/pasa.2014.21>. Cited 2 times on pages 61 and 169.

Kaspi, V. M. The Neutron Star Zoo. In: Weltevrede, P. et al. (Ed.). *Pulsar Astrophysics the Next Fifty Years*. Cambridge, UK: Cambridge University Press, 2017. v. 13, n. S337, p. 3–8. Available at: <https://doi.org/10.1017/S1743921317010390>. Cited 2 times on pages 39 and 120.

Kato, S. Overstable Convection in a Medium Stratified in Mean Molecular Weight. *Publications of the Astronomical Society of Japan*, v. 18, p. 374, jan. 1966. Cited on page 62.

Kawka, A.; Vennes, S. A new extremely low-mass white dwarf in the NLTT catalogue. *Astronomy and Astrophysics*, v. 506, n. 2, p. L25–L28, nov. 2009. Available at: <https://doi.org/10.1051/0004-6361/200912954>. Cited on page 38.

Kepler, J. *New astronomy*. Cambridge, UK: Cambridge University Press, 1992. Translated by William H. Donahue. ISBN 0-521-30131-9. Cited on page 30.

Kepler, J. *The Harmony of the World*. Philadelphia, Pennsylvania, US: American Philosophical Society, 1997. Translated by E. J. Aiton, A. M. Duncan and J. V. Field. ISBN 0871692090,978-0871692092. Cited on page 30.

Kepler, S. O. et al. White dwarf and subdwarf stars in the Sloan Digital Sky Survey Data Release 16. *Monthly Notices of the Royal Astronomical Society*, aug. 2021. ISSN 0035-8711. Stab2411. Available at: <https://doi.org/10.1093/mnras/stab2411>. Cited on page 37.

Kepler, S. O. et al. Magnetic white dwarf stars in the Sloan Digital Sky Survey. *Monthly Notices of the Royal Astronomical Society*, v. 429, n. 4, p. 2934–2944, mar. 2013. Available at: <https://doi.org/10.1093/mnras/sts522>. Cited on page 120.

Kepler, S. O. et al. White dwarf and subdwarf stars in the Sloan Digital Sky Survey Data Release 14. *Monthly Notices of the Royal Astronomical Society*, v. 486, n. 2, p. 2169–2183, jun. 2019. Available at: <https://doi.org/10.1093/mnras/stz960>. Cited on page 37.

Kepler, S. O. et al. The Pulsating White Dwarf G117-B15A: Still the Most Stable Optical Clock Known. *Astrophysical Journal*, v. 906, n. 1, p. 7, jan. 2021. Available at: <https://doi.org/10.3847/1538-4357/abc626>. Cited on page 37.

Keszthelyi, Z. et al. The effects of surface fossil magnetic fields on massive star evolution - III. The case of τ Sco. *Monthly Notices of the Royal Astronomical Society*, v. 504, n. 2, p. 2474–2492, jun. 2021. Available at: <https://doi.org/10.1093/mnras/stab893>. Cited on page 64.

Kilic, M. et al. The Lowest Mass White Dwarf. *Astrophysical Journal*, v. 660, n. 2, p. 1451–1461, May 2007. Available at: <https://doi.org/10.1086/514327>. Cited on page 38.

Kilic, M. et al. The most massive white dwarfs in the solar neighbourhood. *Monthly Notices of the Royal Astronomical Society*, v. 503, n. 4, p. 5397–5408, jun. 2021. Available at: <https://doi.org/10.1093/mnras/stab767>. Cited on page 99.

Kilic, M. et al. The Discovery of Two LISA Sources within 0.5 kpc. *Astrophysical Journal Letters*, v. 918, n. 1, p. L14, sep. 2021. Available at: <https://doi.org/10.3847/2041-8213/ac1e2b>. Cited on page 175.

Kilic, M.; Stanek, K. Z.; Pinsonneault, M. H. The Future Is Now: The Formation of Single Low-Mass White Dwarfs in the Solar Neighborhood. *Astrophysical Journal*, v. 671, n. 1, p. 761–766, Dec 2007. Available at: <https://doi.org/10.1086/522228>. Cited on page 37.

Kippenhahn, R.; Kohl, K.; Weigert, A. Entwicklung in engen Doppelstern systemen II. Die Entstehung von weissen Zwergen durch Massenaustausch. *Zeitschrift fur Astrophysik*, v. 66, p. 58, Jan 1967. Cited on page 45.

Kippenhahn, R.; Ruschenplatt, G.; Thomas, H. C. The time scale of thermohaline mixing in stars. *Astronomy and Astrophysics*, v. 91, n. 1-2, p. 175–180, Nov 1980. Cited on page 67.

Kippenhahn, R.; Thomas, H. C.; Weigert, A. Entwicklung in engen Doppelsternsystemen V. Thermal Pulses in the White Dwarf Component of a Binary System. *Zeitschrift für Astrophysik*, v. 69, p. 265, jan. 1968. Available at: <http://articles.adsabs.harvard.edu/pdf/1968ZA.....69..265K>. Cited on page 80.

Kippenhahn, R.; Weigert, A.; Weiss, A. *Stellar Structure and Evolution*. Berlin Heidelberg: Springer-Verlag, 2012. (Astronomy and Astrophysics Library). Cited 3 times on pages 61, 170, and 171.

Knigge, C. Cataclysmic variables in globular clusters. *Memorie della Società Astronomica Italiana*, v. 83, p. 549, jan. 2012. Cited on page 39.

Knigge, C.; Baraffe, I.; Patterson, J. The Evolution of Cataclysmic Variables as Revealed by Their Donor Stars. *Astrophysical Journal Supplement*, v. 194, n. 2, p. 28, jun. 2011. Available at: <https://doi.org/10.1088/0067-0049/194/2/28>. Cited 2 times on pages 39 and 75.

Kobulnicky, H. A.; Fryer, C. L. A new look at the binary characteristics of massive stars. *The Astrophysical Journal*, IOP Publishing, v. 670, n. 1, p. 747–765, nov 2007. Available at: <https://doi.org/10.1086%2F522073>. Cited on page 53.

Kolb, U.; Ritter, H. A comparative study of the evolution of a close binary using a standard and an improved technique for computing mass transfer. *Astronomy and Astrophysics*, v. 236, p. 385–392, Sep 1990. Cited on page 70.

Kopal, Z. Evolutionary processes in close binary stars. *Annales d'Astrophysique*, v. 19, p. 298, Jan 1956. Cited on page 31.

Kopal, Z. *Close binary systems*. New York: Wiley, 1959. Cited on page 28.

Kopal, Z. *Dynamics of Close Binary Systems*. Dordrecht: Springer Netherlands, 1978. (Astrophysics and Space Science Library). ISBN 9789027708205. Available at: <https://doi.org/10.1007/978-94-009-9780-6>. Cited on page 28.

Korol, V. et al. Prospects for detection of detached double white dwarf binaries with Gaia, LSST and LISA. *Monthly Notices of the Royal Astronomical Society*, v. 470, n. 2, p. 1894–1910, 05 2017. ISSN 0035-8711. Available at: <https://doi.org/10.1093/mnras/stx1285>. Cited 2 times on pages 55 and 175.

Korol, V. et al. Populations of double white dwarfs in Milky Way satellites and their detectability with LISA. *Astronomy & Astrophysics*, v. 638, p. A153, jun. 2020. Available at: <http://doi.org/10.1051/0004-6361/202037764>. Cited 2 times on pages 55 and 176.

Kouwenhoven, M. B. N. et al. The primordial binary population. II. - Recovering the binary population for intermediate mass stars in Scorpius OB2. *Astronomy and Astrophysics*, v. 474, n. 1, p. 77–104, 2007. Available at: <https://doi.org/10.1051/0004-6361:20077719>. Cited on page 53.

Kraft, R. P. Studies of Stellar Rotation. V. The Dependence of Rotation on Age among Solar-Type Stars. *Astrophysical Journal*, v. 150, p. 551, nov. 1967. Available at: <https://doi.org/10.1086/149359>. Cited on page 47.

Kraft, R. P.; Mathews, J.; Greenstein, J. L. Binary Stars among Cataclysmic Variables. II. Nova WZ Sagittae: a Possible Radiator of Gravitational Waves. *Astrophysical Journal*, v. 136, p. 312–315, jul. 1962. Available at: <https://doi.org/10.1086/147381>. Cited on page 33.

Kupfer, T. et al. The First Ultracompact Roche Lobe-Filling Hot Subdwarf Binary. *Astrophysical Journal*, v. 891, n. 1, p. 45, mar. 2020. Available at: <https://doi.org/10.3847/1538-4357/ab72ff>. Cited on page 110.

Kupfer, T. et al. A Summary of Multimessenger Science with Galactic Binaries. *Bulletin of the American Astronomical Society*, v. 51, n. 3, p. 188, May 2019. Cited on page 55.

Kupfer, T. et al. LISA verification binaries with updated distances from Gaia Data Release 2. *Monthly Notices of the Royal Astronomical Society*, v. 480, n. 1, p. 302–309, oct. 2018. Available at: <https://doi.org/10.1093/mnras/sty1545>. Cited 3 times on pages 55, 175, and 176.

Kuroda, K.; Ni, W.-T.; Pan, W.-P. Gravitational waves: Classification, methods of detection, sensitivities and sources. *International Journal of Modern Physics D*, v. 24, n. 14, p. 1530031–129, dec. 2015. Available at: <https://doi.org/10.1142/S0218271815300311>. Cited on page 176.

Kylafis, N. D. Spectral and temporal variability in low-mass x-ray binaries. In: _____. *Currents in High-Energy Astrophysics*. Dordrecht: Springer Netherlands, 1995. p. 45–54. ISBN 978-94-011-0253-7. Available at: <https://doi.org/10.1007/978-94-011-0253-7_5>. Cited on page 40.

Lagos, F. et al. Most EL CVn systems are inner binaries of hierarchical triples. *Monthly Notices of the Royal Astronomical Society*, v. 499, n. 1, p. L121–L125, dec. 2020. Available at: <https://doi.org/10.1093/mnrasl/slaa164>. Cited on page 55.

Lamberts, A. et al. Predicting the LISA white dwarf binary population in the Milky Way with cosmological simulations. *Monthly Notices of the Royal Astronomical Society*, v. 490, n. 4, p. 5888–5903, dec. 2019. Available at: <https://doi.org/10.1093/mnras/stz2834>. Cited on page 175.

Lamers, H. J. G. L. M.; Levesque, E. M. *Understanding Stellar Evolution*. Bristol: IOP Publishing, 2017. (2514-3433). ISBN 978-0-7503-1278-3. Available at: <http://dx.doi.org/10.1088/978-0-7503-1278-3>. Cited 2 times on pages 32 and 34.

Landau, L. D.; Lifshitz, E. M. *The classical theory of fields*. Oxford: Pergamon Press, 1975. Cited on page 30.

Landau, L. D.; Lifshitz, E. M. *Mechanics*. Oxford: Butterworth-Heinemann, 1976. Cited on page 29.

Langanke, K.; Martínez-Pinedo, G. Shell-model calculations of stellar weak interaction rates: II. Weak rates for nuclei in the mass range A=45-65 in supernovae environments. *Nuclear Physics A*, v. 673, p. 481–508, jun 2000. Cited on page 67.

Langer, N. Presupernova evolution of massive single and binary stars. *Annual Review of Astronomy and Astrophysics*, v. 50, n. 1, p. 107–164, 2012. Available at: <https://doi.org/10.1146/annurev-astro-081811-125534>. Cited 2 times on pages 37 and 172.

Langer, N.; Fricke, K. J.; Sugimoto, D. Semiconvective diffusion and energy transport. *Astronomy and Astrophysics*, v. 126, n. 1, p. 207, Sep 1983. Cited on page 67.

Latour, M. et al. Quantitative spectral analysis of the sdB star HD 188112: A helium-core white dwarf progenitor. *Astronomy and Astrophysics*, v. 585, p. A115, jan. 2016. Available at: <https://doi.org/10.1051/0004-6361/201527445>. Cited on page 110.

Lattimer, J. M. The nuclear equation of state and neutron star masses. *Annual Review of Nuclear and Particle Science*, v. 62, n. 1, p. 485–515, 2012. Available at: <https://doi.org/10.1146/annurev-nucl-102711-095018>. Cited on page 78.

Lauffer, G. R.; Romero, A. D.; Kepler, S. O. New full evolutionary sequences of H- and He-atmosphere massive white dwarf stars using MESA. *Monthly Notices of the Royal Astronomical Society*, v. 480, n. 2, p. 1547–1562, 08 2018. ISSN 0035-8711. Available at: <https://doi.org/10.1093/mnras/sty1925>. Cited 2 times on pages 37 and 64.

Lauterborn, D. Evolution with mass exchange of case C for a binary system of total mass 7 M sun. *Astronomy and Astrophysics*, v. 7, p. 150, Jul 1970. Cited on page 45.

Ledoux, P. Stellar Models with Convection and with Discontinuity of the Mean Molecular Weight. *Astrophysical Journal*, v. 105, p. 305, mar. 1947. Available at: <https://doi.org/10.1086/144905>. Cited on page 62.

Leinert, C. et al. A search for companions to nearby southern M dwarfs with near-infrared speckle interferometry. *Astronomy and Astrophysics*, v. 325, p. 159–166, Sep 1997. Cited on page 53.

Lewin, W. H. G.; van der Klis, M. *Compact Stellar X-ray Sources*. Cambridge, UK: Cambridge University Press, 2006. v. 39. Cited on page 81.

Li, J.; Wickramasinghe, D. T. Magnetic braking in magnetic binary stars. *Monthly Notices of the Royal Astronomical Society*, v. 300, n. 3, p. 718–732, 11 1998. ISSN 0035-8711. Available at: <https://doi.org/10.1111/j.1365-8711.1998.t01-1-01913.x>. Cited on page 52.

Li, Z. et al. Formation of extremely low-mass white dwarfs in double degenerates. *The Astrophysical Journal*, American Astronomical Society, v. 871, n. 2, p. 148, jan 2019. Available at: <https://doi.org/10.3847%2F1538-4357%2Faaf9a1>. Cited 4 times on pages 38, 51, 53, and 58.

Li, Z. et al. Gravitational-wave Radiation of Double Degenerates with Extremely Low-mass White Dwarf Companions. *The Astrophysical Journal*, v. 893, n. 1, p. 2, apr. 2020. Available at: <https://doi.org/10.3847/1538-4357/ab7dc2>. Cited 3 times on pages 55, 102, and 176.

Liccardo, V. et al. Nuclear processes in astrophysics: Recent progress. *European Physical Journal A*, v. 54, n. 12, p. 221, dec. 2018. Available at: <https://doi.org/10.1140/epja/i2018-12648-5>. Cited on page 61.

Liebert, J. et al. A helium white dwarf of extremely low mass. *The Astrophysical Journal*, IOP Publishing, v. 606, n. 2, p. L147–L149, apr 2004. Available at: <https://doi.org/10.1086%2F421462>. Cited on page 38.

Lin, J. et al. LMXB and IMXB Evolution: I. The Binary Radio Pulsar PSR J1614-2230. *The Astrophysical Journal*, IOP Publishing, v. 732, n. 2, p. 70, apr 2011. Available at: <https://doi.org/10.1088%2F0004-637x%2F732%2F2%2F70>. Cited 3 times on pages 49, 97, and 98.

Lipunov, V. M. *In the world of binary stars*. Moscow: Mir Publishers, 1989. Cited on page 28.

Littenberg, T. et al. Gravitational wave survey of galactic ultra compact binaries. *Bulletin of the American Astronomical Society*, v. 51, n. 3, p. 34, May 2019. Cited on page 55.

Liu, Q. Z.; van Paradijs, J.; van den Heuvel, E. P. J. A catalogue of low-mass X-ray binaries in the Galaxy, LMC, and SMC (Fourth edition). *Astronomy and Astrophysics*, v. 469, n. 2, p. 807–810, jul. 2007. Available at: <https://doi.org/10.1051/0004-6361:20077303>. Cited on page 39.

Liu, W.-M.; Li, X.-D. On the White Dwarf Mass Problem of Cataclysmic Variables. *Astrophysical Journal*, v. 832, n. 1, p. 80, nov. 2016. Available at: <https://doi.org/10.3847/0004-637X/832/1/80>. Cited on page 98.

Livingston, M. S.; Bethe, H. A. Nuclear Physics C. Nuclear Dynamics, Experimental. *Reviews of Modern Physics*, v. 9, n. 3, p. 245–390, jul. 1937. Available at: <https://doi.org/10.1103/RevModPhys.9.245>. Cited on page 61.

Lopes, J.; Lopes, I. Dark matter capture and annihilation in stars: Impact on the red giant branch tip. *Astronomy and Astrophysics*, v. 651, p. A101, jul. 2021. Available at: <https://doi.org/10.1051/0004-6361/202140750>. Cited on page 64.

Lucatello, S. et al. The incidence of binaries in globular cluster stellar populations. *Astronomy and Astrophysics*, v. 584, p. A52, dec. 2015. Available at: <https://doi.org/10.1051/0004-6361/201526957>. Cited on page 36.

Ma, B.; Li, X.-D. The Bifurcation Periods in Low-Mass X-Ray Binaries: The Effect of Magnetic Braking and Mass Loss. *The Astrophysical Journal*, IOP Publishing, v. 691, n. 2, p. 1611–1617, feb 2009. Available at: <https://doi.org/10.1088%2F0004-637x%2F691%2F2%2F1611>. Cited on page 52.

Maeder, A. et al. The basic role of magnetic fields in stellar evolution. *Proceedings of the International Astronomical Union*, Cambridge University Press, v. 4, n. S259, p. 311–322, 2008. Available at: <https://doi.org/10.1017/S1743921309030671>. Cited on page 48.

Malkov, O.; Chulkov, D. Catalogues, parameters and distributions of orbital binaries. *arXiv e-prints*, p. arXiv:1704.04822, apr. 2017. Cited on page 28.

Manchester, R. N. et al. The Australia Telescope National Facility Pulsar Catalogue. *Astronomical Journal*, v. 129, n. 4, p. 1993–2006, Apr 2005. Cited 4 times on pages 39, 40, 41, and 120.

Marchant, P. et al. A new route towards merging massive black holes. *Astronomy & Astrophysics*, v. 588, p. A50, 2016. Available at: <https://doi.org/10.1051/0004-6361/201628133>. Cited on page 64.

Marchant, P. et al. Pulsational Pair-instability Supernovae in Very Close Binaries. *Astrophysical Journal*, v. 882, n. 1, p. 36, sep. 2019. Available at: <https://doi.org/10.3847/1538-4357/ab3426>. Cited on page 64.

Marsh, T. R. The discovery of a short-period double-degenerate binary star. *Monthly Notices of the Royal Astronomical Society*, v. 275, n. 1, p. L1–L5, 07 1995. ISSN 0035-8711. Available at: <https://doi.org/10.1093/mnras/275.1.L1>. Cited on page 38.

Marsh, T. R.; Dhillon, V. S.; Duck, S. R. Low-mass white dwarfs need friends: five new double-degenerate close binary stars. *Monthly Notices of the Royal Astronomical Society*, v. 275, n. 3, p. 828–840, 08 1995. ISSN 0035-8711. Available at: <https://doi.org/10.1093/mnras/275.3.828>. Cited on page 38.

Martin, A. J. The evolution of magnetic fields from the main-sequence to very late stages. *Contributions of the Astronomical Observatory Skalnate Pleso*, v. 48, n. 1, p. 162–169, jan. 2018. Cited on page 48.

Martins, F.; Palacios, A. A comparison of evolutionary tracks for single Galactic massive stars. *Astronomy and Astrophysics*, v. 560, p. A16, dec. 2013. Available at: <https://doi.org/10.1051/0004-6361/201322480>. Cited on page 69.

Masevich, A. G.; Tutukov, A. V. *Evolyutsiya Zvezd: Teoriya i Nablyudeniya (Evolution of Stars: Theory and Observations)*. Moscow: Izdatel Nauka, 1988. Cited on page 28.

Mason, B. D. et al. ICCD speckle observations of binary stars. XIX. an astrometric/spectroscopic survey of o stars. *The Astronomical Journal*, IOP Publishing, v. 115, n. 2, p. 821–847, feb 1998. Available at: <https://doi.org/10.1086%2F300234>. Cited on page 53.

Mason, S. F. *A history of the sciences*. New York: Collier Books, 1962. (Science Library). Cited 2 times on pages 25 and 28.

Matt, S. P. et al. Spin Evolution of Accreting Young Stars. II. Effect of Accretion-powered Stellar Winds. *The Astrophysical Journal*, IOP Publishing, v. 745, n. 1, p. 101, jan 2012. Available at: <https://doi.org/10.1088%2F0004-637x%2F745%2F1%2F101>. Cited on page 74.

Maxted, P. F. L. et al. Discovery of a stripped red giant core in a bright eclipsing binary system. *Monthly Notices of the Royal Astronomical Society*, v. 418, n. 2, p. 1156–1164, dec. 2011. Available at: <https://doi.org/10.1111/j.1365-2966.2011.19567.x>. Cited on page 55.

Maxted, P. F. L. et al. EL CVn-type binaries - discovery of 17 helium white dwarf precursors in bright eclipsing binary star systems. *Monthly Notices of the Royal Astronomical Society*, v. 437, n. 2, p. 1681–1697, jan. 2014. Available at: <https://doi.org/10.1093/mnras/stt2007>. Cited on page 55.

Maxted, P. F. L. et al. WASP 1628+10 - an EL CVn-type binary with a very low mass stripped red giant star and multiperiodic pulsations. *Monthly Notices of the Royal Astronomical Society*, v. 444, n. 1, p. 208–216, oct. 2014. Available at: <https://doi.org/10.1093/mnras/stu1465>. Cited on page 55.

McDonald, I.; Zijlstra, A. A. Mass-loss on the red giant branch: the value and metallicity dependence of Reimers' η in globular clusters. *Monthly Notices of the Royal Astronomical Society*, v. 448, n. 1, p. 502–521, mar. 2015. Available at: <https://doi.org/10.1093/mnras/stv007>. Cited on page 68.

Meng, X.; Chen, X.; Han, Z. A single-degenerate channel for the progenitors of Type Ia supernovae with different metallicities. *Monthly Notices of the Royal Astronomical Society*, v. 395, n. 4, p. 2103–2116, jun. 2009. Available at: <https://doi.org/10.1111/j.1365-2966.2009.14636.x>. Cited on page 98.

Menon, A. et al. Detailed evolutionary models of massive contact binaries I. Model grids and synthetic populations for the Magellanic Clouds. *Monthly Notices of the Royal Astronomical Society*, aug. 2021. Available at: <https://doi.org/10.1093/mnras/stab2276>. Cited on page 64.

Mestel, L. Magnetic Braking by a Stellar Wind—I. *Monthly Notices of the Royal Astronomical Society*, v. 138, n. 3, p. 359–391, 02 1968. ISSN 0035-8711. Available at: <https://doi.org/10.1093/mnras/138.3.359>. Cited 2 times on pages 47 and 74.

Mestel, L.; Spruit, H. C. On magnetic braking of late-type stars. *Monthly Notices of the Royal Astronomical Society*, v. 226, n. 1, p. 57–66, 05 1987. ISSN 0035-8711. Available at: <https://doi.org/10.1093/mnras/226.1.57>. Cited 2 times on pages 47 and 73.

Michaud, G.; Alecian, G.; Richer, J. *Atomic Diffusion in Stars*. Switzerland: Springer, Cham, 2015. Available at: <https://doi.org/10.1007/978-3-319-19854-5>. Cited on page 68.

Miller, A. et al. 2M17091769+3127589: a mass-transfer binary with an extreme mass ratio. *arXiv e-prints*, p. arXiv:2107.11393, jul. 2021. Cited on page 64.

Miller, D. R. et al. The Ultramassive White Dwarfs of the Alpha Persei Cluster. *arXiv e-prints*, p. arXiv:2110.09668, oct. 2021. Cited on page 99.

Milone, A. P. et al. Photometric binaries in 50 globular clusters. *Memorie della Società Astronomica Italiana*, v. 79, p. 623, jan. 2008. Cited on page 36.

Misner, C. W.; Thorne, K. S.; Wheeler, J. A. *Gravitation*. San Francisco: W.H. Freeman and Co., 1973. Cited on page 175.

Moravveji, E. et al. Tight asteroseismic constraints on core overshooting and diffusive mixing in the slowly rotating pulsating B8.3V star KIC 10526294. *Astronomy and Astrophysics*, v. 580, p. A27, Aug 2015. Cited on page 64.

Mowlavi, N. et al. Stellar mass and age determinations . I. Grids of stellar models from Z = 0.006 to 0.04 and M = 0.5 to 3.5 $M_{\odot}$. *Astronomy and Astrophysics*, v. 541, p. A41, may 2012. Available at: <https://doi.org/10.1051/0004-6361/201117749>. Cited on page 69.

Muslimov, A. G.; Sarna, M. J. Formation of low-mass binaries with millisecond pulsars. *Monthly Notices of the Royal Astronomical Society*, v. 262, n. 1, p. 164–174, 05 1993. ISSN 0035-8711. Available at: <https://doi.org/10.1093/mnras/262.1.164>. Cited 2 times on pages 47 and 49.

Naoz, S.; Noter, S.; Barkana, R. The first stars in the Universe. *Monthly Notices of the Royal Astronomical Society: Letters*, v. 373, n. 1, p. L98–L102, 11 2006. ISSN 1745-3925. Available at: <https://doi.org/10.1111/j.1745-3933.2006.00251.x>. Cited on page 25.

Nelemans, G. AM CVn stars. In: Hameury, J. M.; Lasota, J. P. (Ed.). *The Astrophysics of Cataclysmic Variables and Related Objects*. San Francisco: Astronomical Society of the Pacific, 2005. (Astronomical Society of the Pacific Conference Series, v. 330), p. 27. Cited on page 55.

Nelemans, G. et al. Optical spectra of the carbon-oxygen accretion discs in the ultra-compact X-ray binaries 4U 0614+09, 4U 1543-624 and 2S 0918-549. *Monthly Notices of the Royal Astronomical Society*, v. 348, n. 1, p. L7–L11, feb. 2004. Available at: <https://doi.org/10.1111/j.1365-2966.2004.07486.x>. Cited on page 180.

Nelemans, G. et al. Population synthesis for double white dwarfs. II. Semi-detached systems: AM CVn stars. *Astronomy and Astrophysics*, v. 368, p. 939–949, mar. 2001. Available at: <https://doi.org/10.1051/0004-6361:20010049>. Cited 2 times on pages 55 and 175.

Nelemans, G. et al. Reconstructing the evolution of double helium white dwarfs: envelope loss without spiral-in. *Astronomy and Astrophysics*, v. 360, p. 1011–1018, Aug 2000. Cited on page 54.

Nelemans, G.; Yungelson, L. R.; Portegies Zwart, S. F. The gravitational wave signal from the Galactic disk population of binaries containing two compact objects. *Astronomy and Astrophysics*, v. 375, p. 890–898, sep. 2001. Available at: <https://doi.org/10.1051/0004-6361:20010683>. Cited on page 55.

Nelemans, G. et al. Population synthesis for double white dwarfs . I. Close detached systems. *Astronomy and Astrophysics,*, v. 365, p. 491–507, jan. 2001. Available at: <https://doi.org/10.1051/0004-6361:20000147>. Cited 2 times on pages 55 and 175.

Nissanke, S. et al. Gravitational-wave Emission from Compact Galactic Binaries. *The Astrophysical Journal*, v. 758, n. 2, p. 131, oct. 2012. Available at: <https://doi.org/10.1088/0004-637X/758/2/131>. Cited 2 times on pages 55 and 176.

Nomoto, K.; Kobayashi, C.; Tominaga, N. Nucleosynthesis in Stars and the Chemical Enrichment of Galaxies. *Annual Review of Astronomy and Astrophysics*, v. 51, n. 1, p. 457–509, aug. 2013. Available at: <https://doi.org/10.1146/annurev-astro-082812-140956>. Cited on page 172.

Oda, T. et al. Rate Tables for the Weak Processes of sd-Shell Nuclei in Stellar Matter. *Atomic Data and Nuclear Data Tables*, v. 56, p. 231–403, mar 1994. Cited on page 67.

Orebi Gann, G. D. et al. The Future of Solar Neutrinos. *Annual Review of Nuclear and Particle Science*, v. 71, n. 1, p. 491–528, jul. 2021. Available at: <https://doi.org/10.1146/annurev-nucl-011921-061243>. Cited on page 36.

Osada, J. *Evolução das idéias da física*. São Paulo, SP: Edgard Blücher, 1972. Cited on page 25.

Oswalt, T. D. et al. A lower limit of 9.5 Gyr on the age of the Galactic disk from the oldest white dwarf stars. *Nature*, v. 382, n. 6593, p. 692–694, Aug 1996. Cited on page 37.

Özel, F.; Freire, P. Masses, radii, and the equation of state of neutron stars. *Annual Review of Astronomy and Astrophysics*, v. 54, n. 1, p. 401–440, 2016. Available at: <https://doi.org/10.1146/annurev-astro-081915-023322>. Cited on page 78.

Paczyński, B. Evolution of Close Binaries. I. *Acta Astronomica*, v. 16, p. 231, jan. 1966. Cited on page 48.

Paczyński, B. Evolution of Close Binaries. II. *Acta Astronomica*, v. 17, p. 1, jan. 1967. Cited on page 48.

Paczyński, B. Evolution of Close Binaries. IV. *Acta Astronomica*, v. 17, p. 193, jan. 1967. Cited on page 48.

Paczyński, B. Internal structure and evolutionary changes in binaries: Evolution of close binaries. In: Dommanget, J. (Ed.). *On the Evolution of Double Stars*. Cape Town: IAU Publications, 1967. v. 17, p. 111. Cited on page 31.

Paczyński, B. Evolutionary Processes in Close Binary Systems. *Annual Review of Astron and Astrophys*, v. 9, p. 183, Jan 1971. Available at: <https://doi.org/10.1146/annurev.aa.09.090171.001151>. Cited on page 28.

Paczyński, B.; Sienkiewicz, R. Evolution of Close Binaries VIII. Mass Exchange on the Dynamical Time Scale. *Acta Astronomica*, v. 22, p. 73–91, jan. 1972. Cited 2 times on pages 43 and 49.

Paczyński, B.; Ziółkowski, J. Evolution of Close Binaries. III. *Acta Astronomica*, v. 17, p. 7, jan. 1967. Cited on page 48.

Panei, J. A. et al. Full evolution of low-mass white dwarfs with helium and oxygen cores. *Monthly Notices of the Royal Astronomical Society*, v. 382, n. 2, p. 779–792, 11 2007. ISSN 0035-8711. Available at: <https://dx.doi.org/10.1111/j.1365-2966.2007.12400.x>. Cited 2 times on pages 50 and 58.

Papitto, A.; de Martino, D. Transitional millisecond pulsars. *arXiv e-prints*, p. arXiv:2010.09060, oct. 2020. Cited on page 39.

Papitto, A. et al. Swings between rotation and accretion power in a binary millisecond pulsar. *Nature*, v. 501, n. 7468, p. 517–520, sep. 2013. Available at: <https://doi.org/10.1038/nature12470>. Cited on page 39.

Paquette, C. et al. Diffusion Coefficients for Stellar Plasmas. *Astrophysical Journals*, v. 61, p. 177, May 1986. Cited on page 114.

Patruno, A.; Watts, A. L. Accreting millisecond x-ray pulsars. In: _____. *Timing Neutron Stars: Pulsations, Oscillations and Explosions*. Berlin, Heidelberg: Springer Berlin Heidelberg, 2021. p. 143–208. ISBN 978-3-662-62110-3. Available at: <https://doi.org/10.1007/978-3-662-62110-3_4>. Cited on page 39.

Patterson, J. The evolution of cataclysmic and low-mass X-ray binaries. *Astrophysical Journal Supplement*, v. 54, p. 443–493, apr. 1984. Available at: <http://articles.adsabs.harvard.edu/pdf/1984ApJS...54..443P>. Cited on page 39.

Paxton, B. et al. Modules for Experiments in Stellar Astrophysics (MESA). *Astrophysical Journal, Supplement*, v. 192, p. 3, jan 2011. Available at: <https://doi.org/10.1088/0067-0049/192/1/3>. Cited 2 times on pages 63 and 64.

Paxton, B. et al. Modules for Experiments in Stellar Astrophysics (MESA): Planets, Oscillations, Rotation, and Massive Stars. *Astrophysical Journal, Supplement*, v. 208, p. 4, sep 2013. Available at: <https://doi.org/10.1088/0067-0049/208/1/4>. Cited 3 times on pages 63, 64, and 68.

Paxton, B. et al. Modules for Experiments in Stellar Astrophysics (MESA): Binaries, Pulsations, and Explosions. *Astrophysical Journal, Supplement*, v. 220, p. 15, sep 2015. Available at: <https://doi.org/10.1088/0067-0049/220/1/15>. Cited 4 times on pages 63, 64, 65, and 71.

Paxton, B. et al. Modules for Experiments in Stellar Astrophysics (MESA): Convective Boundaries, Element Diffusion, and Massive Star Explosions. *Astrophysical Journal, Supplement*, v. 234, p. 34, feb 2018. Available at: <https://doi.org/10.3847/1538-4365/aaa5a8>. Cited 2 times on pages 63 and 64.

Paxton, B. et al. Modules for Experiments in Stellar Astrophysics (MESA): Pulsating Variable Stars, Rotation, Convective Boundaries, and Energy Conservation. *Astrophysical Journal, Supplement*, v. 243, n. 1, p. 10, Jul 2019. Available at: <https://doi.org/10.3847/1538-4365/ab2241>. Cited 2 times on pages 63 and 64.

Pelisoli, I. et al. The sdA problem – III. New extremely low-mass white dwarfs and their precursors from Gaia astrometry. *Monthly Notices of the Royal Astronomical Society*, v. 482, n. 3, p. 3831–3842, 11 2018c. ISSN 0035-8711. Available at: <https://dx.doi.org/10.1093/mnras/sty2979>. Cited 7 times on pages 53, 54, 55, 107, 109, 110, and 111.

Pelisoli, I.; Kepler, S. O.; Koester, D. Are sdAs helium core stars? *Open Astronomy*, v. 26, n. 1, p. 169–178, Dec 2017. Available at: <https://doi.org/10.1515/astro-2017-0433>. Cited on page 55.

Pelisoli, I.; Kepler, S. O.; Koester, D. The sdA problem – I. Physical properties. *Monthly Notices of the Royal Astronomical Society*, v. 475, n. 2, p. 2480–2495, 01 2018a. ISSN 0035-8711. Available at: <https://doi.org/10.1093/mnras/sty011>. Cited 6 times on pages 53, 54, 107, 109, 110, and 111.

Pelisoli, I. et al. The sdA problem – II. Photometric and spectroscopic follow-up. *Monthly Notices of the Royal Astronomical Society*, v. 478, n. 1, p. 867–884, 06 2018b. ISSN 0035-8711. Available at: <https://doi.org/10.1093/mnras/sty1101>. Cited 6 times on pages 53, 54, 55, 107, 109, and 110.

Pelisoli, I.; Vos, J. Gaia Data Release 2 catalogue of extremely low-mass white dwarf candidates. *Monthly Notices of the Royal Astronomical Society*, v. 488, n. 2, p. 2892–2903, 07 2019. ISSN 0035-8711. Available at: <https://doi.org/10.1093/mnras/stz1876>. Cited 11 times on pages 37, 38, 54, 55, 56, 103, 107, 110, 111, 112, and 115.

Pennington, R. Interacting binary stars: appendix. In: _____. *Interacting Binary Stars*. Cambridge, UK: Cambridge University Press, 1985. p. 197–199. Cited on page 72.

Perez, J. *Zeta + 80 Ursae Majoris (Struve 1744/Mizar and Alcor)*. 2006. Zeta + 80 Ursae Majoris. Available at: <http://www.perezmedia.net/beltofvenus/archives/000603.html>. Accessed on: 07 sep 2019. Cited on page 26.

Peters, P. C. Gravitational Radiation and the Motion of Two Point Masses. *Physical Review*, v. 136, n. 4B, p. 1224–1232, Nov 1964. Cited on page 30.

Pfahl, E.; Rappaport, S.; Podsiadlowski, P. The Galactic Population of Low- and Intermediate-Mass X-Ray Binaries. *Astrophysical Journal*, v. 597, n. 2, p. 1036–1048, nov. 2003. Available at: <https://doi.org/10.1086/378632>. Cited on page 40.

Piersanti, L.; Tornambé, A.; Yungelson, L. R. He-accreting white dwarfs: accretion regimes and final outcomes. *Monthly Notices of the Royal Astronomical Society*, v. 445, n. 3, p. 3239–3262, dec. 2014. Available at: <https://doi.org/10.1093/mnras/stu1885>. Cited on page 98.

Piersanti, L.; Yungelson, L. R.; Tornambé, A. He-accreting WDs: AM CVn stars with WD donors. *Monthly Notices of the Royal Astronomical Society*, v. 452, n. 3, p. 2897–2910, sep. 2015. Available at: <https://doi.org/10.1093/mnras/stv1452>. Cited 2 times on pages 55 and 98.

Pietrukowicz, P. et al. Blue large-amplitude pulsators as a new class of variable stars. *Nature Astronomy*, v. 1, p. 0166, Aug 2017. Available at: <https://doi.org/10.1038/s41550-017-0166>. Cited 3 times on pages 54, 107, and 110.

Pignatari, M. et al. NuGrid Stellar Data Set. I.Stellar Yields from H to Bi for Stars with Metallicities Z = 0.02 and Z = 0.01. *The Astrophysical Journal Supplement Series*, American Astronomical Society, v. 225, n. 2, p. 24, aug 2016. Available at: <https://doi.org/10.3847%2F0067-0049%2F225%2F2%2F24>. Cited on page 64.

Podsiadlowski, P. Irradiation-driven mass transfer in low-mass X-ray binaries. *Nature*, v. 350, n. 6314, p. 136–138, mar. 1991. Available at: <https://doi.org/10.1038/350136a0>. Cited on page 113.

Podsiadlowski, P.; Rappaport, S.; Pfahl, E. D. Evolutionary Sequences for Low- and Intermediate-Mass X-Ray Binaries. *Astrophysical Journal*, v. 565, n. 2, p. 1107–1133, feb. 2002. Available at: <https://doi.org/10.1086/324686>. Cited 3 times on pages 40, 49, and 52.

Poelarends, A. J. T. et al. The supernova channel of super-AGB stars. *The Astrophysical Journal*, IOP Publishing, v. 675, n. 1, p. 614–625, mar 2008. Available at: <https://doi.org/10.1086%2F520872>. Cited on page 37.

Pols, O. R. et al. Approximate input physics for stellar modelling. *Monthly Notices of the Royal Astronomical Society*, v. 274, p. 964–974, jun 1995. Available at: <https://doi.org/10.1093/mnras/274.3.964>. Cited on page 65.

Postnov, K. A.; Yungelson, L. R. The Evolution of Compact Binary Star Systems. *Living Reviews in Relativity*, v. 17, n. 1, p. 3, May 2014. Available at: <https://doi.org/10.12942/lrr-2014-3>. Cited 2 times on pages 28 and 33.

Potekhin, A. Y.; Chabrier, G. Thermodynamic Functions of Dense Plasmas: Analytic Approximations for Astrophysical Applications. *Contributions to Plasma Physics*, v. 50, p. 82–87, jan 2010. Cited on page 65.

Press, W. H.; Thorne, K. S. Gravitational-Wave Astronomy. *Annual Review of Astronomy and Astrophysics*, v. 10, p. 335, jan. 1972. Available at: <https://doi.org/10.1146/annurev.aa.10.090172.002003>. Cited on page 175.

Pringle, J. E. On the formation of binary stars. *Monthly Notices of the Royal Astronomical Society*, v. 239, p. 361–370, jul. 1989. Available at: <https://doi.org/10.1093/mnras/239.2.361>. Cited on page 35.

Pringle, J. E.; Wade, R. A. *Interacting binary stars*. Cambridge: Cambridge University Press, 1985. Cited on page 43.

Pshirkov, M. S. et al. Discovery of a hot ultramassive rapidly rotating DBA white dwarf. *Monthly Notices of the Royal Astronomical Society*, v. 499, n. 1, p. L21–L25, dec. 2020. Available at: <https://doi.org/10.1093/mnrasl/slaa149>. Cited on page 99.

Pylyser, E.; Savonije, G. J. Evolution of low-mass close binary systems with a compact mass accreting component. *Astronomy and Astrophysics*, v. 191, p. 57–70, Feb 1988. Cited on page 52.

Pylyser, E. H. P.; Savonije, G. J. The evolution of low-mass close binary systems with a compact component. II. Systems captured by angular momentum losses. *Astronomy and Astrophysics*, v. 208, p. 52–62, Jan 1989. Cited on page 52.

Quintin, J. *X-ray Binary Evolution: The Effects of Self-Induced Irradiation*. Sherbrooke, Quebec, Canada: Bishop's University, 2013. Bachelor of Science Thesis. Available at: <https://www.physics.mcgill.ca/~jquintin/thesis.pdf>. Cited on page 113.

Raghavan, D. et al. A Survey of Stellar Families: Multiplicity of Solar-type Stars. *The Astrophysical Journal Supplement Series*, IOP Publishing, v. 190, n. 1, p. 1–42, aug 2010. Available at: <https://doi.org/10.1088%2F0067-0049%2F190%2F1%2F1>. Cited 3 times on pages 51, 53, and 92.

Rappaport, S.; Verbunt, F.; Joss, P. C. A new technique for calculations of binary stellar evolution application to magnetic braking. *Astrophysical Journal*, v. 275, p. 713–731, Dec 1983. Cited 16 times on pages 47, 51, 73, 79, 83, 84, 85, 86, 89, 92, 93, 95, 112, 117, 118, and 180.

Rebassa-Mansergas, A. et al. Accurate mass and radius determinations of a cool subdwarf in an eclipsing binary. *Nature Astronomy*, v. 3, p. 553–560, apr. 2019. Available at: <https://doi.org/10.1038/s41550-019-0746-7>. Cited on page 110.

Reed, B. T. et al. Implications of PREX-2 on the Equation of State of Neutron-Rich Matter. *Physical Review Letters*, v. 126, n. 17, p. 172503, apr. 2021. Available at: <https://doi.org/10.1103/PhysRevLett.126.172503>. Cited 2 times on pages 113 and 178.

Refsdal, S.; Weigert, A. On the Production of White Dwarfs in Binary Systems of Small Mass. *Astronomy and Astrophysics*, v. 13, p. 367, aug. 1971. Cited on page 96.

Reig, P. Be/X-ray binaries. *Astrophysics and Space Science*, v. 332, n. 1, p. 1–29, mar. 2011. Available at: <https://doi.org/10.1007/s10509-010-0575-8>. Cited on page 41.

Reimers, D. Circumstellar envelopes and mass loss of red giant stars. In: _____. *Problems in stellar atmospheres and envelopes*. New York: Springer, 1975. p. 229–256. Cited 2 times on pages 68 and 78.

Renedo, I. et al. New Cooling Sequences for Old White Dwarfs. *The Astrophysical Journal*, IOP Publishing, v. 717, n. 1, p. 183–195, jun 2010. Available at: <https://doi.org/10.1088%2F0004-637x%2F717%2F1%2F183>. Cited 2 times on pages 78 and 94.

Renzo, M.; Götberg, Y. Evolution of accretor stars in massive binaries: broader implications from modeling ζ Ophiuchi. *arXiv e-prints*, p. arXiv:2107.10933, jul. 2021. Cited on page 64.

Réville, V. et al. The Effect of Magnetic Topology on Thermally Driven Wind: Toward a General Formulation of the Braking Law. *The Astrophysical Journal*, IOP Publishing, v. 798, n. 2, p. 116, jan 2015. Available at: <https://doi.org/10.1088%2F0004-637x%2F798%2F2%2F116>. Cited on page 74.

Reylé, C. et al. The 10 parsec sample in the Gaia era. *Astronomy and Astrophysics*, v. 650, p. A201, jun. 2021. Available at: <https://doi.org/10.1051/0004-6361/202140985>. Cited on page 53.

Ritter, C. et al. NuGrid stellar data set - II. Stellar yields from H to Bi for stellar models with $M_{ZAMS} = 1$–$25\ M_{\odot}$ and $Z = 0.0001$–0.02. *Monthly Notices of the Royal Astronomical Society*, v. 480, n. 1, p. 538–571, 06 2018. ISSN 0035-8711. Available at: <https://doi.org/10.1093/mnras/sty1729>. Cited on page 64.

Ritter, H. Turning on and off mass transfer in cataclysmic binaries. *Astronomy and Astrophysics*, v. 202, p. 93–100, aug 1988. Cited on page 70.

Ritter, H. Is irradiation important for the secular evolution of low-mass X-ray binaries? *New Astronomy Reviews*, v. 51, n. 10-12, p. 869–877, may 2008. Available at: <https://doi.org/10.1016/j.newar.2008.03.018>. Cited on page 113.

Ritter, H.; Kolb, U. Catalogue of cataclysmic binaries, low-mass X-ray binaries and related objects (Seventh edition). *Astronomy and Astrophysics*, v. 404, p. 301–303, jun. 2003. Available at: <https://doi.org/10.1051/0004-6361:20030330>. Cited on page 39.

Ritter, H.; Zhang, Z. Y.; Kolb, U. Irradiation and mass transfer in low-mass compact binaries. *Astronomy and Astrophysics*, v. 360, p. 959–990, aug. 2000. Cited on page 113.

Rivera-Sandoval, L. E. et al. Discovery of near-ultraviolet counterparts to millisecond pulsars in the globular cluster 47 Tucanae. *Monthly Notices of the Royal Astronomical Society*, v. 453, n. 3, p. 2707–2717, nov. 2015. Available at: <https://doi.org/10.1093/mnras/stv1810>. Cited on page 92.

Rocha, J. F. *Origens e evolução das idéias da física*. Salvador, BA: EDUFBA, 2002. Cited on page 25.

Rogers, F. J.; Nayfonov, A. Updated and Expanded OPAL Equation-of-State Tables: Implications for Helioseismology. *Astrophysical Journal*, v. 576, p. 1064–1074, sep. 2002. Cited on page 65.

Rohrmann, R. D.; Althaus, L. G.; Kepler, S. O. Lyman α wing absorption in cool white dwarf stars. *Monthly Notices of the Royal Astronomical Society*, v. 411, n. 2, p. 781–791, Feb 2011. Cited on page 69.

Romani, R. W.; Weinberg, M. D. Limits on Cluster Binaries. *Astrophysical Journal*, v. 372, p. 487, may 1991. Available at: <https://doi.org/10.1086/169994>. Cited on page 36.

Romero, A. D.; Campos, F.; Kepler, S. O. The age-metallicity dependence for white dwarf stars. *Monthly Notices of the Royal Astronomical Society*, v. 450, n. 4, p. 3708–3723, 05 2015. ISSN 0035-8711. Available at: <https://doi.org/10.1093/mnras/stv848>. Cited 2 times on pages 78 and 94.

Romero, A. D. et al. On the evolutionary status and pulsations of the recently discovered blue large-amplitude pulsators (BLAPs). *Monthly Notices of the Royal Astronomical Society: Letters*, v. 477, n. 1, p. L30–L34, 03 2018. ISSN 1745-3925. Available at: <https://doi.org/10.1093/mnrasl/sly051>. Cited on page 110.

Ruderman, M. et al. Late Evolution of Very Low Mass X-Ray Binaries Sustained by Radiation from Their Primaries. *Astrophysical Journal*, v. 343, p. 292, aug. 1989. Available at: <https://doi.org/10.1086/167704>. Cited on page 113.

Ruiter, A. J. et al. The LISA Gravitational Wave Foreground: A Study of Double White Dwarfs. *Astrophysical Journal*, v. 717, n. 2, p. 1006–1021, jul. 2010. Available at: <https://doi.org/10.1088/0004-637X/717/2/1006>. Cited on page 175.

Russell, H. N. Notes on white dwarfs and small companions. *Astronomical Journal*, v. 51, p. 13, Jun 1944. Cited on page 36.

Ryden, B.; Peterson, B. *Foundations of Astrophysics*. Cambridge, UK: Cambridge University Press, 2020. ISBN 9781108831956. Cited 2 times on pages 170 and 171.

Sahade, J.; McCluskey, G. E.; Kondo, Y. *The realm of interacting binary stars*. Dordrecht: Kluwer Academic, 1993. v. 177. (Astrophysics and space science library, v. 177). ISBN 0792316754. Cited on page 28.

Sahade, J.; Wood, F. B. *Interacting Binary Stars*. London: Pergamon Press, 1978. (International Series in Natural Philosophy). ISBN 9780080216560. Cited on page 28.

Salaris, M.; Cassisi, S. Chemical element transport in stellar evolution models. *Royal Society Open Science*, v. 4, n. 8, p. 170192, Aug 2017. Cited 2 times on pages 63 and 68.

Salpeter, E. E. The Luminosity Function and Stellar Evolution. *Astrophysical Journal*, v. 121, p. 161, Jan 1955. Cited on page 167.

Sathyaprakash, B. S.; Schutz, B. F. Physics, Astrophysics and Cosmology with Gravitational Waves. *Living Reviews in Relativity*, v. 12, n. 1, p. 2, dec. 2009. Available at: <https://doi.org/10.12942/lrr-2009-2>. Cited on page 175.

Saumon, D.; Chabrier, G.; van Horn, H. M. An Equation of State for Low-Mass Stars and Giant Planets. *Astrophysical Journal, Supplement*, v. 99, p. 713, aug 1995. Cited on page 65.

Savonije, G. J. Roche-lobe overflow in X-ray binaries. *Astronomy and Astrophysics*, v. 62, n. 3, p. 317–338, jan. 1978. Cited on page 43.

Sazonov, S. et al. The Galactic LMXB Population and the Galactic Centre Region. *New Astronomy Reviews*, v. 88, p. 101536, jun. 2020. Available at: <https://doi.org/10.1016/j.newar.2020.101536>. Cited 3 times on pages 39, 40, and 81.

Schatz, H.; Rehm, K. E. X-ray binaries. *Nuclear Physics A*, v. 777, p. 601–622, oct. 2006. Available at: <https://doi.org/10.1016/j.nuclphysa.2005.05.200>. Cited on page 40.

Schatzman, E. A theory of the role of magnetic activity during star formation. *Annales d'Astrophysique*, v. 25, p. 18, Feb 1962. Cited on page 47.

Schenker, K.; King, A. R. A new evolutionary picture for CVs and LMXBs. II. The impact of thermal-timescale mass transfer. In: Gänsicke, B. T.; Beuermann, K.; Reinsch, K. (Ed.). *The Physics of Cataclysmic Variables and Related Objects*. San Francisco: Astronomical Society of the Pacific, 2002. (Astronomical Society of the Pacific Conference Series, v. 261), p. 242. Cited on page 36.

Schmitz, K. New sensitivity curves for gravitational-wave signals from cosmological phase transitions. *Journal of High Energy Physics*, Springer Science and Business Media LLC, v. 2021, n. 1, Jan 2021. ISSN 1029-8479. Available at: <http://dx.doi.org/10.1007/JHEP01(2021)097>. Cited on page 176.

Schneider, D. et al. *Fundamental Parameters of Hot Subdwarf Stars from Gaia Astrometry*. Zenodo, 2019. Available at: <https://doi.org/10.5281/zenodo.3428841>. Cited on page 110.

Schönberner, D.; Driebe, T.; Blöcker, T. The evolution of helium white dwarfs. III. On the ages of millisecond pulsar systems. *Astronomy and Astrophysics*, v. 356, p. 929–934, apr. 2000. Available at: <https://arxiv.org/abs/astro-ph/0002503>. Cited on page 49.

Schreiber, M. R. et al. The origin and evolution of magnetic white dwarfs in close binary stars. *Nature Astronomy*, v. 5, p. 648–654, jan. 2021. Available at: <https://doi.org/10.1038/s41550-021-01346-8>. Cited on page 57.

Schwab, J. Cooling Models for the Most Massive White Dwarfs. *Astrophysical Journal*, v. 916, n. 2, p. 119, aug. 2021. Available at: <https://doi.org/10.3847/1538-4357/ac0336>. Cited on page 64.

Schwab, J. Evolutionary Models for the Remnant of the Merger of Two Carbon-Oxygen Core White Dwarfs. *Astrophysical Journal*, v. 906, n. 1, p. 53, jan. 2021. Available at: <https://doi.org/10.3847/1538-4357/abc87e>. Cited on page 64.

Schwab, J.; Bildsten, L.; Quataert, E. The importance of Urca-process cooling in accreting ONe white dwarfs. *Monthly Notices of the Royal Astronomical Society*, v. 472, n. 3, p. 3390–3406, 08 2017. ISSN 0035-8711. Available at: <https://doi.org/10.1093/mnras/stx2169>. Cited on page 64.

Schwab, J.; Wong, S. *MESA Summer School 2019: Lecture 1*. 2019. MESA Summer School 2019: Lecture 1. Available at: <https://jschwab.github.io/mesa-2019/flowchart.pdf>. Accessed on: 17 sep 2019. Cited on page 66.

Schwarzschild, K. Über das gleichgewicht der sonnenatmosphäre. *Nachrichten von der Gesellschaft der Wissenschaften zu Göttingen, Mathematisch-Physikalische Klasse*, n. 1, p. 41–53, 1906. Cited on page 62.

Seeds, M. A.; Backman, D. *Foundations of Astronomy*. Boston, Massachusetts, US: Cengage Learning, 2018. ISBN 9781337399920. Cited on page 170.

Segelstein, D. J. et al. New millisecond pulsar in a binary system. *Nature*, v. 322, n. 6081, p. 714–717, aug. 1986. Available at: <https://doi.org/10.1038/322714a0>. Cited on page 40.

Serenelli, A. Alive and well: A short review about standard solar models. *European Physical Journal A*, v. 52, n. 4, p. 78, apr. 2016. Available at: <https://doi.org/10.1140/epja/i2016-16078-1>. Cited 2 times on pages 36 and 69.

Serenelli, A. et al. Weighing stars from birth to death: mass determination methods across the HRD. *Astronomy and Astrophysics Reviews*, v. 29, n. 1, p. 4, dec. 2021. Available at: <https://doi.org/10.1007/s00159-021-00132-9>. Cited 2 times on pages 69 and 168.

Serenelli, A. M. et al. Evolution and colours of helium-core white dwarf stars: the case of low-metallicity progenitors. *Monthly Notices of the Royal Astronomical Society*, v. 337, n. 3, p. 1091–1104, 12 2002. ISSN 0035-8711. Available at: <https://dx.doi.org/10.1046/j.1365-8711.2002.05994.x>. Cited 3 times on pages 50, 110, and 115.

Serenelli, A. M. et al. New Solar Composition: The Problem with Solar Models Revisited. *Astrophysical Journal Letters*, v. 705, n. 2, p. L123–L127, nov. 2009. Available at: <https://doi.org/10.1088/0004-637X/705/2/L123>. Cited on page 36.

Seto, N. Search for neutron star binaries in the Local Group galaxies using LISA. *Monthly Notices of the Royal Astronomical Society*, v. 489, n. 4, p. 4513–4519, nov. 2019. Available at: <https://doi.org/10.1093/mnras/stz2439>. Cited on page 176.

Shah, S.; Nelemans, G.; van der Sluys, M. Using electromagnetic observations to aid gravitational-wave parameter estimation of compact binaries observed with lisa - ii. the effect of knowing the sky position. *Astronomy and Astrophysics*, v. 553, p. A82, 2013. Available at: <https://doi.org/10.1051/0004-6361/201321123>. Cited on page 55.

Shah, S.; van der Sluys, M.; Nelemans, G. Using electromagnetic observations to aid gravitational-wave parameter estimation of compact binaries observed with LISA. *Astronomy & Astrophysics*, v. 544, p. A153, aug. 2012. Available at: <https://doi.org/10.1051/0004-6361/201219309>. Cited on page 176.

Shahbaz, T. et al. Time-Resolved Optical Photometry of the Ultracompact Binary 4U 0614+091. *Publications of the Astronomical Society of the Pacific*, v. 120, n. 870, p. 848, aug. 2008. Available at: <https://doi.org/10.1086/590505>. Cited on page 180.

Shao, Y.; Li, X.-D. Formation and Evolution of Galactic Intermediate/Low-Mass X-ray Binaries. *The Astrophysical Journal*, IOP Publishing, v. 809, n. 1, p. 99, aug 2015. Available at: <https://doi.org/10.1088%2F0004-637x%2F809%2F1%2F99>. Cited on page 52.

Shiode, J. H.; Quataert, E. Setting the Stage for Circumstellar Interaction in Core-Collapse Supernovae. II. Wave-driven Mass Loss in Supernova Progenitors. *Astrophysical Journal*, v. 780, n. 1, p. 96, Jan 2014. Cited on page 64.

Shore, S. N.; Livio, M.; van den Heuvel, E. P. J. *Interacting binaries*. Berlin: Springer-Verlag, 1994. Available at: <https://doi.org/10.1007/3-540-31626-4>. Cited on page 34.

Shu, F. H. *The Physical Universe: An Introduction to Astronomy*. Sausalito, CA: University Science Books, 1982. (Series of books in astronomy). ISBN 9780935702057. Cited on page 170.

Siess, L. Evolution of massive AGB stars. III. the thermally pulsing super-AGB phase. *Astronomy & Astrophysics*, v. 512, p. A10, 2010. Available at: <https://doi.org/10.1051/0004-6361/200913556>. Cited on page 37.

Skumanich, A. Time Scales for CA II Emission Decay, Rotational Braking, and Lithium Depletion. *Astrophysical Journal*, v. 171, p. 565, Feb 1972. Cited 2 times on pages 47 and 73.

Sloan, D. et al. *Fine-tuning in the Physical Universe*. Cambridge: Cambridge University Press, 2020. ISBN 9781108484541. Cited on page 51.

Smartt, S. J. Progenitors of Core-Collapse Supernovae. *Annual Review of Astronomy & Astrophysics,*, v. 47, n. 1, p. 63–106, sep. 2009. Available at: <https://doi.org/10.1146/annurev-astro-082708-101737>. Cited on page 172.

Soberman, G. E.; Phinney, E. S.; van den Heuvel, E. P. J. Stability criteria for mass transfer in binary stellar evolution. *Astronomy and Astrophysics*, v. 327, p. 620–635, Nov 1997. Cited on page 46.

Soethe, L. T. T.; Kepler, S. O. Convection and rotation boosted prescription of magnetic braking: application to the formation of extremely low-mass white dwarfs. *Monthly Notices of the Royal Astronomical Society*, Oxford University Press (OUP), v. 506, n. 3, p. 3266–3281, 07 2021. ISSN 0035-8711. Stab1916. Available at: <https://doi.org/10.1093/mnras/stab1916>. Cited on page 187.

Solheim, J. E. The AM CVn Type Stars: an Overview. *Baltic Astronomy*, v. 4, p. 363–377, jan. 1995. Available at: <https://doi.org/10.1515/astro-1995-0314>. Cited on page 55.

Solheim, J. E. AM CVn Stars: Status and Challenges. *Publications of the Astronomical Society of the Pacific*, v. 122, n. 896, p. 1133, oct. 2010. Available at: <https://doi.org/10.1086/656680>. Cited on page 55.

Stancliffe, R. J. et al. Confronting uncertainties in stellar physics. II. Exploring differences in main-sequence stellar evolution tracks. *Astronomy and Astrophysics*, v. 586, p. A119, feb. 2016. Available at: <https://doi.org/10.1051/0004-6361/201527099>. Cited on page 69.

Stanton, L. G.; Murillo, M. S. Ionic transport in high-energy-density matter. *Physical Review E*, v. 93, n. 4, p. 043203, apr. 2016. Available at: <https://doi.org/10.1103/PhysRevE.93.043203>. Cited on page 114.

Starrfield, S. The accretion of solar material onto white dwarfs: No mixing with core material implies that the mass of the white dwarf is increasing. *AIP Advances*, v. 4, n. 4, p. 041007, apr. 2014. Available at: <https://doi.org/10.1063/1.4866984>. Cited on page 98.

Stella, L.; Priedhorsky, W.; White, N. E. The Discovery of a Second Orbital Period from the X-Ray Source 4U 1820-30 in the Globular Cluster NGC 6624. *Astrophysical Journal Letters*, v. 312, p. L17, jan. 1987. Available at: <https://doi.org/10.1086/184811>. Cited on page 180.

Suárez-Andrés, L. et al. Chemical abundances of the secondary star in the neutron star X-ray binary Cygnus X-2. *Monthly Notices of the Royal Astronomical Society*, v. 447, n. 3, p. 2261–2273, mar. 2015. Available at: <https://doi.org/10.1093/mnras/stu2612>. Cited on page 36.

Sukhbold, T.; Woosley, S. E. The Compactness of Presupernova Stellar Cores. *The Astrophysical Journal*, IOP Publishing, v. 783, n. 1, p. 10, feb 2014. Available at: <https://doi.org/10.1088%2F0004-637x%2F783%2F1%2F10>. Cited on page 64.

Sun, M.; Arras, P. Formation of extremely low-mass white dwarf binaries. *The Astrophysical Journal*, American Astronomical Society, v. 858, n. 1, p. 14, apr 2018. Available at: <https://doi.org/10.3847%2F1538-4357%2Faab9a4>. Cited 6 times on pages 38, 51, 53, 58, 64, and 78.

Tailo, M. et al. Mass-loss along the red giant branch in 46 globular clusters and their multiple populations. *Monthly Notices of the Royal Astronomical Society*, v. 498, n. 4, p. 5745–5771, nov. 2020. Available at: <https://doi.org/10.1093/mnras/staa2639>. Cited on page 68.

Tailo, M. et al. Mass-loss law for red giant stars in simple population globular clusters. *Monthly Notices of the Royal Astronomical Society*, v. 503, n. 1, p. 694–703, may 2021. Available at: <https://doi.org/10.1093/mnras/stab568>. Cited on page 68.

Tauris, T. M. Disentangling coalescing neutron-star–white-dwarf binaries for LISA. *Physical Review Letters*, American Physical Society, v. 121, p. 131105, Sep 2018. Available at: <https://link.aps.org/doi/10.1103/PhysRevLett.121.131105>. Cited 2 times on pages 55 and 176.

Tauris, T. M.; Langer, N.; Kramer, M. Formation of millisecond pulsars with CO white dwarf companions – II. Accretion, spin-up, true ages and comparison to MSPs with He white dwarf companions. *Monthly Notices of the Royal Astronomical Society*, v. 425, n. 3, p. 1601–1627, 09 2012. ISSN 0035-8711. Available at: <https://doi.org/10.1111/j.1365-2966.2012.21446.x>. Cited on page 53.

Tauris, T. M.; Savonije, G. J. Formation of millisecond pulsars. I. Evolution of low-mass X-ray binaries with $P_{orb} > 2$ days. *Astronomy & Astrophysics*, v. 350, p. 928–944, Oct 1999. Cited 2 times on pages 97 and 98.

Tauris, T. M.; van den Heuvel, E. P. J. Formation and evolution of compact stellar X-ray sources. In: _____. *Compact stellar X-ray sources*. Cambridge: Cambridge University Press, 2006. (Cambridge Astrophysics Series, 39), p. 623–665. ISBN 78-0-521-82659-4, 0-521-82659-4. Cited 4 times on pages 42, 52, 71, and 173.

Thoul, A. A.; Bahcall, J. N.; Loeb, A. Element Diffusion in the Solar Interior. *Astrophysical Journal*, v. 421, p. 828, Feb 1994. Cited on page 68.

Timmes, F. X.; Swesty, F. D. The Accuracy, Consistency, and Speed of an Electron-Positron Equation of State Based on Table Interpolation of the Helmholtz Free Energy. *Astrophysical Journal, Supplement*, v. 126, p. 501–516, feb 2000. Cited on page 65.

Tohline, J. E. The Origin of Binary Stars. *Annual Review of Astronomy and Astrophysics*, v. 40, p. 349–385, jan. 2002. Available at: <https://doi.org/10.1146/annurev.astro.40.060401.093810>. Cited on page 35.

Toloza, O. et al. Understanding the evolution of close white dwarf binaries. *Bulletin of the American Astronomical Society*, v. 51, n. 3, p. 168, May 2019. Cited on page 55.

Torres, G.; Andersen, J.; Giménez, A. Accurate masses and radii of normal stars: modern results and applications. *Astronomy and Astrophysics Reviews*, v. 18, n. 1-2, p. 67–126, feb. 2010. Available at: <https://doi.org/10.1007/s00159-009-0025-1>. Cited on page 36.

Tout, C. A. Evolution of binary systems. *EAS Publications Series*, v. 19, p. 31–49, 2006. Available at: <https://doi.org/10.1051/eas:2006024>. Cited on page 28.

Tout, C. A. et al. Rapid binary star evolution for N-body simulations and population synthesis. *Monthly Notices of the Royal Astronomical Society*, v. 291, n. 4, p. 732–748, 11 1997. ISSN 0035-8711. Available at: <https://doi.org/10.1093/mnras/291.4.732>. Cited on page 46.

Tout, C. A. et al. Binary star origin of high field magnetic white dwarfs. *Monthly Notices of the Royal Astronomical Society*, v. 387, n. 2, p. 897–901, 05 2008. ISSN 0035-8711. Available at: <https://doi.org/10.1111/j.1365-2966.2008.13291.x>. Cited on page 57.

Tremblay, P. E. et al. The field white dwarf mass distribution. *Monthly Notices of the Royal Astronomical Society*, v. 461, p. 2100–2114, Sep 2016. Available at: <https://doi.org/10.1093/mnras/stw1447>. Cited on page 37.

Tremblay, P. E. et al. White Dwarf Cosmochronology in the Solar Neighborhood. *Astrophysical Journal*, v. 791, n. 2, p. 92, Aug 2014. Available at: <https://doi.org/10.1088%2F0004-637x%2F791%2F2%2F92>. Cited on page 37.

Tremblay, P. E. et al. Pure-hydrogen 3D model atmospheres of cool white dwarfs. *Astronomy & Astrophysics*, v. 552, p. A13, Apr 2013. Available at: <https://doi.org/10.1051/0004-6361/201220813>. Cited on page 67.

Tremblay, P. E. et al. Spectroscopic analysis of DA white dwarfs with 3D model atmospheres. *Astronomy & Astrophysics*, v. 559, p. A104, Nov 2013. Available at: <https://doi.org/10.1051/0004-6361/201322318>. Cited on page 67.

Truemper, J.; Lewin, W. H. G.; Brinkmann, W. *The evolution of galactic x-ray binaries*. Dordrecht, Holland: D. Reidel Publishing Company, 1986. v. 167. (NATO Advanced Study Institute (ASI) Series C, v. 167). Cited on page 81.

Tutukov, A. V.; Cherepashchuk, A. M. Evolution of close binary stars: theory and observations. *Physics Uspekhi*, v. 63, n. 3, p. 209–244, mar. 2020. Available at: <https://doi.org/10.3367/UFNe.2019.03.038547>. Cited 6 times on pages 28, 33, 34, 35, 51, and 92.

Tutukov, A. V. et al. The evolutionary status of MXB 1820-30 and other short-period low-mass X-ray sources. *Soviet Astronomy Letters*, v. 13, p. 328, oct. 1987. Cited on page 52.

Ulrich, R. K. Thermohaline Convection in Stellar Interiors. *Astrophysical Journal*, v. 172, p. 165, Feb 1972. Cited on page 67.

van den Heuvel, E. P.; Rappaport, S. *X-Ray binaries and recycled pulsars*. Berlin/Heidelberg, Germany: Springer Science & Business Media Dordrecht, Originally published by Kluwer Academic Publishers, 1992. v. 377. (NATO Advanced Study Institute (ASI) Series C, v. 377). Cited on page 81.

van den Heuvel, E. P. J. Interacting binaries: topics in close binary evolution. In: *Saas-Fee Advanced Course 22: Interacting Binaries*. Berlin: Springer-Verlag, 1994. p. 263–474. Cited on page 34.

van der Sluys, M. V.; Verbunt, F.; Pols, O. R. Creating ultra-compact binaries in globular clusters through stable mass transfer. *Astronomy and Astrophysics*, v. 431, p. 647–658, feb. 2005. Available at: <https://doi.org/10.1051/0004-6361:20041777>. Cited on page 52.

Van, K. X.; Ivanova, N. Evolving LMXBs: CARB Magnetic Braking. *The Astrophysical Journal*, American Astronomical Society, v. 886, n. 2, p. L31, nov 2019. Available at: <https://doi.org/10.3847%2F2041-8213%2Fab571c>. Cited 15 times on pages 58, 68, 73, 74, 77, 78, 79, 83, 84, 85, 86, 91, 117, 118, and 181.

Van, K. X.; Ivanova, N.; Heinke, C. O. Low-mass X-ray binaries: the effects of the magnetic braking prescription. *Monthly Notices of the Royal Astronomical Society*, v. 483, n. 4, p. 5595–5613, Dec 2018. ISSN 0035-8711. Available at: <https://doi.org/10.1093/mnras/sty3489>. Cited 4 times on pages 58, 73, 74, and 91.

van Kerkwijk, M. H. et al. Optical Studies of Companions to Millisecond Pulsars. In: Rasio, F. A.; Stairs, I. H. (Ed.). *Binary Radio Pulsars*. San Francisco: Astronomical Society of the Pacific, 2005. (Astronomical Society of the Pacific Conference Series, v. 328), p. 357. Available at: <http://aspbooks.org/custom/publications/paper/328-0357.html>. Cited on page 98.

van Kerkwijk, M. H. et al. The Temperature and Cooling Age of the White Dwarf Companion to the Millisecond Pulsar PSR B1855+09. *The Astrophysical Journal*, IOP Publishing, v. 530, n. 1, p. L37–L40, feb 2000. Available at: <https://doi.org/10.1086%2F312478>. Cited on page 40.

van Kerkwijk, M. H.; Bergeron, P.; Kulkarni, S. R. The Masses of the Millisecond Pulsar J1012+5307 and Its White Dwarf Companion. *The Astrophysical Journal*, IOP Publishing, v. 467, n. 2, p. L89–L92, aug 1996. Available at: <https://doi.org/10.1086%2F310209>. Cited 2 times on pages 38 and 98.

van Roestel, J. et al. Discovery of 36 eclipsing EL CVn binaries found by the Palomar Transient Factory. *Monthly Notices of the Royal Astronomical Society*, v. 475, n. 2, p. 2560–2590, apr. 2018. Available at: <https://doi.org/10.1093/mnras/stx3291>. Cited on page 55.

Verbunt, F.; Zwaan, C. Magnetic braking in low-mass X-ray binaries. *Astronomy and Astrophysics*, v. 100, p. L7–L9, Jul 1981. Cited on page 47.

Walker, M. A.; Ćirković, M. M. Astrophysical fine tuning, naturalism, and the contemporary design argument. *International Studies in the Philosophy of Science*, Routledge: Taylor & Francis, v. 20, n. 3, p. 285–307, 2006. Available at: <https://doi.org/10.1080/02698590600960945>. Cited on page 51.

Wang, B. et al. Ultracompact X-ray binaries with He star companions. *Monthly Notices of the Royal Astronomical Society*, v. 506, n. 3, p. 4654–4666, sep. 2021. Available at: <https://doi.org/10.1093/mnras/stab2032>. Cited on page 179.

Wang, B.; Podsiadlowski, P.; Han, Z. He-accreting carbon–oxygen white dwarfs and Type Ia supernovae. *Monthly Notices of the Royal Astronomical Society*, v. 472, n. 2, p. 1593–1599, 08 2017. ISSN 0035-8711. Available at: <https://doi.org/10.1093/mnras/stx2192>. Cited on page 64.

Wang, J. Physical Environment of Accreting Neutron Stars. *Advances in Astronomy*, v. 2016, p. 3434565, jan. 2016. Available at: <https://doi.org/10.1155/2016/3424565>. Cited on page 40.

Wang, L. et al. The Pre-He White Dwarf in the Post-mass Transfer Binary EL CVn. *Astronomical Journal*, v. 159, n. 1, p. 4, jan. 2020. Available at: <https://doi.org/10.3847/1538-3881/ab52fa>. Cited on page 55.

Warner, B. The AM Canum Venaticorum Stars. *Astrophysics and Space Science*, v. 225, n. 2, p. 249–270, mar. 1995. Available at: <https://doi.org/10.1007/BF00613240>. Cited on page 55.

Webbink, R. F. Double white dwarfs as progenitors of R Coronae Borealis stars and type I supernovae. *Astrophysical Journal*, v. 277, p. 355–360, Feb 1984. Cited on page 54.

Webbink, R. F. Stellar Evolution and Binaries. In: _____. *Interacting Binary Stars*. Cambridge: Cambridge University Press, 1985. (Cambridge Astrophysics Series), cap. 2, p. 39. Cited 2 times on pages 43 and 45.

Webbink, R. F.; Rappaport, S.; Savonije, G. J. On the evolutionary status of bright, low-mass X-ray sources. *Astrophysical Journal*, v. 270, p. 678–693, jul. 1983. Available at: <https://doi.org/10.1086/161159>. Cited on page 96.

Weber, E. J.; Davis, L. J. The Angular Momentum of the Solar Wind. *Astrophysical Journal*, v. 148, p. 217–227, Apr 1967. Cited 2 times on pages 47 and 74.

Wei, D. et al. Mass transfer of low-mass binaries and chemical anomalies among unevolved stars in globular clusters. *Monthly Notices of the Royal Astronomical Society*, v. 493, n. 4, p. 5479–5488, apr. 2020. Available at: <https://doi.org/10.1093/mnras/staa613>. Cited on page 36.

Weinberg, S. *To explain the world: The discovery of modern science*. New York: Harper Collins, 2015. ISBN 9780062346674. Cited on page 51.

Weiss, A. Key problems in stellar evolution. In: Battrick, B. et al. (Ed.). *Stellar Structure and Habitable Planet Finding*. Noordwijk, The Netherlands: ESA Publications Division, 2002. (ESA Special Publication, v. 485), p. 57–64. Cited on page 36.

Weiss, A.; Aguirre, V. S.; Christensen-Dalsgaard, J. Using low-mass stars as a tool: efforts towards precise models. In: Chiappini, C. et al. (Ed.). *Rediscovering Our Galaxy*. Cambridge, UK: Cambridge University Press, 2018. v. 334, p. 178–181. Available at: <https://doi.org/10.1017/S1743921317008894>. Cited on page 69.

Weiss, A. et al. Stellar Evolution Challenge. In: Vazdekis, A.; Peletier, R. (Ed.). *Stellar Populations as Building Blocks of Galaxies*. Paris: International Astronomical Union, 2007. v. 241, p. 28–36. Available at: <https://doi.org/10.1017/S1743921307007363>. Cited on page 69.

Weiss, A.; Schlattl, H. GARSTEC—the Garching Stellar Evolution Code. The direct descendant of the legendary Kippenhahn code. *Astrophysics and Space Science*, v. 316, n. 1-4, p. 99–106, aug. 2008. Available at: <https://doi.org/10.1007/s10509-007-9606-5>. Cited on page 69.

White, N. E.; Swank, J. H. The periodic absorption events from 4U 1915-05. *Astrophysical Journal Letters*, v. 253, p. L61–L66, feb. 1982. Available at: <https://doi.org/10.1086/183737>. Cited on page 180.

White, R. J.; Ghez, A. M. Observational Constraints on the Formation and Evolution of Binary Stars. *Astrophysical Journal*, v. 556, n. 1, p. 265–295, jul. 2001. Available at: <https://doi.org/10.1086/321542>. Cited on page 35.

Wijnen, T. P. G.; Zorotovic, M.; Schreiber, M. R. White dwarf masses in cataclysmic variables. *Astronomy and Astrophysics*, v. 577, p. A143, may 2015. Available at: <https://doi.org/10.1051/0004-6361/201323018>. Cited on page 98.

Wilhelm, M. J. C. et al. The Milky Way's bar structural properties from gravitational waves. *Monthly Notices of the Royal Astronomical Society*, v. 500, n. 4, p. 4958–4971, jan. 2021. Available at: <https://doi.org/10.1093/mnras/staa3457>. Cited on page 175.

Willems, B.; Kolb, U. Detached white dwarf main-sequence star binaries. *Astronomy & Astrophysics*, v. 419, n. 3, p. 1057–1076, 2004. Available at: <https://doi.org/10.1051/0004-6361:20040085>. Cited 2 times on pages 28 and 36.

Winget, D. E. et al. An Independent Method for Determining the Age of the Universe. *Astrophysical Journall*, v. 315, p. L77, Apr 1987. Available at: <https://doi.org/10.1086/184864>. Cited on page 37.

Winget, D. E.; Kepler, S. O. Pulsating white dwarf stars and precision asteroseismology. *Annual Review of Astronomy and Astrophysics*, v. 46, p. 157–199, sep. 2008. Available at: <https://doi.org/10.1146/annurev.astro.46.060407.145250>. Cited 2 times on pages 36 and 37.

Wolf, W. M. et al. Hydrogen Burning on Accreting White Dwarfs: Stability, Recurrent Novae, and the Post-nova Supersoft Phase. *Astrophysical Journal*, v. 777, n. 2, p. 136, Nov 2013. Cited 2 times on pages 64 and 120.

Wong, T. L. S.; Bildsten, L. Mass Transfer and Stellar Evolution of the White Dwarfs in AM CVn Binaries. *arXiv e-prints*, p. arXiv:2109.13403, sep. 2021. Cited on page 55.

Woosley, S. E.; Heger, A. The Remarkable Deaths of 9-11 Solar Mass Stars. *The Astrophysical Journal*, IOP Publishing, v. 810, n. 1, p. 34, aug 2015. Available at: <https://doi.org/10.1088%2F0004-637x%2F810%2F1%2F34>. Cited on page 37.

Wu, C. et al. Mass retention efficiencies of He accretion onto carbon-oxygen white dwarfs and type Ia supernovae. *Astronomy and Astrophysics*, v. 604, p. A31, jul. 2017. Available at: <https://doi.org/10.1051/0004-6361/201630099>. Cited 2 times on pages 98 and 120.

Wu, Y. et al. Formation of hot subdwarf B stars with neutron star components. *Astronomy and Astrophysics*, v. 618, p. A14, oct. 2018. Available at: <https://doi.org/10.1051/0004-6361/201832686>. Cited on page 51.

Xing, Z.-P.; Li, X.-D. On the Rapid Orbital Expansion in the Compact Low-mass X-Ray Binary 2A 1822-371. *The Astrophysical Journal*, American Astronomical Society, v. 887, n. 2, p. 201, dec 2019. Available at: <https://doi.org/10.3847%2F1538-4357%2Fab55e1>. Cited on page 52.

Yu, J. et al. The Formation of Subdwarf A-type Stars. *Astrophysical Journal*, v. 885, n. 1, p. 20, nov. 2019. Available at: <https://doi.org/10.3847/1538-4357/ab44b5>. Cited on page 51.

Zhang, X. et al. Post-merger evolution of carbon–oxygen + helium white dwarf binaries and the origin of R Coronae Borealis and extreme helium stars. *Monthly Notices of the Royal Astronomical Society*, v. 445, n. 1, p. 660–673, 09 2014. ISSN 0035-8711. Available at: <https://doi.org/10.1093/mnras/stu1741>. Cited on page 54.

Zhang, Y. et al. Impact of mass transfer schemes on mass-orbital period relation. *Monthly Notices of the Royal Astronomical Society*, v. 502, n. 1, p. 383–389, mar. 2021. Available at: <https://doi.org/10.1093/mnras/stab020>. Cited on page 70.

Zinnecker, H. Binary Stars: Historical Milestones. In: Zinnecker, H.; Mathieu, R. (Ed.). *The Formation of Binary Stars*. Cambridge, UK: Cambridge University Press, 2001. v. 200, p. 1–12. Available at: <https://doi.org/10.1017/S0074180900224996>. Cited on page 27.

Ziółkowski, J. Evolution of Close Binaries. VI. A Program for Computation of Evolution with Mass Exchange. *Acta Astronomica*, v. 20, p. 59, jan. 1970. Cited on page 49.

Ziółkowski, J. Evolution of Close Binaries. VII. Evolution of Binaries of Low and Moderate Mass. *Acta Astronomica*, v. 20, p. 213, jan. 1970. Cited on page 49.

Zorotovic, M.; Schreiber, M. R. Cataclysmic variable evolution and the white dwarf mass problem: A Review. *Advances in Space Research*, v. 66, n. 5, p. 1080–1089, sep. 2020. Available at: <https://doi.org/10.1016/j.asr.2019.08.044>. Cited on page 39.

Zou, Z.-C.; Zhou, X.-L.; Huang, Y.-F. The gravitational wave emission of double white dwarf coalescences. *Research in Astronomy and Astrophysics*, v. 20, n. 9, p. 137, sep. 2020. Available at: <https://doi.org/10.1088/1674-4527/20/9/137>. Cited on page 176.

Zurek, D. R. et al. An Ultracompact X-Ray Binary in the Globular Cluster NGC 1851. *Astrophysical Journal*, v. 699, n. 2, p. 1113–1118, jul. 2009. Available at: <https://doi.org/10.1088/0004-637X/699/2/1113>. Cited on page 180.

Appendix

APPENDIX A – Overview of stellar evolution of single stars

Since the evolution of *single stars* is not the main theme of this work, but it is important for the general understanding of the subject, we will present here only an overview of the topic.

Stars form inside primordial clouds of cool gas which are composed mostly of the lightest elements — hydrogen and helium — that were created just after the Big Bang. These clouds are initially huge (from tenths to dozens of parsecs) and, as a natural adjustment between pressure and gravity, fragments into small and more compact clumps of matter. In fact, the details of how this occurs depends on a number of factors, such as the total gas mass, temperature, particle density, and the type of gas considered. This was shown in the work of Jeans (1902), which introduced the concepts that we know today as Jeans mass and Jeans length, so that the Jeans mass is the mass contained in a volume with radius the Jeans length. Therefore, the Jeans mass is such that perturbations larger than the Jeans length will collapse the cloud under their own gravity. Metallicity also plays a role. Hydrodynamic simulations found that there is no critical metallicity below which fragmentation is impossible. Nevertheless, there is a clear change in the behaviour of the clouds at very low metallicity ($Z \lesssim 10^{-5}\ Z_{\odot}$), indicating that fragmentation takes longer to occur (Dopcke et al., 2013).

This process repeats until the point that a clump of matter has the mass of a star (something between tenths and tens of times the mass of the Sun), giving rise to the so-called protostar. If this object has a mass greater than $\sim 0.08\ M_{\odot}$, the temperature at its centre will reach $\sim 10^7$ K and the hydrogen will begin to fuse into helium. A new star has been born. The stage at which the star begins to ignite hydrogen is known as Zero Age Main Sequence (ZAMS). As long as hydrogen is available for burning in the core, the star will be in the so-called Main Sequence (MS).

The empirical function that describes the initial distribution of masses for a given population of stars is called initial mass function, and it indicates that there are many more low mass stars being born than massive ones. In fact, the most widely used initial mass function today is that of Salpeter (1955) ($\mathrm{d}N/\mathrm{d}M \propto M^{-2.35}$), which shows that we have $N = 300$ stars of $M = 1\ M_{\odot}$ for each star of $M = 10\ M_{\odot}$.

Several criteria are used in the classification of stars, whether indicating their possible composition, their kinematics, current evolutionary stage, or the way we see it from Earth. However, the main factor determining the evolutionary path a star will follow

is the mass with which it forms (e.g., see Serenelli et al., 2021 for an extensive, fresh review). Other factors that also have some importance are chemical composition, rotation, and mass loss by winds. Figure 25 illustrates the different possible paths for the evolution of a star, depending on the protostar's initial mass.

Figure 25 – An artistic depiction of the main evolutionary paths of a single star. Time evolves from left to right. Sizes and time are not to scale.

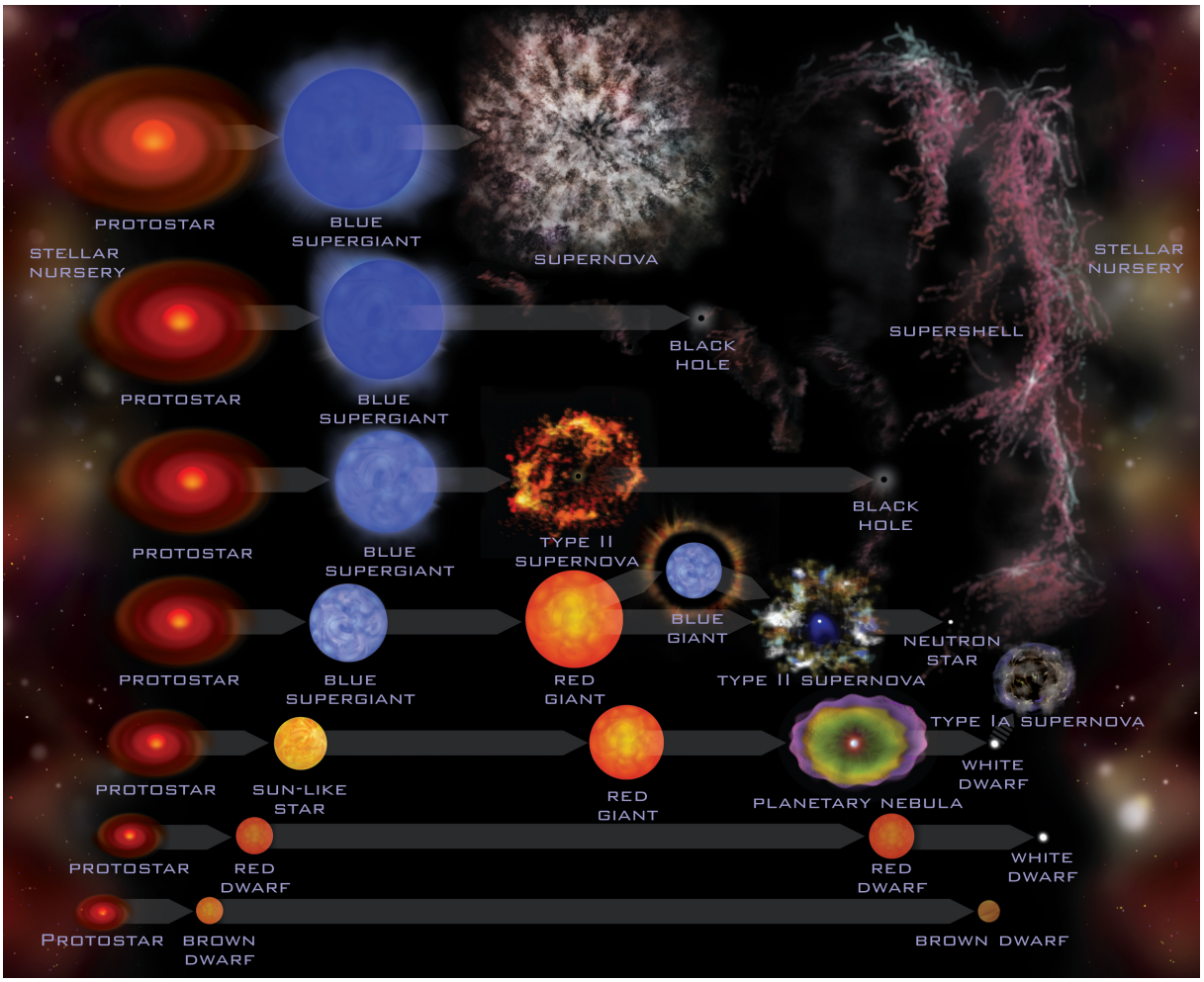

Credit: Courtesy NASA/JPL-Caltech (Jet Propulsion Laboratory, 2019).

From a theoretical point of view, stars are usually divided into three categories, according to their initial mass:

a) low-mass stars: $0.08 \lesssim M/M_\odot \lesssim 2.0$;

b) intermediate-mass stars: $2.0 \lesssim M/M_\odot \lesssim 10.0$;

c) high-mass stars: $M \gtrsim 10.0 M_\odot$.

A more detailed classification for the initial mass can be found in Figure 26, where the sequence of evolutionary phases (y-axis) as a function of the initial mass (x-axis) is

shown. Substellar objects formed with a mass less than $\sim 0.08\ M_\odot$ cannot fuse hydrogen at the centre, and are therefore called brown dwarfs rather than stars.

Figure 26 – A schematic showing how the initial stellar mass (x-axis) determines the main nuclear burning phases of different elements (y-axis) at solar metallicity, as well as the type of the final remnant.

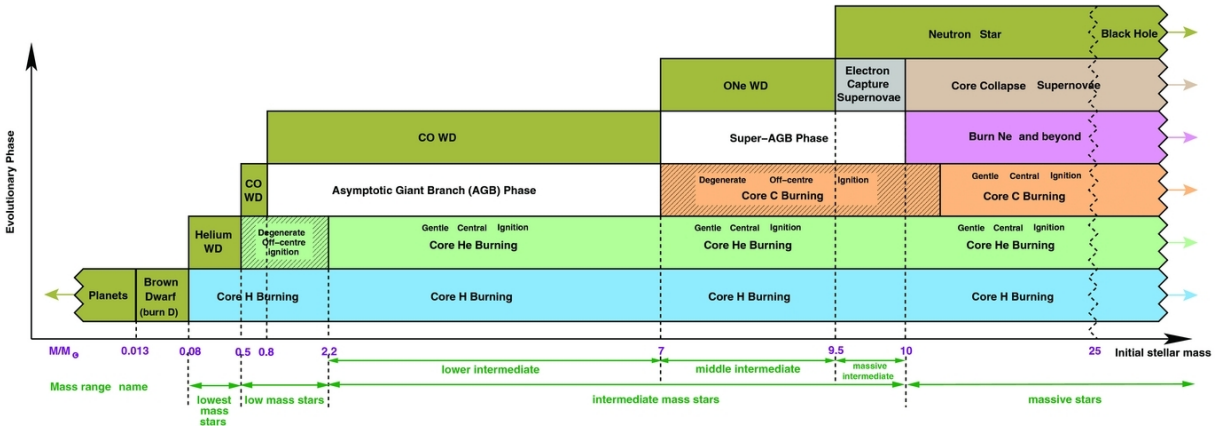

Credit: Karakas & Lattanzio (2014).

Details of the evolution of stars with a mass between 1 and 15 $M_\odot$ were presented in depth in the seminal works of Iben (1965b), Iben (1965a), Iben (1965c), Iben (1966a), Iben (1966b), Iben (1966c), Iben (1967b), Iben (1967c), Iben (1967d), Iben (1967a), Iben (1991).

Observationally, one of the best ways to study stars is by measuring their luminosities and colours. The colour of a star reflects the temperature on its surface, the photosphere. The effective temperature ($T_{\rm eff}$) of a star is the temperature of a black body that would emit the same total amount of electromagnetic radiation as such a star, i.e., the temperature of a black body with the same luminosity per surface area as the star. The luminosity L is the power of the star, the total amount of energy it radiates per unit of time. In good approximation, these quantities are related, considering the approximation of black body radiation in the equation

$$L = 4\pi\sigma R^2 T_{\rm eff}^4\ , \tag{A.1}$$

where R is the radius of the star. L is the luminosity and σ is the Stefan-Boltzmann constant. This relation shows that both the radius and the temperature influence the luminosity of the star.

The diagram that presents these quantities is called an Hertzsprung–Russell diagram (HRD, see Figure 27), proposed by Ejnar Hertzsprung (1873–1967), in 1911, and Henry Norris Russell (1877–1957), in 1913. In general, an HRD is presented as having the luminosity on the vertical axis and the temperature on the horizontal axis. It is also

common to present the spectral classification next to the effective temperature since much of the information about the physical properties of stars is obtained directly or indirectly from their spectra (temperatures, densities, compositions, etc). The stars are classified by decreasing temperature according to the following order: O, B, A, F, G, K and M, corresponding to the range 35,000–3,000 K.

Placing all the stars of a given sample into an HRD gives us an excellent idea of the properties of the population. The most striking feature of an HRD of any star population is that stars tend to fall only into certain regions of the diagram, being the diagonal the most prominent one. This region represents precisely the main sequence (MS), which is the stage in which the stars spend most of their lifetime. For low-mass stars, a good approximation of this time is given by

$$t_{\rm MS} \approx 10^{10} \left(\frac{M}{M_\odot} \right)^{-2} \ {\rm yr} \ , \tag{A.2}$$

where $M_\odot$ is the mass of the Sun. See Hurley, Pols & Tout (2000) for a more comprehensive analytic formulae.

Figure 27 shows the theoretical path of a 1 $M_\odot$ star in the HRD diagram from ZAMS to its end as a white dwarf. A 1 $M_\odot$ star will spend about 10^{10} years on the MS, for metallicities similar to the Sun. When the hydrogen in the core is exhausted, the central temperature is not high enough for helium to fuse into heavier elements in low mass stars. At this point the internal pressure will not be enough to avoid gravitational collapse and the core slowly starts to contract. According to the Virial theorem, half of the gravitational energy released by the contracting core is balanced by an increase in the thermal energy, while the other half will be lost by radiation from the surface. This causes the outer layers of the star to expand. On the other hand, the centre is getting hotter, and so the hydrogen burning will restart, but this time only in a shell surrounding the helium core. As the star is now bigger, this burning phase will make the star shine brighter than before. The energy coming from the burning shell is transferred to the envelope, causing it to expand and cool. The radius of the star expands 10 to 100 times its original size during this phase. At this stage, the star is very bright, very large and cold (that is, red). Hence, the name red-giant phase. In low-mass stars, the core becomes degenerate during this phase. This means that the electron degeneracy pressure is stronger than the thermal pressure. The main difference of this configuration is that the pressure is a function only of the density, while for an ideal gas it also depends on the temperature. The high central temperature causes more efficient and energetic nuclear reactions to occur, so the ignition of helium occurs explosively in a phenomenon called helium core flash (Shu, 1982; Carroll; Ostlie, 2017; Seeds; Backman, 2018; Hansen; Kawaler; Trimble, 2004). This is an extremely rapid — of the order of few seconds or minutes — and high energetic — the local luminosity is comparable to that of an entire galaxy — event (Ryden; Peterson, 2020; Kippenhahn;

Figure 27 – An illustration of the theoretical path of a solar-mass star in the HRD. Note the MS in the diagonal, the current evolutionary state of the Sun. The illustration highlights some important points of evolution, such as the increase of radius in the red giant phase, the start of helium burning, the burning of elements in the outer shells, the ejection of the planetary nebula, and the white dwarf cooling track.

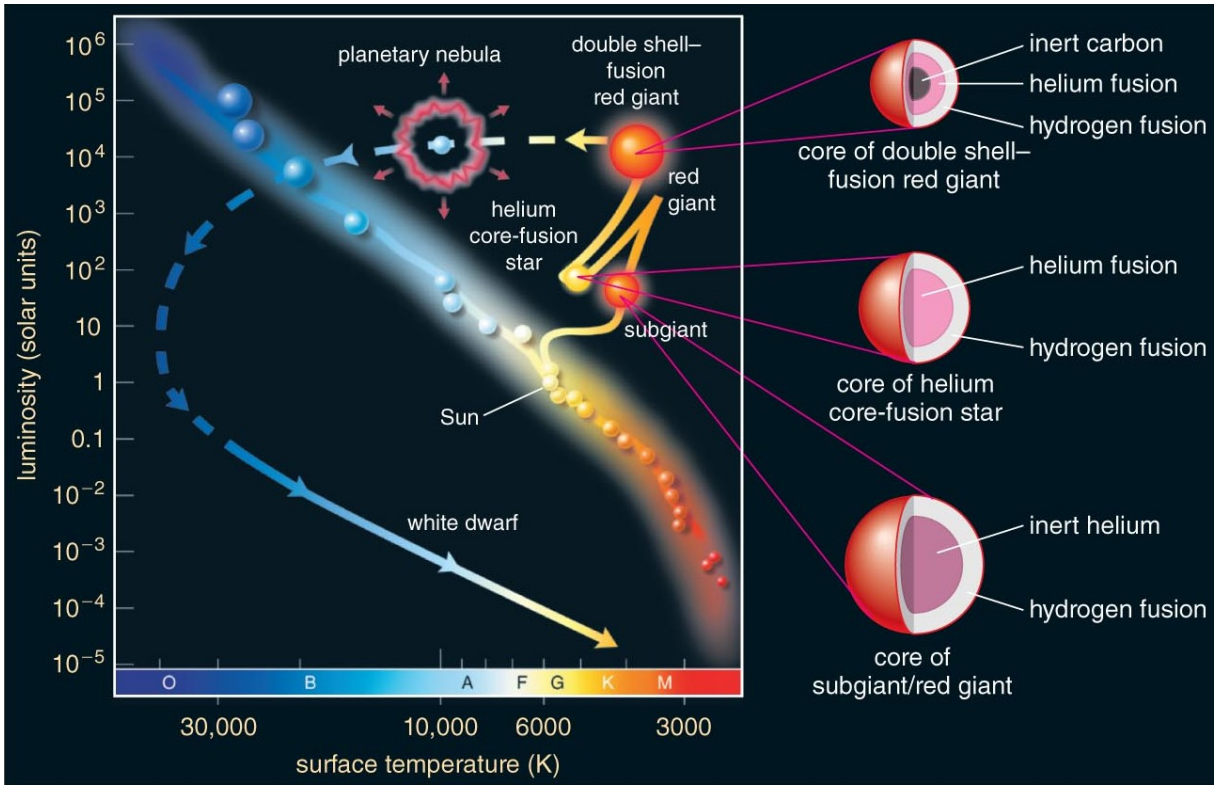

Credit: Bennett et al. (2017).

Weigert; Weiss, 2012). However, almost nothing of this energy reaches the surface, since it is absorbed by expansion of the non-degenerate layers above. Low-mass stars ignite helium in their cores essentially at the same core mass of 0.45 $M_{\odot}$.

With the centre even hotter, new nuclear reactions — namely, triple alpha — take place, and the core becomes dominated by carbon and oxygen. In low-mass stars, the helium core flash marks the beginning of the helium burning into carbon, which is followed by a decrease in luminosity. Then the star settles in the horizontal branch, where the core now is burning helium under non-degenerate conditions and is already enriched in carbon by $\sim 5\%$. Oxygen is a by-product of the same nuclear process: newly formed carbon reacts with existing helium and forms oxygen. Thus, the core of the star becomes rich in carbon and oxygen nuclei, and the surface temperature goes up while the star moves towards the horizontal branch in the HRD.

Now helium forms a shell around the core and the hydrogen is in the envelope of

the star. The reactions in the centre will cease, occurring only on the outer layers. An expansion and cooling phase similar to the previous one occurs again, this time called asymptotic giant branch — AGB. In this phase, the interior structure of the star is characterised by an inert core of carbon and oxygen, a shell where helium is undergoing fusion to form carbon, another shell where hydrogen is undergoing fusion forming helium, and a very large envelope where no nuclear reactions are occurring. Finally, the helium burning will become unstable and will cause the thermal pulses, which will eject the outer layers, potentially forming a planetary nebula. Actually, the shapes of most of the planetary nebulae are not spherically symmetric. Thus, there is a strong debate over what makes and shapes the circumstellar gas of these evolved, intermediate mass stars. The most debated hypothesis by the community in the last decades is that single stars cannot trivially manufacture planetary nebulae with nonspherical shapes, and a binary companion might be needed in a majority of cases. However, this theoretical conjecture has not been tested observationally. We refer to de Marco (2009) for a recent review. In one way or another, the end product of this wonderful event is called white dwarf: a core of carbon and oxygen with a hydrogen and helium mantle in the form of an extremely dense object the size of the earth. If the progenitor star had a mass larger than 6–10 $M_{\odot}$, the central temperature reaches 6×10^8 K and carbon burning starts. For masses smaller than about 10.5 $M_{\odot}$, forming a O-Ne core white dwarf.

Intermediate and high-mass stars are hotter and more luminous than their lighter companions, thus occupying the upper left region of the HRD while in the main sequence. Massive stars are rarer and evolve very fast when compared to low-mass stars, making their studies more complicated. Its evolution differs in many aspects when compared to less massive stars, just to name a few, wind mass loss, rotation, transport of angular momentum, and internal mixing processes (de Loore, 1980). More details can be found in the recent reviews of Smartt (2009), Langer (2012), Nomoto, Kobayashi & Tominaga (2013). Roughly speaking, the vast majority of stars with intermediate initial mass will become white dwarfs, where the central composition will depend on the initial mass. Massive stars will become neutron stars (NS) or black holes (BH).

Regarding the production of elements in massive stars, the main difference is that they will be able to synthesise increasingly heavy elements according to their mass. Table 2 summarises the main nuclear processes that can take place in stellar interiors. The threshold temperature must be compared to the temperature of the centre of the star for a reaction to occur. Massive stars continue to have nuclear reactions through several other stages of nuclear fusion until iron is synthesised in the nucleus. In fact, it is believed that all elements between atomic number 8 (oxygen) and 37 (rubidium) came from either exploding massive stars or white dwarfs (Johnson, 2017). Massive stars will end their life in an extremely energetic explosion called a supernova. It is believed that elements heavier than iron require a supernova for their formation (Greenwood; Earnshaw,

Table 2 – Summary of the nuclear reactions and their end products that can take place inside a star. In a low-mass star the core temperature is relatively low, so only p-p chain and CNO cycle act significantly. As a result, we should not expect significant amounts of elements heavier than hydrogen and helium in these stars.

Nuclear fuel	**Process**	**Threshold temperature (K)**	**Comparative efficiency**	**Produtcs**
H	p-p chain	$\sim 4 \times 10^6$	$\epsilon_{\text{p-p}} \propto T^4$	He
H	CNO cycle	15×10^6	$\epsilon_{\text{CNO}} \propto T^{20}$	He
He	3 α	100×10^6	$\epsilon_{3\alpha} \propto T^{40}$	C, O
C	C + C	600×10^6		O, Ne, Na, Mg
O	O + O	1000×10^6		Mg, S, P, Si
Si	Disintegration	3000×10^6		Co, Fe, Ni

2012). Supernovae are so energetic that during a few weeks their luminosity is comparable to the luminosity of the whole galaxy in which they are located. The remaining object of a supernova will also have different characteristics. When exceeding the limit mass of $\sim 1.4\ M_\odot$ — called the Chandrasekhar limit — the degenerate electron pressure will no longer be able to withstand the gravity of the star and the nucleons will be disrupted. The only remaining possibility to sustain gravity is via degenerate neutron pressure, giving rise to a neutron star (NS). The main process in the neutronization is the inverse β-decay ($e^- + p \rightarrow n + \nu_e$), that acts consuming electrons and protons and generating neutrons. The temperature of a newborn NS is around 10^{12} K and they have a mass of about 1–2 $M_\odot$ compressed into a sphere of radius of about 10 km. An extreme case occurs if the object cannot sustain itself, becoming a completely collapsed object called a black hole (BH). Table 3 shows the three possible types of compact objects predicted by stellar evolution, depending on the initial mass.

Table 3 – End products comparison between single versus binary stellar evolution as a function of the initial mass. In the case of white dwarfs, the most likely composition at the end of evolution is indicated. These are rough estimates. Exact values depend on a number of other factors as discussed in the text.

		Final product	
Initial mass ($M_\odot$)	**He-core mass** ($M_\odot$)	**Single star**	**Binary star**
< 2.3	0.45	CO WD	He WD
2.3–6	0.6–1.9	CO WD	CO WD
6–8	1.9–2.1	O-Ne-Mg WD or C-deflagration SN	O-Ne-Mg WD
8–12	2.1–2.8	NS	O-Ne-Mg WD
12–25	2.8–8	NS	NS
> 25	> 8	BH	BH

Credit: Tauris & van den Heuvel (2006).

APPENDIX B – Gravitational waves and X-ray emission from systems containing (pre-) ELM WDs

In contrast to electromagnetic (EM) waves, gravitational waves (GW, Press; Thorne, 1972; Misner; Thorne; Wheeler, 1973; Hawking; Israel, 1989) observations provide measurements of the amplitude of the waves rather than the energy flux. This implies that the observed GW signals scales as $1/d$ rather than $1/d^2$, allowing to generally detect sources in GWs at larger distances than in the traditional EMs observational bands (Wilhelm et al., 2021). Furthermore, GW radiation hardly interacts with matter, and therefore retains its original properties even far from the emitting source (Camp; Cornish, 2004). Along with photons (EM radiation), neutrinos and cosmic rays, gravitational waves now join multimessenger astronomy (Bartos; Kowalski, 2017; Burns et al., 2019; Bailes et al., 2021). In particular, double WD systems emit GWs in the mHz band and should also contribute to the multimessenger astronomy (Baker et al., 2019b). For an extensive review of the impact of space experiments on our knowledge of the physics of the universe, we refer the reader to Giovannelli & Sabau-Graziati (2004), Sathyaprakash & Schutz (2009).

The Milky Way is expected to contain $\mathcal{O}(10^7)$ semi-detached double WDs (Nelemans et al., 2001) and $\mathcal{O}(10^8)$ close detached systems (Nelemans et al., 2001). The shortest period ELM WD binaries will serve as multimessenger laboratories (Korol et al., 2017; Kupfer et al., 2018). In particular, Brown et al. (2020) discovered the first He+He WD LISA[1] verification binary, a dominant LISA source along with He-CO double WDs (Lamberts et al., 2019). Very recently, Kilic et al. (2021b) discovered the two brightest detached binary white dwarfs with periods less than an hour. These systems are characterized by 0.230 and 0.209 $M_\odot$ ELM WDs in companion to more massive WDs. The merger rate of disc ELM WD binaries in the Milky Way is approximately 4×10^{-5} yr^{-1} (Brown et al., 2011b). Even more, Ruiter et al. (2010) found that $> 99\%$ of remnant binaries that have orbital periods within the LISA sensitivity range are WD binaries.

The LISA sensitivity band frequency is from 10^{-1} to 10^{-5} Hz, with a peak around 4 mHz. We can approximate the frequency of the gravitational wave emitted by the binary systems as

$$f_{\rm GW} = \frac{2}{P} \ , \tag{B.1}$$

indicating that systems of ELM WDs with lower mass will populate the region of the

[1] LISA: Laser Interferometer Space Antenna, <https://lisa.nasa.gov/>.

greatest sensitivity. In order to estimate the gravitational radiation emitted by our models, we adopt the same approach as in Kupfer et al. (2018), Tauris (2018), Seto (2019), Li et al. (2020), Korol et al. (2020). The signal-to-noise ratio is directly proportional to the dimensionless gravitational wave amplitude, that after averaging over inclination, sky-location and amplitude reads[2]

$$\mathcal{A} = \Xi \pi^{2/3} \frac{G^{5/3}}{c^4} \frac{\mathcal{M}^{5/3} f_{\rm GW}^{2/3}}{d} \ , \tag{B.2}$$

where

$$\mathcal{M} = \frac{(M_{\rm d} M_{\rm a})^{3/5}}{(M_{\rm d} + M_{\rm a})^{1/5}} \tag{B.3}$$

is the chirp mass and d is the distance of the binary system to the Sun. For an inspiralling binary system that emits monochromatic radiation, the characteristic strain is

$$h_{\rm c} = \mathcal{A} \sqrt{N_{\rm cycle}} \ , \tag{B.4}$$

where

$$N_{\rm cycle} = f_{\rm GW} T_{\rm obs} \tag{B.5}$$

give us the total orbital periods observed over the detector's operation time. For the purpose of facilitating comparisons and conversions, unless otherwise indicated, in this work we fix the distances to $d = 1$ kpc and adopt the nominal LISA mission duration time of $T_{\rm obs} = 4$ yr.

In Figure 28, Figure 29, and Figure 30, we plot the characteristic strain ($h_{\rm c}$, Equation B.4) of some of our selected models along with sensitivity strain noise curves ($h_{\rm n}$), which are taken from: TianQin (Huang et al., 2020), LISA (Schmitz, 2021), and ASTROD-GW (Kuroda; Ni; Pan, 2015). They are shown in purple, green, and orange dashed lines, respectively.

In Figure 28 we show evolutionary tracks of four system with different initial orbital periods between 3.25 and 10 days. All systems have $M_{\rm d,i} = 1.0\ M_\odot$ and $M_{\rm a,i} = 1.4\ M_\odot$. The observational time and the source distance are fixed to 4 years and 1 kpc for all tracks.

We find that, with this configuration, no system will produce gravitational waves intense enough to be detected by the LISA and TianQin detectors. However, the ASTROD-GW detector will have greater sensitivity at lower frequencies, and will be able to detect signals from the more compact systems, with $P_{\rm i} \lesssim 3$ d, after the mass transfer phase (i.e., with the ELM WD already formed).

Since systems with lower metallicity or more massive donors have longer final orbital periods, we do not address these variations here.

[2] The Ξ factor depends on the definitions of variables averaging, and different authors point values from 2 to 4. One can find: $\Xi = 2$ (Kupfer et al., 2018; Li et al., 2020; Korol et al., 2020); $\Xi = \sqrt{32/5} \approx 2.52$ (Evans; Iben; Smarr, 1987; Nissanke et al., 2012; Tauris, 2018; Zou; Zhou; Huang, 2020); $\Xi = 8/\sqrt{5} \approx 3.57$ (Seto, 2019); $\Xi = 4$ (Creighton; Anderson, 2011; Shah; van der Sluys; Nelemans, 2012). We adopt $\Xi = 2$.

Figure 28 – Evolutionary tracks of four (pre-)ELM WDs with a 1.4 $M_\odot$ NS accretor and a 1.0 $M_\odot$ main sequence donor in the characteristic strain amplitude vs. GW frequency diagram. The initial orbital periods are: $P_\mathrm{i} = 3.25$ (red), 3.5 (blue), 4 (green), and 10 (black) days.

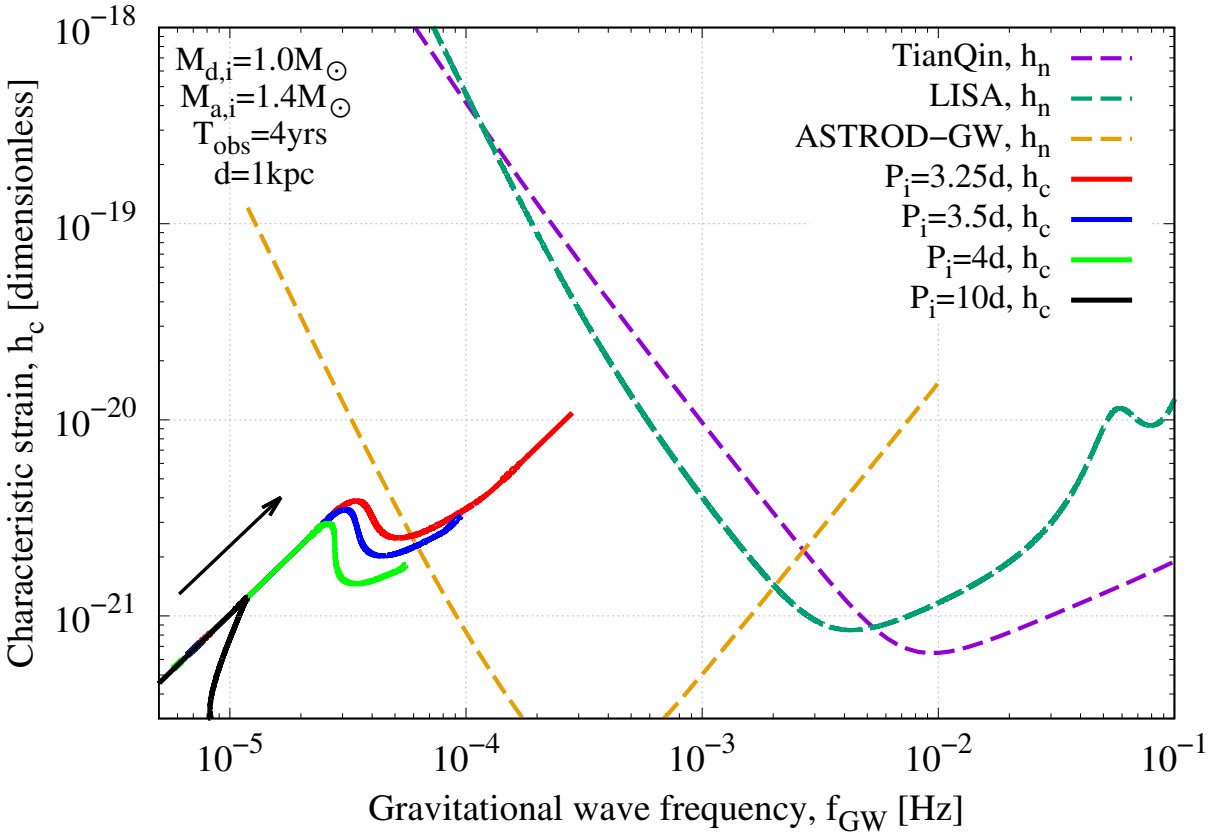

In Figure 29 we show five evolutionary tracks with fixed initial orbital period ($P_\mathrm{i} = 3.25$ d) but different observational time and source distance. The solid black line serves as a reference for comparison with the configuration in the previous figure (Figure 28), i.e., $d = 1$ kpc and $T_\mathrm{obs} = 4$ yr.

If we consider the extended observation time ($T_\mathrm{obs} = 10$ yr, green solid line), we find that the GW signal would be observed by ASTROD-GW right after the end of the mass transfer.

The blue (red) line considers the nominal (extended) observation time of $T_\mathrm{obs} = 4$ yr ($T_\mathrm{obs} = 10$ yr) and the distance to the nearest ELM WD ($d = 0.185$ kpc) according to the ELM Survey (Brown et al., 2020). In these cases, the model sequences presented are above the ASTROD-GW detection limit even before the mass transfer phase, and reach the LISA detection limit at the end of evolution.

X-ray binaries are binary stars luminous in X-rays. The X-rays are produced from the energy released during accretion of matter from the donor component onto the accretor, an NS in our case. X-ray binaries with NSs accretors may evolve to become millisecond

Figure 29 – Evolutionary tracks of five (pre-)ELM WDs with a 1.4 $M_\odot$ NS accretor and a 1.0 $M_\odot$ main sequence donor with $P_\mathrm{i} = 3.25$ in the characteristic strain amplitude vs. GW frequency diagram. Different observation times and distance from the source are presented.

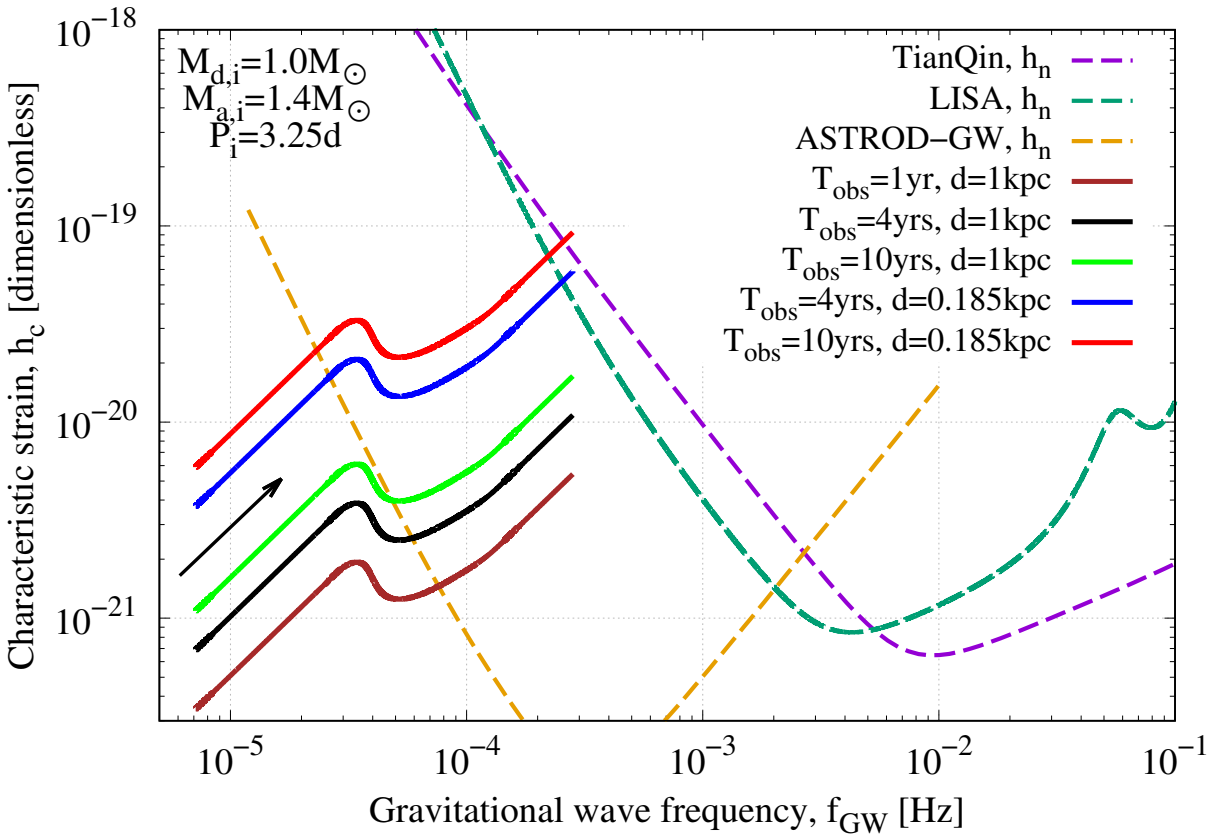

pulsars. Such high-energy binaries may reach X-ray luminosities much greater than the luminosity of the donor star, especially in cases of the shorter initial orbital period.

We then follow the evolution of the ELM WDs through the ultra-compact X-ray binary (UCXB) stage. These systems are characterised by the fact that the mass transfer does not cease or begin again in advanced ages of evolution. In other words, we have a second phase of mass transfer, from the already formed ELM WD to the NS. Systems of this type are not part of our model grid, but as they present more intense emission of gravitational waves, we will present them here along with estimates of the X-ray emission.

To calculate the X-ray emission, we adopted the approach already described in section 3.8, i.e., the X-ray luminosity is given by

$$L_\mathrm{X} = \frac{G M_\mathrm{NS} \dot{M}_\mathrm{acc}}{R_\mathrm{NS}} \eta_\mathrm{X} \ , \tag{B.6}$$

where M_NS is the neutron star mass, $\dot{M}_\mathrm{acc}$ is the accretion rate (that is, the total mass transfer rate times the accretion efficiency β_mt), R_NS is the (constant) radius of the neutrons star (setted to 13 km following the recent result of Adhikari et al., 2021, Reed et al., 2021),

and the X-ray efficiency term is fixed to $\eta_{\rm X} = 0.2$. Since we have set $\beta_{\rm mt} = 0.3$ in the models presented in this section, we have that only 6% of the mass lost by the donor contributes to the X-ray luminosity.

Figure 30 – Evolutionary tracks of four UCXB systems with a 1.4 $M_\odot$ NS accretor and a 1.0 $M_\odot$ main sequence donor in the characteristic strain amplitude vs. GW frequency diagram. Observational data from eight UCXB systems, from which we derive the value of $h_{\rm c}$, are also presented. See also Table 4.

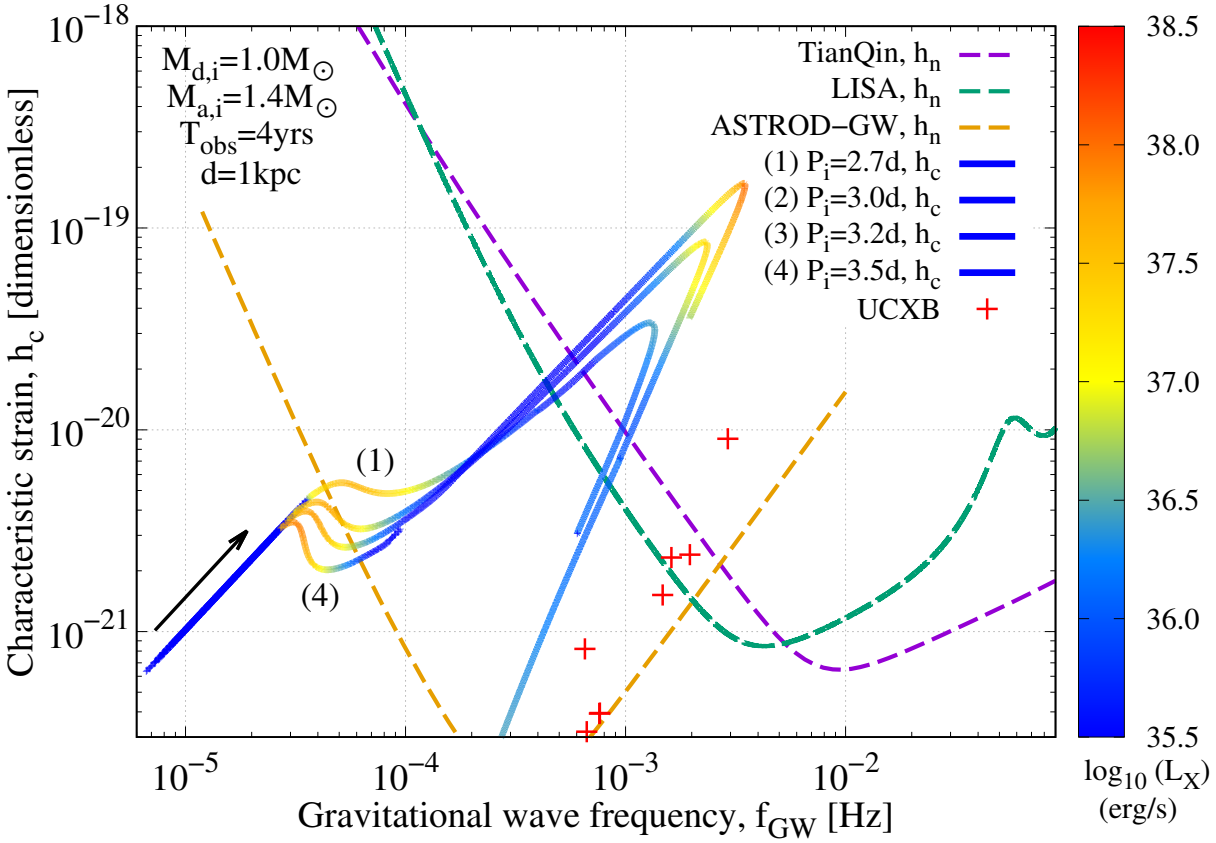

In Figure 30 we again set back $d = 1$ kpc and $T_{\rm obs} = 4$ yr. The $P_{\rm i} = 3$ d track serves as a reference and is the only one that forms a detached ELM WD. The other three evolutionary tracks resume the mass transfer and therefore represent UCXB systems (Wang et al., 2021).

Figure 30 shows the important result that systems containing (pre-)ELM WDs are strong candidates to be observed as sources of gravitational and electromagnetic waves simultaneously. As we have highlighted before, this represents an invaluable opportunity within multimessenger astronomy.

Some of the systems that will become UCXB are above the sensitivity of ASTROD-WD even at the time of the first mass transfer. On the other hand, during the UCXB epoch, the systems will have intense X-ray emission at the same time that the emission of gravitational waves will have a frequency in the region of greater sensitivity in detectors,

including LISA and TianQin.

In a diagram of frequency versus characteristic strain, the signal-to-noise is given by the ratio between the signal (h_c) and the sensitivity curve (h_n). Therefore, Figure 30 anticipates that we will be able to detect GWs with a signal-to-noise of about 100 at the same time as the maximum intensity of X-ray emission.

Our results concerning UCXBs are similar to those found by Chen, Liu & Wang (2020), despite they pointed out that an extreme fine-tuning of the initial orbital period is necessary to produce these LISA sources. Given that they used the Rappaport, Verbunt & Joss (1983) magnetic braking in their study, we point out that the investigation of the formation of UCXB systems using CARB magnetic braking is a topic of great interest.

Table 4 – The observed and derived parameters of eight UCXBs. h_c and f_{GW} were derived considering $M_a = 1.6\ M_\odot$, as in Chen, Liu & Wang (2020).

Mass ($M_\odot$)	P **(d)**	d **(kpc)**	h_c	f_{GW}	**Reference**
0.069	0.007928	7.6	9.0224E-21	2.9198E-03	1, 2
0.046	0.01181	12	2.4040E-21	1.9600E-03	3, 4
0.038	0.01431	8.2	2.3267E-21	1.6176E-03	5
0.035	0.01569	10.4	1.5186E-21	1.4753E-03	3, 6
0.018	0.03028	9.6	3.9427E-22	7.6447E-04	7, 8
0.018	0.03042	9.6	3.9215E-22	7.6095E-04	9
0.016	0.03472	9.0	3.1880E-22	6.6671E-04	10
0.015	0.03542	3.2	8.2141E-22	6.5353E-04	11, 12

Credit: Observational data: (1) Stella, Priedhorsky & White (1987), (2) Güver et al. (2010), (3) Harris (1996), (4) Zurek et al. (2009), (5) Homer et al. (1996), (6) Dieball et al. (2005), (7) Heinke, Edmonds & Grindlay (2001), (8) in't Zand, Jonker & Markwardt (2007), (9) Deutsch, Margon & Anderson (2000), (10) White & Swank (1982), (11) Nelemans et al. (2004), (12) Shahbaz et al. (2008).

APPENDIX C – Model tables

In this section we present our LM/ELM WDs model grid. The CARB magnetic braking (Van; Ivanova, 2019) is considered in all cases. Both rotation and diffusion are included in all models. Values quoted refer to the final age, i.e., 14 Gyrs.

Models considering neutron star accretors are presented in the following tables: Table 5, Table 6, Table 7.

Table 5 – Models for $M_{\rm d,i} = 1.0\ M_\odot$, $M_{\rm a,i} = 1.4\ M_\odot$, $Z = 0.02$.

metallicity (Z)	**initial/final** $M_{\rm d}(M_\odot)$	**initial/final** $M_{\rm a}(M_\odot)$	**initial/final** P **(d)**	**hydrogen shell flash**	**rotational velocity at equator (km/s)**
0.02	1.0/0.4102	1.4/1.451	300/847	1	0.0900
0.02	1.0/0.3936	1.4/1.465	200/648	1	0.0948
0.02	1.0/0.3648	1.4/1.486	100/386	1	2.07
0.02	1.0/0.3492	1.4/1.496	70/277	1	0.598
0.02	1.0/0.3312	1.4/1.507	50/183	1	1.25
0.02	1.0/0.3165	1.4/1.515	40/124	1	0.745
0.02	1.0/0.2876	1.4/1.528	30/56.2	2	2.32
0.02	1.0/0.2706	1.4/1.535	25/31.3	2	3.00
0.02	1.0/0.2550	1.4/1.541	20/17.6	2	0.807
0.02	1.0/0.2502	1.4/1.542	19/14.7	2	0.822
0.02	1.0/0.2454	1.4/1.544	18/12.1	2	3.26
0.02	1.0/0.2405	1.4/1.545	17/10.0	2	3.28
0.02	1.0/0.2341	1.4/1.548	16/8.60	2	2.34
0.02	1.0/0.2219	1.4/1.551	15/7.73	3	1.02
0.02	1.0/0.2151	1.4/1.553	14/6.31	3	1.83
0.02	1.0/0.2082	1.4/1.555	13/5.09	3	1.99
0.02	1.0/0.2020	1.4/1.556	12/4.06	3	3.57
0.02	1.0/0.1967	1.4/1.558	11/3.19	3	3.38
0.02	1.0/0.1914	1.4/1.559	10/2.53	3	2.67
0.02	1.0/0.1852	1.4/1.560	9/2.03	3	2.79
0.02	1.0/0.1809	1.4/1.561	8/1.59	3	3.47
0.02	1.0/0.1698	1.4/1.564	7/1.40	4	2.94
0.02	1.0/0.1697	1.4/1.564	6/1.00	3	4.84
0.02	1.0/0.1586	1.4/1.566	5/0.815	3	4.68
0.02	1.0/0.1504	1.4/1.568	4/0.489	2	7.57

The following tables refer to models with initially more massive donors: Table 8, Table 9, Table 10.

The following tables refer to massive white dwarf accretors: Table 11, Table 12, Table 13.

Table 6 – Models for $M_{\rm d,i} = 1.0\ M_\odot$, $M_{\rm a,i} = 1.4\ M_\odot$, $Z = 0.01$.

metallicity (Z)	**initial/final** $M_{\mathbf{d}}(M_\odot)$	**initial/final** $M_{\mathbf{a}}(M_\odot)$	**initial/final** P (**d**)	**hydrogen shell flash**	**rotational velocity at equator (km/s)**
0.01	1.0/0.4078	1.4/1.461	200/617	1	0.0263
0.01	1.0/0.3957	1.4/1.470	150/508	1	0.3468
0.01	1.0/0.3787	1.4/1.482	100/378	1	0.5508
0.01	1.0/0.3632	1.4/1.492	70/280	1	0.7303
0.01	1.0/0.3464	1.4/1.501	50/197	1	0.9221
0.01	1.0/0.3331	1.4/1.508	40/143	1	1.4912
0.01	1.0/0.3087	1.4/1.521	30/75.2	1	2.0771
0.01	1.0/0.2760	1.4/1.533	20/29.4	2	0.7645
0.01	1.0/0.2498	1.4/1.543	15/11.8	2	1.2312
0.01	1.0/0.2061	1.4/1.555	10/4.96	4	1.4314
0.01	1.0/0.2035	1.4/1.556	9/3.80	4	1.9760
0.01	1.0/0.1974	1.4/1.557	8/3.08	4	1.8769
0.01	1.0/0.1910	1.4/1.559	7/2.53	4	2.0178
0.01	1.0/0.1873	1.4/1.560	6/1.99	4	2.5167
0.01	1.0/0.1835	1.4/1.561	5/1.56	3	3.0766
0.01	1.0/0.1756	1.4/1.562	4/1.27	3	3.6200
0.01	1.0/0.1680	1.4/1.564	3/0.942	3	4.4660
0.01	1.0/0.1671	1.4/1.564	2/0.395	0	9.0567

Table 7 – Models for $M_{\rm d,i} = 1.0\ M_\odot$, $M_{\rm a,i} = 1.4\ M_\odot$, $Z = 0.001$.

metallicity (Z)	**initial/final** $M_{\mathbf{d}}(M_\odot)$	**initial/final** $M_{\mathbf{a}}(M_\odot)$	**initial/final** P (**d**)	**hydrogen shell flash**	**rotational velocity at equator (km/s)**
0.001	1.0/0.4087	1.4/1.479	70/244	1	0.3826
0.001	1.0/0.3903	1.4/1.489	50/181	1	0.4934
0.001	1.0/0.3759	1.4/1.497	40/140	1	0.6182
0.001	1.0/0.3580	1.4/1.505	30/99.8	1	0.8956
0.001	1.0/0.3253	1.4/1.518	20/51.2	2	0.5811
0.001	1.0/0.3021	1.4/1.527	15/30.3	2	0.9692
0.001	1.0/0.2704	1.4/1.538	10/18.2	3	1.1038
0.001	1.0/0.2642	1.4/1.540	9/16.2	4	0.7975
0.001	1.0/0.2607	1.4/1.541	8/14.0	4	1.0113
0.001	1.0/0.2561	1.4/1.543	7/12.3	4	1.0359
0.001	1.0/0.2523	1.4/1.544	6/10.7	4	1.1952
0.001	1.0/0.2482	1.4/1.545	5/9.40	4	1.3862
0.001	1.0/0.2448	1.4/1.546	4/8.12	4	1.4668
0.001	1.0/0.2409	1.4/1.547	3/6.98	4	1.6646
0.001	1.0/0.2348	1.4/1.549	2/5.78	5	1.7058
0.001	1.0/0.2187	1.4/1.553	1/3.03	1	2.6079
0.001	1.0/0.2184	1.4/1.553	0.9/2.57	0	2.4300
0.001	1.0/0.2150	1.4/1.554	0.8/2.20	0	3.1121
0.001	1.0/0.2108	1.4/1.555	0.7/1.81	0	3.5135
0.001	1.0/0.2052	1.4/1.556	0.6/1.39	0	4.0430
0.001	1.0/0.1941	1.4/1.558	0.5/0.822	0	5.3848

Table 8 – Models for $M_{\rm d,i} = 1.2\ M_\odot$, $M_{\rm a,i} = 1.4\ M_\odot$, $Z = 0.02$.

metallicity (Z)	**initial/final** $M_{\mathbf{d}}(M_\odot)$	**initial/final** $M_{\mathbf{a}}(M_\odot)$	**initial/final** P (**d**)	**hydrogen shell flash**	**rotational velocity at equator (km/s)**
0.02	1.2/0.3938	1.4/1.509	150/648	1	0.0048582
0.02	1.2/0.3751	1.4/1.522	100/469	1	0.1246
0.02	1.2/0.3577	1.4/1.533	70/332	1	0.2833
0.02	1.2/0.3386	1.4/1.544	50/216	1	0.4740
0.02	1.2/0.3225	1.4/1.553	40/145	1	0.7420
0.02	1.2/0.2922	1.4/1.567	30/64.5	2	0.6024
0.02	1.2/0.2602	1.4/1.579	20/21.6	2	1.4069
0.02	1.2/0.2332	1.4/1.588	15/8.58	2	1.2335
0.02	1.2/0.1991	1.4/1.597	10/3.24	3	1.4653
0.02	1.2/0.1948	1.4/1.598	9/2.60	3	1.9370
0.02	1.2/0.1895	1.4/1.599	8/2.14	3	2.2122
0.02	1.2/0.1853	1.4/1.600	7/1.74	3	2.6998
0.02	1.2/0.1794	1.4/1.602	6/1.45	3	2.6893
0.02	1.2/0.1751	1.4/1.603	5/1.18	3	3.0599
0.02	1.2/0.1699	1.4/1.604	4/0.952	3	3.8866
0.02	1.2/0.1601	1.4/1.606	3/0.757	3	4.5196
0.02	1.2/0.1523	1.4/1.608	2/0.323	1	7.0409

Table 9 – Models for $M_{\rm d,i} = 1.2\ M_\odot$, $M_{\rm a,i} = 1.4\ M_\odot$, $Z = 0.01$.

metallicity (Z)	**initial/final** $M_{\mathbf{d}}(M_\odot)$	**initial/final** $M_{\mathbf{a}}(M_\odot)$	**initial/final** P (**d**)	**hydrogen shell flash**	**rotational velocity at equator (km/s)**
0.01	1.2/0.4090	1.4/1.504	150/627	1	0.005367
0.01	1.2/0.3900	1.4/1.517	100/460	1	0.06263
0.01	1.2/0.3728	1.4/1.528	70/337	1	0.1285
0.01	1.2/0.3547	1.4/1.538	50/233	1	0.1974
0.01	1.2/0.3399	1.4/1.546	40/167	1	0.3705
0.01	1.2/0.3132	1.4/1.559	30/84.6	1	0.7546
0.01	1.2/0.2809	1.4/1.572	20/34.8	2	0.5633
0.01	1.2/0.2547	1.4/1.581	15/14.3	2	0.5260
0.01	1.2/0.2138	1.4/1.593	9/4.96	3	1.4372
0.01	1.2/0.2089	1.4/1.595	8/4.06	3	1.6887
0.01	1.2/0.2038	1.4/1.596	7/3.35	3	1.8387
0.01	1.2/0.1994	1.4/1.597	6/2.76	3	2.1087
0.01	1.2/0.1918	1.4/1.599	5/2.39	4	1.8422
0.01	1.2/0.1902	1.4/1.599	4/1.91	3	2.6610
0.01	1.2/0.1848	1.4/1.600	3/1.59	3	2.9306
0.01	1.2/0.1753	1.4/1.602	2/1.33	4	2.9894
0.01	1.2/0.1640	1.4/1.605	1/0.267	0	1.0872

Table 10 – Models for $M_{\rm d,i} = 1.2\ M_\odot$, $M_{\rm a,i} = 1.4\ M_\odot$, $Z = 0.001$.

metallicity (Z)	**initial/final** $M_{\mathbf{d}}(M_\odot)$	**initial/final** $M_{\mathbf{a}}(M_\odot)$	**initial/final** P (**d**)	**hydrogen shell flash**	**rotational velocity at equator (km/s)**
0.001	1.2/0.4011	1.4/1.526	50/214	1	0.4312
0.001	1.2/0.3858	1.4/1.533	40/165	1	0.4552
0.001	1.2/0.3674	1.4/1.541	30/117	1	0.4867
0.001	1.2/0.3338	1.4/1.555	20/61.4	2	0.3487
0.001	1.2/0.3134	1.4/1.563	15/38.0	2	0.5672
0.001	1.2/0.2848	1.4/1.574	10/25.6	3	0.6418
0.001	1.2/0.2804	1.4/1.575	9/23.1	3	0.8244
0.001	1.2/0.2761	1.4/1.577	8/20.9	3	0.8010
0.001	1.2/0.2726	1.4/1.578	7/18.7	3	0.8489
0.001	1.2/0.2690	1.4/1.579	6/16.6	3	0.9524
0.001	1.2/0.2633	1.4/1.581	5/15.2	4	0.7289
0.001	1.2/0.2604	1.4/1.582	4/13.3	4	0.8536
0.001	1.2/0.2571	1.4/1.583	3/11.5	4	1.0935
0.001	1.2/0.2474	1.4/1.586	2/8.91	4	1.1112
0.001	1.2/0.2292	1.4/1.590	1/4.59	4	1.8159
0.001	1.2/0.2201	1.4/1.592	0.8/3.12	2	2.4387
0.001	1.2/0.2163	1.4/1.593	0.7/2.30	0	3.6714
0.001	1.2/0.2098	1.4/1.595	0.6/1.72	0	3.7899
0.001	1.2/0.2064	1.4/1.596	0.5/1.47	0	4.2465
0.001	1.2/0.1990	1.4/1.597	0.4/1.03	0	4.7374

Table 11 – Models for $M_{\rm d,i} = 1.0\ M_\odot$, $M_{\rm a,i} = 0.8\ M_\odot$, $Z = 0.02$.

metallicity (Z)	**initial/final** $M_{\mathbf{d}}(M_\odot)$	**initial/final** $M_{\mathbf{a}}(M_\odot)$	**initial/final** P (**d**)	**hydrogen shell flash**	**rotational velocity at equator (km/s)**
0.02	1.0/0.4016	0.8/0.862	300/736	1	0.889
0.02	1.0/0.3809	0.8/0.878	200/519	1	1.11
0.02	1.0/0.3671	0.8/0.888	150/401	1	1.89
0.02	1.0/0.3483	0.8/0.899	100/271	1	2.37
0.02	1.0/0.3306	0.8/0.909	70/179	1	1.03
0.02	1.0/0.3107	0.8/0.919	50/105	1	3.05
0.02	1.0/0.2922	0.8/0.927	40/64.5	2	2.19
0.02	1.0/0.2645	0.8/0.938	30/24.7	2	1.84
0.02	1.0/0.2557	0.8/0.941	25/17.7	2	2.92
0.02	1.0/0.2348	0.8/0.948	20/9.49	2	2.58
0.02	1.0/0.2249	0.8/0.950	19/8.70	3	1.36
0.02	1.0/0.2195	0.8/0.952	18/7.43	3	1.52
0.02	1.0/0.2151	0.8/0.953	17/6.19	3	1.42
0.02	1.0/0.2087	0.8/0.955	16/5.25	3	1.92
0.02	1.0/0.2052	0.8/0.956	15/4.25	3	2.54
0.02	1.0/0.1996	0.8/0.957	14/3.52	3	1.99
0.02	1.0/0.1946	0.8/0.958	13/2.93	3	2.62
0.02	1.0/0.1911	0.8/0.959	12/2.37	3	3.24
0.02	1.0/0.1874	0.8/0.960	11/1.93	3	2.41
0.02	1.0/0.1830	0.8/0.961	10/1.60	3	3.20
0.02	1.0/0.1765	0.8/0.962	9/1.37	3	3.56
0.02	1.0/0.1729	0.8/0.963	8/1.11	3	4.24
0.02	1.0/0.1654	0.8/0.965	7/0.953	3	4.04
0.02	1.0/0.1639	0.8/0.965	6/0.702	2	6.42
0.02	1.0/0.1534	0.8/0.967	5/0.528	2	7.58
0.02	1.0/0.1513	0.8/0.968	4/0.154	0	39.1

Table 12 – Models for $M_{\rm d,i} = 1.0\ M_\odot$, $M_{\rm a,i} = 0.8\ M_\odot$, $Z = 0.01$.

metallicity (Z)	**initial/final** $M_{\mathbf{d}}(M_\odot)$	**initial/final** $M_{\mathbf{a}}(M_\odot)$	**initial/final** P (**d**)	**hydrogen shell flash**	**rotational velocity at equator (km/s)**
0.01	1.0/0.3960	0.8/0.873	200/509	1	0.317
0.01	1.0/0.3624	0.8/0.895	100/275	1	0.729
0.01	1.0/0.3449	0.8/0.904	70/189	1	0.896
0.01	1.0/0.3261	0.8/0.914	50/120	1	0.921
0.01	1.0/0.3102	0.8/0.921	40/78.2	1	1.66
0.01	1.0/0.2840	0.8/0.931	30/37.6	2	1.04
0.01	1.0/0.2740	0.8/0.934	25/27.1	2	0.776
0.01	1.0/0.2551	0.8/0.941	20/14.2	2	1.26
0.01	1.0/0.2494	0.8/0.943	19/12.7	2	2.33
0.01	1.0/0.2391	0.8/0.946	18/11.7	3	0.899
0.01	1.0/0.2335	0.8/0.948	17/10.1	3	1.05
0.01	1.0/0.2280	0.8/0.949	16/8.66	3	1.23
0.01	1.0/0.2227	0.8/0.951	15/7.29	3	1.77
0.01	1.0/0.2171	0.8/0.952	14/6.14	3	1.69
0.01	1.0/0.2125	0.8/0.954	13/5.09	3	1.79
0.01	1.0/0.2077	0.8/0.955	12/4.21	4	1.68
0.01	1.0/0.2005	0.8/0.957	11/3.63	4	1.58
0.01	1.0/0.1986	0.8/0.957	10/2.92	3	2.21
0.01	1.0/0.1948	0.8/0.958	9/2.42	3	2.55
0.01	1.0/0.1882	0.8/0.960	8/2.09	4	2.52
0.01	1.0/0.1856	0.8/0.960	7/1.71	3	3.04
0.01	1.0/0.1792	0.8/0.962	6/1.46	3	3.19
0.01	1.0/0.1743	0.8/0.963	5/1.20	3	3.69
0.01	1.0/0.1664	0.8/0.964	4/0.988	3	4.12
0.01	1.0/0.1604	0.8/0.966	3/0.691	2	5.76
0.01	1.0/0.1560	0.8/0.967	2/0.163	0	19.1

Table 13 – Models for $M_{\rm d,i} = 1.0\ M_\odot$, $M_{\rm a,i} = 0.8\ M_\odot$, $Z = 0.001$.

metallicity (Z)	**initial/final** $M_{\mathbf{d}}(M_\odot)$	**initial/final** $M_{\mathbf{a}}(M_\odot)$	**initial/final** P (**d**)	**hydrogen shell flash**	**rotational velocity at equator (km/s)**
0.001	1.0/0.4518	0.8/0.854	200/441	0	0.0033
0.001	1.0/0.4099	0.8/0.881	100/247	1	0.36
0.001	1.0/0.3892	0.8/0.892	70/176	1	0.547
0.001	1.0/0.3674	0.8/0.903	50/119	1	0.734
0.001	1.0/0.3519	0.8/0.909	40/87.6	1	0.739
0.001	1.0/0.3314	0.8/0.916	30/57.6	2	0.577
0.001	1.0/0.3171	0.8/0.922	25/41.4	2	0.913
0.001	1.0/0.2938	0.8/0.931	20/30.3	3	0.542
0.001	1.0/0.2890	0.8/0.932	19/27.9	3	0.990
0.001	1.0/0.2845	0.8/0.934	18/25.7	3	1.09
0.001	1.0/0.2803	0.8/0.935	17/23.4	3	1.49
0.001	1.0/0.2764	0.8/0.937	16/21.2	3	0.916
0.001	1.0/0.2727	0.8/0.938	15/19.2	3	1.07
0.001	1.0/0.2692	0.8/0.939	14/17.2	3	1.23
0.001	1.0/0.2656	0.8/0.940	13/15.4	3	1.28
0.001	1.0/0.2606	0.8/0.941	12/14.0	4	0.961
0.001	1.0/0.2571	0.8/0.942	11/12.6	4	1.03
0.001	1.0/0.2547	0.8/0.943	10/11.1	4	1.22
0.001	1.0/0.2509	0.8/0.944	9/10.0	4	1.31
0.001	1.0/0.2476	0.8/0.945	8/9.00	4	1.39
0.001	1.0/0.2453	0.8/0.946	7/7.97	4	1.62
0.001	1.0/0.2412	0.8/0.947	6/7.21	4	1.48
0.001	1.0/0.2397	0.8/0.948	5/6.34	4	1.88
0.001	1.0/0.2343	0.8/0.949	4/5.77	4	1.64
0.001	1.0/0.2323	0.8/0.949	3/5.00	4	1.95
0.001	1.0/0.2273	0.8/0.951	2/4.10	4	2.25
0.001	1.0/0.2103	0.8/0.955	1/1.75	0	3.33

APPENDIX D – Main publication

Title: Convection and rotation boosted prescription of magnetic braking: application to the formation of extremely low-mass white dwarfs (Soethe; Kepler, 2021).

Journal: Monthly Notices of the Royal Astronomical Society

Volume 506, Issue 3, September 2021, Pages 3266–3281.

DOI: 10.1093/mnras/stab1916

Received: 16 April 2021. Revision received: 29 May 2021. Accepted: 28 June 2021. Published: 09 July 2021.

arXiv: arXiv:2107.03952

adsabs: 2021MNRAS.506.3266S

Monthly Notices of the ROYAL ASTRONOMICAL SOCIETY

MNRAS **506,** 3266–3281 (2021) https://doi.org/10.1093/mnras/stab1916
Advance Access publication 2021 July 9

Convection and rotation boosted prescription of magnetic braking: application to the formation of extremely low-mass white dwarfs

L. T. T. Soethe★ and S. O. Kepler

Instituto de Física, Universidade Federal do Rio Grande do Sul, Av. Bento Gonçalves 9500, Porto Alegre, 91501-970 RS, Brazil

Accepted 2021 June 28. Received 2021 May 29; in original form 2021 April 16

ABSTRACT

Extremely low-mass white dwarfs (ELM WDs) are the result of binary evolution in which a low-mass donor star is stripped by its companion leaving behind a helium-core white dwarf (WD). We explore the formation of ELM WDs in binary systems considering the Convection And Rotation Boosted magnetic braking treatment. Our evolutionary sequences were calculated using the Modules for Experiments in Stellar Astrophysics code, with initial masses of 1.0 and 1.2 $M_\odot$ (donor), and 1.4 (accretor), compatible with low-mass X-ray binary (LMXB) systems. We obtain ELM models in the range 0.15–0.27 $M_\odot$ from a broad range of initial orbital periods, 1–25 d. The bifurcation period, where the initial period is equal to the final period, ranges from 20 to 25 d. In addition to LMXBs, we show that ultracompact X-ray binaries (UCXBs) and wide-orbit binary millisecond pulsars can also be formed. The relation between mass and orbital period obtained is compatible with the observational data from He WD companions to pulsars.

Key words: binaries: close – stars: low-mass – white dwarfs.

1 INTRODUCTION

Extremely low-mass (ELM) white dwarfs (WD) are helium-core WDs with masses $M \leq 0.3$ $M_\odot$, most likely formed through binary interactions, since they would take more than the age of the Universe to evolve out of the main sequence as single stars. There are several definitions for the upper mass limit for the class in the literature, e.g. 0.18 $M_\odot$ (Sun & Arras 2018), 0.20 $M_\odot$ (Kawka & Vennes 2009; Althaus, Miller Bertolami & Córsico 2013; Chen et al. 2017), 0.25 $M_\odot$ (Hermes et al. 2013a,b) 0.30 $M_\odot$ (Li et al. 2019; Pelisoli & Vos 2019). In the most common binary evolution scenario, a main-sequence star reaches the red giant branch, fills its Roche lobe, and then starts stable mass transfer through Roche lobe overflow (RLOF) to the accretor companion – either a WD (Kilic et al. 2007; Kulkarni & van Kerkwijk 2010; Tauris, Langer & Kramer 2012; Sun & Arras 2018; Li et al. 2019) or a neutron star (NS; Bhattacharya & van den Heuvel 1991; Podsiadlowski, Rappaport & Pfahl 2002; van Kerkwijk et al. 2005; Shao & Li 2015; Cadelano et al. 2019; Mata Sánchez et al. 2020). These systems are then associated with the cataclysmic variables (CV) and low-mass X-ray binary (LMXB) systems, respectively.

Most known ELMs will merge in less than a Hubble time resulting in new exotic objects such as R Corona Borealis stars (Webbink 1984; Zhang et al. 2014), underluminous supernovae (Bildsten et al. 2007; Brown et al. 2011), Type Ia supernovae (Iben & Tutukov 1984), and AM CVn systems (Breedt et al. 2012; Brown et al. 2016b). The shortest period extremely low-mass white dwarf (ELM WD) binaries will serve as multimessenger laboratories (Korol et al. 2017; Kupfer et al. 2018). In particular, Brown et al. (2020b) discovered the first He+He WD LISA verification binary, a dominant LISA source along with He–CO double WDs (Lamberts et al. 2019). Furthermore, it is expected that compact post-LMXB/pre-UCXB systems can provide a very accurate measurement for the mass of NSs, imposing restrictions on their state equation (Tauris 2018).

In the past decade, more than a hundred systems containing ELMs have been discovered by several surveys. For example, the ELM Survey (Brown et al. 2010, 2012, 2013, 2016a, 2020a; Kilic et al. 2011, 2012; Gianninas et al. 2015) now counts 62 ELMs in the clean sample,[1] where 65 per cent were identified as Galactic Disc objects and 35 per cent as halo objects at distances up to 3.752 kpc. Orbital periods were measured as 12.8 min $\leq P \leq$ 1.48567 d and estimated ELMs masses are in the range $0.15 \leq M/M_\odot \leq 0.30$. In the ELM Survey, mass estimates are obtained spectroscopically by fitting $\log(g)$ and $T_{\rm eff}$ to a set of atmospheric models, without a proper accounting of metallicity difference or envelope mass differences. Therefore, these masses are not precise estimates. The ELM Survey has started the search for ELM WDs in the southern sky (Kosakowski et al. 2020), identifying ELMs in systems with periods as short as 2 h and also the second closest (72 pc) known ELM to date.[2]

Chen et al. (2017) and Sun & Arras (2018) concluded that the formation of an ELM WD with $M \lesssim 0.18$–0.20 $M_\odot$ by unstable mass transfer or a common envelope (CE) event is unlikely. Also, Li et al. (2019) found that ELM WDs with $M \lesssim 0.3$ $M_\odot$ in double-degenerate systems may be formed either from a stable mass transfer

★ E-mail: tayno32@gmail.com

[1]They define the clean ELM WD sample as ELM WDs in the dereddened magnitude range $15 < g_0 < 20$, located in the SDSS footprint, with $8800 < T_{\rm eff}/{\rm K} < 22,000$ and $5.5 \leq \log(g) \leq 7.1$.

[2]The nearest ELM WD position was recently overtaken by an ≈0.17 $M_\odot$ ELM and ≈71 pc away (Kawka et al. 2020).

process or CE ejection, although the Roche lobe formation channel has a greater contribution to the formation of He WD with mass $\lesssim$0.22 $M_\odot$, and the CE channel for higher masses. The currently observed binarity rate of known ELM WDs – close to 100 per cent – supports both channels. Their companions include millisecond pulsars, main-sequence stars (the so-called EL CVns, Maxted et al. 2014; Chen et al. 2017), hot subdwarf B stars (Kupfer et al. 2015), and more commonly canonical mass WDs (e.g. Kilic et al. 2007; Kulkarni & van Kerkwijk 2010; Tauris et al. 2012; Brown, Kilic & Gianninas 2017). However, observations are likely to be biased considering current optical spectroscopy is more sensitive to short orbital period systems (Brown et al. 2010; Kilic et al. 2012; Toloza et al. 2019). In addition, failure to observe isolated ELM WDs does not necessarily mean that they do not exist.

The formation and the evolution of ELM WDs through the LMXB and CV channels were studied extensively in the literature, although the input physics – e.g. donor and accretor masses, accretion efficiency, metallicity, use of rotation and diffusion, mechanisms of angular momentum loss, mass transfer formalism – considered in each of them is widely varied (e.g. Podsiadlowski et al. 2002; Serenelli et al. 2002; Panei et al. 2007; Althaus et al. 2009; Lin et al. 2011; Althaus et al. 2013; Istrate, Tauris & Langer 2014; Istrate et al. 2016).

In general, theoretical models are able to reproduce with good accuracy the physical parameters observed in ELM WDs, such as chemical abundance, final mass, effective temperature, and surface gravity. Despite these successes, there are still open questions. For instance, a severe fine-tuning – of the order of a dozen minutes – in the initial orbital period was necessary to reproduce the observed millisecond pulsars in compact (2 h $\leq P \leq$ 9 h) binaries with He WD companions of mass $\lesssim$0.20 $M_\odot$ (Istrate et al. 2014). This extreme fine-tuning in the initial orbital period suggests that something is missing in the standard input physics of LMXB modelling. As most angular momentum loss mechanisms are reasonably well understood, the problem seems to fall on the magnetic braking. In addition, irreconcilable discrepancies are found in some systems where it is possible to obtain the mass of the components with good precision and independently of the evolutionary ELM WDs models (Liu et al. 2020; Mata Sánchez et al. 2020).

The most used empirical torque formula for magnetic braking of Rappaport, Verbunt & Joss (1983, hereafter R83) was derived from observations of solar-mass main-sequence stars that exhibit a strong correlation between equatorial rotation velocity and age (Skumanich 1972; Smith 1979). R83 formula has been used and discussed extensively in the literature in calculations of the evolution and the formation of binary systems, including low and intermediate-mass X-ray binaries, millisecond radio pulsars, cataclysmic binaries, and subdwarf B stars (Patterson 1984; Bhattacharya & van den Heuvel 1991; Podsiadlowski et al. 2002; Han et al. 2003; Knigge, Baraffe & Patterson 2011). Van, Ivanova & Heinke (2018, hereafter V18) and Van & Ivanova (2019, hereafter V19) proposed a physically motivated magnetic braking prescription. In their formalism, the magnetic braking of the system is calculated from a rotating spherically symmetric star, considering a radial magnetic field in the dipole approximation. The mass lost by winds – assumed isotropic – corotates with the star up to a distance that depends on the size of the convective zone, rotation velocity, and the magnitude of the surface magnetic field. V18 showed that the braking law from R83 is not suitable to explain most of the observed persistent LMXBs, specially the observed mass transfer rates. Instead, the V19 prescription was successful in reproducing the observed mass transfer rates of persistent LMXB for all observed mass ratio and orbital periods. Furthermore, Deng et al. (2021) studied the LMXB evolution with five proposed magnetic braking laws and found that both the V18 and the V19 laws are more preferred in reproducing the properties of persistent and transient LMXBs systems.

Although the formulations V18 and V19 have very similar physical motivations, the formula presented in V18 has three free parameters. This makes the results depend on the chosen parameters. On the other hand, the V19 formulation has a more consistent deduction and does not have any free parameters.

Chen et al. (2021) used the V18 formulation to study the evolutionary link from low-mass X-ray binaries (LMXBs) to binary millisecond pulsars (BMSPs) and ultracompact X-ray binaries (UCXBs). Although Chen et al. (2021) focused on the parameter space for the formation of UCXBs, they found that the V18 prescription fails to form wide-orbit BMSPs. In addition, both V18 and Chen et al. (2021) made it clear that the issue of free parameters gave significantly different outcomes, making it more difficult to draw general conclusions.

In this work, we apply the Convection And Rotation Boosted (CARB) prescription for the magnetic braking presented by V19 to study the formation and evolution of low-mass and ELM WDs. We show that the use of CARB magnetic braking reproduces the LMXB phase as well as being able to form UCXBs and wide BMSPs systems.

The layout of this paper is as follows. In Section 2, we describe the physical ingredients considered in computing the grid of models; in Section 3, we present the results obtained from the fully evolutionary computations and compare with observational data. Concluding remarks are presented in Section 4.

2 NUMERICAL METHODS AND SIMULATIONS

The model grid presented in this work is computed using Modules for Experiments in Stellar Astrophysics code (MESA Paxton et al. 2011, 2013, 2015, 2018, 2019), release 11701. We compute the binary evolution of the system following the evolution of the donor star from the zero-age main sequence (ZAMS) until it reached a model age of 14 Gyr. The accretor is treated as a point mass. For the rest of the manuscript, we adopt the nomenclature 'd' for the donor and 'a' for the accretor. Initial and final ages will be indicated by 'i' and 'f', respectively.

Below, we describe the input physics and the computational details used to calculate the evolutionary sequences.

2.1 Stellar evolution input

The equation of state (EoS) is a blend of the OPAL (Rogers & Nayfonov 2002), SCVH (Saumon, Chabrier & van Horn 1995), PTEH (Pols et al. 1995), HELM (Timmes & Swesty 2000), and PC (Potekhin & Chabrier 2010) EoSs. A smooth transition between the EoSs guarantees the appropriate usage across the entire required range of density and temperature. Radiative opacities are primarily from OPAL (Iglesias & Rogers 1993, 1996), with low-temperature data from Ferguson et al. (2005) and the high-temperature, Compton-scattering-dominated regime by Buchler & Yueh (1976). Electron conduction opacities are from Cassisi et al. (2007).

Nuclear reaction rates are from JINA REACLIB (Cyburt et al. 2010) plus additional weak reaction rates (Fuller, Fowler & Newman 1985; Oda et al. 1994; Langanke & Martínez-Pinedo 2000). Screening is included via the prescription of Chugunov, Dewitt & Yakovlev (2007). Thermal neutrino loss rates are from Itoh et al. (1996). Hydrogen burning (p-p chain and CNO cycle) are computed by using the `cno_extras.net` network that accounts for the following 21

isotopes: ^{1}H, ^{3}He, ^{4}He, ^{12}C, ^{13}C, ^{13}N, ^{14}N, ^{15}N, ^{14}O, ^{15}O, ^{16}O, ^{17}O, ^{18}O, ^{17}F, ^{18}F, ^{19}F, ^{18}Ne, ^{19}Ne, ^{20}Ne, ^{22}Mg, and ^{24}Mg. As calcium is one of the easiest elements to be detected in the spectra of a WD, we also include the ^{40}Ca isotope in our models.

Convection is treated using the simple local formulation of the mixing-length theory (Böhm-Vitense 1958) in the variation of Henyey, Vardya & Bodenheimer (1965) allowing the convective efficiency to vary with the opacity. Following Istrate et al. (2016), $\alpha_{\rm MLT} = 2$ is adopted as the mixing-length parameter. We consider the Ledoux criterion of stability, which takes into account the influence of composition gradients on mixing. Semiconvection is considered in the regions unstable with respect to the Schwarzschild criterion but stable to Ledoux, with an efficiency parameter $\alpha_{\rm sc} = 0.001$. Thermohaline mixing is included during all the evolution with efficiency $\alpha_{\rm th} = 1$.

Following Istrate et al. (2016), for each burning/non-burning core/shell region we include an exponential overshooting below and above the interface limit with $f = 0.01$ and $f_0 = 0.005$. An extra step overshooting of $f = 0.25$ and $f_0 = 0.05$ above the burning H core is also included.

For comparison, we calculated models with and without diffusion. For the models with diffusion, element diffusion and gravitational settling is included by solving Burger's equations and using the method of Thoul, Bahcall & Loeb (1994) with diffusion coefficients similar to Iben & MacDonald (1985). Unlike Istrate et al. (2016) who clumps elements into classes, we treat each isotope as a separate class. This treatment does not affect the results, as we will discuss in Section 3.

The effects of rotation may become important near the rotation limit and are included by following Heger, Langer & Woosley (2000) and Heger, Woosley & Spruit (2005), where we include the effects for four different rotationally induced mixing processes: Goldreich–Schubert–Fricke instability, Eddington–Sweet circulation, secular shear instability, and dynamical shear instability. More details about rotation and rotational element transport mechanisms can be found in the review of Salaris & Cassisi (2017). The Spruit–Tayler dynamo transports angular momentum and chemicals by magnetic fields. Here, we must set two efficiency factors to calibrate the diffusion coefficients: the contribution of the rotationally induced instabilities to the diffusion coefficient is reduced by the factor $f_{\rm c} = 1/30$, and the sensitivity of the rotationally induced mixing is $f_\mu = 0.05$. These values follow Istrate et al. (2016). See Heger et al. (2000) for a discussion of these calibration parameters.

For the atmosphere boundary conditions, we consider the simple photosphere option for the pre-WD phase and the hydrogen atmosphere tables for cool WDs from Rohrmann, Althaus & Kepler (2011) for $T_{\rm eff} < 10,000$ K and $\log_{10}(L/L_\odot) < -2$.

2.2 Binary evolution input

Given the initial donor ($M_{\rm d,\,i}$) and accretor ($M_{\rm a,\,i}$) masses, each system starts with both stars in a circular orbit with separation a, and initial orbital period $P_{\rm i} = 2\pi \left[a^3/G(M_{\rm d,i} + M_{\rm a,i})\right]^{\frac{1}{2}}$. At the beginning of evolution, the rotation of the donor star is relaxed to the orbital period of the system by applying tidal torque considering the synchronization time-scale for convective envelopes (Hurley, Tout & Pols 2002).

The rate of change of the angular momentum of the system is computed considering contributions from gravitational wave radiation, mass-loss, magnetic braking, and spin−orbit coupling as follows:

$$\dot{J}_{\rm orb} = \dot{J}_{\rm gr} + \dot{J}_{\rm ml} + \dot{J}_{\rm mb} + \dot{J}_{\rm ls}. \tag{1}$$

In the absence of outer convective zones, the gravitational wave radiation term dominates in very compact orbits ($P \lesssim 3$ d) and is given by (see e.g. Landau & Lifshitz 1975)

$$\dot{J}_{\rm gr} = -\frac{32}{5c^5}\left(\frac{2\pi G}{P}\right)^{7/3}\frac{(M_{\rm d}M_{\rm a})^2}{(M_{\rm d}+M_{\rm a})^{2/3}}, \tag{2}$$

where G is the gravitational constant and c is the speed of light in vacuum.

The mass transfer stability criteria is given by Soberman, Phinney & van den Heuvel (1997). We calculated models with $\beta_{\rm mt} = 0.3$ and 0.8 for the fraction of mass lost from the vicinity of the accretor as fast wind, implying a mass transfer efficiency of 70 and 20 per cent, respectively. The former value is for better comparison with models in the literature, and the latter was chosen given that there is observational evidence that mass transfer during the LMXB phase is extremely inefficient, corresponding to accretion efficiencies of only ∼5–40 per cent (Antoniadis et al. 2012, 2013, 2016).

Roche lobe radii in binary systems are computed using the fit of Eggleton (1983), while mass transfer rates are determined following the prescription of Kolb & Ritter (1990). We consider the RLOF to take place when the mass transfer rate exceeds the value of $\dot{M} = 10^{-10}$ M$_\odot$ yr^{-1}. We stress that this is just an arbitrary limit that has no effect in our results.

2.3 Magnetic braking prescription

Magnetic braking plays an important role, specially in the early stages of evolution in interacting binary systems. Considering that stars of different spectral types on the main sequence have different rotational speeds, Schatzman (1962) was the first to suggest that the convective envelope could be the reason for some stars to have low rotation velocities. He suggested that in convective stars the high magnetic field forces that ejected matter spinning along with the star, even at very high distances, carries a large amount of angular momentum per unit mass. The first numerical estimate came from Skumanich (1972), who showed that the equatorial rotation velocities of G-type main-sequence stars decrease with time, suggesting the empirical dependence $\Omega \propto t^{-1/2}$. A more elaborate expression appeared in the seminal work of Rappaport et al. (1983), where the mass and radius of the star are time-dependent quantities. The MESA implementation follows

$$\dot{J}_{\rm mb} = -6.82\times10^{34}\left(\frac{M_{\rm d}}{M_\odot}\right)\left(\frac{R_{\rm d}}{R_\odot}\right)^{\gamma}\left(\frac{1\ {\rm d}}{P}\right)^{3}, \tag{3}$$

where $R_{\rm d}$ is the radius of the donor and $\gamma = 4$ is adopted for the magnetic braking index.

Van & Ivanova (2019) alternative formulation for the magnetic braking is called the CARB magnetic braking. CARB magnetic braking considers the dependence of the Alfvén radius ($R_{\rm A}$) on the rotation rate of the donor, and the dependence of the magnetic field strength on the outer convective zone. The Alfvén surface is the surface where the ram pressure is equal to the magnetic pressure (Mestel & Spruit 1987), marking the maximum distance at which the stellar wind is still in corotation with the star. At larger distances, the mass is assumed to be lost from the star. Spherical symmetry is assumed, which results in the angular momentum lost by magnetic breaking through an Alfvén surface to be (Weber & Davis 1967; Mestel 1968)

$$\dot{J}_{\rm mb} = -\frac{2}{3}\Omega\dot{M}_W R_A^2, \tag{4}$$

where Ω is the rotation rate and $\dot{M}_W$ is the wind mass-loss rate. The wind mass-loss is assumed to be isotropic, and depends on the density and the velocity of the mass flux through the Alfvén surface. Including the effects of rotation in the expression for the Alfvén radius, the CARB magnetic braking then reads[3]

$$\dot{J}_{\rm mb,CARB} = -\frac{2}{3}\Omega \dot{M}_W^{-1/3} R_{\rm d}^{14/3} \left(v_{\rm esc}^2 + \frac{2\Omega R_{\rm d}^2}{K_2^2} \right)^{-2/3} \times \Omega_\odot B_\odot^{8/3} \left(\frac{\Omega}{\Omega_\odot} \right)^{11/3} \left(\frac{\tau_{\rm conv}}{\tau_{\odot,\rm conv}} \right)^{8/3}, \quad (5)$$

where $v_{\rm esc} = \sqrt{2GM/R}$ is the escape velocity, $K_2 = 0.07$ is a constant obtained via simulations (Réville et al. 2015). $\tau_{\rm conv}$ is the turnover time of convective eddies, given by

$$\tau_{\rm conv} = \int_{R_{\rm bot}}^{R_{\rm top}} \frac{{\rm d}r}{v_{\rm conv}}, \quad (6)$$

where $v_{\rm conv}$ is the local convective velocity and the integration limits, $R_{\rm bot}$ and $R_{\rm top}$, are the bottom and the top of the outer convective zone, respectively. Thus, this description assumes the total magnetic field is generated by the convection eddies, i.e. no fossil fields. The surface magnetic field is given by $B_{\rm s} = \tau_{\rm conv}\Omega$, as in Ivanova (2006) and Van et al. (2018). The last terms of equation (5) are normalized according to a solar calibration, resulting in $\Omega_\odot \approx 3 \times 10^{-6}$ s^{-1} and $\tau_{\odot,\rm conv} = 2.8 \times 10^6$ s. We adopt the Reimers (1975) wind mass-loss scheme, as it was done in Van & Ivanova (2019). The prescriptions of Rappaport et al. (1983) and Van & Ivanova (2019) differ essentially by the fact that the former is an empirical fit, and the latter is obtained through a self-consistent deduction considering wind mass-loss, rotation, and that the magnetic field is generated due to motions in the convective zone. The main limitations of this model will be addressed in the conclusion (Section 4).

2.4 Model grid

We consider initial donor masses of 1.0 and 1.2 $M_\odot$ with initial metallicity of $Z = 0.02$. The initial accretor mass is 1.4 $M_\odot$, consistent with NS companions. Systems are initialized with orbital periods between 1 and 300 d. The exact minimum initial orbital period for each configuration is defined so that the systems are completely detached at the end of the evolution. The step in the initial orbital period varies between 1 and 100 d, for the short and long initial orbital periods, respectively. Rotation is considered in all configurations, and element diffusion is also included in some configurations, as listed in Table 1. For brevity, the general discussion of the effect of the CARB magnetic braking on the formation of binary systems containing ELM WDs will be done with a single initial configuration, facilitating the comparison with the models of Istrate et al. (2016, Sections 3.1 and 3.2). More detailed discussions on different initial masses, accretion efficiencies, and diffusion of elements will be presented on Section 3.3, where we show the $P_{\rm i}$–$P_{\rm f}$ and the $M_{\rm f}$–$P_{\rm f}$ relations. The main properties – i.e. initial and final masses of both components, initial and final orbital period, number of hydrogen shell flashes – of our model grid can be found in Appendix A. For quick use of our results, in Appendix B we provide polynomial fits to the final ELM WD mass ($M_{\rm d,f}$) as a function of the initial orbital period ($P_{\rm i}$). We also present a simple estimate of the gravitational wave strain and the merging time for our most compact binary models, as detailed in Appendix C.

[3]We note that there is a missing minus factor in the exponential argument of the wind mass-loss rate in equation (5) of Van & Ivanova (2019). Also, in the code made available online by the authors, the argument 2/3 of the exponential in line 320 should be 1/3 in order to make it correctly fit in the corresponding equations in the paper.

Table 1. Summary of the three different initial set-ups studied in this work. The second and third columns are the initial masses of the donor and the accretor, respectively. The fourth column is the initial metallicity. The fifth column is the fraction of mass lost from the vicinity of the accretor. The last column indicates whether the diffusion of elements was considered.

#	$M_{\rm i,d}/M_\odot$	$M_{\rm i,a}/M_\odot$	Z	$\beta_{\rm mt}$	rot/dif
1	1.0	1.4	0.02	0.3	rot
2	1.2	1.4	0.02	0.3	rot
3	1.0	1.4	0.02	0.8	rot+dif

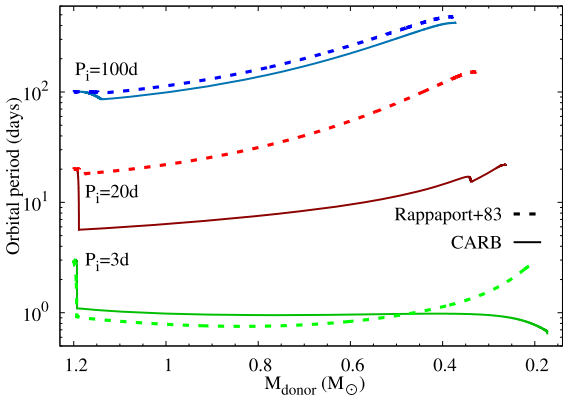

Figure 1. The evolution of orbital period as a function of decreasing donor resulting mass. Two prescriptions for magnetic braking are compared: Rappaport et al. (1983; the dashed lines) and Van & Ivanova (2019; the solid lines). For each prescription, three initial orbital periods are analysed: 3 (green), 20 (red), and 100 (blue) days. Initial masses are $M_{\rm d,i} = 1.2$ $M_\odot$ and $M_{\rm a,i} = 1.4$ $M_\odot$ for all sequences.

3 RESULTS AND DISCUSSION

3.1 Effects of the magnetic braking

We first show how each of the two prescriptions for magnetic braking differ in the formation of LMXBs systems. We start with one single initial set-up and vary the initial orbital period searching for representative cases of different evolutionary scenarios.

Fig. 1 shows the orbital period evolution as a function of the resulting donor mass for three systems, with $M_{\rm d,i} = 1.2$ $M_\odot$ and $M_{\rm a,i} = 1.4$ $M_\odot$, and for three different initial orbital periods, $P_{\rm i}$ = 3 (green), 20 (red), and 100 (blue) days. Each configuration is shown for both R83 (the dashed lines) and CARB (V19, the solid lines) magnetic braking, totalizing six evolutionary sequences. The evolution of the main physical quantities that govern magnetic braking are shown in Fig. 2 for the cases of $P_{\rm i} = 3$ and 100 d. All other parameters are identical for all sequences. All sequences produce detached He–COre ELM WD + NS binaries as output.

From short to long initial orbital periods, the final masses for CARB (R83) sequences are 0.173 (0.205), 0.263 (0.325), and 0.371 (0.377) solar masses, respectively. In the same way, the final orbital periods are 0.64 (2.55), 22 (152), and 424 (481) days, respectively.

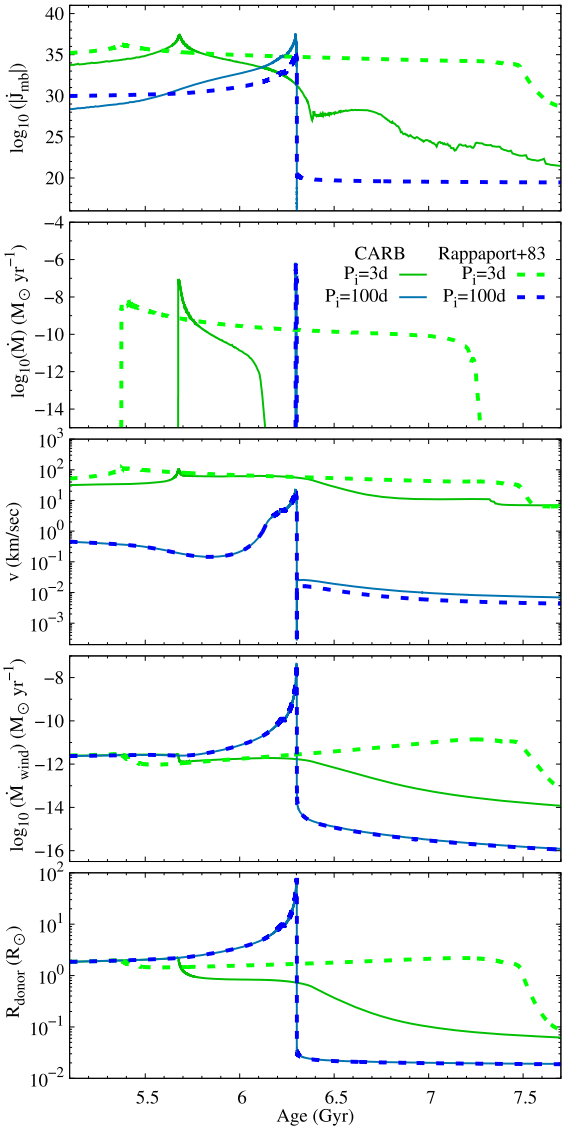

Figure 2. The evolution of key parameters during the mass transfer epoch. Two prescriptions for magnetic braking are compared: Rappaport et al. (1983, the dashed lines) and Van & Ivanova (2019, the solid lines). For each prescription, two initial orbital periods are analysed: 3 (green) and 100 (blue) days. Initial masses are $M_{\rm d,\,i} = 1.2$ M$_\odot$ and $M_{\rm a,\,i} = 1.4$ M$_\odot$ for all sequences. Magnetic braking (first panel), mass transfer rate (second panel), surface rotational velocity at equator (third panel), wind mass-loss (fourth panel), and radius of the donor star (fifth panel) are shown.

Fig. 1 shows the existence of two different evolutionary scenarios when we compare the prescriptions of R83 and CARB for magnetic braking. The first scenario corresponds to intermediate and long initial orbital periods (∼20–100 d), where the evolution of the donor mass star has similar shapes for the two prescriptions of magnetic braking. The orbital period increases as the donor star loses mass, regardless of the adopted magnetic braking. The second scenario corresponds to the case of short initial orbital periods (∼3 d), and is characterized by a decrease in the orbital period at the end of the evolution of the sequences that consider the CARB formula.

Also, for intermediate and long initial orbital periods, the binary components do not come closer before RLOF begins if the R83 magnetic braking is considered. For the case in which the CARB magnetic braking is considered, the components get closer before the beginning of the RLOF, and the difference in relation to the prescription of R83 is as large as the shorter the $P_{\rm i}$. Finally, in the case of short initial orbital periods, both prescriptions for magnetic braking (R83 and CARB) considerably decrease the separation of the binary components before the RLOF begins. In summary, the effect of magnetic braking increases with the decreasing of orbital periods for both prescriptions, but it alters differently along initial orbital periods for each prescription.

For $P_{\rm i} = 100$ d, both R83 and CARB prescriptions results in diverging systems; and for $P_{\rm i} = 3$ d, they both converge (see Fig. 1 and Section 3.2). The relation between the initial and final orbital periods for each magnetic braking prescription is, however, completely different. Looking for the limit that separates the converging from the diverging systems (i.e, $P_{\rm i} = P_{\rm f}$), we find ∼3 d for the R83 magnetic braking but 20 d if the CARB prescription is used. With the only exception of the $P_{\rm i} = 100$ d models, in all other cases the use of the CARB prescription causes the mass transfer to start earlier when compared to the R83 prescription (second panel in Fig. 2). Also, the duration of the mass transfer is longer for shorter $P_{\rm i}$. In fact, for $P_{\rm i} =$ 100 d the mass transfer phase is so fast that we can barely distinguish it in the figure.

We now examine how the variables that determine the intensity of magnetic braking evolve. During most of the evolution, the R83 prescription results in stronger magnetic braking than the CARB prescription (first panel in Fig. 2). The exception occurs during mass transfer, where the CARB braking prescription becomes more intense. This inversion can occur up to about 500 Myr before the mass transfer begins. Although these two prescriptions for magnetic braking differ for systems of any initial orbital period, their effects are much more intense in systems of short and intermediate orbital periods ($P_{\rm i} \sim$ 3–50 d) than in long orbital periods ($P_{\rm i} \sim 100$ d).

The $P_{\rm i} = 100$ d sequences show minimal differences in the evolution of the orbital period and donor mass (Fig. 1). This occurs because the rotation rate, the radius of the donor, and the the donor mass evolve in a very similar way in both prescriptions, for this initial orbital period (third and fifth panels in Fig. 2; the evolution of the mass of the donor is not show, for simplicity). The small difference in the orbital period behaviour during the evolution of these sequences is due to the role of the size of the convective zone in the CARB prescription, which, in turn, affects the magnetic braking (first panel in Fig. 2). For the $P_{\rm i} = 100$ d sequence with the CARB formula, the convective zone at the beginning of the RLOF accounts for ∼0.82 M$_\odot$ of the model. Finally, the angular momentum loss from magnetic braking has a very limited impact on the evolution of binaries with long orbital periods. During the pre-RLOF evolution of the $P_{\rm i} = 100$ d systems, magnetic braking has an almost null contribution in both prescriptions. On the other hand, for $P_{\rm i} = 3$ d, magnetic braking is the dominant mechanism in the R83 prescription; and has an increasing contribution in the CARB prescription, dominating from 2 Gyr before RLOF onwards.

In the second scenario, $P_{\rm i} = 3$ d, the mass transfer begins when the donor star has just left the main sequence and the convective zone is not extended enough (∼0.25 M$_\odot$ in the CARB sequence) to contribute significantly with magnetic braking. Thus, the consideration of the size of the convective zone foreseen by the CARB prescription has little effect. Until the beginning of the RLOF, the wind mass-loss and the radius of the donor star behave similarly in

both prescriptions, assuming values of $10^{-11.5}$ $M_\odot$ yr^{-1} and 2 $R_\odot$ immediately before the beginning of the mass transfer, respectively (fourth and fifth panels in Fig. 2). On the other hand, the rotation rate in the CARB (R83) prescription is 32 km s^{-1} (59 km s^{-1}) at age 5.2 Gyr (third panel in Fig. 2). Since the donor mass and the donor radius behave similarly in this case, contributions are limited to the rotation rate, the wind mass-loss, and the convection turnover time in this case. These are the contributions that make the mass transfer start when the system has an orbital period of 1.1 d (CARB) and 0.9 d (R83). When the R83 prescription is used in the P_i = 3 d system, the rotation rate, the radius of the donor star, and the donor mass react smoothly to the mass-loss (third and fifth panels in Fig. 2). Thus, the magnetic braking in this case also remains approximately constant $\log_{10}(|\dot{J}_{mb}|) = 35$ during a few Gyr after the mass transfer (first panel in Fig. 2). On the other hand, when the CARB prescription is considered, the donor star contracts, and the wind mass-loss decays after the end of the RLOF, causing the magnetic braking to be reduced to $\log_{10}(|\dot{J}_{mb}|) = 28$. In the case where P_i = 3 d, although the R83 prescription results in a considerably longer RLOF, the CARB prescription reaches $\dot{M} = 10^{-7}$ $M_\odot$ yr^{-1}, while the previous one only $\dot{M} = 10^{-8.2}$ $M_\odot$ yr^{-1}. In addition, the moment the mass transfer ends, the system using the R83 prescription has an increasing orbital period, while the CARB prescription has a decreasing orbital period. At this point, the contributions of magnetic braking and mass-loss to the total angular momentum loss are around 88 (98) and 12 (2) per cent for R83 (CARB), respectively. Gravitational radiation will dominate the angular momentum loss only about 2 Gyr after the RLOF terminates. Furthermore, at this point, the donor star has a radius about 2.3 times larger for R83 than for CARB. In both cases, the donor radius remains close to the Roche lobe after the end of the mass transfer, but for R83 these two quantities are increasing, and for CARB they are decreasing. The analysis of these factors makes it clear that the evolution of the donor star and the binary system combine differently for each prescription of magnetic braking, which will be presented in more detail in the next section.

Although the P_i = 20 d sequences behave similarly to the P_i = 100 d sequences, they differ in the evolution of the orbital period before the RLOF. For P_i = 20 d, the RLOF starts when P = 18 d in the case of R83 magnetic braking and when P = 5.7 d in the case of the CARB prescription (see Fig. 1). This means that the entire mass transfer takes place with the stars much closer together when CARB magnetic braking is considered. This reinforces the fact that each magnetic braking prescription leads to a different shrinkage of the orbit, and therefore to a different evolutionary stage of the donor and orbital separation at the onset of the mass transfer. Both the radius of the donor star and the loss of mass by winds reach higher values (around 60 $R_\odot$ and 10^{-8} $M_\odot$ yr^{-1}, respectively) during mass transfer when R83 braking is considered. On the other hand, when CARB braking is considered, the radius of the donor star remains stable around 9 $R_\odot$ during mass transfer. In addition, the loss of mass by winds intensifies in this case and remains around $10^{-9.5}$ $M_\odot$ yr^{-1} for about 1.5 Gyr. For both braking prescriptions, these two variables drop dramatically as soon as the RLOF ends. The consequence is that the mass transfer lasts about three times longer when the CARB prescription is considered.

For any P_i, the CARB magnetic braking is more intense than the R83 prescription at a time when the mass transfer rate is maximum (first panel in Fig. 2). In addition, for any initial orbital period, the CARB magnetic braking is less intense than the R83 prescription braking after mass transfer.

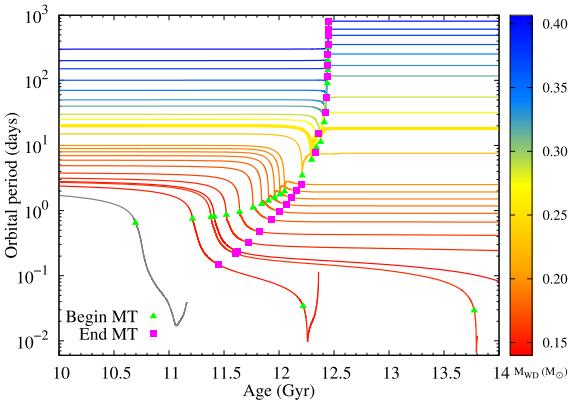

Figure 3. The evolution of the orbital period as a function of age for selected models between $2.7 \leq P_i/d \leq 300$. Initial orbital periods, from top to bottom: 300, 200, 150, 100, 70, 50, 40, 30, 25, 20, 15, 10, 9, 8, 7, 6, 5, 4, 3.5, 3.25, 3.2, 3, and 2.7 d. The bifurcation period occurs between 20 and 25 d. The extra thick line marks the first convergent system. Above it, all systems are divergent. The beginning and end of the mass transfer are indicated by the green triangles and the pink squares, respectively. The colour of each line indicates the mass of the donor at the end of the mass transfer. The sequence shown in grey never becomes detached. The initial configuration is $M_{d,i} = 1.0$ $M_\odot$ and $M_{a,i} = 1.4$ $M_\odot$ for all sequences. The enhanced CARB magnetic braking is considered. Convergent binaries will continue to contract their orbits, forming a cataclysmic variable or an ultracompact X-ray binary system. Divergent binaries will become relatively wide systems containing a recycled NS and a He or CO WD.

3.2 Orbital period evolution and period bifurcation

There is a critical initial orbital period – called the bifurcation period – that separates the systems in converging ($P_f < P_i$) and diverging ($P_f > P_i$). The converging systems are the ones that, after the RLOF, evolve with decreasing orbital period until the donor star becomes degenerate and an ultracompact binary is formed. The diverging systems are the ones that, after the RLOF, evolve with increasing orbital period and a wide detached binary is formed (Pylyser & Savonije 1988, 1989). In theoretical models, the bifurcation period depends on the strength of the magnetic braking (e.g. Tauris & van den Heuvel 2006). A systematic study made by Ma & Li (2009) considering systems with a 1.4 $M_\odot$ NS and a 0.5–2 $M_\odot$ donor star found that the strength of the magnetic braking is the dominant factor in determining the value of bifurcation period compared with mass-loss.

In this section, we expand our model grid using the CARB prescription of the magnetic braking into the initial orbital period parameter space. Fig. 3 shows the evolution of the orbital period as a function of age for the CARB prescription, for initial masses $M_{d,i}$ = 1.0 $M_\odot$ and $M_{a,i}$ = 1.4 $M_\odot$. The initial orbital periods range from 2.7 to 300 d. Because of the initial donor mass and metallicity, no model shows a significant orbital period variation before a model age of 10 Gyr. The shorter the P_i, the sooner the systems starts mass transfer. Up to this point, we are only discussing models without element diffusion. However, we draw attention to the fact that this does not affect the main results discussed so far, as diffusion has a small effect on the quantities studied. The effects of diffusion will be discussed from Section 3.3.1 onwards.

Using the Rappaport et al. (1983, R83) magnetic braking, Istrate et al. (2016) found that the bifurcation period that separates the converging systems from the diverging ones occurs between 2.75 and

2.8 d if $M_{\rm d,\,i} = 1.0$ M$_\odot$ and $M_{\rm a,\,i} = 1.4$ M$_\odot$. Considering the CARB magnetic braking prescription of V19, a $P_{\rm i} = 20$ d system with the same initial masses is still a convergent system. This corresponds to a 0.255 M$_\odot$ ELM WD – the thickest line in Fig. 3.

We should emphasize that even in the lower limit of orbital period, our models (as shown in Appendix A) are completely detached at a model age of 14 Gyr. Simulations considering shorter initial orbital periods still have a small rate of mass transfer ($\dot{M} > 10^{-10}$ M$_\odot$ yr^{-1}) at the final computed age and therefore are not part of our model grid. In such cases, the donor star is expected to be completely consumed, i.e. transfer all its mass to the NS within a few billion years – or they may merge due to emission of gravitational radiation, similar to the known ultracompact binaries (bottom three sequences in Fig. 3).

The bifurcation period is shifted to longer ones (from 2.75–2.8 to 20–25 d) when the CARB magnetic braking is considered, i.e. the CARB magnetic braking allows us to get ELM WDs models with masses as low as 0.26 M$_\odot$ in converging binary systems even with initial orbital periods as long as 20 d, which is not possible with the magnetic braking of R83. This is important because it shows that the entire extension of low-mass and ELM WDs in systems with pulsars can be obtained via RLOF evolution from a more uniform distribution of initial orbital periods (on a logarithmic scale), without favouring only the most massive ones.

Although not the focus of this work, the upper and lower sequences in Fig. 3 show that the use of CARB magnetic braking makes it possible to form UCXB systems and wide-orbit binary millisecond pulsars, which is not possible with the V18 prescription.

At this point, we should consider whether there are new problems appearing with the use of CARB, since even the binaries with $P_{\rm i} = 20$ d can produce ELM WDs in millisecond pulsar systems. In fact, the analysis of Istrate et al. (2014) indicates with a high level of confidence that the distribution of orbital periods of observed recycled pulsars with He WD companions in the Galactic Field is not compatible with the simulations that use the R83 prescription. They pointed out that the range of initial orbital periods that lead to the formation of this type of system must be expanded. In addition, the $P_{\rm i}$–$M_{\rm d,\,f}$ relation we found is much closer to the expected lognormal orbital period distribution (see e.g. Duchêne & Kraus 2013; Tutukov & Cherepashchuk 2020) than when using the R83 prescription. Thus, the results we found using the CARB prescription are encouraging and a study comparing these results with simulations of binary population synthesis looks promising.

3.3 ELM with neutron stars

In this subsection, we expand our study of systems with point mass accretors of 1.4 M$_\odot$.

3.3.1 *Initial orbital period and final mass*

In this section, we show how the relation between the initial orbital period and the final WD mass is modified when we change the initial mass of the donor star and the NS mass accretion efficiency. In Fig. 4, we depict the relation between the initial orbital period (y-axis) and the low-mass/ELM final mass (x-axis). The red triangles correspond to models with $M_{\rm d,\,i} = 1.0$ M$_\odot$, 70 per cent accretion efficiency (i.e. $\beta_{\rm mt} = 0.3$), and that take into account rotation only. Blue circles are for $M_{\rm d,\,i} = 1.2$ M$_\odot$; and the green squares are for 20 per cent accretion efficiency (i.e. $\beta_{\rm mt} = 0.8$) with both rotation and diffusion. For comparison, Istrate et al. (2016) LMXB models using the Rappaport et al. (1983) magnetic braking prescription are shown in black '$*$' signs.

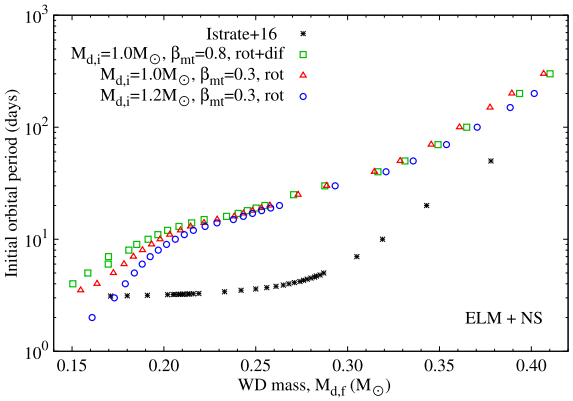

Figure 4. The relation between the initial orbital period and the ELM WD mass at the end of 14 Gyr evolution for different set-ups. Istrate et al. (2016) LMXB models using the Rappaport et al. (1983) magnetic braking prescription are shown in black '$*$' signs. Green '□' signs: $M_{\rm d,\,i} = 1.0\,M_\odot$, 20 per cent accretion efficiency, rotation plus diffusion. Red '△' signs: $M_{\rm d,\,i} = 1.0$ M$_\odot$, 70 per cent accretion efficiency, rotation only. Blue '○' signs: $M_{\rm d,\,i} = 1.2$ M$_\odot$, 20 per cent accretion efficiency, rotation only. All configurations have $M_{\rm a,\,i} = 1.4$ M$_\odot$.

As we already mentioned in Section 1, the empirical treatment of the magnetic braking by Rappaport et al. (1983) leads to a fine-tuning of the order of a dozen minutes in the initial orbital period to reproduce the observed orbital periods of millisecond pulsars in compact ($2 < P/{\rm h} < 9$) binaries with He WD companions of mass $\lesssim 0.20\,M_\odot$ (Istrate et al. 2014).

It is notable that each prescription for magnetic braking has a completely different pattern in the $P_{\rm i}$–$M_{\rm d,\,f}$ plane. For final donor masses between 0.17 and 0.25 M$_\odot$, we can see in Fig. 4 that the range of corresponding initial orbital periods is extremely narrow (between 2 and 4 d) for the prescription of R83. On the other hand, when the CARB (V19) formulation is considered, the same range of final masses is obtained for initial orbital periods between 3 and 20 d. Thus, the use of the CARB prescription does not require a fine-tuning of initial periods for the formation of ELM WDs. Using initial masses $M_{\rm d,\,i} = 1.0$ M$_\odot$ and $M_{\rm a,\,i} = 1.4$ M$_\odot$, we were able to produce detached WD systems within the range $3.25 \leq P_{\rm i}/{\rm d} \leq 300$ (see Fig. 5), which corresponds to ELM and low-mass WDs with masses in the range $0.1456 \leq M_{\rm d,\,f}/M_\odot \leq 0.4067$.

We will now consider only the sequences that use CARB (V19) magnetic braking. In Fig. 4, the set-up discussed in the previous subsection ($M_{\rm d,\,i} = 1.0$ M$_\odot$, $\beta_{\rm mt} = 0.3$) is shown in the red triangles. The first comparison concerns an initially more massive donor, with 1.2 M$_\odot$ (the blue circles in Fig. 4). There is a systematic shift of the final mass towards larger masses, for the same initial period $P_{\rm i}$, in comparison to the case when the donor mass is $M_{\rm d,\,i} = 1.0$ M$_\odot$. The difference in final masses increases for shorter initial orbital periods. For example, we find the final donor mass to be 0.1790 M$_\odot$ if $M_{\rm d,\,i} = 1.2$ M$_\odot$, but 0.1636 M$_\odot$ if $M_{\rm d,\,i} = 1.0$ M$_\odot$. For $P_{\rm i} \leq 11$ d, no sequence undergoes hydrogen shell flashes, regardless of the initial mass of the donor. The configuration with $M_{\rm d,\,i} = 1.2$ M$_\odot$ is the only one where it is possible to obtain detached systems for $P_{\rm i} < 3$ d.

Using a $M_{\rm d,\,i} = 1.2$ M$_\odot$ donor instead of 1.0 M$_\odot$ does not significantly affect the binary evolution. The difference in the ELMs final mass is due to the more massive model being able to burn more H into He before mass transfer begins. For example, for the $P_{\rm i} = 20$ d case, this is reflected in the He core to be 0.0054 M$_\odot$ more massive

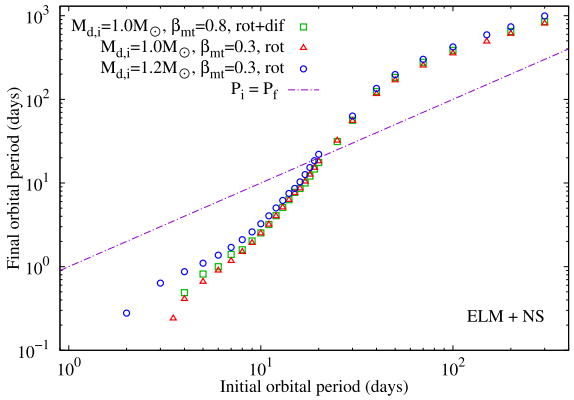

Figure 5. The relation between the final (P_f) and the initial orbital period (P_i). Each initial configuration is as follows. Green '□' signs: initial donor mass $M_{d,i} = 1.0$ M$_\odot$, 70 per cent accretion efficiency, rotation plus diffusion. Red '△' signs: $M_{d,i} = 1.0$ M$_\odot$, 20 per cent accretion efficiency, rotation only. Blue '○' signs: $M_{d,i} = 1.2$ M$_\odot$, 20 per cent accretion efficiency, rotation only. All configurations have $M_{a,i} = 1.4$ M$_\odot$. The purple dot–dashed line serves as an indicator to distinguish between convergent and divergent systems.

for the initially more massive donor. This difference increases to 0.015 M$_\odot$ for $P_i = 300$ d. Note that for this metallicity ($Z = 0.02$) and $M_{d,i} = 1.0$ M$_\odot$, because of the long main sequence lifetime, it is difficult to produce (pre-)ELMs in less than 10–11 Gyr. Thus, younger (pre-)ELMs require either lower metallicity or initially more massive donors.

The next comparison concerns the accretion efficiency to the NS and the use of diffusion (green squares in Fig. 4). The effect of diffusion on the relation shown in Fig. 4 is negligible for $M_{d,f} \gtrsim 0.3$ M$_\odot$. For $M_{d,f} \lesssim 0.3$ M$_\odot$, the diffusion of elements leads to slightly smaller final masses, given a P_i, because diffusion brings more fuel to the burning zone, in addition to leading to more hydrogen shell flashes.

On the other hand, different accretion efficiencies have a significant effect only for $M_{d,f} \gtrsim 0.3$ M$_\odot$. In this case, low accretion efficiency results in low-mass/ELM WDs with a slightly higher final mass, for a given P_i. This is because the mass transfer rate reaches slightly higher values as the accretion efficiency to the point-like NS is higher. Another consequence is that, for a given P_i, the orbital separation after the mass transfer is shorter when the accretion efficiency is higher.

The occurrence of different numbers of hydrogen shell flashes can also be noted in Fig. 4 when looking at the systems with diffusion (the green squares). In this case, the $P_i = 7$ and 6 d systems have practically the same donor final mass (0.1698 and 0.1697 M$_\odot$, respectively), but the $P_i = 7$ d sequence undergoes one hydrogen shell flash more than the other. This causes a discontinuity in the form of a step in the curve formed by the models in this figure. In summary, the variation of the initial mass of the donor stars and efficiency rate to the accreting star, and the consideration of diffusion of elements cause significant effects in the P_i–$M_{d,f}$ plane for $P_i \lesssim 10$ d or, equivalently, $M_{d,f} \lesssim 0.2$ M$_\odot$.

3.3.2 *Initial and final orbital period*

In this section, we show how the initial–final orbital period relation is modified when we change the initial mass of the donor star and the mass accretion efficiency to the NS. In Fig. 5, we show the final orbital period (y-axis) as a function of the initial orbital period (x-axis). The red triangles are for sequences with $M_{d,i} = 1.0$ M$_\odot$, 70 per cent accretion efficiency (i.e. $\beta_{mt} = 0.3$), and that takes into account rotation only. Similarly, the blue circles are for $M_{d,i} = 1.2$ M$_\odot$; and the green squares are for 20 per cent accretion efficiency (i.e. $\beta_{mt} = 0.8$) with both rotation and diffusion. The purple dot–dashed line serves as an indicator to distinguish between convergent and divergent systems.

Fig. 5 shows that the division between convergent and divergent systems is around $P_i = 20$ d, regardless of the initial configuration. Therefore, the pattern of orbital evolution shown in Fig. 3 for that specific initial configuration is similar also for the other configurations presented here.

For any initial orbital period, an initially more massive donor always leads to a wider binary, regardless of the accretion efficiency to the NS. In fact, it is possible to identify a tendency for initially short ($P_i < 10$ d) and long ($P_i > 40$ d) orbital period systems. In these cases, we find that, for a given initial orbital period, higher accretion efficiency leads to shorter final orbital periods; and an initially more massive donor leads to longer final orbital periods. For orbital periods closer to the bifurcation period, however, there is no clear trend, and the P_i–P_f relations are quite similar for each configuration studied.

These results can be understood as the mass transfer begins earlier for systems that have a donor with a 1.2 M$_\odot$ (5–6 Gyr) compared to a 1.0 M$_\odot$ donor (11–12 Gyr) due to their main-sequence lifetimes. Angular momentum loss mechanisms have more time to act on systems with less-massive donors, leading to mass transfer beginning when the components of the binary system are closer.

In Fig. 5, we compare models with diffusion and low accretion efficiency (the green squares) against models without diffusion and high accretion efficiency (the red triangles). We found that diffusion of elements and accretion rate efficiency affect evolution at different times. Until the beginning of the mass transfer, neither the inclusion of diffusion or different accretion rates affect significantly the evolution. At the end of mass transfer, low accretion efficiency to the NS makes sequences with $\beta_{mt} = 0.8$ with their components closer together. Still, for a given P_i, the masses of each configuration are similar at that time. What happens next for sequences of $M_{d,f} \lesssim 0.3$ M$_\odot$ depends on the inclusion or not of the diffusion of elements. For most non-diffusing sequences, none or one hydrogen shell flashes occurs. On the contrary, in most sequences with diffusion, there are two or three hydrogen shell flashes. As the loss of angular momentum during hydrogen shell flashes is dominated by mass-loss for a more massive accretor, each hydrogen shell flash increases orbital separation. Thus, the inclusion of diffusion of elements tends to decrease the final donor mass and increase the orbital separation of the components.

We also found a clear relation between the final orbital period and the rotation rate of the WD. For models with diffusion, systems with a short initial orbital period ($P_i \lesssim 15$ d) present greater synchronization with the orbit, at the end of the evolution. In such cases, the ratio between the rotation rate of the ELM WD and the orbital period of the system assumes values between 1 and 0.1. On the other hand, this ratio in $P_i \gtrsim 20$ d systems is $P_{rot}/P_f \simeq 0.1$–10^{-3}, indicating WDs rotating more slowly than the orbital period. Looking at the P_i–P_f diagram in Fig. 5, we notice that this value of the initial orbital period (20 d) coincides with the bifurcation period. Thus, convergent systems are more likely to have synchronization between the rotation of the WD and the orbit. This occurrence might be a tool to observationally estimate the convergence period. Even for systems with a shorter initial orbital period, we find that from ∼1 Gyr after the end of RLOF onwards, the time needed for synchronization exceeds the

age of the Universe. This means that we should not expect tidal forces to change the rotation of the newly formed low-mass/ELM WDs.

Note that the bottom left-hand corner of Fig. 5 is dominated by systems with $P < 1$ d. Such close systems are strong candidates to be observable in gravitational waves (e.g. Chen et al. 2021). Simple estimates of the amplitude, the characteristic strain, and the frequency of the gravitational waves emitted by our models at final age are described in Appendix C and presented in Appendix A.

3.3.3 Final mass–orbital period relation

The determination of relations between the orbital period and the mass of low-mass and ELM WDs in systems with NSs is of great interest because this relation can be used to examine the evolutionary channel for such a binary. These relations allow the estimation of the masses of ELM WDs from the orbital period of the binary system, which is, in general, easier to measure and independent of the $T_{\rm eff}$ and $\log(g)$ determinations.

The cores masses and radii of low-mass stars in the red giant branch follow a tight, well-known relation (Refsdal & Weigert 1971; Webbink, Rappaport & Savonije 1983; Joss, Rappaport & Lewis 1987). For a red giant donor in a binary system, its radius is approximately equal to its Roche lobe radius during the mass transfer phase. The latter, in turn, depends on the binary separation and on the mass ratio. At the end of the mass transfer phase, the H-rich envelope is almost completely removed, and the final mass of the donor star is approximately the mass of its He core. Therefore, the final mass of a degenerate-core donor and the orbital period are correlated quantities.

Fig. 6 shows the final mass of donor versus period ($M_{\rm d,\,f}$–$P_{\rm f}$) relation for all computed models with a 1.4 $M_\odot$ point mass accretor. Although the CARB (V19) prescription for the magnetic braking completely changes the relation between $P_{\rm i}$ and $M_{\rm d,\,f}$, the relation between the final period ($P_{\rm f}$) and final donor mass ($M_{\rm d,\,f}$) is much less affected in relation to the models calculated with the Rappaport et al. (1983, R83) magnetic braking formalism (Istrate et al. 2016). The use of the CARB prescription produces models that maintain agreement with other theoretical adjustments and also with observational data.

Our results are in good agreement with the Lin et al. (2011) theoretical fit, which is based on low and intermediate-mass X-ray binaries models computed with gravitational radiation, mass-loss, and R83 magnetic braking contributions to the angular momentum loss. In particular, our models for $M_{\rm d,\,f} \lesssim 0.30$ $M_\odot$ and $\beta_{\rm mt} = 0.3$ are in excellent agreement with the Lin et al. (2011) fit. For $\beta_{\rm mt} = 0.8$, although the agreement with the fit is good for $M_{\rm d,\,f} \gtrsim 0.23$ $M_\odot$, we found orbital periods slightly longer than Lin et al. (2011) if $M_{\rm d,\,f} \lesssim 0.23$ $M_\odot$, for a given mass. Between $M_{\rm d,\,f} = 0.23$ and 0.26 $M_\odot$, our models are in good agreement with both Lin et al. (2011) and Tauris & Savonije (1999, Pop. I) fits. It is important to note that these fits were made based on a broader initial donor masses distribution than we are considering here.

Although the angular momentum losses of the systems are calculated differently in each work, the $M_{\rm d,\,f}$–$P_{\rm f}$ relation is determined by the state of the He cores therefore it should not be changed with the angular momentum loss. In fact, Chen et al. (2013) have shown that the mass transfer efficiency and the way that angular momentum is lost impose only a small influence on the $M_{\rm d,\,f}$–$P_{\rm f}$ relations. On the other hand, the mixing-length and the metallicity affect this relation (e.g. Rappaport et al. 1995; Tauris & Savonije 1999). Also, the calibration of other internal processes – such as the opacity and the convective overshooting – can influence the radius of red giant stars and hence the $M_{\rm d,\,f}$–$P_{\rm f}$ relation. As already mentioned, we found that the inclusion of diffusion of elements leads to less-massive donors, given an initial orbital period. Analysing the effects of including diffusion and low accretion efficiency separately, we find that both decrease the final mass of the donor, for a given initial orbital period, although the former has a more pronounced effect than the latter. Thus, in Fig. 6 we attribute the discrepancy between the green squares and the fit of Lin et al. (2011) primarily to the effects of diffusion.

An important result is that the relation between the orbital period and the final mass of ELM WDs is not significantly affected when we consider different initial donor masses (1.0 and 1.2 $M_\odot$), although considerable differences are expected for donors of initial masses 1.3–1.6 $M_\odot$ (Istrate et al. 2014). On the other hand, for $M_{\rm d,\,f} \lesssim 0.23$ $M_\odot$, low accretion efficiencies always lead to more compact systems, for a given mass.

Fig. 6 also shows observational data, which include 16 systems of (millisecond) pulsar plus He WDs with individual component mass measurements.[4] Each pulsar companion is shown with a black dot and an $\pm 1\sigma$ uncertainty bar in the mass measurement. The dots without an uncertainty bar have uncertainty in the measure of mass smaller than the dots size. This list contains only systems in which there is no mass transfer nor significant mass-loss observed.

Instead of commenting on each of the pulsars separately, we highlight some systems that deviate most from the theoretical estimates of Tauris & Savonije (1999) and Lin et al. (2011). It is well known that, for a given final mass, lower metallicities lead to shorter final orbital periods (TS99 Pop. II curve in Fig. 6). Therefore, most of the observational points shown in Fig. 6 can be reached by modifying the metallicity of the models. Still, some observational points are located above the theoretical adjustments, not finding agreement even considering the uncertainty in the measured masses.

The He WD in the PSR J2043+1711 system ($P = 1.48$ d) has a mass estimate of 0.173 $M_\odot$. Our model for $M_{\rm d,\,i} = 1.0$ $M_\odot$, $\beta = 0.8$ (the green squares in Fig. 6) of $P_{\rm i} = 7$ d has $P_{\rm f} = 1.40$ d and $M_{\rm d,\,f} = 0.1689$ $M_\odot$, far from the theoretical fits from Lin et al. (2011) and Tauris & Savonije (1999), but in great agreement with the observation.

For PSR J1713+0747 ($P = 67.8$ d), the millisecond pulsar has 1.35 $M_\odot$ and the He WD companion has 0.292 $M_\odot$. PSR J1713+0747 is one of the most precisely timed pulsars and provides one of the best pulsar limit on the variation of the gravitational constant, on violations of the universality of free-fall, and post-Newtonian parameters measurements (Desvignes et al. 2016; Zhu et al. 2019). Our model for $M_{\rm d,\,i} = 1.2$ $M_\odot$, $\beta = 0.8$ (the blue circles in Fig. 6) of $P_{\rm i} = 30$ d has $P_{\rm f} = 63.1$ d and $M_{\rm d,\,f} = 0.2932$ $M_\odot$, but $M_{\rm a,\,f} = 1.98$ $M_\odot$, not matching the mass of the pulsar. However, for a rotation plus diffusion sequence with $M_{\rm d,\,i} = 1.0$ $M_\odot$, $M_{\rm a,\,i} = 1.3$ $M_\odot$, $P_{\rm i} = 32$ d and $\beta_{\rm mt} = 0.9$ we find $M_{\rm a,\,f} = 1.36$ $M_\odot$, $P_{\rm f} = 64.7$ d, and $M_{\rm d,\,f} = 0.2918$ $M_\odot$, in much better agreement with the three measured parameters.

PSR J1946+3417 ($P = 27.0$ d) hosts the fourth most massive millisecond pulsar (1.828 $M_\odot$), and its He WD companion has 0.2656 $M_\odot$ (Barr et al. 2017). In this case, taking a rotation plus diffusion sequence with $M_{\rm d,\,i} = 1.0$ $M_\odot$, $M_{\rm a,\,i} = 1.7$ $M_\odot$, $P_{\rm i} = 21$ d,

[4] Observational data of pulsars were taken from https://www3.mpifr-bonn.mpg.de/staff/pfreire/NS_masses.html (see also Özel & Freire 2016; Antoniadis et al. 2016), Barr et al. (2017, PSR J1946+3417), and Fonseca et al. (2021, PSR J0740+6620).

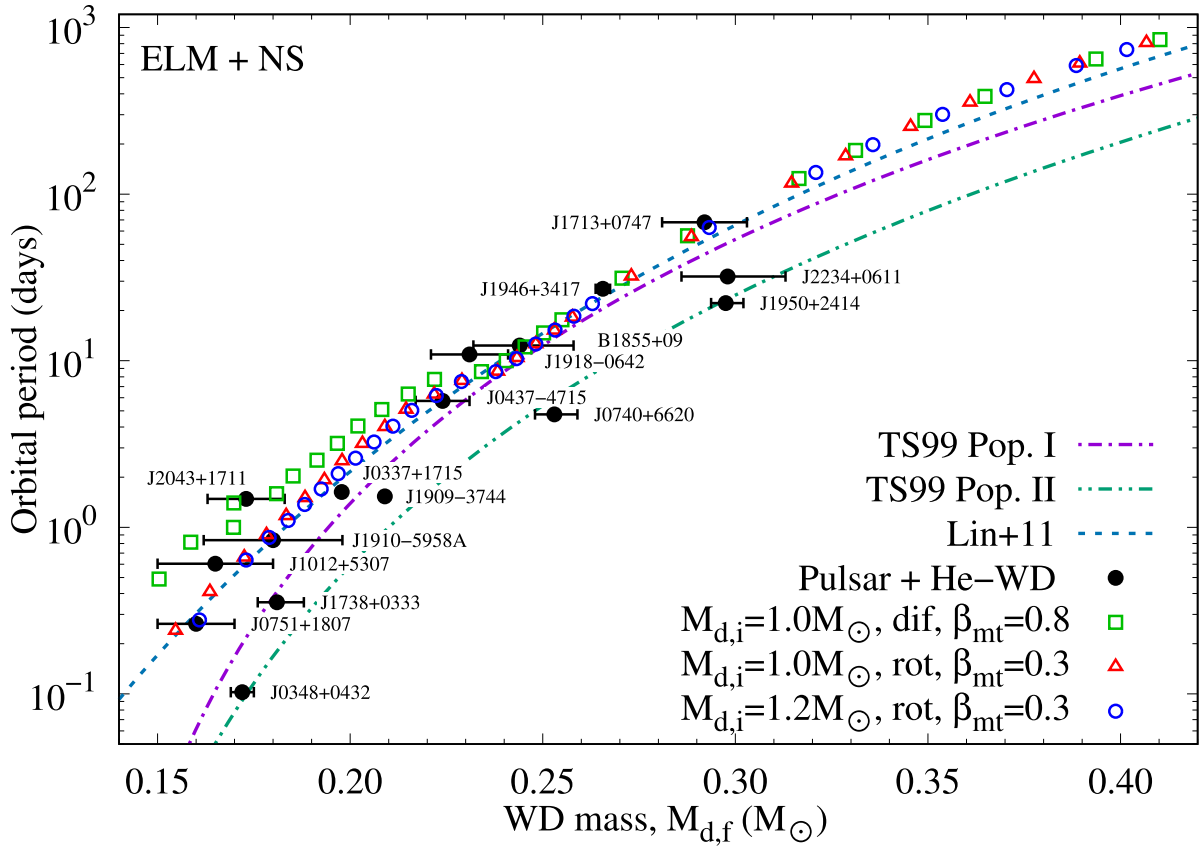

Figure 6. The relation between the low-mass/ELM WD final mass and the orbital period. Each initial configuration is as follows. Green '□' signs: $M_{\rm d,\,i}$ = 1.0 $M_\odot$, 70 per cent accretion efficiency, rotation plus diffusion. Red '△' signs: $M_{\rm d,\,i}$ = 1.0 $M_\odot$, 20 per cent accretion efficiency, rotation only. Blue '○' signs: $M_{\rm d,\,i}$ = 1.2 $M_\odot$, 20 per cent accretion efficiency, rotation only. All configurations have $M_{\rm a,\,i}$ = 1.4 $M_\odot$. The dash–dotted curves represent the theoretical relations from Tauris & Savonije (1999, TS99) and the dotted curve from Lin et al. (2011, Lin+11). Observational data (the black dots) are from pulsar + He WD systems, with 16 systems in total. The dots without an uncertainty bar mean that the uncertainty is less than the dot size.

and $\beta_{\rm mt}$ = 0.8, we find $M_{\rm a,\,f}$ = 1.836 $M_\odot$, $P_{\rm f}$ = 26.8 d, and $M_{\rm d,\,f}$ = 0.2664 $M_\odot$, in excellent agreement with the measured parameters.

In summary, the CARB magnetic braking seems to be compatible with the formation of ELM WDs in systems with millisecond pulsars. The use of low accretion efficiency to the neutrons stars, between 5 and 20 per cent, revealed to be appropriate, as suggested by Antoniadis et al. (2012, 2013, 2016). Even in cases where the pulsars have masses far from the canonical value (1.4 $M_\odot$), a simple adjustment of the initial masses has considerably improved possible matchings of the masses. Still, we emphasize that different metallicities were not considered up to now.

3.3.4 Impact of the CARB magnetic braking on the formation of ELM WDs in double degenerates

Although most of the first ELMs discovered had NSs as companions (e.g. van Kerkwijk, Bergeron & Kulkarni 1996; van Kerkwijk et al. 2005), none of the ELMs in the clean sample of the ELM Survey was proven to have an NS as a companion (Brown et al. 2020a). Thus, we present preliminary results for models of ELM WDs formed in companion to other WDs. For WD accretors with $M_{\rm a,\,i}$ = 0.8 $M_\odot$, we find that there is a systematic shift towards lower final masses, for each given initial period $P_{\rm i}$, when compared to the 1.4 $M_\odot$ NS accretor case. This result can be easily understood since the evolution of the orbital separation depends on the mass ratio. Even so, the general behaviour and trends of the $M_{\rm d,\,f}$–$P_{\rm i}$, $P_{\rm i}$–$P_{\rm f}$, and $M_{\rm d,\,f}$–$P_{\rm f}$ relations are similar to what we found for NS accretors. None the less, observational data of ELM WDs in double-degenerate systems (e.g. Pelisoli & Vos 2019; Brown et al. 2020a) are widely dispersed in the $M_{\rm d,\,f}$–$P_{\rm f}$ plane, moving away from the theoretical low-mass/ELM WDs RLOF models. This seems to indicate that objects that are not in the region of the quoted theoretical models should have been formed via evolutionary channels other than stable mass transfer, such as CE, mergers, triple systems, etc. Thus, this topic requires further study to say to what extent the disagreement has to do with the quality of the data or with the differences between the parameters of the observed system and the input of the simulations.

4 CONCLUSIONS

We first investigated the formation of ELM WDs in binary systems with millisecond pulsars with the proposed CARB prescription for magnetic braking of Van & Ivanova (2019) and compared their effects

on the evolution of LMXB systems with the classic prescription of Rappaport et al. (1983).

We also computed a grid of models of ELM WDs from de ZAMS until a model age of 14 Gyr. We have considered canonical NSs as the accretor, compatible with milliseconds pulsars in LMXBs systems. Different accretion efficiencies ($\beta_{\rm mt}$ = 0.3 and 0.8), and donor initial masses (1.0 and 1.2 $M_\odot$) were considered. The parameter space of the initial orbital period ($P_{\rm i}$) was explored between 1 and 300 d, which corresponds to low mass or extremely low mass WD models of final masses between 0.15 and 0.40 $M_\odot$. For the evolution of the binary system, we take into account energy loss as gravitational waves, mass-loss, spin-orbit coupling, and magnetic braking. Magnetic braking follows the CARB prescription (V19), which was obtained through a self-consistent deduction considering wind mass-loss, rotation, and that the magnetic field is generated due to motions in the convective zone. Although the CARB model is still considerably simplified – only radial magnetic fields are considered and the dipole approximation is used, the Alfvenic surface estimated does not depend on the polar angle, the wind considered is isotropic and the rotation axis is assumed aligned to the magnetic field axis – it has a consistent physical deduction and presents more plausible results when modelling ELM WDs in binary systems.

The use of the CARB magnetic braking prescription by V19 strongly modifies the loss of the total angular momentum of the binary systems and, as a natural consequence, also the relation between the orbital period and the WD becomes completely different. In particular, fine-tuning the initial orbital period is not required. A range of final masses for the ELM WDs (0.15–0.27 $M_\odot$) can be obtained from a large range of initial orbital periods (1–25 d), and up to 0.40 $M_\odot$ for initial orbital periods up to 300 d. The bifurcation period ($P_{\rm i} = P_{\rm f}$) is shifted to longer ones (from 2.75–2.8 to 20–25 d) when the CARB magnetic braking is considered, i.e. the CARB magnetic braking allows us to get ELM WDs models as light as 0.26 $M_\odot$ in converging binary systems even with initial orbital periods as long as 20 d, which is not possible with the empirical magnetic braking prescription of R83. Else, in addition to the LMXB systems, the use of CARB magnetic braking makes it possible to form UCXB systems and also wide-orbit binary millisecond pulsars, which is not possible with the V18 prescription.

The orbital period is one of the main factors that relate an ELM WDs as we observe it today with its progenitor system since the initial orbital period is directly linked with the final orbital period and the final mass. Comparing our models with observational data from He WDs in binary systems with millisecond pulsars, the use of CARB magnetic braking is shown to be compatible with the formation of ELM WDs in LMXBs.

The main properties of our model grid can be found in Appendix A. In Appendix B, we provide polynomial fits to the final ELM WD mass ($M_{\rm d,\,f}$) as a function of the initial orbital period ($P_{\rm i}$).

ACKNOWLEDGEMENTS

We thank the anonymous referee for the careful reading and helpful suggestions on our work. We thank Dr. Alejandra Daniela Romero and Dr. Alina Istrate for strong help throughout the research, and Dr. Ingrid Pelisoli for providing the *Gaia* DR2 data with reddening corrections. We thank the Ada IF-UFRGS cluster staff for their support. This research was developed with the support of the National Supercomputing Center (CESUP), Federal University of Rio Grande do Sul (UFRGS). This work was carried out with the financial support of the Conselho Nacional de Desenvolvimento Científico e Tecnológico (CNPq), by the Coordenação de Aperfeiçoamento de Pessoal de Nível Superior – Brasil (CAPES) – Finance Code 001 and Fundação de Amparo à Pesquisa do Estado do Rio Grande do Sul (FAPERGS). This research has extensively used NASA's Astrophysics Data System.

DATA AVAILABILITY

The data underlying this article will be shared on reasonable request to the corresponding author.

REFERENCES

Althaus L. G., Panei J. A., Romero A. D., Rohrmann R. D., Córsico A. H., García-Berro E., Miller Bertolami M. M., 2009, A&A, 502, 207
Althaus L. G., Miller Bertolami M. M., Córsico A. H., 2013, A&A, 557, A19
Antoniadis J., van Kerkwijk M. H., Koester D., Freire P. C. C., Wex N., Tauris T. M., Kramer M., Bassa C. G., 2012, MNRAS, 423, 3316
Antoniadis J. et al., 2013, Science, 340, 448
Antoniadis J., Tauris T. M., Ozel F., Barr E., Champion D. J., Freire P. C. C., 2016, ApJ, preprint (arXiv:1605.01665)
Barr E. D., Freire P. C. C., Kramer M., Champion D. J., Berezina M., Bassa C. G., Lyne A. G., Stappers B. W., 2017, MNRAS, 465, 1711
Bhattacharya D., van den Heuvel E. P. J., 1991, Phys. Rep., 203, 1
Bildsten L., Shen K. J., Weinberg N. N., Nelemans G., 2007, ApJ, 662, L95
Böhm-Vitense E., 1958, Z. Astrophys., 46, 108
Breedt E., Gänsicke B. T., Marsh T. R., Steeghs D., Drake A. J., Copperwheat C. M., 2012, MNRAS, 425, 2548
Brown W. R., Kilic M., Allende Prieto C., Kenyon S. J., 2010, ApJ, 723, 1072
Brown W. R., Kilic M., Allende Prieto C., Kenyon S. J., 2011, MNRAS, 411, L31
Brown W. R., Kilic M., Allende Prieto C., Kenyon S. J., 2012, ApJ, 744, 142
Brown W. R., Kilic M., Allende Prieto C., Gianninas A., Kenyon S. J., 2013, ApJ, 769, 66
Brown W. R., Gianninas A., Kilic M., Kenyon S. J., Allende Prieto C., 2016a, ApJ, 818, 155
Brown W. R., Kilic M., Kenyon S. J., Gianninas A., 2016b, ApJ, 824, 46
Brown W. R., Kilic M., Gianninas A., 2017, ApJ, 839, 23
Brown W. R. et al., 2020a, ApJ, 889, 49
Brown W. R., Kilic M., Bédard A., Kosakowski A., Bergeron P., 2020b, ApJ, 892, L35
Buchler J. R., Yueh W. R., 1976, ApJ, 210, 440
Cadelano M., Ferraro F. R., Istrate A. G., Pallanca C., Lanzoni B., Freire P. C. C., 2019, ApJ, 875, 25
Cassisi S., Potekhin A. Y., Pietrinferni A., Catelan M., Salaris M., 2007, ApJ, 661, 1094
Chen X., Han Z., Deca J., Podsiadlowski P., 2013, MNRAS, 434, 186
Chen X., Maxted P. F. L., Li J., Han Z., 2017, MNRAS, 467, 1874
Chen H.-L., Tauris T. M., Han Z., Chen X., 2021, MNRAS, 503, 3540
Chugunov A. I., Dewitt H. E., Yakovlev D. G., 2007, Phys. Rev. D, 76, 025028
Cyburt R. H. et al., 2010, ApJS, 189, 240
Deng Z.-L., Li X.-D., Gao Z.-F., Shao Y., 2021, ApJ, 909, 174
Desvignes G. et al., 2016, MNRAS, 458, 3341
Duchêne G., Kraus A., 2013, ARA&A, 51, 269
Eggleton P. P., 1983, ApJ, 268, 368
Ferguson J. W., Alexander D. R., Allard F., Barman T., Bodnarik J. G., Hauschildt P. H., Heffner-Wong A., Tamanai A., 2005, ApJ, 623, 585
Fonseca E. et al., 2021, ApJ, 915, L12
Fuller G. M., Fowler W. A., Newman M. J., 1985, ApJ, 293, 1
Gianninas A., Kilic M., Brown W. R., Canton P., Kenyon S. J., 2015, ApJ, 812, 167
Han Z., Podsiadlowski P., Maxted P. F. L., Marsh T. R., 2003, MNRAS, 341, 669
Heger A., Langer N., Woosley S. E., 2000, ApJ, 528, 368
Heger A., Woosley S. E., Spruit H. C., 2005, ApJ, 626, 350
Henyey L., Vardya M. S., Bodenheimer P., 1965, ApJ, 142, 841
Hermes J. J. et al., 2013a, MNRAS, 436, 3573
Hermes J. J. et al., 2013b, ApJ, 765, 102

Hurley J. R., Tout C. A., Pols O. R., 2002, MNRAS, 329, 897
Iben I., MacDonald J., 1985, ApJ, 296, 540
Iben I., Tutukov A. V., 1984, ApJS, 54, 335
Iglesias C. A., Rogers F. J., 1993, ApJ, 412, 752
Iglesias C. A., Rogers F. J., 1996, ApJ, 464, 943
Istrate A. G., Tauris T. M., Langer N., 2014, A&A, 571, A45
Istrate A. G., Marchant P., Tauris T. M., Langer N., Stancliffe R. J., Grassitelli L., 2016, A&A, 595, A35
Itoh N., Hayashi H., Nishikawa A., Kohyama Y., 1996, ApJS, 102, 411
Ivanova N., 2006, ApJ, 653, L137
Joss P. C., Rappaport S., Lewis W., 1987, ApJ, 319, 180
Kawka A., Vennes S., 2009, A&A, 506, L25
Kawka A., Simpson J. D., Vennes S., Bessell M. S., Da Costa G. S., Marino A. F., Murphy S. J., 2020, MNRAS, 495, L129
Kilic M., Brown W. R., Allende Prieto C., Pinsonneault M. H., Kenyon S. J., 2007, ApJ, 664, 1088
Kilic M., Brown W. R., Allende Prieto C., Agüeros M. A., Heinke C., Kenyon S. J., 2011, ApJ, 727, 3
Kilic M., Brown W. R., Allende Prieto C., Kenyon S. J., Heinke C. O., Agüeros M. A., Kleinman S. J., 2012, ApJ, 751, 141
Knigge C., Baraffe I., Patterson J., 2011, ApJS, 194, 28
Kolb U., Ritter H., 1990, A&A, 236, 385
Korol V. et al., 2020, A&A, 638, A153
Korol V., Rossi E. M., Groot P. J., Nelemans G., Toonen S., Brown A. G. A., 2017, MNRAS, 470, 1894
Kosakowski A., Kilic M., Brown W. R., Gianninas A., 2020, ApJ, 894, 53
Kraft R. P., Mathews J., Greenstein J. L., 1962, ApJ, 136, 312
Kulkarni S. R., van Kerkwijk M. H., 2010, ApJ, 719, 1123
Kupfer T. et al., 2015, A&A, 576, A44
Kupfer T. et al., 2018, MNRAS, 480, 302
Lamberts A., Blunt S., Littenberg T. B., Garrison-Kimmel S., Kupfer T., Sanderson R. E., 2019, MNRAS, 490, 5888
Landau L. D., Lifshitz E. M., 1975, The Classical Theory of Fields. Pergamon Press, Oxford
Langanke K., Martínez-Pinedo G., 2000, Nucl. Phys. A, 673, 481
Li Z., Chen X., Chen H.-L., Han Z., 2019, ApJ, 871, 148
Li Z., Chen X., Chen H.-L., Li J., Yu S., Han Z., 2020, ApJ, 893, 2
Lin J., Rappaport S., Podsiadlowski P., Nelson L., Paxton B., Todorov P., 2011, ApJ, 732, 70
Liu K. et al., 2020, MNRAS, 499, 2276
Ma B., Li X.-D., 2009, ApJ, 691, 1611
Mata Sánchez D., Istrate A. G., van Kerkwijk M. H., Breton R. P., Kaplan D. L., 2020, MNRAS, 494, 4031
Maxted P. F. L. et al., 2014, MNRAS, 437, 1681
Mestel L., 1968, MNRAS, 138, 359
Mestel L., Spruit H. C., 1987, MNRAS, 226, 57
Moore C. J., Cole R. H., Berry C. P. L., 2015, Class. Quantum Gravity, 32, 015014
Oda T., Hino M., Muto K., Takahara M., Sato K., 1994, At. Data Nucl. Data Tables, 56, 231
Panei J. A., Althaus L. G., Chen X., Han Z., 2007, MNRAS, 382, 779
Patterson J., 1984, ApJS, 54, 443
Paxton B., Bildsten L., Dotter A., Herwig F., Lesaffre P., Timmes F., 2011, ApJS, 192, 3
Paxton B. et al., 2013, ApJS, 208, 4
Paxton B. et al., 2015, ApJS, 220, 15
Paxton B. et al., 2018, ApJS, 234, 34
Paxton B. et al., 2019, ApJS, 243, 10
Pelisoli I., Vos J., 2019, MNRAS, 488, 2892
Podsiadlowski P., Rappaport S., Pfahl E. D., 2002, ApJ, 565, 1107
Pols O. R., Tout C. A., Eggleton P. P., Han Z., 1995, MNRAS, 274, 964
Potekhin A. Y., Chabrier G., 2010, Contrib. Plasma Phys., 50, 82
Pylyser E., Savonije G. J., 1988, A&A, 191, 57
Pylyser E. H. P., Savonije G. J., 1989, A&A, 208, 52
Rappaport S., Verbunt F., Joss P. C., 1983, ApJ, 275, 713
Rappaport S., Podsiadlowski P., Joss P. C., Di Stefano R., Han Z., 1995, MNRAS, 273, 731
Refsdal S., Weigert A., 1971, A&A, 13, 367
Reimers D., 1975, Circumstellar Envelopes and Mass-Loss of Red Giant Stars. Springer, New York, p. 229
Réville V., Brun A. S., Matt S. P., Strugarek A., Pinto R. F., 2015, ApJ, 798, 116
Rogers F. J., Nayfonov A., 2002, ApJ, 576, 1064
Rohrmann R. D., Althaus L. G., Kepler S. O., 2011, MNRAS, 411, 781
Salaris M., Cassisi S., 2017, R. Soc. Open Sci., 4, 170192
Saumon D., Chabrier G., van Horn H. M., 1995, ApJS, 99, 713
Schatzman E., 1962, Ann. Astrophys., 25, 18
Serenelli A. M., Althaus L. G., Rohrmann R. D., Benvenuto O. G., 2002, MNRAS, 337, 1091
Shao Y., Li X.-D., 2015, ApJ, 809, 99
Skumanich A., 1972, ApJ, 171, 565
Smith M. A., 1979, PASP, 91, 737
Soberman G. E., Phinney E. S., van den Heuvel E. P. J., 1997, A&A, 327, 620
Sun M., Arras P., 2018, ApJ, 858, 14
Tauris T. M., 2018, Phys. Rev. Lett., 121, 131105
Tauris T. M., Savonije G. J., 1999, A&A, 350, 928
Tauris T. M., van den Heuvel E. P. J., 2006, Formation and Evolution of Compact Stellar X-ray Sources. Cambridge Univ. Press,Cambridge, p. 623
Tauris T. M., Langer N., Kramer M., 2012, MNRAS, 425, 1601
Thoul A. A., Bahcall J. N., Loeb A., 1994, ApJ, 421, 828
Timmes F. X., Swesty F. D., 2000, ApJS, 126, 501
Toloza O. et al., 2019, BAAS, 51, 168
Tutukov A. V., Cherepashchuk A. M., 2020, Phys. Usp., 63, 209
van Kerkwijk M. H., Bergeron P., Kulkarni S. R., 1996, ApJ, 467, L89
van Kerkwijk M. H., Bassa C. G., Jacoby B. A., Jonker P. G., 2005, in Rasio F. A., Stairs I. H., eds, ASP Conf. Ser. Vol. 328, Binary Radio Pulsars. Astron. Soc. Pac.,San Fransisco, p. 357
Van K. X., Ivanova N., 2019, ApJ, 886, L31
Van K. X., Ivanova N., Heinke C. O., 2018, MNRAS, 483, 5595
Webbink R. F., 1984, ApJ, 277, 355
Webbink R. F., Rappaport S., Savonije G. J., 1983, ApJ, 270, 678
Weber E. J., Davis Leverett J., 1967, ApJ, 148, 217
Zhang X., Jeffery C. S., Chen X., Han Z., 2014, MNRAS, 445, 660
Zhu W. W. et al., 2019, MNRAS, 482, 3249
Özel F., Freire P., 2016, ARA&A, 54, 401

APPENDIX A: COMPUTED MODELS

In Tables A1–A3, we present the properties of the computed models at final age (14 Gyr). These three tables correspond to the initial set-ups # 1, 2, and 3 in Table 1, respectively. The CARB magnetic braking prescription (Van & Ivanova 2019) is considered in all cases. For each model we show the initial and final orbital periods, the final masses of the donor and the accreting stars, and the number of hydrogen shell flashes that occurred during evolution. More details are given in the caption of each table.

Table A1. Grid of ELM WDs models considering the use of the enhanced CARB magnetic braking prescription proposed by Van & Ivanova (2019) in the angular momentum evolution of the LMXB systems for various initial orbital periods (third column). The first and second columns show the final donor and accretor masses for each simulation after 14 Gyr, respectively. The fourth column indicates the number of hydrogen shell flashes (#HSF). The fifth column is the frequency of the gravitational wave emitted by the binaries. The sixth and the seventh columns are the dimensionless gravitational wave amplitude and the characteristic strain, respectively. The last column is the merging time due to gravitational radiation. Details on how we calculate the values on the last four columns are provided in the Appendix C. $M_{\rm d,\,i} = 1.0\ {\rm M}_\odot$, $M_{\rm a,\,i} = 1.4\ {\rm M}_\odot$, $Z = 0.02$, and $\beta_{\rm mt} = 0.3$ for all models. Rotation is taking into account in all models.

$M_{\rm d,\,f}$ ($M_\odot$)	$M_{\rm a,\,f}$ ($M_\odot$)	$P_{\rm i}/P_{\rm f}$ (d)	#HSF	$f_{\rm GW}$ (Hz)	$\mathcal{A}$	$h_{\rm c}$	$\tau_{\rm GW}$ (Myr)
0.4067	1.594	300/809	0				
0.3894	1.645	200/609	0				
0.3775	1.677	150/492	0				
0.3609	1.716	100/355	0				
0.3455	1.749	70/254	0				
0.3286	1.783	50/169	0				
0.3146	1.808	40/116	0				
0.2886	1.850	30/55.3	1				
0.2730	1.873	25/32.1	1				
0.2577	1.891	20/18.2	1				
0.2530	1.896	19/15.2	1				
0.2482	1.902	18/12.6	1				
0.2433	1.907	17/10.4	1				
0.2383	1.913	16/8.62	1				
0.2290	1.923	15/7.58	2				
0.2218	1.931	14/6.28	2				
0.2145	1.938	13/5.10	2				
0.2090	1.943	12/4.01	0				
0.2032	1.948	11/3.18	0				
0.1979	1.952	10/2.50	0				
0.1933	1.956	9/1.92	0	1.21×10^{-5}	9.15×10^{-24}	3.57×10^{-22}	9.15×10^{5}
0.1883	1.960	8/1.50	0	1.54×10^{-5}	1.05×10^{-23}	4.65×10^{-22}	4.86×10^{5}
0.1834	1.964	7/1.17	0	1.98×10^{-5}	1.21×10^{-23}	6.06×10^{-22}	2.56×10^{5}
0.1783	1.968	6/0.90	0	2.57×10^{-5}	1.41×10^{-23}	8.02×10^{-22}	1.31×10^{5}
0.1725	1.973	5/0.66	0	3.51×10^{-5}	1.68×10^{-23}	1.12×10^{-21}	5.89×10^{4}
0.1636	1.980	4/0.41	0	5.65×10^{-5}	2.20×10^{-23}	1.85×10^{-21}	1.74×10^{4}
0.1547	1.986	3.5/0.24	0	9.65×10^{-5}	2.98×10^{-23}	3.29×10^{-21}	4.40×10^{3}
0.1456	1.993	3.25/0.082	0	2.82×10^{-4}	5.76×10^{-23}	1.09×10^{-20}	2.65×10^{2}

Table A3. Grid of ELM WDs models considering the use of the enhanced CARB magnetic braking prescription proposed by Van & Ivanova (2019), as in Table A1 but for $\beta_{\rm mt} = 0.8$, element diffusion and rotation is taking into account in all models.

$M_{\rm d,\,f}$ ($M_\odot$)	$M_{\rm a,\,f}$ ($M_\odot$)	$P_{\rm i}/P_{\rm f}$ (d)	#HSF	$f_{\rm GW}$ (Hz)	$\mathcal{A}$	$h_{\rm c}$	$\tau_{\rm GW}$ (Myr)
0.4102	1.451	300/847	1				
0.3936	1.465	200/648	1				
0.3648	1.486	100/386	1				
0.3492	1.496	70/277	1				
0.3312	1.507	50/183	1				
0.3165	1.515	40/124	1				
0.2876	1.528	30/56.2	2				
0.2706	1.535	25/31.3	2				
0.2550	1.541	20/17.6	2				
0.2502	1.542	19/14.7	2				
0.2454	1.544	18/12.1	2				
0.2405	1.545	17/10.0	2				
0.2341	1.548	16/8.60	2				
0.2219	1.551	15/7.73	3				
0.2151	1.553	14/6.31	3				
0.2082	1.555	13/5.09	3				
0.2020	1.556	12/4.06	3				
0.2967	1.558	11/3.19	3				
0.1914	1.559	10/2.53	3				
0.1852	1.560	9/2.03	3	1.14×10^{-5}	7.22×10^{-24}	2.74×10^{-22}	1.30×10^{6}
0.1809	1.561	8/1.59	3	1.46×10^{-5}	8.31×10^{-24}	3.56×10^{-22}	6.91×10^{5}
0.1698	1.564	7/1.40	4	1.65×10^{-5}	8.53×10^{-24}	3.89×10^{-22}	5.23×10^{5}
0.1697	1.564	6/1.00	3	2.31×10^{-5}	1.07×10^{-23}	5.76×10^{-22}	2.13×10^{5}
0.1586	1.566	5/0.815	3	2.84×10^{-5}	1.15×10^{-23}	6.86×10^{-22}	1.32×10^{5}
0.1504	1.568	4/0.489	2	4.73×10^{-5}	1.53×10^{-23}	1.18×10^{-21}	3.55×10^{4}

Table A2. Grid of ELM WDs models considering the use of the enhanced CARB magnetic braking prescription proposed by Van & Ivanova (2019), as in Table A1 but for $M_{\rm d,\,i} = 1.2\,{\rm M}_\odot$.

$M_{\rm d,\,f}$ ($M_\odot$)	$M_{\rm a,\,f}$ ($M_\odot$)	$P_{\rm i}/P_{\rm f}$ (d)	#HSF	$f_{\rm GW}$ (Hz)	$\mathcal{A}$	$h_{\rm c}$	$\tau_{\rm GW}$ (Myr)
0.4212	1.716	300/994	0				
0.4016	1.769	200/737	0				
0.3885	1.802	150/591	0				
0.3705	1.842	100/424	0				
0.3538	1.877	70/301	0				
0.3357	1.913	50/198	0				
0.3209	1.940	40/135	0				
0.2932	1.984	30/63.1	1				
0.2629	2.024	20/22.0	1				
0.2581	2.030	19/18.5	1				
0.2532	2.036	18/15.3	1				
0.2482	2.042	17/12.6	1				
0.2432	2.048	16/10.3	1				
0.2378	2.054	15/8.60	1				
0.2289	2.063	14/7.49	2				
0.2224	2.070	13/6.18	2				
0.2160	2.076	12/5.04	2				
0.2111	2.081	11/4.05	0				
0.2062	2.085	10/3.25	0				
0.2014	2.090	9/2.60	0				
0.1969	2.093	8/2.10	0	1.10×10^{-5}	9.20×10^{-24}	3.43×10^{-22}	1.09×10^{6}
0.1925	2.097	7/1.70	0	1.36×10^{-5}	1.04×10^{-23}	4.30×10^{-22}	6.33×10^{5}
0.1882	2.101	6/1.37	0	1.69×10^{-5}	1.17×10^{-23}	5.42×10^{-22}	3.63×10^{5}
0.1839	2.104	5/1.10	0	2.10×10^{-5}	1.33×10^{-23}	6.85×10^{-22}	2.07×10^{5}
0.1790	2.108	4/0.870	0	2.66×10^{-5}	1.52×10^{-23}	8.79×10^{-22}	1.13×10^{5}
0.1730	2.112	3/0.636	0	3.64×10^{-5}	1.81×10^{-23}	1.23×10^{-21}	5.08×10^{4}
0.1609	2.121	2/0.278	0	8.33×10^{-5}	2.94×10^{-23}	3.01×10^{-21}	5.98×10^{3}

APPENDIX B: POLYNOMIAL FITS

In Table B1, we show polynomial fits to the final ELM WD mass ($M_{\rm d,\,f}$) as a function of the initial orbital period ($P_{\rm i}$) for our models in the form of $y = {\rm A} + {\rm B}x + {\rm C}x^2 + {\rm D}x^3 + {\rm E}x^4$. The quality of the fits is indicated by the coefficient of determination (R^2).

Table B1. Coefficients for the third degree polynomials that best fit the final ELM WD mass ($M_{\rm d,\,f}$) as a function of the initial orbital period ($P_{\rm i}$), i.e. $M_{\rm d,\,f}(P_{\rm i})$. The fits are only valid for $M_{\rm d,\,f} < 0.35$ M$_\odot$. The first column shows the set-up, as in Table 1. Columns two to six shows the coefficients in the form $y = {\rm A} + {\rm B}x + {\rm C}x^2 + {\rm D}x^3 + {\rm E}x^4$, as discussed in the text. The last column shows the coefficient of determination (R^2).

#	A	B	C	D	E	R^2
1	1.3209×10^{-1}	7.9247×10^{-3}	-1.0617×10^{-4}	6.2084×10^{-7}	-1.2798×10^{-9}	0.9977
2	1.4805×10^{-1}	7.0866×10^{-3}	-8.8185×10^{-5}	4.9107×10^{-7}	-9.7816×10^{-10}	0.9980
3	1.1415×10^{-1}	9.2348×10^{-3}	-1.3749×10^{-4}	9.0360×10^{-7}	-2.0138×10^{-9}	0.9972

APPENDIX C: GRAVITATIONAL WAVES

The LISA sensitivity band frequency is from 10^{-1} to 10^{-5} Hz, with a peak around 4 mHz. We can approximate the frequency of the gravitational wave emitted by the binary systems as $f_{\rm GW} = 2/P_{\rm f}$, indicating that systems of ELM WDs with lower mass will populate the region of greatest sensitivity.

In order to estimate the gravitational radiation emitted by our models, we adopt the same approach as in Kupfer et al. (2018), Li et al. (2020), and Korol et al. (2020). We choose to present our estimates in terms of the characteristic strain since the difference between the source signal and the sensitivity of the detector is directly related to the signal-to-noise ratio (Moore, Cole & Berry 2015). Thus, with the data available in Appendix A, it is immediate to obtain estimates for other values of observation time, distance, and also to calculate the signal-to-noise ratio for specific configurations of the detectors.

The signal-to-noise ratio is directly proportional to the dimensionless gravitational wave amplitude, which after averaging over inclination, sky-location, and amplitude reads

$$\mathcal{A} = 2\pi^{2/3}\frac{G^{5/3}}{c^4}\frac{\mathcal{M}^{5/3} f_{\rm GW}^{2/3}}{d}, \tag{C1}$$

where $\mathcal{M} = (M_{\rm d,f}M_{\rm a,f})^{3/5}(M_{\rm d,f} + M_{\rm a,f})^{-1/5}$ is the chirp mass and d is the distance of the binary system to the Sun.

For an inspiralling binary system that emits monochromatic radiation, the characteristic strain is

$$h_{\rm c} = \sqrt{N_{\rm cycle}}\mathcal{A}, \tag{C2}$$

where $N_{\rm cycle} = f_{\rm GW}T_{\rm obs}$ give us the total orbital periods observed over the detector's operation time. For the purpose of facilitating comparisons and conversions, in this work we fix the distances to $d = 1$ kpc and adopt the nominal LISA mission duration time of $T_{\rm obs} = 4$ yr.

When compared to the equation (2) of Brown et al. (2020a) in the case of inclination $i = 90^\circ$, our calculated characteristic strain is 1.42 times larger; or, alternatively, equivalent to $i \approx 66^\circ$.

Finally, starting from equation (2) in Kraft, Mathews & Greenstein (1962), we obtained the following expression for the merging time due to gravitational radiation[5]

$$\tau_{\rm GW} = 47100\mathcal{M}^{-5/3}P_{\rm f}^{8/3}\ {\rm Myr}, \tag{C3}$$

where again the chirp mass and the orbital period should be given in solar masses and days, respectively. Since the expression above accounts only for the angular momentum loss due to the gravitational radiation ($\dot{J}_{\rm gr}$), the merging time should be greater in models that may have significant contributions from other processes of loss of angular momentum (see equation 1). In our models, this is the case when $P_{\rm i} \gtrsim 25$ d, where $\dot{J}_{\rm ml}$ is the term that has the greatest contribution at the end of evolution.

[5]We would like to point out that the multiplicative constant that we found is slightly different from that found by Brown et al. (2020a).

This paper has been typeset from a TEX/LATEX file prepared by the author.

APPENDIX E – Other publication

Title: Phase transitions in neutron stars (Dexheimer et al., 2018).

Journal: International Journal of Modern Physics E

Vol. 27, No. 11, 1830008 (2018) Review Article

DOI: 10.1142/S0218301318300084

Received: 7 September 2018. Revised: 16 November 2018. Accepted: 26 November 2018. Published: 31 December 2018.

arXiv: arXiv:1901.03252

adsabs: 2018IJMPE..2730008D

International Journal of Modern Physics E
Vol. 27, No. 11 (2018) 1830008 (13 pages)

DOI: 10.1142/S0218301318300084

World Scientific
www.worldscientific.com

Phase transitions in neutron stars

V. Dexheimer*,§, L. T. T. Soethe†, J. Roark*, R. O. Gomes‡,
S. O. Kepler† and S. Schramm‡

*Department of Physics, Kent State University,
Kent OH 44242, USA

†Instituto de Física,
Universidade Federal do Rio Grande do Sul,
Av. Bento Gonçalves 9500 Porto Alegre,
Rio Grande do Sul 91501-970, Brazil

‡Frankfurt Institute for Advanced Studies,
Frankfurt am Main, Germany
§vdexheim@kent.edu

Received 7 September 2018
Revised 16 November 2018
Accepted 26 November 2018
Published 31 December 2018

In this paper, we review the most common descriptions for the first-order phase transition to deconfined quark matter in the core of neutron stars. We also present a new description of these phase transitions in the core of proto-neutron stars, in which more constraints are enforced so as to include trapped neutrinos. Finally, we calculate the emission of gravitational waves associated with deconfinement phase transitions, discuss the possibility of their detection, and how this would provide information about the equation of state of dense matter.

Keywords: Neutron star; quark deconfinement; gravitational waves.

PACS Number(s): 26.60.Dd, 25.75.Nq, 26.60.Kp, 97.10.Nf, 97.10.Pg, 04.30.Db

1. Introduction

Neutron stars (NSs) are a natural laboratory for the study of dense matter. Their interiors cover a large range of densities going from about $1\,\mathrm{g/cm^3}$ in the atmosphere to about $10^{15}\,\mathrm{g/cm^3}$ — a number density of about 1 baryon per $\mathrm{fm^3}$ — in the stellar core. The latter value corresponds to a volume per baryon less than the size of a nucleon, implying that at such densities baryons overlap. This can be understood as a strong indication of deconfined quark matter in the interior of NSs. From a stability point of view, it was long ago established that 3-flavored quark matter could be more energetically stable than hadronic matter[1,2] and, more recently, the same was shown for 2-flavored quark matter.[3]

After the first work proposing pure quark stars in 1970,[4] Glendenning started the discussion of conserved charges in hybrid hadronic-quark stars in 1992. He highlighted the fact that, if allowed, a mixture of phases will take place when first-order phase transitions take place.[5] Consequently, the pressure is not constant in the extended mixture, as the concentrations of the substances change together with the chemical potentials associated with the constraints (two in this case, global baryon number and global electric charge). This became known as Gibbs construction, as equilibrium conditions require the Gibbs free energy per particle (i.e., the baryon chemical potential), temperature and pressure to be equal in both phases within the mixture. Finally, a volume fraction of each substance can be calculated at any point in the mixture which fulfills the globally required constraints. Note that previous works had studied mixtures of hadronic and quark phases, although not in the context of astrophysics.[5–7]

If charge neutrality is imposed locally in each phase, there is no mixture of phases. The pressure is constant, in the sense that it relates to the value of the chemical potential associated with the conserved quantity (which is different in each phase). The Gibbs free energy per particle, temperature, and pressure are still equal in both phases. This is known as Maxwell construction, as it does not allow the pressure to change as a function of number density. But, as a result, constant pressure means that this region does not occupy a physical space under the influence of gravity in a star (unlike the mixture of phases). More recently, this discussion appeared again in the literature in a more general form and using the terms congruent and noncongruent referring to Maxwell and Gibbs constructions, including two or more constraints in the context of astrophysics and heavy-ion collision physics.[8–10]

The determination of the way phase transitions take place in nature, with local or global charge neutrality (and in the latter also the extent of mixed phase), depends directly on the surface tension between the two phases. For deconfinement phase transitions, surface tension has been calculated, but shown to be model dependent.[11–20] The description of hybrid stars under both scenarios of global and local charge neutrality has been studied in many works in the past, and also recently used to constrain even further the equation of state (EoS) of nuclear matter in attempts to reproduce tidal deformability measurements from neutron star mergers.[21–28] In this paper, we review some of the points related to phase transitions already raised in our previous works, but focusing on their relation with the possibility of identifying such phase transitions through the detection of gravitational waves (GW's).

We have recently and definitively entered the age of gravitational wave astrophysics with the discoveries of black hole and NS mergers made by the LIGO and Virgo collaborations.[29,30] The next runs of the interferometers will be able to detect GW's of smaller and smaller amplitudes, raising the possibility of detecting even more subtle events,[31] such as the ones described in Sec. 4 of this work. This requires prior knowledge of the signal waveform, making the identification of possible sources

and wave frequencies a relevant problem in the detection strategy. Using the EoS's presented in this paper, we estimate the initial amplitude and frequency of the gravitational waves (GW's) emitted by a NS that undergoes a phase transition going from a purely hadronic star to a hybrid one with the same number of baryons. Note that this is different from what has been recently presented in Ref. 32 or previously in Ref. 33, where different EoS's were used to generate purely hadronic and purely quark branches. Finally, we estimate the decay of GW amplitudes with time for some selected pulsars.

2. Microscopic Description

As matter in the inner core of NS's is very dense but strongly interacting, it cannot be currently described by first principle theories. Alternatively, we can rely on effective models, which after being calibrated to work in the desired regime of energies, can produce reliable results concerning the matter EoS and associated particle population. For this purpose, we choose the Chiral Mean Field (CMF) model, which is based on a nonlinear realization of the SU(3) sigma model.[34] It is an quantum relativistic model that describes hadrons (nucleons and hyperons) and 3 light flavors of quarks interacting via meson exchange, as a way to describe the attractive and repulsive components of the strong force.[9,35] The model is constructed to be chirally-invariant, in a manner similar to the linear-sigma model, as the particle masses originate from (instead of being modified by) interactions with the medium and, therefore, decrease at high densities/temperatures. The nonlinear realization refers to the kind of chiral transformation imposed, which has the pseudo-scalar mesons as parameters. This setup results in a framework in which there is no distinction between left- and right-handed space and, therefore, in a larger freedom in the calculation of the mesonic couplings. The mesons included are the lowest mass ones that are scalar iso-scalar, vector iso-scalar, scalar iso-vector, and vector iso-vector (with and without hidden strangeness).

After applying the mean-field theory approximation, the hadronic coupling constants of the model were calibrated to reproduce the vacuum masses of baryons and mesons, and were fitted to reproduce nuclear constraints for isospin symmetric matter (together with the symmetry energy) at saturation with reasonable values for the hyperon potentials. The quark coupling constants were constrained using lattice QCD data at zero baryon chemical potential,[36,37] as well as information about the the remaining QCD phase diagram for isospin asymmetric and symmetric matter. The latter include the point where the coexistence line ends at the zero-temperature axis and the position of the critical point,[38] among others. As a consequence, this formalism reproduces the nuclear liquid-gas phase transition as well as the deconfinement/chiral symmetry restoration phase transitions expected to be found in the QCD phase diagram, as shown in Fig. 1. As a final test, we have used perturbative QCD (PQCD) results, calculated by taking into account beta equilibrium and charge neutrality,[39] in order to determine until which density/chemical potential

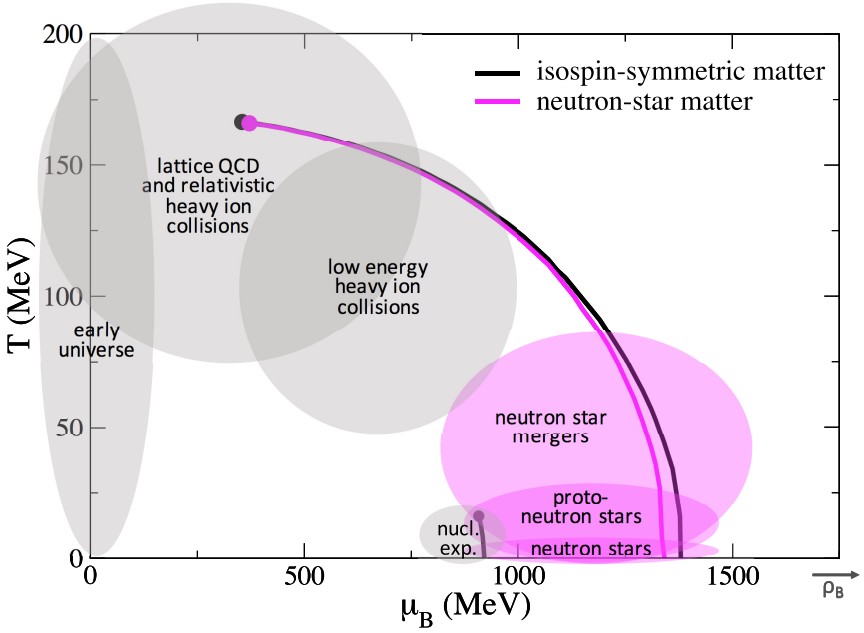

Fig. 1. QCD phase diagram (temperature versus baryon chemical potential) resulting from the CMF model with lines indicating first-order phase transition coexisting lines. The line on the bottom stands for the nuclear liquid-gas transition, while the lines on the top-right stand for the chiral-symmetry restoration/quark deconfinement transitions. The dots mark the respective critical end-points. The shaded regions exemplify relevant scenarios.

our model is valid. We found that our model is fully consistent with PQCD in the whole regime of densities achieved inside NS's and proto-neutron stars (PNS's).[10,39]

The lines in Fig. 1 represent first-order transitions and the dots mark the critical end-points. Isospin-symmetric matter refers to zero-isospin matter with zero net strangeness, as the one created in heavy-ions collisions or any nuclear experiment performed in the laboratory. NS matter stands for charged neutral matter in chemical equilibrium, such as the one inside the core of neutron stars. The shaded regions exemplify in which regimes these kinds of matter can exist. Other scenarios showed in the figure (and colored accordingly) correspond to matter created in the early universe, also isospin symmetric with zero net strangeness, and matter created in supernova explosions and neutron star mergers, also charge neutral. Chemical equilibrium is not establish immediately in supernovae and stellar mergers, but instead these events present a temporary large lepton fraction. For the case of proto-neutron star matter, a fixed lepton fraction discussion will be presented in the following.

We model PNS matter by imposing another constraint to characterize the neutrinos trapped by the dense and hot medium, lepton fraction. This is the ratio of the amount of electrons/electron neutrinos to the amount of baryons and it is fixed according to supernova simulations to be $Y_l = 0.4$.[40,41] The extra constraint has the effect of suppressing the hyperons (due to the presence of negatively charged electrons) and pushing the phase transition to higher chemical potentials (as it makes the quark matter EoS softer than the hadronic one), with respect to the NS case. The results from this description can be seen in the left panel of Fig. 2 for the

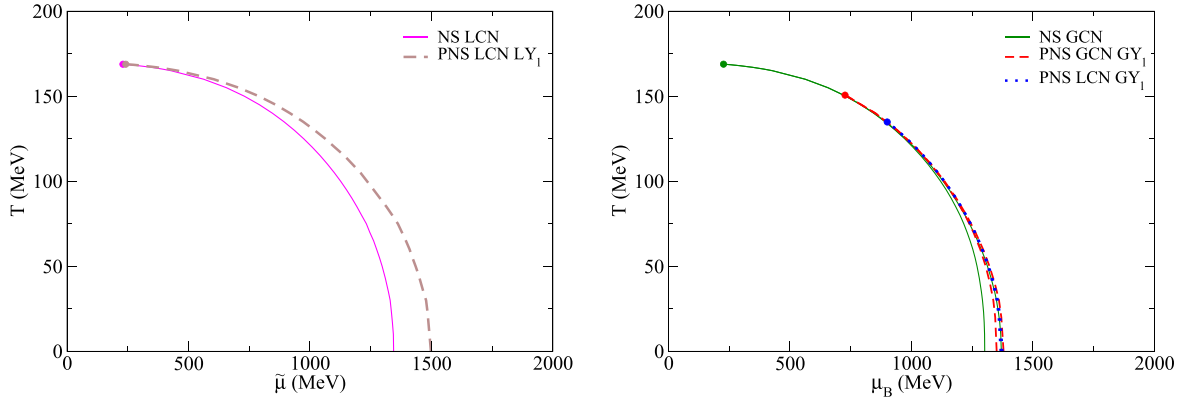

Fig. 2. QCD phase diagrams, as in Fig. 1, but including one extra constraint to describe proto-neutron stars. In the left panel, electric charge neutrality and lepton fraction are enforced locally. In the right panel one or both constraints are enforced globally, creating regions with mixtures of phases.

case that all constraints (except baryon number) are enforced locally in each phase. Although, this locally enforced condition might be the case for electric charge if the surface tension is large,[18,19] it is not the case for lepton fraction. This is because there is no long range force associated with this quantity (such as Coulomb's force for electric charge),[8] what leads us to refer to this case as "forced-congruent", in which case the Gibbs free energy $\tilde{\mu}$ is not the baryon chemical potential, but a function of the lepton chemical potential $\tilde{\mu} = \mu_B + Y_l \mu_l$.

The right panel of Fig. 2 illustrates what happens if one or two constraints (in addition to baryon number) are allowed to be conserved globally. In this description, mixtures of phases appear, although PNS matter possess much smaller mixtures of phases than those of NS matter (i.e., they extend through much smaller ranges of chemical potentials and smaller ranges of densities). In the case of global lepton fraction conservation, specially when electric charge neutrality is constrained locally, the mixtures of phases become so narrow at large temperatures that it become numerically impossible to find them. In practice, this would mean that these mixtures of phases would not impact significantly any stellar properties. Note that finite size effects tend to shrink the size of mixtures of phases even further.[42,43]

3. Macroscopic Description

Although thermal energy is negligible in NS's, this is not the case for PNS's, as they can reach tens of MeV temperature in their centers.[44,45] To simulate that, we add the additional (local) constraint of fixed entropy density per baryon density $S_B = 2$ in our PNS EoS's. It results in a temperature gradient in stars that, as a consequence of fixing entropy per baryon locally and not globally, has a small (practically negligible) jump across the phase transition, as discussed in detail in Ref. 46.

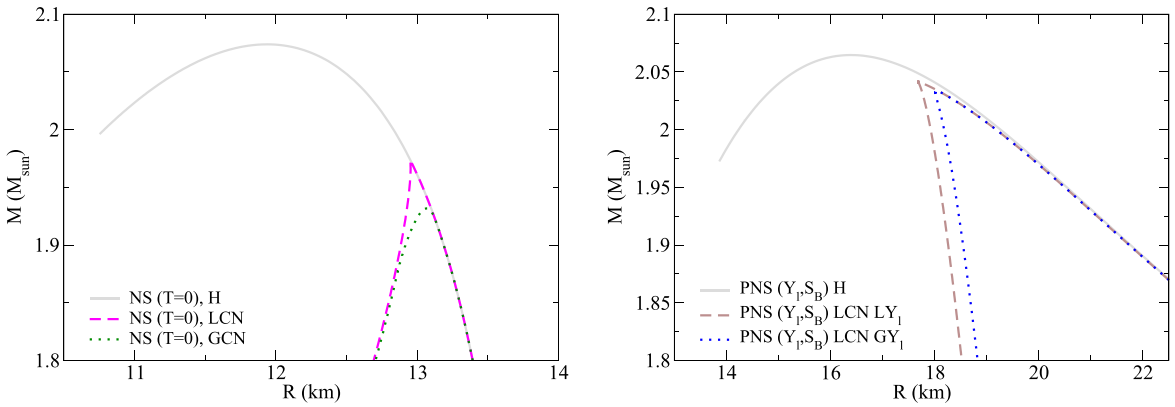

Fig. 3. Solution of TOV equations showing stellar masses and radii for neutron stars (left panel) and proto-neutron stars with fixed entropy density per baryon density (right panel). The following cases are shown: when quark matter is artificially suppressed (H), when quark matter is allowed and electric charge neutrality is constrained locally (LCN) or globally (GCN) and lepton fraction is constrained locally (LCN) or globally (GCN).

Next, we use our different NS and PNS EoS's in the Tolman–Oppenheimer–Volkoff (TOV) equations to find a family of stellar solutions for each EoS, as shown in Fig. 3. For NS's, we show three curves, for hadronic matter only (H) and with a first order phase transition assuming local charge neutrality (LCN) or global charge neutrality (GCN). In the case with the local constraint, stars that reach the threshold central density for the phase transition are unstable but, in the case with the global constraint, there is an extended mixture of phases that reaches about 2 km of radius in the most massive stable star. For PNS's, we show again three curves, for hadronic matter only (H), with a first order phase transition assuming local charge neutrality and lepton fraction (LCN LGY$_l$), and with a first order phase transition assuming local charge neutrality and global lepton fraction (LCN GY$_l$). In the case with both local constraints, stars that reach the threshold central density for the phase transition are unstable but, as before, in the case with the global constraint, there is an extended mixture of phases that reaches about 1 km of radius in the most massive stable star. The case in which all constraints are conserved globally for PNS's is not shown in the figure, as it is very demanding numerically and does not differentiate dramatically from the LCN GY$_l$ case.

It is important to note that, in all hybrid PNS cases, there are quarks present in stable stars. This is because the CMF model allows for the existence of soluted quarks in the hadronic phase and soluted hadrons in the quark phase at finite temperature. This is discussed in detail in Ref. 46. Regardless, quarks will always give the dominant contribution in the quark phase, and hadrons in the hadronic phase and the phases can be distinguished from one another though their order parameters. We assume that this inter-penetration of quarks and hadrons (that increases with temperature) is indeed physical, and is required to achieve the crossover transition known to take place at small chemical potential values.[47]

4. Gravitational Wave Emission Due to Phase Transition

Even though only GW's from NS's in a binary system have been detected until 2018,[29,30] it is predicted that isolated NS's could also irradiate detectable GW's through different processes. In particular, newly formed neutron stars that reach high enough central densities in their cores could undergo a phase transition to deconfined quark matter. In this case, the new hybrid configurations would be more compact (than their purely hadronic counterparts) but have the same number of baryons. Such dense metastable hadronic stars could be formed, for example, by the merging of two low mass neutron stars, two white dwarfs, or a combination of both.[48–50]

The conversion from a purely hadronic to a hybrid star would decrease the star's gravitational mass ΔM_G and, therefore, also gravitational energy $\Delta M_G c^2 = (M_G^{\mathrm{Hyb}} - M_G^{\mathrm{Had}})c^2 = \Delta E_T$. Among other things, this energy can excite pulsating modes of the star. NS's have a large number of distinct vibrational modes, being the fundamental (f) mode, in general, the one that radiates most mechanical energy.[51,52] A star of mass M and size R has a natural GW frequency of $f = (1/4\pi)\sqrt{3GM/R^3}$.[53] So, considering typical NS values, we expect to detect waves in the range of 1–3 kHz when using the prescription from Ref. 54 and considering that a deconfinement phase transition occurs. Because it is a sudden event, this phenomenon is usually classified as a burst, although the damping of the oscillation of the star's surface may in some cases last for years, as we shall discuss later.

Assuming the quadrupole moment of an arbitrary mass distribution Q_{ij}, the energy lost via gravitational radiation is given by the time derivative of the energy (see, e.g., Ref. 55):

$$-\frac{\mathrm{d}E}{\mathrm{d}t} = \frac{G}{45c^2}\left(\frac{\partial^3 Q_{ij}}{\partial t^3}\right)^2, \tag{1}$$

which provides the mean luminosity of the gravitational wave emitted L_{GW}. We are interested in the fundamental mode, which is characterized by being a surface mode between the star interface and its surroundings.[51] Then, by conceiving a nonradial axisymmetric oscillation in a sphere of a given radius, we can express an oscillation at its surface by describing an expansion of $r(\theta)$ Ref. 56. If only linear terms are considered, the expansion is reduced to its first two terms, leading up to the relation:

$$L_{\mathrm{GW}} = \frac{2E_2}{\tau}, \tag{2}$$

where E_2 represents the approximation in the energy and τ is the damping time scale, which is expected to be relatively large for the f mode, indicating a slow damping. Then, if we consider that most of the mechanical energy is in the f

mode, the gravitational strain amplitude can be written as[57]:

$$h_0 = \frac{4}{2\pi f_0 r}\left(\frac{G\Delta E}{\tau c^3}\right)^{1/2}, \tag{3}$$

where r is the distance to the source and h_0 the amplitude measured at distance r.

The frequency of the fundamental mode (in kHz), is well fitted by[58]:

$$f_0 \approx 0.17 + 2.30\sqrt{\left(\frac{10\,\mathrm{km}}{R}\right)^3\left(\frac{M}{1.4\mathrm{M}_\odot}\right)} \tag{4}$$

and the damping time scale by GW emission is[56]:

$$\tau = 1.8\left(\frac{\mathrm{M}_\odot}{M}\right)\left(\frac{P^4}{R^2}\right), \tag{5}$$

where P is the period of rotation of the star (in ms).

Before using the change in gravitational stellar mass due to the deconfinement phase transition ΔM_G as available energy as in Eq. (3), we must keep in mind that not all the energy released in the transition is converted into mechanical energy. Instead, some of it is dissipated into thermal, shear and bulk viscosity processes. Thus, we must introduce an efficiency term η in this relation. Early works[59–61] suggest $10^{-3} \lesssim \eta \lesssim 0.5$, while more recent calculations[62] estimate $10^{-7} \lesssim \eta \lesssim 10^{-5}$, depending on the model used. Given the large uncertainty in this parameter and the difficulty of evaluating the best value, we scale our relation with an intermediate value $\eta = 10^{-4}$.

In our setup, the initial amplitude of the measured GW depends on mass, radius, and rotation period of the star; the distance between the star and Earth; and also of the energy released via the phase transition. Although the TOV equations only describe spherical stars, any corrections to that due to rotation and magnetic fields would deform further the star and, therefore, cause a larger emission of GWs. For each star (calculated with a given EoS and central density), rotation period and distance of the source are additional parameters that will differentiate the initial amplitude of the GW. Here, we use data from 2572 pulsars cataloged in Ref. 63.

The previous equations also allow us to describe the wave oscillation behavior in time, which is given by[56,61]:

$$h(t) = h_0 e^{-(1/\tau - i2\pi f_0)t}. \tag{6}$$

In the case of an interferometric detector with an arm of length L, $h = \Delta L/L$ is measured, where ΔL is a small change in the length L caused by the GW. Using this framework, we estimate the GW amplitude when metastable hadronic stars go through deconfinement phase transitions in two cases, first, assuming stars that are cold and in chemical equilibrium (previously referred to as NSs) and, second, assuming stars to be hot and with trapped neutrinos (previously referred to as PNSs).

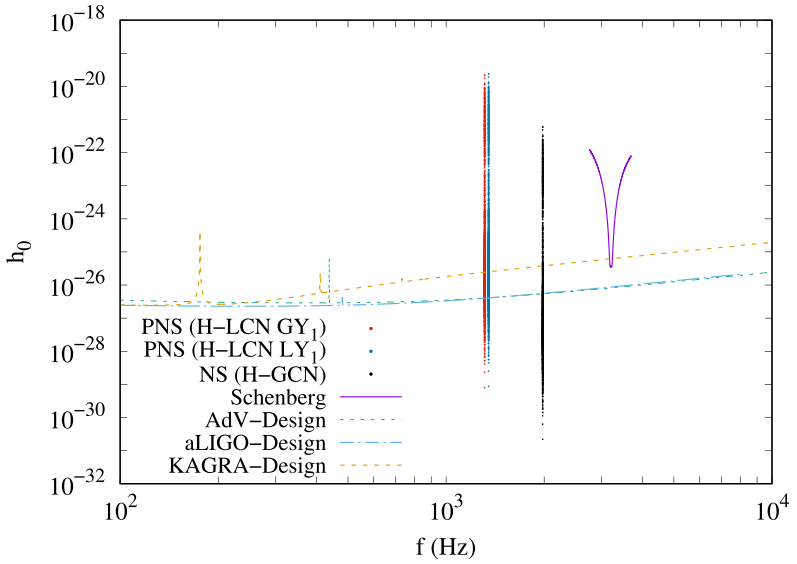

Fig. 4. Initial amplitude of GW's and respective frequencies when phase transitions take place in NS's allowing the existence of a mixed phase and in PNS's allowing for the existence of a mixed phase, or not. Different lines show the sensitivity of several gravitational-wave detectors.[64,65]

Figure 4 shows the results of our estimates of h_0 in comparison with the sensitivity of different GW detectors. Note that the GW amplitude $h_0 \propto \Delta E^{1/2}$, $1/r, R^{5/2}, 1/P^2$. The quantities ΔE and R vary considering all the possible NS's that can undergo a deconfinement phase transition (from the hadronic to the hybrid branch with a mixed phase in the left panel in Fig. 3) at fixed baryon number. They generate very similar results. The case without a mixed phase is not considered as it does not produce stable hybrid NS's. For PNSs or, to be more specific, stars that follow more closely PNS conditions such as finite temperature and fixed lepton fraction effects, the quantities ΔE and R vary considering only massive stars from the hadronic to the hybrid branch with and without a mixed phase (see right panel in Fig. 3) that can go through a deconfinement phase transition at fixed baryon number. The case without a mixed phase produces stable stars with quarks only due to the finite temperature assumed in PNSs. Less massive stars are not considered, as they generate lower energy release upon transitioning.

As explained above, the distance r and the pulsar period P are varied according to available pulsar data. As a result, the pulsars with the largest h_0 are the ones with smallest periods and/or which are closest to Earth. We estimate that h_0 varies from 2.2×10^{-31} to $5.9 \times 10^{-22}\,(\eta/10^{-4})$ and the frequency is around 2.0 kHz for NSs. For PNS's, h_0 varies from 8.0×10^{-30} to 2.4×10^{-20} $(\eta/10^{-4})$ and the frequency is around 1.3 kHz. In the case of PNSs, the estimated initial signal for more than two thousand (83%) pulsars are above the sensitivity limit of the LIGO and Virgo detectors, and more than one thousand (54%) for KAGRA detector, depending on $\eta/10^{-4}$. For NS, there are six hundred (25%) for LIGO and Virgo, and four hundred (17%) for KAGRA. Note that the GW frequency $f \propto 1/R^{3/2}$ and $M^{1/2}$ only, so this results could be in principle used to distinguish among different EoS's and, in

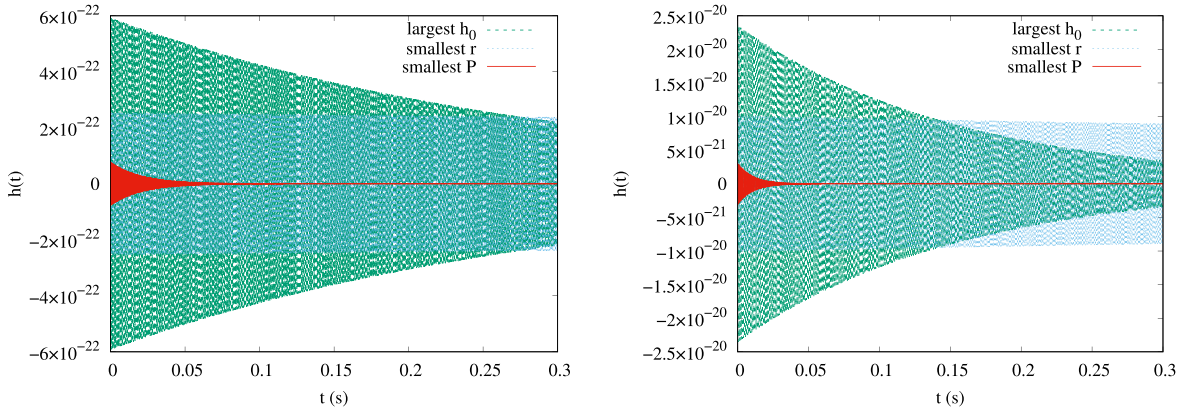

Fig. 5. Decay of GW amplitude with time for three selected pulsars for NS H-LCN (left panel) and PNS H-LCN LY$_l$ (right panel) conditions, the one with the highest estimated amplitude ($h_0 = 1.9 \times 10^{-21}$), the one with the shortest rotation period ($P = 1.396$ ms), and the closest to the Earth ($r = 90$ pc).

the case that the stellar mass is known, the stellar radius of neutron stars. This in return could provide information about the interior of the stars.

Another point that must be highlighted is the order of magnitude of the damping time scale τ, as it is proportional to the fourth power of P. Typical pulsars period values can lead to a τ of some milliseconds or several years, making the detection in the latter case very difficult, given the time of operation of the detectors. This becomes clear in Fig. 5, where we present the wave pattern for three pulsars selected from the catalog: the one with the highest estimated amplitude ($h_0 = 1.9 \times 10^{-21}$), the one with the shortest rotation period ($P = 1.396$ ms) and the closest to the Earth ($r = 90$ pc). Here, both r and P are very important, but it is their combination that determines the highest amplitude of the GW signal. Pulsars with slow rotation rate, in addition to tending to decrease the amplitude of the GW, have a very long damping time and would require a very extensive operating time for the detectors. This is also the case with the pulsar with smaller distance. The left and right figure panels of Fig. 5 show results for NS H-LCN and PNS H-LCN LY$_l$ conditions, respectively. In the case of PNS's with global Y$_l$, the results are similar to what is presented in the right panel of Fig. 5, but with slightly reduced overall amplitude magnitude. Note that although pulsars with large damping time are not of interest for detection, they are of great importance for the establishment of background noise, since their signal remains practically constant for a long time.

5. Conclusions

In this work, we have revisited the topic of phase transitions in the interior of neutron and proto-neutron stars making use of a realistic equation of state that accounts for hadronic and quark degrees of freedom. Different possible scenarios, in which global and local charge neutrality and lepton fraction constraints were imposed. The possibility of deconfinement to quark matter in the core different stars was investigated. Although mixtures of phases extend through larger portions

of cold deleptonized neutron stars, in our framework, quarks are present in hot stars even outside these mixtures. As a consequence, stars at all stages of evolution can present quarks in extended portions (if they possess large enough central density). When we compared massive but purely hadronic stars (that had the quarks suppressed artificially), and respective hybrid stars (with same number of baryons), they presented distinguished compactnesses, for all the conditions analyzed.

We then investigated the possibility of detecting GWs emitted in the case of metastable hadronic stars undergoing a deconfinement phase transition and converting to hybrid stars. This could be the case of isolated newly formed massive neutron stars formed, for example, by the merger of low mass stars. In this case, the phase transition from a hadronic star to a more compact hybrid star with the same number of baryons would release gravitational energy and excite pulsation modes that could eventually be detected. Most of the uncertainties in our predictions refer more to the amplitude of the detected GWs and less to their frequency, which is mainly equation of state dependent. In this way, a possible detection will be able to provide solutions to outstanding issues regarding dense matter, such as which degrees of freedom exist in the center of neutron stars, in addition to an alternative way to measure stellar radii, complimentary to electromagnetic wave measurements.

Although not unique, our scenario predicts gravitational waves that could be measured in the near future. Our results are consistent for example with the ones from Ref. 66, which uses simple equations of state but a very sophisticated treatment of the oscillations including simulations performed using a code that solves the general relativistic hydrodynamic equations and includes rotation. We must emphasize that we used in our work an integration time of 1 month for the GW detectors and an efficiency of $\eta/10^{-4}$ for the relation between released gravitational energy and available energy for GW emission. Modifying η will modify our results for the amplitudes by a factor $\eta^{1/2}$. Moreover, for simplicity we consider only the fundamental mode of oscillation, but we point out that the addition of other vibrational modes can increase the values of GWs amplitude. Ref. 67, for example, assesses the gravitational waveform that would result from r-mode driven spindown of magnetized neutron stars.

Acknowledgments

Support comes from Conselho Nacional de Desenvolvimento Científico e Tecnológico (CNPq-Brazil) and by the National Science Foundation Under Grant PHY-1748621.

References

1. A. R. Bodmer, *Phys. Rev. D* **4** (1971) 1601.
2. E. Witten, *Phys. Rev. D* **30** (1984) 272.
3. B. Holdom, J. Ren and C. Zhang, *Phys. Rev. Lett.* **120** (2018) 222001.
4. N. Itoh, *Prog. Theor. Phys.* **44** (1970) 291.
5. N. K. Glendenning, *Phys. Rev. D* **46** (1992) 1274.

6. B. Lukacs, J. Zimanyi and N. L. Balazs, *Phys. Lett. B* **183** (1987) 27.
7. U. W. Heinz, K. S. Lee and M. J. Rhoades-Brown, *Mod. Phys. Lett. A* **2** (1987) 153.
8. M. Hempel, G. Pagliara and J. Schaffner-Bielich, *Phys. Rev. D* **80** (2009) 125014.
9. M. Hempel, V. Dexheimer, S. Schramm and I. Iosilevskiy, *Phys. Rev. C* **88** (2013) 014906.
10. J. Roark and V. Dexheimer, arXiv:1803.02411 [nucl-th].
11. M. G. Alford, K. Rajagopal, S. Reddy and F. Wilczek, *Phys. Rev. D* **64** (2001) 074017.
12. D. N. Voskresensky, M. Yasuhira and T. Tatsumi, *Nucl. Phys. A* **723** (2003) 291.
13. T. Maruyama, S. Chiba, H.-J. Schulze and T. Tatsumi, *Phys. Rev. D* **76** (2007) 123015.
14. T. Maruyama, S. Chiba, H.-J. Schulze and T. Tatsumi, *Phys. Lett. B* **659** (2008) 192.
15. L. F. Palhares and E. S. Fraga, *Phys. Rev. D* **82** (2010) 125018.
16. M. B. Pinto, V. Koch and J. Randrup, *Phys. Rev. C* **86** (2012) 025203.
17. N. Yasutake, H. Chen, T. Maruyama and T. Tatsumi, *J. Phys. Conf. Ser.* **665** (2016) 012068.
18. G. Lugones, A. G. Grunfeld and M. Al Ajmi, *Phys. Rev. C* **88** (2013) 045803.
19. A. F. Garcia and M. B. Pinto, *Phys. Rev. C* **88** (2013) 025207.
20. G. Lugones and A. G. Grunfeld, *Phys. Rev. C* **95** (2017) 015804.
21. D. Bandyopadhyay, S. A. Bhat, P. Char and D. Chatterjee, *Eur. Phys. J. A* **54** (2018) 26.
22. V. Paschalidis, K. Yagi, D. Alvarez-Castillo, D. B. Blaschke and A. Sedrakian, *Phys. Rev. D* **97** (2018) 084038.
23. E. Annala, T. Gorda, A. Kurkela and A. Vuorinen, *Phys. Rev. Lett.* **120** (2018) 172703.
24. R. Nandi and P. Char, *Astrophys. J.* **857** (2018) 12.
25. E. R. Most, L. R. Weih, L. Rezzolla and J. Schaffner-Bielich, *Phys. Rev. Lett.* **120** (2018) 261103.
26. G. F. Burgio, A. Drago, G. Pagliara, H. J. Schulze and J. B. Wei, *Astrophys. J.* **860** (2018) 139.
27. I. Tews, J. Margueron and S. Reddy, arXiv:1804.02783 [nucl-th].
28. D. E. Alvarez-Castillo, D. B. Blaschke, A. G. Grunfeld and V. P. Pagura, arXiv: 1805.04105 [hep-ph].
29. LIGO Scientific and Virgo (Collabs. B. P. Abbott *et al.*), *Phys. Rev. Lett.* **116** (2016) 061102.
30. LIGO Scientific and Virgo Collabs. (B. P. Abbott *et al.*), *Phys. Rev. Lett.* **119** (2017) 161101.
31. B. P. Abbott *et al.*, *Living Rev. Relativ.* **21** (2018) 3.
32. C. A. Graeff, M. D. Alloy, K. D. Marquez, C. Providencia and D. P. Menezes, arXiv:1806.04170 [astro-ph.HE].
33. A. Drago, A. Lavagno, G. Pagliara and D. Pigato, *Eur. Phys. J. A* **52** (2016) 40.
34. P. Papazoglou, D. Zschiesche, S. Schramm, J. Schaffner-Bielich, H. Stoecker and W. Greiner, *Phys. Rev. C* **59** (1999) 411.
35. V. A. Dexheimer and S. Schramm, *Phys. Rev. C* **81** (2010) 045201.
36. C. Ratti, M. A. Thaler and W. Weise, *Phys. Rev. D* **73** (2006) 014019.
37. S. Rossner, C. Ratti and W. Weise, *Phys. Rev. D* **75** (2007) 034007.
38. Z. Fodor and S. D. Katz, *J. High Energy Phys.* **4** (2004) 50.
39. A. Kurkela and A. Vuorinen, *Phys. Rev. Lett.* **117** (2016) 042501.
40. T. Fischer, S. C. Whitehouse, A. Mezzacappa, F. K. Thielemann and M. Liebendorfer, *Astron. Astrophys.* **517** (2010) A80.

41. L. Hudepohl, B. Muller, H. T. Janka, A. Marek and G. G. Raffelt, *Phys. Rev. Lett.* **104** (2010) 251101, Erratum **105** (2010) 249901.
42. N. Yasutake, S. Benic, D. Blaschke, T. Maruyama and T. Tastumi, *Acta Astron. Sin.* **56** (2015) 85.
43. X. Wu and H. Shen, *Phys. Rev. C* **96** (2017) 025802.
44. A. Burrows and J. M. Lattimer, *Astrophys. J.* **307** (1986) 178.
45. J. A. Pons, S. Reddy, M. Prakash, J. M. Lattimer and J. A. Miralles, *Astrophys. J.* **513** (1999) 780.
46. J. Roark, X. Du, C. Constantinou, V. Dexheimer, A. W. Steiner and J. R. Stone Hyperons and quarks in proto-neutron stars, In progress (2018), arXiv:1812.08157 [astro-ph.HE].
47. Y. Aoki, G. Endrodi, Z. Fodor, S. D. Katz and K. K. Szabo, *Nature* **443** (2006) 675.
48. F. Foucart, R. Haas, M. D. Duez, E. O'Connor, C. D. Ott, L. Roberts, L. E. Kidder, J. Lippuner, H. P. Pfeiffer and M. A. Scheel, *Phys. Rev. D* **93** (2016) 044019.
49. Y. Zenati, H. B. Perets and S. Toonen, arXiv:1807.09777 [astro-ph.HE].
50. J. A. Rueda, R. Ruffini, Y. Wang, C. L. Bianco, J. M. Blanco-Iglesias, M. Karlica, P. Loren-Aguilar, R. Moradi and N. Sahakyan, arXiv:1807.07905 [astro-ph.HE].
51. K. D. Kokkotas, Pulsating relativistic stars, in *Relativistic Gravitation and Gravitational Radiation*, eds. J.-A. Marck and J.-P. Lasota (Cambridge Cantemporary Astrophysics, Cambridge, 1997), p. 89.
52. L. Lindblom and S. L. Detweiler, *Astrophys. J. Suppl.* **53** (1983) 73.
53. B. Schutz, Gravitational radiation, in *Encyclopedia of Astronomy and Astrophysics*, ed. P. Murdin (Taylor & Francis Group, 2000), p. 2110, doi: 10.1888/0333750888/2110.
54. S. A. Hughes, *Phys. Dark Univ.* **4** (2014) 86, DARK TAUP2013.
55. L. D. Landau and E. M. Lifshitz, The classical theory of fields, in *Course of Theoretical Physics*, 4th Rev. Engl. Ed (Pergamon Press, Oxford, 1975), .
56. W.-Y. Chau, *Astrophys. J.* **147** (1967) 664.
57. J. A. F. Pacheco, Potential gravitational wave sources and laser beam interferometers, in *Relativistic Aspects of Nuclear Physics* (World Scientific, 2011), pp. 158–172.
58. N. Andersson and K. D. Kokkotas, *Phys. Rev. Lett.* **77** (1996) 4134.
59. J. L. Houser, J. M. Centrella and S. C. Smith, *Phys. Rev. Lett.* **72** (1994) 1314.
60. B. F. Schutz, *Class. Quantum Gravit.* **13** (1996) A219.
61. G. F. Marranghello, C. A. Z. Vasconcellos and J. A. de Freitas Pacheco, *Phys. Rev. D* **66** (2002) 064027.
62. A. Passamonti, E. Gaertig and K. D. Kokkotas, *J. Phys. Conf. Ser.* **453** (2013) 012011.
63. R. N. Manchester, G. B. Hobbs, A. Teoh and M. Hobbs, *Astron. J.* **129** (2005) 1993.
64. VIRGO, KAGRA, LIGO Scientific Collabs. (B. P. Abbott *et al.*), *Living Rev. Relativ.* **21** (2018) 3; *Living Rev. Relativ.* **19** (2016) 1.
65. O. D. Aguiar *et al.*, *J. Phys. Conf. Ser.* **363** (2012) 012003.
66. E. B. Abdikamalov, H. Dimmelmeier, L. Rezzolla and J. C. Miller, *Mon. Not. Roy. Astron. Soc.* **394** (2009) 52.
67. J. E. Staff, P. Jaikumar, V. Chan and R. Ouyed, *Astrophys. J.* **751** (2012) 24.

APPENDIX F – MESA inlist and extras files

Below we present an example of `inlist` and `extras` files used in our work.

`inlist1`:

```
! Soethe, L.T.T. & Kepler, S.O., 2021.
! Convection and rotation boosted prescription of magnetic braking:
   application to the formation of extremely low-mass white dwarfs
! Monthly Notices of the Royal Astronomical Society
! Volume 506, Issue 3, September 2021, Pages 3266--3281.
! DOI: https://doi.org/10.1093/mnras/stab1916
! arXiv: https://arxiv.org/abs/2107.03952
! adsabs: https://ui.adsabs.harvard.edu/abs/2021MNRAS.506.3266S/abstract
!
! Before using, please read also:
! https://arxiv.org/abs/1911.05790
! https://arxiv.org/abs/1606.04947
! and its respective inlist files.
!
! Files intended to be used with: MESA r11701 and SDK 20190503.
!
! This is a BETA version of the files.
! The final version will be made public in the future.

&star_job

!## VAN/IVANOVA OTHER PARAMETERS ####################
  ! start a run from a saved model
    load_saved_model = .false.

  ! setting intial model number
    set_initial_model_number = .true.
    initial_model_number = 0

  ! setting initial age
    set_initial_age = .false.

  ! set_initial_dt = .true.
  ! years_for_initial_dt = 1d5

    ! change whether MESA evolves a (radial) velocity variable, v,
    ! defined at cell boundaries
!    change_v_flag = .true. !def=F
!    new_v_flag = .true. !def=F

```

```
    ! change_rotation_flag = .true.
    ! new_rotation_flag = .true.

    ! lnPgas variables
    ! `lnPgas_flag` is true if we are using lnPgas variables in place of
    lnd
!    change_lnPgas_flag = .true. !def=F
!    new_lnPgas_flag = .true. !def=F

    ! Due to changing the `run_star_extras` functions to hooks
    warn_run_star_extras = .false.
!#####################################################

!#####################################################
!## output
   show_log_description_at_start = .true.
   show_net_species_info = .true. !list of the species in the current
   net
   show_net_reactions_info = .true. !information about the reactions in
   the current net
   list_net_reactions = .true. !list of the reactions in the current net
   save_model_when_terminate = .true.
   save_model_filename = "final.mod"
   write_profile_when_terminate = .true.
   filename_for_profile_when_terminate = "final_profile.data"
   pgstar_flag = .true. !if true, activates pgplot output

!## rotation controls
   new_rotation_flag = .true.
   change_rotation_flag = .true.
   set_initial_surface_rotation_v = .true.
   new_surface_rotation_v = 10 !1 10 100
   num_steps_to_relax_rotation = 100

!## nuclear reactions
   change_net = .true.
   new_net_name = "my_cno_extras.net" !same as cno_extras but with "
   add_isos(ca40)"
!    new_net_name = "cno_extras.net" !use this if you do not need Ca40.

!## modifications to model
   relax_initial_Z = .true.
   new_Z = 0.02 !0.01 0.001

!#####################################################

/ !end of star_job namelist
```

```
83
84 &controls
85
86 !## CARB VAN/IVANOVA PARAMETERS ####################
87     x_ctrl(1) = 1d-4 ! velocity ratio
88     x_ctrl(2) = 1.0  ! tau limit
89 ! velocity ratio       ! need to ensure that the convective velocity is
       within our defined limits
90 ! tau/opacity limit    ! opacity of the given cell. If the cell isn't
       near the surface (low tau)
91                        ! then include it in our integration !if (s% tau(
       k) .gt. tau_lim) then...
92 !#########################################################
93
94 !#########################################################
95 !## controls for output
96    extra_terminal_output_file = "log1"
97    photo_directory = "photos1"
98    log_directory = "LOGS1"
99
100   photo_interval = 100
101   profile_interval = 100
102   history_interval = 1
103   terminal_interval = 1
104   write_header_frequency = 10
105
106 !    num_trace_history_values = 6
107 !    trace_history_value_name(1) = "surface ca40"
108 !    trace_history_value_name(2) = "total_mass_h1"
109 !    trace_history_value_name(3) = "surf_v_rot"
110 !    trace_history_value_name(4) = "surface h1"
111 !    trace_history_value_name(5) = "surf_omega_div_omega_crit"
112 !    trace_history_value_name(6) = "log_total_angular_momentum"
113
114 !## when to stop
115    max_age =1.4d10
116    !max_model_number = 10000
117    min_timestep_limit = 1d-15
118
119 !## timestep controls
120    delta_HR_limit = 0.005d0
121    delta_HR_hard_limit = 0.02d0
122    delta_lgL_H_limit = 0.01 !0.001
123    delta_lgL_H_hard_limit = 0.1 !0.01 0.02
124    lgL_H_burn_min = -1.0d0
125    delta_lg_XH_cntr_limit = 0.05d0
126    delta_lg_XH_cntr_max = -3
```

```
127    delta_lg_XH_cntr_min = -6.0d0
128    delta_lg_XH_cntr_hard_limit = -1
129    report_why_dt_limits = .true. !If true, produce terminal output about
        choice of timestep.
130    varcontrol_target = 5d-4 !def=1d-4
131    report_hydro_solver_progress = .true.
132    limit_for_rel_error_in_energy_conservation = 5d-4
133    hard_limit_for_rel_error_in_energy_conservation = 5d-2
134
135    !dt_div_dt_thermal_limit = 0.05
136    !dt_div_dt_thermal_hard_limit = 0.5
137
138 !## mesh adjustment
139    max_allowed_nz = 30000 !Maximum number of grid points allowed.
140    min_dq_for_xa = 1d-5 ! default 1d-14
141    max_dq = 1d-3 !0.001 ! 1d-2 (max size cell as fraction total mass)
142
143    xa_function_species(1) = "he4"
144    xa_function_weight(1) = 10 !
145    xa_function_param(1) = 1d-2 !
146    xa_function_species(2) = "h1"
147    xa_function_weight(2) = 10 !def=30
148    xa_function_param(2) = 1d-2 !def=1d-2
149
150    mesh_dlog_pp_dlogP_extra = 0.2d0
151    mesh_dlog_cno_dlogP_extra = 0.2d0
152
153    xtra_coef_above_xtrans = 0.1 !1
154    xtra_coef_below_xtrans = 0.1 !1
155    !xtra_dist_above_xtrans = 2d0 !0.2d0
156    !xtra_dist_below_xtrans = 2d0 !0.2d0
157
158    !log_tau_function_weight = 20
159    !log_kap_function_weight = 20
160
161    !max_num_subcells = 2 !Limits number of new cells from 1 old one.
162
163 !## mixing parameters
164     mixing_length_alpha = 2.0
165     MLT_option = "Henyey" !def="Cox"
166     use_Ledoux_criterion = .true.
167     alpha_semiconvection = 1d-3 !only applies if Ledoux is true.
168     thermohaline_coeff = 1d0    !only applies if Ledoux is true.
169     smooth_convective_bdy = .false. !def=T
170
171     do_conv_premix = .true.
172     conv_premix_avoid_increase = .false.
```

```
173     conv_premix_time_factor = 0.0
174
175 !## step overshooting
176     step_overshoot_f_above_burn_h_core = 0.25
177     overshoot_f0_above_burn_h_core = 0.05
178     step_overshoot_D0_coeff = 1.0 !def=1
179
180 !## exponential overshooting ! we only include a bit of exponential
       overshooting to smooth things out
181     overshoot_f0_above_nonburn_core = 0.005
182     !overshoot_f0_above_burn_h_core = 0.005
183     overshoot_f0_above_burn_he_core = 0.005
184     overshoot_f0_above_burn_z_core = 0.005
185
186     overshoot_f_above_nonburn_core = 0.01
187     !overshoot_f_above_burn_h_core = 0.01
188     overshoot_f_above_burn_he_core = 0.01
189     overshoot_f_above_burn_z_core = 0.01
190
191     overshoot_f0_above_nonburn_shell = 0.005
192     overshoot_f0_above_burn_h_shell = 0.005
193     overshoot_f0_above_burn_he_shell = 0.005
194     overshoot_f0_above_burn_z_shell = 0.005
195
196     overshoot_f_above_nonburn_shell = 0.01
197     overshoot_f_above_burn_h_shell = 0.01
198     overshoot_f_above_burn_he_shell = 0.01
199     overshoot_f_above_burn_z_shell = 0.01
200
201     overshoot_f0_below_nonburn_shell = 0.005
202     overshoot_f0_below_burn_h_shell = 0.005
203     overshoot_f0_below_burn_he_shell = 0.005
204     overshoot_f0_below_burn_z_shell = 0.005
205
206     overshoot_f_below_nonburn_shell = 0.01
207     overshoot_f_below_burn_h_shell = 0.01
208     overshoot_f_below_burn_he_shell = 0.01
209     overshoot_f_below_burn_z_shell = 0.01
210
211     !limit_mixing_length_by_dist_to_bdy = 1
212     !conv_bdy_mix_softening_f  = 0.001 !def=0
213     !conv_bdy_mix_softening_f0 = 0.003 !def=0
214     !conv_bdy_mix_softening_min_D_mix = 1d-3 !def=0
215     xtra_coef_czb_full_on = 1.0d0 !def=1d-4
216     xtra_coef_czb_full_off = 1.0d0 !def=0.1d0
217     xtra_coef_a_l_nb_czb = 0.5d0 !def=1
218     xtra_coef_b_l_nb_czb = 0.5d0 !def=1
```

```
219     xtra_dist_a_l_nb_czb = 2d0 !def=0.2d0
220     xtra_dist_b_l_nb_czb = 2d0 !def=0.2d0
221
222 !## rotation controls
223    am_nu_ST_factor = 1.0 ! < 0 means use D_ST_factor
224    D_visc_factor = 0.0 !Should be = 0 because viscosity doesn't mix
       chemical elements.
225    am_nu_SH_factor = 0.0 !def=-1 ! < 0 means use D_SH_factor
226    D_ST_factor = 0.0  !Spruit-Tayler dynamo
227    D_SH_factor = 0.0  !Solberg-Hoiland
228    D_GSF_factor = 1.0 !Goldreich-Schubert-Fricke
229    D_ES_factor = 1.0  !Eddington-Sweet circulation
230    D_SSI_factor = 1.0 !secular shear instability
231    D_DSI_factor = 1.0 !dynamical shear instability
232    am_D_mix_factor = 0.0333333333333333
233    am_nu_factor = 1.0
234    am_gradmu_factor = 0.05
235
236 !## atmosphere boundary conditions ! See run_star_extras.f
237    !which_atm_option = "WD_tau_25_tables" !def="simple_photosphere"
238
239 !## structure equations
240 !    use_dedt_form_of_energy_eqn = .true.
241 !    min_cell_energy_fraction_for_dedt_form = 0
242 !    use_eps_correction_for_KE_plus_PE_in_dLdm_eqn = .true.
243
244 !## miscellaneous controls
245 !    use_eps_mdot = .true
246
247 !## element diffusion
248    show_diffusion_info = .true. ! terminal output for diffusion
249    !show_diffusion_substep_info = .true. ! terminal output for diffusion
250    !show_diffusion_timing = .true.
251
252 ! Diffusion is ON! See run_star_extras.f
253    do_element_diffusion = .false. !determines whether or not we do
       diffusion
254    diffusion_dt_limit =  3.15d7 !def=3.15d7
255
256    diffusion_use_iben_macdonald = .true. !def=F !true=Iben & MacDonald
       1985 / false=Stanton & Murillo 2016
257    diffusion_use_cgs_solver = .false. !def=T !false=Thoul et al. 1994 /
       true=Burgers
258
259 ! Diffusion is ON! See run_star_extras.f
260    diffusion_use_full_net = .false. ! Bypasses the need to set up
       diffusion classes.
```

```
261
262    ! solver controls.
263    diffusion_use_isolve = .true. !def=F
264    diffusion_rtol_for_isolve = 1d-4 !def=1d-4
265    diffusion_atol_for_isolve = 1d-5 !def=1d-5
266    diffusion_maxsteps_for_isolve = 1000 !def=1000
267    diffusion_isolve_solver = "ros2_solver" !def="ros2_solver"
268
269    !diffusion_steps_limit = 20 !def=500 !If diffusion solver uses more
       steps than this, reduce the next timestep.
270    !diffusion_steps_hard_limit = 50 !def=700 !If diffusion solver uses
       more steps than this, retry.
271    !diffusion_iters_limit = 50 !def=600 !If use a total number of iters
       > this, reduce the next timestep.
272    !diffusion_iters_hard_limit = 100 !def=800 !If use a total number of
       iters > this, retry.
273
274    ignore_species_in_max_correction = .true.
275    scale_max_correction = 0.05d0
276
277 !## solver controls
278    newton_iterations_limit =25
279    newton_itermin = 6
280    tol_residual_norm1 = 1d-9!1d-10
281    tol_max_residual1 = 1d-8!1d-9
282
283    !iter_for_resid_tol2 = 6
284    !tol_residual_norm2 = 1d-7
285    !tol_max_residual2 = 1d-5
286    !iter_for_resid_tol3 = 15
287
288     ! if solver mass fraction < limit, reject
289     !min_xa_hard_limit = -1d-4
290     !min_xa_hard_limit_for_highT = -3d-4
291     tiny_corr_coeff_limit = 999999 !def=5
292
293    report_why_dt_limits = .true.
294    timestep_factor_for_retries =  0.7
295    timestep_factor_for_backups = 0.7
296    min_timestep_factor = 0.9
297    max_timestep_factor = 1.05
298    backup_hold = 10
299    retry_hold = 5  !def=1
300    redo_limit =  -1 !100
301    newton_iterations_limit = 20 !def=7
302    use_gold_tolerances = .false.
303
```

```
!#######################################################

!## VAN/IVANOVA OTHER PARAMETERS ####################
  ! maximum number of profiles
  ! Less than zero means no limit.
!    max_num_profile_models = -1

!## mass gain or loss
    hot_wind_scheme = "Reimers" !def=""
    cool_wind_RGB_scheme = "Reimers" !def=""
    Reimers_scaling_factor = 1.0 !def=0
    mass_change_full_on_dt = 1d-99 !def=1d-99
    mass_change_full_off_dt = 1d-99 !def=1d-99
    wind_boost_full_off_L_div_Ledd = 1d99 !def=1.5d0
    wind_boost_full_on_L_div_Ledd = 1d99 !def=5

!## mixing parameters
!    smooth_convective_bdy = .true. !def=T
!    alt_scale_height_flag = .true. !def=T

!## structure equations
!    min_dxm_Eulerian_div_dxm_removed = -1 !def=2

!    max_age = 1d10

!#######################################################

/! end of controls namelist

&pgstar

!### ADD
   read_extra_pgstar_inlist1 = .true.
   extra_pgstar_inlist1_name = "inlist_pgstar1"
!###

/ ! end of pgstar namelist
```

inlist_project:

```
! Soethe, L.T.T. & Kepler, S.O., 2021.
! Convection and rotation boosted prescription of magnetic braking:
   application to the formation of extremely low-mass white dwarfs
! Monthly Notices of the Royal Astronomical Society
! Volume 506, Issue 3, September 2021, Pages 3266--3281.
! DOI: https://doi.org/10.1093/mnras/stab1916
! arXiv: https://arxiv.org/abs/2107.03952
! adsabs: https://ui.adsabs.harvard.edu/abs/2021MNRAS.506.3266S/abstract
```

```
!
! Before using, please read also:
! https://arxiv.org/abs/1911.05790
! https://arxiv.org/abs/1606.04947
! and its respective inlist files.
!
! Files intended to be used with: MESA r11701 and SDK 20190503.
!
! This is a BETA version of the files.
! The final version will be made public in the future.

&binary_job

   inlist_names(1) = "inlist1"
   !inlist_names(2) = "inlist2"

    !evolve_both_stars = .false.

    !which_for_pgstar = 0 ! 0 means none; < 0 means all; i > 0 means
   stari
    evolve_both_stars = .false.
    warn_binary_extra = .false.

/ ! end of binary_job namelist

&binary_controls

!######################################################

!## specifications for starting model
   m1 = 1.0 !1.2 1.4 !donor mass in Msun
   m2 = 1.4 !0.8 1.2 !companion mass in Msun
   initial_period_in_days = 20d0 !initial orbital period in days
   !terminal_interval = 100000

!## controls for output
   !append_to_star_history = .true.
   log_directory = "."
   history_name = "binary_history.data"
   history_interval = 1
   append_to_star_history = .true. !def=.true.
   extra_binary_terminal_output_file = "log-bin" !def=""

!## timestep controls: fr: change in (r-rl)/rl
   fr = 0.01
   fr_limit = 1d-2
   varcontrol_case_a = 5d-4
```

```
54    varcontrol_case_b = 5d-4
55    varcontrol_ms = 5d-4
56    varcontrol_post_ms = 5d-4
57
58 !## orbital jdot controls:
59    do_jdot_gr = .true.
60    do_jdot_ml = .true.
61    do_jdot_ls = .true.
62    do_jdot_missing_wind = .false.
63 !    do_jdot_mb = .true.
64 !    keep_mb_on = .false. !def=F
65 !    magnetic_braking_gamma = 4.0d0 !def=3.0d0
66
67 !## mass transfer controls
68    mass_transfer_alpha = 0.0d0
69    mass_transfer_beta = 0.8d0 !0.3d0
70    mass_transfer_delta = 0.0d0
71    mass_transfer_gamma = 0.0d0
72
73    mdot_scheme = "Kolb" !def=Ritter
74 !    limit_retention_by_mdot_edd = .true. !def=F
75    max_change_factor = 1.25d0 !def=1.5d0
76    min_change_factor = 1.01d0 !def=1.05d0
77    max_tries_to_achieve = 100 !def=20
78    implicit_scheme_tolerance = 0.01 !def=5d-2
79
80    report_rlo_solver_progress = .true. !def=.false.
81
82 !## rotation and sync controls
83    do_tidal_sync = .true. !def=F
84    do_initial_orbit_sync_1 = .true. !def=F
85    sync_mode_1 = "Uniform"
86    sync_type_1 = "Hut_conv" !def=Hut_conv
87    Ftid_1 = 1 !def=1 !Tidal strength factor. Synchronisation and
      circularisation timescales are divided by this.
88
89 !########################################################
90
91 !## VAN/IVANOVA OTHER PARAMETERS ####################
92     !terminal_interval = 10
93     !write_header_frequency = 5
94
95    !photo_interval = 100
96    !profile_interval = 100
97    !history_interval = 1
98    terminal_interval = 1
99    write_header_frequency = 10
```

```
100
101 !    initial_period_in_days = 10d0 ! period
102
103     use_other_jdot_mb = .true. ! Logicals to deploy the use_other
    routines.
104     use_other_mdot_edd = .true.
105 !    terminate_if_initial_overflow = .false. !def=T ! terminate
    evolution if first model of run is overflowing
106 !    limit_retention_by_mdot_edd = .true.
107 !    use_es_opacity_for_mdot_edd = .true. !def=T !If .true., then the
    opacity for 'mdot_edd' is computed as 0.2*(1+X)
108
109 !    max_explicit_abs_mdot = 1d100 ! Limit the explicit mass transfer
    rate to 'max_explicit_abs_mdot', in Msun/secyer
110                                   ! def=1d-7
111     fm = 0.01d0  !b_envelope
112     fa = 0.01d0  !b_separation
113 !    fr = 0.10d0  !b_RL
114     fj = 0.001d0 !b_jorb
115
116 !    m1 = 1.2 !2.0 ! donor mass
117 !    m2 = 1.4 !0.6 ! accretor mass
118 !    max_tries_to_achieve = 50 ! The implicit method will modify the
    mass transfer rate and redo the step
119     magnetic_braking_gamma = 4.0 ! gamma exponent for magnetic braking.
120
121 / ! end of binary_controls namelist
```

run_binary_extras.f:

```
1  ! Soethe, L.T.T. & Kepler, S.O., 2021.
2  ! Convection and rotation boosted prescription of magnetic braking:
     application to the formation of extremely low-mass white dwarfs
3  ! Monthly Notices of the Royal Astronomical Society
4  ! Volume 506, Issue 3, September 2021, Pages 3266--3281.
5  ! DOI: https://doi.org/10.1093/mnras/stab1916
6  ! arXiv: https://arxiv.org/abs/2107.03952
7  ! adsabs: https://ui.adsabs.harvard.edu/abs/2021MNRAS.506.3266S/abstract
8  !
9  ! Before using, please read also:
10 ! https://arxiv.org/abs/1911.05790
11 ! https://arxiv.org/abs/1606.04947
12 ! and its respective inlist files.
13 !
14 ! Files intended to be used with: MESA r11701 and SDK 20190503.
15 !
16 ! This is a BETA version of the files.
17 ! The final version will be made public in the future.
```

```
18
19          module run_binary_extras
20
21          use star_lib
22          use star_def
23          use const_def
24          use const_def
25          use chem_def
26          use num_lib
27          use binary_def
28          use crlibm_lib
29
30          implicit none
31
32          contains
33
34  subroutine extras_binary_controls(binary_id, ierr)
35              integer :: binary_id
36              integer, intent(out) :: ierr
37              type (binary_info), pointer :: b
38              ierr = 0
39              call binary_ptr(binary_id, b, ierr)
40              if (ierr .ne. 0) then
41                  write(*,*) "failed in binary_ptr"
42                  return
43              end if
44              ! write(*,*) "hello from extra_binary_controls"
45      b% other_mdot_edd => mdot_edd_routine
46      b% other_jdot_mb => jdot_mb_routine
47
48      b% how_many_extra_binary_history_columns =>
       how_many_extra_binary_history_columns
49      b% data_for_extra_binary_history_columns =>
       data_for_extra_binary_history_columns
50
51      b% extras_binary_startup => extras_binary_startup
52      b% extras_binary_check_model => extras_binary_check_model
53      b% extras_binary_finish_step => extras_binary_finish_step
54      b% extras_binary_after_evolve => extras_binary_after_evolve
55      b% warn_binary_extra =.false.
56  end subroutine extras_binary_controls
57
58  subroutine mdot_edd_routine(binary_id, mdot_edd, ierr)
59              use const_def, only: dp
60              integer, intent(in) :: binary_id
61              real(dp), intent(out) :: mdot_edd
62              integer, intent(out) :: ierr
```

```
63              type (binary_info), pointer :: b
64              ierr = 0
65              call binary_ptr(binary_id, b, ierr)
66              if (ierr .ne. 0) then
67                  write(*,*) "failed in binary_ptr"
68                  return
69              end if
70
71 ! changing mdot_edd from default MESA from BH to NS
72
73 ! mdot_edd = 4*pi*clight*b% s1% x_ctrl(5)/(0.2*(1+b% s1% surface_h1))
74 ! hard coding in the radius of 11.5km into the equation results in the
     next line.
75              mdot_edd = 2.1666d18 / ((1.d0 + b% s1% surface_h1))
76 ! write (*,*) "Modified Mdot_edd = ", mdot_edd
77 ! write (*,*) "mdot_system_transfer = ", b% mdot_system_transfer(b% a_i)
78 ! write (*,*) " "
79 end subroutine mdot_edd_routine
80
81 subroutine check_radiative_core(b)
82              type (binary_info), pointer :: b
83              type (star_info), pointer :: s
84
85              real(dp) :: sum_conv, q_loc, sum_div_qloc
86              integer :: i, k, id
87
88              include "formats.inc"
89
90              do i=1,2
91                  if (i == 1) then
92                      s => b% s_donor
93                      id = b% d_i
94                  else if (b% point_mass_i == 0 .and. b%
     include_accretor_mb) then
95                      s => b% s_accretor
96                      id = b% a_i
97                  else
98                      exit
99                  end if
100
101 ! calculate how much of inner region is convective
102                 sum_conv = 0; q_loc = 0
103                 do k = s% nz, 1, -1
104                     q_loc = s% q(k)
105                     if (q_loc > 0.5d0) exit
106                     if (s% mixing_type(k) == convective_mixing) &
107                         sum_conv = sum_conv + s% dq(k)
```

```
                end do

                sum_div_qloc = (b% sum_div_qloc(id) + sum_conv/q_loc)/2
                b% sum_div_qloc(id) = sum_div_qloc

                if (b% have_radiative_core(id)) then ! check if still have rad core
                    if (sum_div_qloc > 0.75d0) then
                        b% have_radiative_core(id) = .false.
                        write(*,*)
                        write(*,*) "turn off magnetic braking because radiative core has gone away"
                        write(*,*)
! required mdot for the implicit scheme may drop drastically,
! so its neccesary to increase change factor to avoid implicit
! scheme from getting stuck
                        b% change_factor = b% max_change_factor
                    end if
                else if (sum_div_qloc < 0.25d0) then ! check if now have rad core
                    if (.not. b% have_radiative_core(id)) then
                        write(*,*)
                        write(*,*) "turn on magnetic braking"
                        write(*,*)
                    end if
                    b% have_radiative_core(id) = .true.
                end if
            end do
end subroutine check_radiative_core

subroutine jdot_mb_routine(binary_id, ierr)
            integer, intent(in) :: binary_id
            integer, intent(out) :: ierr
            integer :: k, nz
            type (binary_info), pointer :: b
            type (star_info), pointer :: s
            real(dp) :: turnover_time, tt_temp, tt_temp_scaled, tt_old, tt_diff
            real(dp) :: vel, vel_ratio, vel_diff, upper_lim, lower_lim, scaled_vel
            real(dp) :: eps_nuc_lim, eps_nuc
            real(dp) :: dr, tau_lim, delta_mag_chk
            real(dp) :: rsun4, two_pi_div_p3, two_pi_div_p2, K2
            real(dp) :: tt_ratio, tt4
            real(dp) :: rot_ratio, rot4
            real(dp) :: rad4
            real(dp) :: v_esc2, v_mod2
```

```
150             real(dp) :: alfven_no_R, R_alfven
151             real(dp) :: jdot_mb_old, jdot_mb_new
152             real(dp) :: conv_env_r, conv_env_m, sonic_cross_time,
    mag_field
153             real(dp) :: Bs ! surface magnetic field
154             common/ old_var/ tt_old
155             common /mycommonblock/ jdot_mb_old, jdot_mb_new ! add
156             logical :: conv_env_found
157             ierr = 0
158             call binary_ptr(binary_id, b, ierr)
159             if (ierr .ne. 0) then
160                 write(*,*) "failed in binary_ptr"
161                 return
162             end if
163
164 ! INITIALIZE THE VARIABLES
165
166             s => b% s_donor
167             nz = s% nz
168             vel_ratio = s% x_ctrl(1)     ! originally x_ctrl(3)
169             tau_lim = s% x_ctrl(2)       ! originally x_ctrl(4)
170
171             conv_env_found = .false.
172
173             turnover_time = 0.0
174             tt_temp = 0.0
175             tt_temp_scaled = 0.0
176
177             eps_nuc_lim = 1.0d-2
178             vel_diff = 0.0
179             scaled_vel = 0.0
180
181 ! INITIAL TURNOVER TIME CALCULATION
182
183             do k = nz, 1, -1 ! beginning of do loop to calculate
    convective turnover time
184
185                 eps_nuc = s% eps_nuc(k)
186 ! check if the cell we are looping through satisfies our convection
    criteria
187                 if ((s% gradr(k) .gt. s% grada(k)) .and. (eps_nuc .lt.
    eps_nuc_lim)) then
188 ! toggle the boolean to begin integration
189                     conv_env_found = .true.
190                 end if
191
192 ! only enter this portion if the convective boolean is true
```

```
193 ! this loop will go from the innermost cell that is convective to
194 ! the surface. This is to try and smooth through any numeric issues
195 ! with convective zones appearing and disappearing in MESA.
196                 if (conv_env_found) then
197
198 ! loop to calculate the size of the cell, the innermost cell
199 ! needs special consideration as it is above the core
200                     if (k .lt. s% nz) then
201                         dr = (s% r(k) - s% r(k + 1))
202                     else
203                         dr = (s% r(k) - s% R_center)
204                     end if
205
206 ! determine the convective velocity inside each given cell
207                     if (s% mixing_type(k) == convective_mixing) then
208
209 ! need to ensure that the convective velocity is within
210 ! our defined limits, if they are outside of these limits
211 ! set them to be the max/min value allowed.
212                         vel = s% conv_vel(k)
213                         lower_lim = vel_ratio * s% csound(k)
214                         upper_lim = 1.0 * s% csound(k)
215
216                         if (vel .lt. lower_lim) then
217                             vel = lower_lim
218                         else if (vel .gt. upper_lim) then
219                             vel = upper_lim
220                         end if
221
222 ! if the cell isnt defined by MESA to be convective take the
223 ! convective velocity to be equal to sound speed
224                     else
225                         vel = s% csound(k)
226                     end if
227
228 ! Final check involving the opacity of the given cell. If the
229 ! cell isn't near the surface (low tau) then include it in our
    integration
230                     if (s% tau(k) .gt. tau_lim) then
231                         sonic_cross_time = sonic_cross_time + (dr / s%
    csound(k))
232                         conv_env_r = conv_env_r + dr
233                         conv_env_m = conv_env_m + s% dm(k)
234                         tt_temp = tt_temp + (dr / vel)
235                     end if
236                 end if
237
```

```
238             end do ! end of do loop to calculate convective turnover
    time
239
240 ! reset the boolean just in case
241             conv_env_found = .false.
242
243 ! TURNOVER TIME CHECK, THIS IS TO TRY AND AVOID LARGE CHANGES
244
245 ! simply set the turnover time to the internal variable calculated above
246             turnover_time = tt_temp
247
248             if (s% model_number .gt. 1) then
249 ! calculate the variables used to check if our system is rapidly
    evolving
250                 tt_diff = abs(tt_old - tt_temp) / tt_old
251                 delta_mag_chk = s% dt / tt_old
252
253                 write (*,*) "tt_diff       = ", tt_diff
254                 write (*,*) "delta_mag     = ", delta_mag_chk
255                 write (*,*) "turnover_time = ", turnover_time
256                 write (*,*) "tt_old        = ", tt_old
257
258 ! check if timesteps are very small or if the relative change is very
    large
259                 if (tt_diff .gt. delta_mag_chk) then
260                     write (*,*) "large change, adjusting accordingly"
261                     turnover_time = tt_old + (tt_temp - tt_old) * min((s
    % dt / tt_old), 0.5)
262                     mag_field = (turnover_time / 2.8d6) * (2073600. / b%
     period)
263                     write (*,*) "mag_field    = ", mag_field
264
265                 end if ! end of timestep/relative change check
266             end if
267
268 ! remember the current values to be used as comparison in the next step
269
270             tt_old = turnover_time
271
272 ! MAGNETIC BRAKING CALCULATION
273
274             b% jdot_mb = 0
275             rsun4 = pow4(rsun)
276
277             call check_radiative_core(b)
278
279             two_pi_div_p3 = (2.0*pi/b% period)*(2.0*pi/b% period)*(2.0*
```

```
   pi/b% period)
280            two_pi_div_p2 = (2.0*pi/b% period)*(2.0*pi/b% period)
281
282            K2 = 0.07 * 0.07
283
284 ! use the formula from rappaport, verbunt, and joss.  apj, 275, 713-731.
     1983.
285            !### IN
286            if (b% have_radiative_core(b% d_i) .or. b% keep_mb_on) then
287
288               jdot_mb_old = -3.8d-30*b% m(b% d_i)*rsun4* &
289                  pow_cr(min(b% r(b% d_i),b% rl(b% d_i))/rsun,b%
   magnetic_braking_gamma)* &
290                  two_pi_div_p3
291
292               tt_ratio = turnover_time / 2.8d6
293               tt4 = pow4(tt_ratio)
294               ! write (*,*) "tt4 = ", tt4
295
296               rot_ratio = (2073600. / b% period )
297               rot4 = pow4(rot_ratio)
298               ! write (*,*) "rot4 = ", rot4
299
300               rad4 = pow4(b% r(b% d_i))
301               ! write (*,*) "rad4 = ", rad4
302
303               v_esc2 = 2.0 * standard_cgrav * b% m(b% d_i) / b% r(b%
   d_i)
304               v_mod2 = v_esc2 + 2.0 * two_pi_div_p2 * b% r(b% d_i) * b
   % r(b% d_i) / K2
305
306               alfven_no_R = rad4 * rot4 * tt4 / (b% mdot_system_wind(b
   % d_i) * b% mdot_system_wind(b% d_i)) * (1.0 / v_mod2)
307
308               Bs = ((rot4 * tt4)**(1.d0/4.d0)) ! surface magnetic
   field.  ADD
309
310               R_alfven = b% r(b% d_i) * alfven_no_R**(1.d0/3.d0) ! was
    wrong in the original file. I changed from 2/3 to 1/3.
311
312               jdot_mb_new = (2.0/3.0) * (2.0*pi/b% period) * b%
   mdot_system_wind(b% d_i) * R_alfven * R_alfven
313                write (*,*) "Bs           = ", Bs ! ADD
314                write (*,*) "jdot_mb_old  = ", jdot_mb_old
315                write (*,*) "jdot_mb_new  = ", jdot_mb_new
316
317               b% jdot_mb = jdot_mb_new
```

```
318
319             end if
320             !### OUT
321
322             if (b% point_mass_i == 0 .and. b% include_accretor_mb .and.
    &
323                 (b% have_radiative_core(b% a_i) .or. b% keep_mb_on))
    then
324                 b% jdot_mb = b% jdot_mb - &
325                                     3.8d-30*b% m(b% a_i)*rsun4* &
326                                     pow_cr(min(b% r(b% a_i),b% rl(b% a_i
    ))/rsun,b% magnetic_braking_gamma)* &
327                                     two_pi_div_p3
328             end if
329
330             s% xtra1 = turnover_time
331             s% xtra2 = mag_field
332             s% xtra3 = conv_env_r
333             s% xtra4 = conv_env_m
334             s% xtra5 = sonic_cross_time
335             s% xtra6 = Bs           ! ADD
336             s% xtra7 = jdot_mb_old ! ADD
337             s% xtra8 = jdot_mb_new ! ADD
338 end subroutine jdot_mb_routine
339
340 integer function how_many_extra_binary_history_columns(binary_id)
341             use binary_def, only: binary_info
342             integer, intent(in) :: binary_id
343             how_many_extra_binary_history_columns = 8 !7 !5 !7
344 end function how_many_extra_binary_history_columns
345
346 subroutine data_for_extra_binary_history_columns(binary_id, n, names,
    vals, ierr)
347             use const_def, only: dp
348             type (binary_info), pointer :: b
349             type (star_info), pointer :: s
350             integer, intent(in) :: binary_id
351             integer, intent(in) :: n
352             character (len=maxlen_binary_history_column_name) :: names(n
    )
353             real(dp) :: vals(n)
354             integer, intent(out) :: ierr
355             real(dp) :: beta
356             ierr = 0
357             call binary_ptr(binary_id, b, ierr)
358             if (ierr .ne. 0) then
359                 write(*,*) "failed in binary_ptr"
```

```
                return
            end if

            s => b% s_donor

            names(1) = "turnover_time"
            vals(1) = s% xtra1

            names(2) = "mag_field"
            vals(2) = s% xtra2

            names(3) = "conv_env_r"
            vals(3) = s% xtra3

            names(4) = "conv_env_m"
            vals(4) = s% xtra4

            names(5) = "sonic_cross_time"
            vals(5) = s% xtra5

            names(6) = "Bs" ! ADD
            vals(6) = s% xtra6 ! ADD

            names(7) = "jdot_mb_old" ! ADD
            vals(7) = s% xtra7 ! ADD

            names(8) = "jdot_mb_new" ! ADD
            vals(8) = s% xtra8 ! ADD
end subroutine data_for_extra_binary_history_columns


integer function extras_binary_startup(binary_id,restart,ierr)
            type (binary_info), pointer :: b
            integer, intent(in) :: binary_id
            integer, intent(out) :: ierr
            logical, intent(in) :: restart
            call binary_ptr(binary_id, b, ierr)
            if (ierr .ne. 0) then ! failure in  binary_ptr
                return
            end if

            ! b% s1% job% warn_run_star_extras = .false.
            ! extras_binary_startup = keep_going

            write(*,*) "starting modified MB"
            if (b% angular_momentum_j <= 0) then
                write(*,*) "angular_momentum_j <= 0", b%
```

```
   angular_momentum_j
                b% s1% dt_next = min(b% s1% dt * 0.50, b% s1% dt_next)
                extras_binary_startup = retry
            end if
end function  extras_binary_startup

        !Return either retry,backup,keep_going or terminate
integer function extras_binary_check_model(binary_id)
            type (binary_info), pointer :: b
            integer, intent(in) :: binary_id
            integer :: ierr
            real(dp) :: j_check1
            call binary_ptr(binary_id, b, ierr)
            if (ierr .ne. 0) then ! failure in  binary_ptr
                return
            end if

            if (b% angular_momentum_j <= 0) then
                write(*,*) "bad angular momentum"
                b% s1% dt_next = min(b% s1% dt * 0.50, b% s1% dt_next)
                extras_binary_check_model = retry
            end if

            extras_binary_check_model = keep_going
end function extras_binary_check_model


! returns either keep_going or terminate.
! note: cannot request retry or backup; extras_check_model can do that.
integer function extras_binary_finish_step(binary_id)
            type (binary_info), pointer :: b
            integer, intent(in) :: binary_id
            integer :: ierr
            call binary_ptr(binary_id, b, ierr)
            if (ierr .ne. 0) then ! failure in binary_ptr
                return
            end if
            extras_binary_finish_step = keep_going
end function extras_binary_finish_step

subroutine extras_binary_after_evolve(binary_id, ierr)
            type (binary_info), pointer :: b
            integer, intent(in) :: binary_id
            integer, intent(out) :: ierr
            call binary_ptr(binary_id, b, ierr)
            if (ierr .ne. 0) then ! failure in binary_ptr
                return
```

```
            end if
end subroutine extras_binary_after_evolve

end module run_binary_extras
```

run_star_extras.f:

```
! Soethe, L.T.T. & Kepler, S.O., 2021.
! Convection and rotation boosted prescription of magnetic braking:
   application to the formation of extremely low-mass white dwarfs
! Monthly Notices of the Royal Astronomical Society
! Volume 506, Issue 3, September 2021, Pages 3266--3281.
! DOI: https://doi.org/10.1093/mnras/stab1916
! arXiv: https://arxiv.org/abs/2107.03952
! adsabs: https://ui.adsabs.harvard.edu/abs/2021MNRAS.506.3266S/abstract
!
! Before using, please read also:
! https://arxiv.org/abs/1911.05790
! https://arxiv.org/abs/1606.04947
! and its respective inlist files.
!
! Files intended to be used with: MESA r11701 and SDK 20190503.
!
! This is a BETA version of the files.
! The final version will be made public in the future.

      module run_star_extras

      use star_lib
      use star_def
      use const_def
      use const_def
      use chem_def
      use binary_def
      use utils_lib, only: mesa_error

      implicit none

      integer :: time0, time1, clock_rate
      real(dp), parameter :: expected_runtime = 1 ! minutes

      integer, parameter :: restart_info_alloc = 1
      integer, parameter :: restart_info_get = 2
      integer, parameter :: restart_info_put = 3

      contains

subroutine extras_controls(id, ierr)
```

```
41          integer, intent(in) :: id
42          integer, intent(out) :: ierr
43          type (star_info), pointer :: s
44
45          ierr = 0
46          call star_ptr(id, s, ierr)
47          if (ierr /= 0) return
48
49      s% extras_startup => extras_startup
50      s% extras_check_model => extras_check_model
51      s% extras_finish_step => extras_finish_step
52      s% extras_after_evolve => extras_after_evolve
53      s% how_many_extra_history_columns => how_many_extra_history_columns
54      s% data_for_extra_history_columns => data_for_extra_history_columns
55      s% how_many_extra_profile_columns => how_many_extra_profile_columns
56      s% data_for_extra_profile_columns => data_for_extra_profile_columns
57  end subroutine extras_controls
58
59  integer function extras_startup(id, restart, ierr)
60          use crlibm_lib, only: safe_log10_cr
61          integer, intent(in) :: id
62          logical, intent(in) :: restart
63          integer, intent(out) :: ierr
64          type (star_info), pointer :: s
65          type (binary_info), pointer :: b
66          integer :: restart_time, prev_time_used
67          ierr = 0
68          call star_ptr(id, s, ierr)
69          if (ierr /= 0) return
70          call binary_ptr(s% binary_id, b, ierr)
71          if (ierr /= 0) return
72
73          if (.not. restart) then
74             call system_clock(time0,clock_rate)
75             call alloc_restart_info(s)
76          else
77             call unpack_restart_info(s)
78             call system_clock(restart_time,clock_rate)
79             prev_time_used = time1 - time0
80             time1 = restart_time
81             time0 = time1 - prev_time_used
82          end if
83
84          s% xtra1 = log10(abs(b% mtransfer_rate/(Msun/secyer)))
85          write(*,*) "central hydrogen ", s% center_h1
86          if (s% center_h1 >0.25) then
87             s% lxtra2 =.false.
```

```
88          else
89            s% lxtra2 =.true.
90          end if
91          if (s% center_h1 > 0.0001) then
92             s% lxtra1 = .false.
93          else
94            s% lxtra1 = .true.
95         end if
96
97         if (safe_log10_cr(s% L(1)/Lsun) < -2.5) then
98             s% lxtra3 = .true.
99         else
100           s% lxtra3 = .false.
101
102        end if
103        extras_startup = keep_going
104 end function extras_startup
105
106 integer function extras_check_model(id, id_extra)
107          use crlibm_lib, only: safe_log10_cr !#  ADD
108          type (star_info), pointer :: s
109          type (binary_info), pointer :: b
110          integer, intent(in) :: id, id_extra
111          integer :: ierr
112          ierr = 0
113          call star_ptr(id, s, ierr)
114          if (ierr /= 0) return
115          call binary_ptr(s% binary_id, b, ierr)
116          if (ierr /= 0) return
117          if (s% model_number > 1 ) then
118              s%  do_element_diffusion = .true.
119              s%  diffusion_use_full_net = .true.
120                write(*,*) "element diffusion is ON" ! DIF is on!
121 !               write(*,*) "IS WORKING"
122              end if
123
124           if ((s% Teff < 10000) .and. (safe_log10_cr(s% L(1)/Lsun) < -2)
     ) then
125            s% which_atm_option = "WD_tau_25_tables"
126            write(*,*) "Teff < 10000 and log10(L(1)/Lsun) < -2, so using
     WD_tau_25_tables atmosphere boundary conditions"
127           end if
128
129          extras_check_model = keep_going
130 end function extras_check_model
131
132 integer function how_many_extra_history_columns(id, id_extra)
```

```
133         integer, intent(in) :: id, id_extra
134         how_many_extra_history_columns = 1
135  end function how_many_extra_history_columns
136
137 subroutine data_for_extra_history_columns(id, id_extra, n, names, vals,
       ierr)
138         integer, intent(in) :: id, id_extra, n
139         character (len=maxlen_history_column_name) :: names(n)
140         real(dp) :: vals(n)
141         integer, intent(out) :: ierr
142         real(dp) :: dt
143         ierr = 0
144         if (n /= 1) then
145            stop "bad n for data_for_extra_history_columns"
146         end if
147         dt = dble(time1 - time0) / clock_rate / 60
148         names(1) = "runtime_minutes"
149         vals(1) = dt
150 end subroutine data_for_extra_history_columns
151
152 integer function how_many_extra_profile_columns(id, id_extra)
153         integer, intent(in) :: id, id_extra
154         how_many_extra_profile_columns = 3
155 end function how_many_extra_profile_columns
156
157 subroutine data_for_extra_profile_columns(id, id_extra, n, nz, names,
       vals, ierr)
158         integer, intent(in) :: id, id_extra, n, nz
159         character (len=maxlen_profile_column_name) :: names(n)
160         real(dp) :: vals(nz,n)
161         integer, intent(out) :: ierr
162         integer :: k
163         type (star_info), pointer :: s
164         type (binary_info), pointer :: b
165         call star_ptr(id, s, ierr)
166         if (ierr /= 0) return
167         call binary_ptr(s% binary_id, b, ierr)
168         if (ierr /= 0) return
169
170         !ierr = 0
171         names(1) = "d_Lrad_dlnR"
172         names(2) = "lrad_extra"
173         names(3)= "dL_dm"
174         do k=1, s% nz
175
176     if (s% gradT(k) < s% gradr(k)) then
177                 vals(k,1) = s % L(k)*( &
```

```
                                    s% d_gradT_dlnR(k)/s% gradr(k) &
                                    -s% gradT(k)*s% d_gradr_dlnR(k)/(s%
   gradr(k)*s% gradr(k)))
                 else
                        vals(k,1) = 0d0
               end if
               vals(k,2) = s% L(k)*s% gradT(k)/s% gradr(k)
               vals(k,3)= s% dL_dm_expected(k)
         end do
         ierr = 0

end subroutine data_for_extra_profile_columns

integer function extras_finish_step(id, id_extra)
         use crlibm_lib, only: safe_log10_cr
         integer, intent(in) :: id, id_extra
         integer :: ierr
         type (star_info), pointer :: s
         type (binary_info), pointer :: b

         ierr = 0

          call star_ptr(id, s, ierr)
         if (ierr /= 0) return
         call binary_ptr(s% binary_id, b, ierr)
         if (ierr /= 0) return


         extras_finish_step = keep_going
         call system_clock(time1,clock_rate)
         call store_restart_info(s)

         if (log10(abs(b% mtransfer_rate/(Msun/secyer))) >-15.0 .and.  &
            log10(abs(b% mtransfer_rate_older/(Msun/secyer))) <-15.0)
   then
    write(*,*) "begining of mass transfer"
          s% need_to_save_profiles_now = .true.
          s% save_profiles_model_priority = 6
         end if

         if (log10(abs(b% mtransfer_rate)/(Msun/secyer)) <-12.0 .and.
   log10(abs(b% mtransfer_rate_older)/(Msun/secyer)) >-12.0) then
          write(*,*) "end of mass transfer"
              s% need_to_save_profiles_now = .true.
              s% lxtra4 =.true.
         !s% xtra1=s %xtra1+1
              s% save_profiles_model_priority = 7
```

```
222          end if
223
224          if ((s% center_h1 < 0.0001) .and. (s% lxtra1.eqv..false.)) then
225           write(*,*) "end of main sequence"
226               s% need_to_save_profiles_now = .true.
227               s% save_profiles_model_priority = 5
228               s% lxtra1 =.true.
229          end if
230
231          if ((s% center_h1 < 0.25) .and.(s% lxtra2.eqv..false.))  then
232           write(*,*) "0.25 hydrogen  main sequence"
233               s% need_to_save_profiles_now = .true.
234               s% save_profiles_model_priority = 4
235               s% lxtra2 =.true.
236          end if
237
238          if ((safe_log10_cr(s% L(1)/Lsun) < -2.5) .and.(s% lxtra3.eqv..
    false.))  then
239           write(*,*) "cooling track : log L =2.5"
240               s% need_to_save_profiles_now = .true.
241               s% save_profiles_model_priority = 8
242               s% lxtra3 =.true.
243         end if
244
245        if (safe_log10_cr(s% power_h_burn) > 1.7) then
246               s% tol_correction_norm =
247               s% tol_max_correction =
248               write(*,*) "relax tolerance"
249        else
250                 s% tol_correction_norm = 3d-5
251                 s% tol_max_correction = 3d-3
252                 write(*,*) "normal tolerance"
253        end if
254
255       call store_restart_info(s)
256 end function extras_finish_step
257
258 subroutine extras_after_evolve(id, id_extra, ierr)
259          integer, intent(in) :: id, id_extra
260          integer, intent(out) :: ierr
261          type (star_info), pointer :: s
262          real(dp) :: dt
263          ierr = 0
264          call star_ptr(id, s, ierr)
265          if (ierr /= 0) return
266          dt = dble(time1 - time0) / clock_rate / 60
267          if (dt > 10*expected_runtime) then
```

```
268             write(*,'(/,a30,2f18.6,a,/)') '>>>>>>> EXCESSIVE runtime', &
269                dt, expected_runtime, '   <<<<<<<<<  ERROR'
270          else
271             write(*,'(/,a50,2f18.6,99i10/)') 'runtime, retries, backups,
     steps', &
272                dt, expected_runtime, s% num_retries, s% num_backups, s%
    model_number
273          end if
274 end subroutine extras_after_evolve
275
276 ! routines for saving and restoring data so can do restarts
277
278 subroutine alloc_restart_info(s)
279          type (star_info), pointer :: s
280          call move_restart_info(s,restart_info_alloc)
281 end subroutine alloc_restart_info
282
283 subroutine unpack_restart_info(s)
284          type (star_info), pointer :: s
285          call move_restart_info(s,restart_info_get)
286 end subroutine unpack_restart_info
287
288
289 subroutine store_restart_info(s)
290          type (star_info), pointer :: s
291          call move_restart_info(s,restart_info_put)
292 end subroutine store_restart_info
293
294 subroutine move_restart_info(s,op)
295          type (star_info), pointer :: s
296          integer, intent(in) :: op
297
298          integer :: i, j, num_ints, num_dbls, ierr
299
300          i = 0
301          ! call move_int or move_flg
302          call move_int(time0)
303          call move_int(time1)
304
305          num_ints = i
306
307          i = 0
308          ! call move_dbl
309
310          num_dbls = i
311
312          if (op /= restart_info_alloc) return
```

```
313         if (num_ints == 0 .and. num_dbls == 0) return
314
315         ierr = 0
316         call star_alloc_extras(s% id, num_ints, num_dbls, ierr)
317         if (ierr /= 0) then
318            write(*,*) "failed in star_alloc_extras"
319            write(*,*) "alloc_extras num_ints", num_ints
320            write(*,*) "alloc_extras num_dbls", num_dbls
321            call mesa_error(__FILE__,__LINE__)
322         end if
323
324         contains
325
326 subroutine move_dbl(dbl)
327            real(dp) :: dbl
328            i = i+1
329            select case (op)
330            case (restart_info_get)
331               dbl = s% extra_work(i)
332            case (restart_info_put)
333               s% extra_work(i) = dbl
334            end select
335 end subroutine move_dbl
336
337 subroutine move_int(int)
338            integer :: int
339            include "formats"
340            i = i+1
341            select case (op)
342            case (restart_info_get)
343               !write(*,3) "restore int", i, s% extra_iwork(i)
344               int = s% extra_iwork(i)
345            case (restart_info_put)
346               !write(*,3) "save int", i, int
347               s% extra_iwork(i) = int
348            end select
349 end subroutine move_int
350
351 subroutine move_flg(flg)
352            logical :: flg
353            i = i+1
354            select case (op)
355            case (restart_info_get)
356               flg = (s% extra_iwork(i) /= 0)
357            case (restart_info_put)
358               if (flg) then
359                  s% extra_iwork(i) = 1
```

```
360                else
361                   s% extra_iwork(i) = 0
362                end if
363             end select
364 end subroutine move_flg
365
366 end subroutine move_restart_info
367
368 end module run_star_extras
```

APPENDIX G – Nota de imprensa (press release)

O freamento magnético e a misteriosa dança das estrelas duplas

Porto Alegre, 6 de janeiro de 2022 — Aluno de doutorado do Curso de Astrofísica do Instituto de Física da UFRGS dá passo importante no entendimento da formação de estrelas duplas e estudo é publicado na revista *Monthly Notices of the Royal Astronomical Society*.

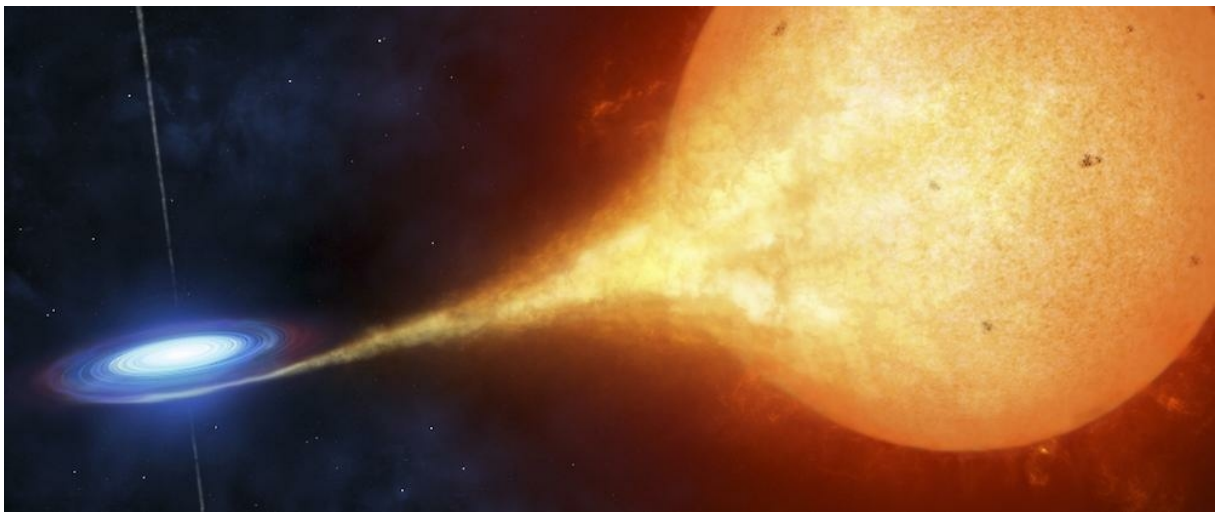

Certamente o que mais chama a atenção de todos ao observarmos o céu noturno são as estrelas. A maioria das estrelas nascem com massa de até 10 vezes a massa do Sol. Isso implica que, ao final da evolução, mais de 95% delas se tornarão anãs brancas canônicas, com cerca de 0,6 vezes a massa do Sol. Ao contrário da crença popular, entretanto, a maioria delas não são estrelas isoladas, mas sim duplas. Assim como os planetas orbitam o Sol devido à atração gravitacional, estrelas binárias são sistemas de duas estrelas que se orbitam devido à essa força. Em sistemas binários, cada estrela se forma afastada da companheira, mas elas vão se aproximando ao longo da evolução. Diversos mecanismos colaboram para a perda de energia do sistema. Por exemplo, a perda de massa e a emissão de radiação gravitacional fazem com que os componentes estelares se aproximem. Durante meu doutorado na UFRGS, investiguei o freamento magnético, um poderoso mecanismo que consome grande quantidade de energia orbital do sistema logo nos estágios iniciais da evolução. O freamento magnético ocorre quando o alto campo magnético de uma estrela aprisiona grande quantidade de matéria ao seu redor, podendo alcançar dezenas de vezes o raio solar. Isso faz com que as estrelas componentes de um sistema

binário se aproximem rapidamente, levando à transferência de matéria entre uma estrela e outra. Um exemplo é mostrado na figura, que traz a interpretação artística de uma estrela semelhante ao Sol perdendo massa para uma estrela de nêutrons. Ao perder a maior parte de sua massa, a estrela que se tornaria uma anã branca canônica acaba por se tornar uma anã branca de massa extremamente baixa, até quatro vezes menos massiva. A receita para quantificar o freamento magnético, no entanto, nunca foi bem estabelecida. Mesmo trabalhos recentes consideram aproximações empíricas feitas nas décadas de 60 a 80, encontrando grandes dificuldades para conciliar as previsões teóricas com as observações astronômicas que medem o período orbital desses sistemas. Tomando como ponto de partida uma nova proposta para o freamento magnético recentemente publicada, utilizei um código computacional de evolução estelar para fazer centenas de simulações computacionais da evolução de sistemas binários que contém estrelas de baixa massa em companhia de estrelas de nêutrons. Essa nova fórmula inclui detalhes sobre a intensidade do campo magnético, a rotação, o raio, a estrutura interna, e a massa da estrela que perde matéria, apresentando resultados teóricos em muito melhor acordo com o que é observado nas anãs brancas de massa extremamente baixa em sistemas binários e seus períodos orbitais. Dessa forma, contribuímos com um pequeno, mas importante passo no entendimento da evolução de sistemas de estrelas duplas e na formação de anãs brancas de baixa massa. O trabalho foi realizado juntamente com o Prof. Dr. S. O. Kepler, líder do grupo de Anãs Brancas do Departamento de Astronomia, e foi publicado na edição de setembro de 2021 na Monthly Notices of the Royal Astronomical Society.

Link para o artigo: 10.1093/mnras/stab1916

Palavras-chave: anãs brancas, estrelas binárias, freamento magnético.

Imagem: <http://www.novacelestia.com/images/binary_starsystems_lowmass_xray_binary.html>. Crédito: Fahad Sulehria, Nova Celestia.

Contato: tayno32@gmail.com, +55 (51) 995726234